Investigation into the surface modification of Ti-6Al-4V to facilitate antimicrobial ionic silver integration for use in implantable orthopaedic devices

Prepared by:

Iosif Vazirgiantzikis

VZRIOS001

Department of Mechanical Engineering
Centre for Materials Engineering
University of Cape Town

Prepared for:

Dr Sarah George

Department of Mechanical Engineering
Centre for Materials Engineering
University of Cape Town

February 2019

Key Words: anodising, $AgTiO_2$, silver, ion implantation, silver release

Declaration

1. I know that plagiarism is wrong. Plagiarism is to use another's work and pretend that it is one's own.
2. I have used the Nature style for citation and referencing. Each contribution to, and quotation in, this PhD Thesis from the work(s) of other people, has been attributed and has been cited and referenced.
3. This PhD Thesis project report is my own work.
4. I have not allowed, and will not allow, anyone to copy my work with the intention of passing it off as their own work or part thereof

Name: **Iosif Vazirgiantzikis**

Signature: Signed by candidate **Date:** 24 October 2019

Acknowledgements

I would like to express my deep gratitude to my supervisor Dr. Sarah George for her guidance and encouragement during this research. To all the staff at CME I would like to say thank you for the support in the labs, this project would not have been possible without you. Thanks to Helen George for the wonderful assistance with editing the thesis. I would like to thank the NRF and LRS implant for providing funding for this research project. I would like to thank the friendly staff at the Nelson Mandela University CHRTEM for their assistance with the TEM and FIB analysis. I would like to thank iThemba labs Gauteng for the RBS work. Additionally, I would like to express my appreciation to Dr. Luc Pichon from the Institut Pprime at the Université de Poitiers, France for collaboration with regards to the silver ion implantation. Finally, I would like to thank my wife and family for their continued love and support during this project.

Abstract

Malignant bone tumours often require a patient to make the choice between limb salvage surgery and complete amputation. The Ti-6Al-4V alloy is the material of choice for implantable orthopaedic devices as it provides a favourable combination of biocompatibility, corrosion resistance and mechanical properties. The only drawback of titanium is that, owing to its bio-inertness, living tissue struggles to attach, creating an opportunity for bacterial adhesion.

The "race for the surface" is the term given for the competition between living tissue and bacteria to colonise the implant surface. If bacterial adhesion occurs at a higher rate than tissue adhesion, the chance of infection rises significantly. It has been shown that there is an opportunity to give tissue adhesion the edge by slowing down the initial colonisation of the implant surface by free-swimming bacteria. Silver has a relatively low toxicity level of 28 mg/kg in the body. Current research has focussed mainly on reducing bio-inertness and improving the antimicrobial properties of titanium via the incorporation of silver. In general, the studies conducted on antibacterial surfaces are limited to testing the final sample directly in contact with bacteria, with no attempt to measure silver release rate profiles.

The research in this dissertation aimed to investigate methodologies for the incorporation of silver into a modified surface of Ti-6Al-4V in order to facilitate an antimicrobial effect for use in orthopaedic implants. The methodologies investigated were: anodic oxidation of Ti-6Al-4V, followed by silver ion exchange; Ag-doped TiO_2 fused to the surface of Ti-6Al-4V via anodic oxidation; and Ag ion implantation into anodically oxidised and polished Ti-6Al-4V. The generated surfaces and sub-surfaces were characterised microstructurally via SEM, FIB, TEM and AFM and chemically by RBS, XRD, AAS and EDS. Ag^+ release rate investigations were conducted with the use of ICP-MS. This study was limited to the use of two anodising electrolytes (*i.e.* 0.5M H_2SO_4 and 2.1M H_3PO_4) and altering the $AgNO_3$ concentration (0.05 - 5.0M) and Ag implantation dosage (0.4 - 1.2x10^{17} ions/cm^2), where applicable to the method.

Results from the Ag ion exchanged samples showed that, microstructurally, the surface produced via anodising in 0.5M H_2SO_4 and 2.1M H_3PO_4 were different in terms of pore morphology, R_a, pore homogeneity across the surface and crystal structure. Sub-surface analysis via FIB/TEM found that the *ca*. 200nm thick TiO_2 samples all contained silver nanoparticles (AgNPs). Samples anodised in 0.5M H_2SO_4 produced an anatase crystal structure, whilst those anodised in 2.1M H_3PO_4 produced rutile crystal structures. Silver uptake by samples anodised in 0.5M H_2SO_4 showed decreases in Ag absorption at high (5.0M) $AgNO_3$ ion exchange concentrations, relative to low (0.05M) concentrations. The opposite effect was observed for samples anodised in 2.1M H_3PO_4. Ag^+ release curves corroborated the absorption data by displaying the same trends in terms of Ag^+ release post ion exchange. It was concluded that it was a combination of diffusion bottlenecking and higher reactivity of the anatase phase formed during anodising in 0.5M H_2SO_4 with Ag^+ *versus* the rutile phase that led to these trends.

Synthesis of TiO_2 powders showed that increasing the $AgNO_3$ concentration (0.05-5M) resulted in Ag-TiO_2 powders with increasing Ag content. Ag-TiO_2 powder was successfully fused to the surfaces via anodic oxidation in 0.5M H_2SO_4 and 2.1M H_3PO_4 at 100V. Ag-TiO_2 powder fused preferentially in areas where downward pressure was present. Microstructurally, the sub-surfaces produced an anodic oxide approximately 200nm thick, to which a significantly thicker, AgNP-containing, TiO_2 was attached. XRD data indicated additional Brookite (020) peaks, owing to the presence of the attached Ag-TiO_2 powder

on the surfaces. Ag-TiO_2 powders attached via 0.5M H_2SO_4 showed a higher overall Ag^+ release at all investigated powder concentrations (0.48 – 76.93 wt% Ag) *versus* those attached via 2.1M H_3PO_4. This was concluded to be due to the anatase phase produced by 0.5M H_2SO_4 having greater oxidative power, thus accelerating oxidative dissolution of the AgNPs. RBS data corroborated these trends. Relative to their Ag ion exchange counterparts, the Ag-TiO_2 samples had a lower Ag^+ release at 0.05M and 0.5M $AgNO_3$ concentrations. However, at 5.0M $AgNO_3$ the Ag-TiO_2 samples had a higher Ag^+ release. This was the trend irrespective of the anodising electrolyte.

Both the anatase and rutile TiO_2s showed a reduction in R_a post Ag ion implantation and the polished Ti6Al4V samples showed an increase in R_a. This was due to preferential erosion of areas with high free surface energy. In the case of both TiO_2s these were "high points" in the oxide and for polished Ti6Al4V these were the grain boundaries. Both TiO_2s were amorphised during ion implantation. All ion implanted TiO_2 showed the presence of AgNPs within the first 50nm of the surface. These AgNPs increased in size as the implantation dosage was increased. Polished Ti6Al4V showed no AgNP formation but EDS mapping confirmed that the silver was also located 50nm within the surface. TiO_2 Ag^+ release was similar for both implantation dosages because the surfaces had been supersaturated at the low dose, thus an increase in implantation dose had no significant effect on further silver uptake. The release rates were also similar between the oxides because of amorphisation. Polished Ti6Al4V showed an increase in Ag uptake and Ag^+ release when the implantation dose was increased. RBS results corroborated the observed Ag^+ release results.

In comparison, both the ion exchanged samples and the Ag-TiO_2 fused samples showed performances in similar ranges of Ag^+ release. The Ag-TiO_2 samples showed a greater degree of tailorability of the Ag^+ release, whereas the ion exchanged samples showed a lesser sensitivity to an increase in $AgNO_3$ concentration. Ag ion implanted samples showed an order of magnitude lower Ag^+ release relative to the other studied methods. In comparison to literature, all ion exchanged and Ag-TiO_2 samples had the potential to have a 100% antimicrobial effect (AE). Ion implanted oxides had a 55-100% potential, while the polished Ti6Al4V had a 55% AE at low dose and a 100% AE at high dose.

In order to achieve maximum silver ion release and the associated antimicrobial effect, the technique of Ag-TiO_2 fused to the surface using the 2.1M H_3PO_4 and 0.5M H_2SO_4 electrolytes yielded the best results, with a silver ion release of 550 and 600 ppb respectively over two weeks. This technique also satisfied the research aim, in that the methodology offered a combination of tailorability of silver release and commercial scalability.

Table of Contents

Contents

List of Figures

List of Tables

1. Introduction

1.1 Background to the Study

A malignant bone tumour often requires the removal of large portions of the affected bone or the entire bone from the body of a patient. A common location of malignant bone tumours is the femur. The patient often has to make a decision between limb salvage surgery and complete amputation. Limb amputation has many repercussions regarding the quality of life and the degree of disability of the patient post-surgery [1].

The Ti-6V-4Al alloy is the material of choice when it comes to limb salvage surgery. This alloy of titanium provides a favourable combination of biocompatibility, corrosion resistance and mechanical properties [2,3]. The only drawback of titanium is that, owing to its bio-inertness, living tissue struggles to attach, creating an opportunity for bacterial adhesion [4].

Studies conducted by A. Racano *et al.* [5] and L.M. Jeys *et al.* [6] showed infection rates of 10% and 11% respectively. However, higher infection rates of 23.5% have been reported [7]. The most common cause of infection is via bacteria. The bacteria that are most commonly responsible for post limb-salvage surgery infections are Staphylococcus aureus (*S. aureus*) and Staphylococcus epidermidis (*S. epidermidis*) [5,6].

Silver has found many uses throughout history because of its antimicrobial activity [8,9]. In modern times silver is used in the water purification and medical industries. The antibacterial property of silver comes from its ability to release silver ions (Ag^+) when in contact with water. The Ag^+ is bioactive and thus has the ability to interact with the proteins, amino acids and receptors located on the bacterial cell wall [10,11].

Silver has a relatively low toxicity level in the body. The accepted No-Observed-Adverse-Effect Level (NOAEL) is 28 mg/kg [7]. The Agluna® method, a technique that incorporates ionic silver into anodised titanium surfaces, has shown successful antibacterial properties achieved with the application of 0.5-5 mg of silver per implant surface. This concentration is well below the accepted NOAEL level [7]. There are still concerns regarding the possible discolouration of skin (argyria) and eyes (agryosis) caused by silver/sulphur complex build-up. However, these conditions are merely cosmetic [12].

Owing to the high infection rates of titanium medical implants and the well-known antimicrobial properties of ionic silver, research has focused mainly on the surface modification of titanium alloy in order to reduce the level of bio-inertness and the incorporation of silver into/on to the titanium surface to impart anti-microbial properties.

In reference to the surface modification of titanium, there have been many studies conducted on anodised titanium surfaces with regards to surface characterisation [2,13–16], bioactivity [17,18] and electrochemical parameters [19–22]. Additionally, there are studies that have focussed on producing antibacterial titanium oxide powders [23,24] or polymer nanofibers [25]. In general, these studies were conducted on antibacterial surfaces where final samples were in direct contact with bacteria, with no attempt to measure silver release rate profiles. In addition, the studies do not offer any methods for the fixation of powder (other than conventional sintering or sputtering) to the surface of the titanium base material in order to prevent detachment during use.

The research below attempts to fill in the above gaps in the literature by the generation of silver release profiles from various surfaces, as well as to offer a novel method for the attachment of titanium oxide particles to the surface of titanium using anodisation, which would therefore not require any high-temperature sintering. Before the research is discussed a literature review is presented to provide background context.

1.2 Aims and Objectives of this Study

1.2.1 *Aims*

The aim of this study is to investigate methodologies for the incorporation of silver into a modified surface of Ti-6Al-4V in order to facilitate an antimicrobial effect for use in orthopaedic implants.

The process should be scalable for later commercialisation.

1.2.2 *Objectives*

In order to achieve the aim of the project, the following objectives must be achieved:

- Investigate the effect of various surface modification techniques on the final surface characteristics of Ti-6Al-4V.
- Use characterisation and analysis techniques to measure the effectiveness of incorporating silver on to modified surfaces by three processes.
- Predict the potential antimicrobial effect by measuring the release of silver from the modified Ti-6Al-4V surfaces in a controlled environment that simulates human body fluid.

The following research questions will be addressed relating to the surface modification and silver incorporation:

- How do process parameters affect the surface morphology, crystal structure and elemental composition of the following surface modification techniques?
    - Polishing
    - Anodic oxidation using phosphoric acid
    - Anodic oxidation using sulphuric acid
    - Doped TiO_2 powders attached through high voltage anodisation

- How do the surface characteristics affect the ability to incorporate silver on to the surface using the following techniques?
    - Ag ion exchange using silver nitrate
    - Ag doped TiO_2 powders attached through high voltage anodisation
    - Ag ion implantation

The following research questions will be addressed relating to the silver release and associated antimicrobial effect:

- How do the anodising electrolytes and crystal structures affect Ag^+ release in all investigated instances?
- How does altering the ion dose affect Ag^+ release from ion implanted surfaces?
- What are the potential antimicrobial effects of these surfaces according to available literature?

For potential commercialisation, scalability must be addressed through the following research question:

- Which of these surface modification methods would be most easily scalable in terms of cost, complexity, production time and tailorability?

1.3 Scope and Limitations

The focus of the study was the development of processes that incorporated silver on to the surface of Ti-6Al-4V for antimicrobial purposes. It focussed primarily on the use of anodic oxidation followed by Ag ion exchange, Ag ion implantation and silver doped TiO_2(Ag-TiO_2) to incorporate silver into/on to the surface of the base Ti-6Al-4V. The study included an investigation into the surface and sub-surface characterisation of the generated surfaces in terms of morphology, crystal structure and elemental composition. It also included *in-vitro* Ag^+ release studies conducted under static conditions. It attempted to compare the Ag^+ release of different produced surfaces. This study was limited to the use of two anodising electrolytes, *i.e.* 0.5M H_2SO_4 and 2.1M H_3PO_4, and to the altering of the $AgNO_3$ concentration and the Ag implantation dosage where applicable to the method, which in general were the only parameters changed within each method. Other anodising conditions were kept constant throughout the differing methodologies to make direct comparison more reliable. This study did not include antibacterial testing data but did infer from literature data whether surfaces should be antibacterial. Finally, in future it will be important to consider the biocompatibility of the surfaces generated in this study, hence, this will not be in the scope of this study.

2. Glossary of Terms

TERM	DEFINITION
ASD	Anodic Spark Deposition
MEM	Minimum Essential Medium
FIB	Focussed Ion Beam
AG^+	Ionic silver
AGNP(S)	Silver Nanoparticle(s)
S. AUREUS	Staphylococcus Aureus
S. EPIDERMIDIS	Staphylococcus Epidermidis
TIO_2	Titanium Oxide
TITANIA	Titanium Oxide
SBF	Simulated Body Fluid
NPS	Nanoparticles
MRSA	Methicillin Resistant Staphylococcus Aureus
MRSE	Methicillin Resistant Staphylococcus Epidermidis
METHICILLIN RESISTANT	Antibiotic Resistant
PASSIVE OXIDE	Able to rapidly self-repair if damaged
COLLOIDAL SILVER	Suspension of sub microscopic metallic silver
FIBROBLAST	Cells that form part of connective tissue
AFM	Atomic Force Microscopy
DI WATER	Deionised Water
CFU	Colony Forming Units
DAE	Dual Acid Etch(ed)
	The energy difference in eV between the top of the valence
PHOTOCATALYST	The ability of nano materials such as TiO_2 to speed up "photoreactions" as a catalyst in combination with light
BAND-GAP	The energy difference (in electron volts) between the top of the valence band and the bottom of the conduction band.
OSSEOINTEGRATION	Bone to implant bonding.
PORE MORPHOLOGY	Related to the description of the distribution, size and shape of the pores.

3. Literature Review

3.1 *In-vitro* Environment for Metallic Materials

Human body fluid is a mixture of many fluid types, such as tissue, lymph and blood fluid. This mixture contains 0.9% NaCl, amino acids, proteins and leukocytes, etc. The pH of body fluid is 7 and may become more acidic (pH 4-5) if inflammatory response is caused by surgery. The normal human body temperature is 37°C [26]. The conditions above are generally considered to be strongly corrosive toward metallic materials. As will be seen, many metallic materials prevent corrosion by the formation of a passive oxide layer, for example chromium oxide on stainless steel and TiO_2 on titanium alloys [26].

3.2 Requirements of Biomaterials

In order for a material to be considered a biomaterial it must fulfil four requirements [26].
These are:

1) **Biocompatibility:** The material must not induce a long-term negative response from the host tissue *i.e.* inflammation or recurring infections.
2) **Sterilisability**: The material must be able to undergo one of various sterilisation techniques such as, autoclaving and gamma radiation without degradation of the material's properties.
3) **Functionablility**: The material must be able to be economically shaped/machined to suit a specific function.
4) **Manufacturability:** The material must be easily or viably manufacturable in terms of cost.

3.3 Properties of Titanium

Titanium is an allotropic material that has an HCP (α) crystal structure at low temperatures and a BCC (β) structure above a temperature of 882°C. Relative to stainless steel and cobalt-chromium alloys, titanium has superior corrosion resistance, which is provided by a naturally-occurring passive titanium oxide (TiO_2) layer. Titanium is an attractive material for the aerospace and medical prosthetics industries as it also has an excellent strength to weight ratio and biocompatibility [27]. The biocompatibility of titanium is due to a dense TiO_2 layer that is passive under virtually all physiological conditions. Since the oxide layer provides a constant barrier between the metal surface and surrounding tissue, it is biocompatible [2,26].

The one drawback of titanium is that the material has poor shear strength, which makes it unsuitable for screws [26]. The introduction of alloying elements can change the allotropic transformation temperature of titanium and can thus stabilise the α, β or α+β phases at room temperature. The stabilisation of different phases at room temperature effects the mechanical properties of the material. Typical α and β stabilisers are aluminium (Al) and vanadium (V) respectively. If a combination of α and β stabilisers is used, both the α and β structures are stable at room temperature, such as in the case of the Ti-6Al-4V alloy. The Ti-6Al-4V alloy is one of the most commonly-used titanium alloys. It has a tensile strength of 1000MPa and a yield strength of 960MPa and has moderate ductility, making it suitable for applications in the aerospace and automotive industries. See Table 1 below for a summary of the properties of α, β and α+β titanium alloys [27]. It must be noted that heat-treatment of the alloy, can affect the microstructure and mechanical properties and thus the values reported in Table 1 are just "average" values.

Table 1 : Summary of the mechanical properties of commercially pure and alloyed titanium [27].

Material	Tensile Strength(MPa)	Vickers hardness	Yield Strength (MPa)	% Elongation
Commercially pure Ti (99%)	551	200	480	15
Alpha Ti alloys 5% Al – 2.5% Sn	860	-	780	15
Beta Ti alloys (13% V–11% Cr-3% Al	1300	-	1200	5
Alpha-beta Ti alloys	1000	349	960	8

3.4 Properties and Mechanisms of Nano-Silver and Ionic Silver

Silver has found many uses throughout history as a result of its antimicrobial activity [8,9]. In modern times, silver has found use in the water purification industry, the main use being colloidal supported on activated carbon or other support materials to assist with removal of bacteria from water. In the medical industry silver as found use in wound dressings, antimicrobial creams and recently in biomedical implants. The antibacterial property of silver comes from its ability to release Ag^+ {silver ion(s)} when in contact with water. The ionisation capacity of various forms of silver are summarised qualitatively in Table 2. Ag^+ are bioactive and thus are able to interact with proteins, amino acids and receptors located at the bacterial cell walls. Therefore, a higher ionisation capacity would lead to greater amounts of Ag^+ release and therefore a greater expected antimicrobial effect. The Ag^+ cation interacts strongly with electron donating groups that contain sulphur, nitrogen and oxygen [28].

Table 2 : Ionisation capacity of various silver compounds [28].

COMPOUND	IONISATION CAPACITY
METALLIC SILVER	Low
SILVER NITRATE	Very High
COLLOIDAL SILVER PREPARATIONS	Moderate to high
SILVER OXIDE	low

The Agluna method, an Ag^+ based surface modification, has shown that successful antibacterial properties are achieved with the application of 0.5 - 5mg of silver into the implant surface. This is well below the accepted NOAEL level [7]. However, there are concerns about the possible discolouration of the skin (argyria) and the eyes (agryosis) caused by silver/sulphur complex build-up, but these conditions are merely cosmetic [28]. The mechanism of Ag^+ antibacterial activity is represented in Figure 1 below.

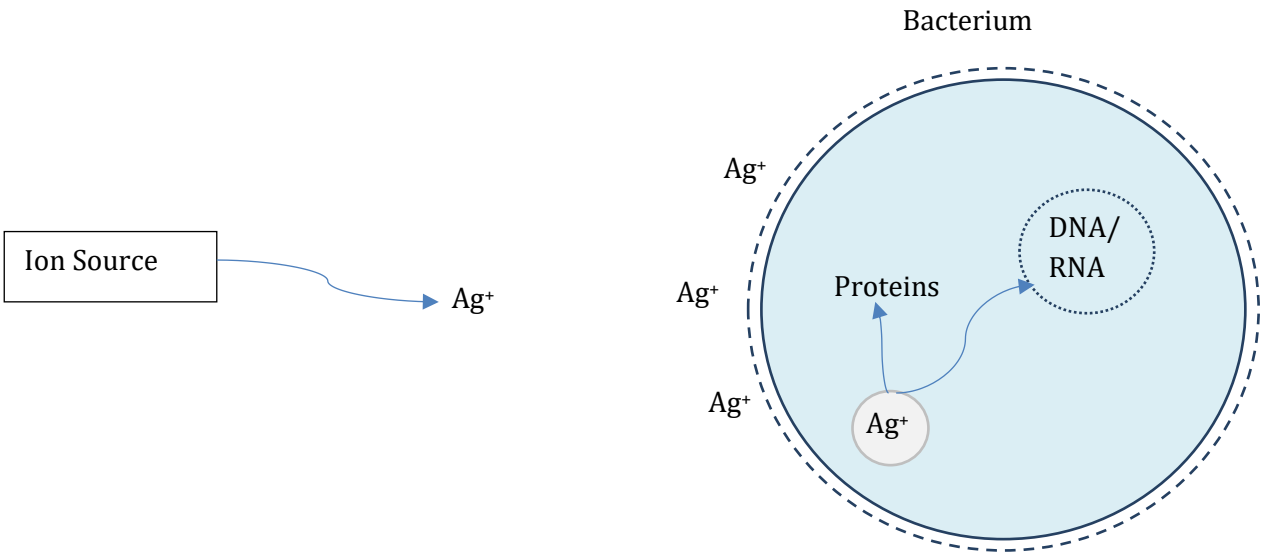

Figure 1 : Illustration of the mechanism of the antibacterial action of silver ions against bacterial cells.

Ag^+ are released from a particular source, such as those presented in Table 2. The Ag^+ interacts with the negatively charged electron donating groups attached to the cell membrane of the bacterium. This stimulates the bacterium to absorb the Ag^+ via endocytosis. Once inside the bacterial cell, the Ag^+ binds and inhibits proteins essential for cellular respiration. The Ag^+ are also able to denature the DNA/RNA of the bacterium cell. As the concentration of Ag^+ increases on the outside of the bacterial cell wall, there is saturation of the binding sites, which allow for the diffusion of nutrients into the bacterium. This results in the starvation and subsequent death of the bacterium cell. Ag^+ also causes the denaturing of the cell wall itself. These multiple mechanisms by which Ag^+ can be fatal to bacteria are the main reasons why bacteria have a low probability to develop resistance towards Ag^+ [11,28].

The mechanism by which silver nanoparticles (AgNPs) act as antimicrobials is not yet completely understood. Some studies attribute the antibacterial properties of AgNPs to their acting in a manner similar to that of ionic silver, *i.e.* by accumulation at the bacterial cell wall, causing its breakdown and, consequently, bacterial cell death [29,30]. Other studies have reported that the antibacterial action of AgNPs is due to the release of Ag^+ from the AgNPs via oxidative dissolution when in contact with dissolved atmospheric O_2 in water, which acts as the oxidising agent [31,32,33]. The important role of O_2 in the dissolution process of AgNPs was confirmed in studies by Z. Xiu *et al.* [33] and C.N. Lok *et al.* [31] on the synthesis of AgNPs in anaerobic and aerobic conditions. It has also been reported that Ag^+ ions are associated with the surface of AgNPs [31,34]. Studies have also shown that the size of the AgNPs and the method of production, *i.e.* which reagents are used, affect the bioactivity of the AgNPs [31,35]. However, it does seem that there is general agreement that Ag^+ release via oxidative dissolution is the main mechanism of the antibacterial action of AgNPs [11,29,31,32,33]. Figure 2 illustrates the discussed AgNP reaction pathways.

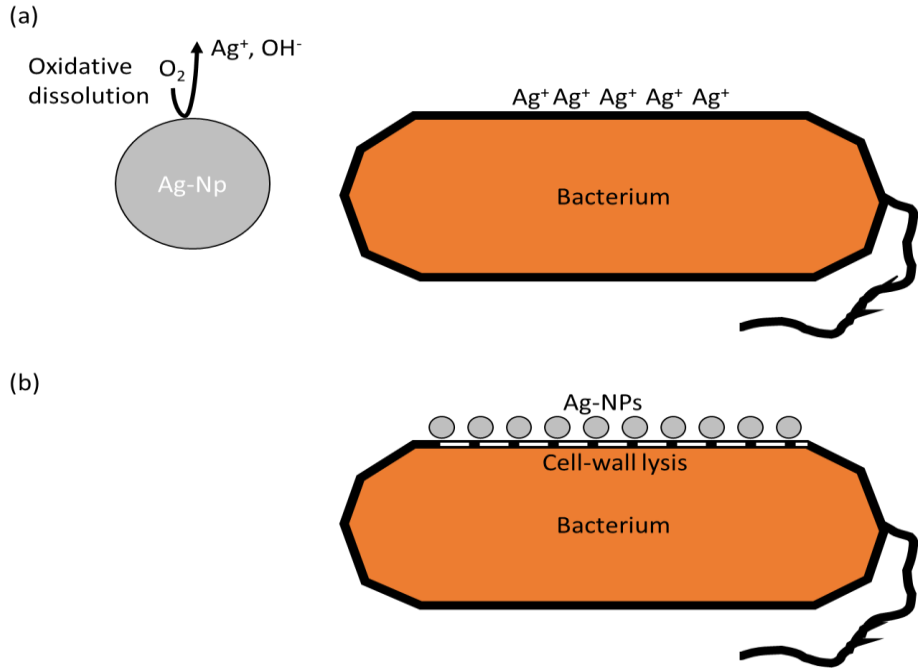

Figure 2 : Illustration of reaction paths of silver nanoparticles with bacterium cell walls (a) via oxidative dissolution and (b) AgNP accumulation at the cell wall [33].

A study by I. Sondi *et al.* [30] investigated at which concentration of AgNPs gram-negative *E.coli* was inhibited. The results are summarised in Figure 3. Figure 3 (a) shows the range of AgNP solutions tested during their study. Their study showed that above an AgNP concentration of 10 µg/ml (0.1ppb) bacterial growth inhibition was significant. The study also inoculated varied AgNP-containing solutions with *E.coli* and found that increasing the AgNP concentration delayed the bacterial growth for up to four hours under the tested conditions after which bacterial growth resumed Figure 3(b). This result was significant as it showed that bacterial growth could be inhibited significantly during the early stages of bacterial colonisation by using AgNPs.

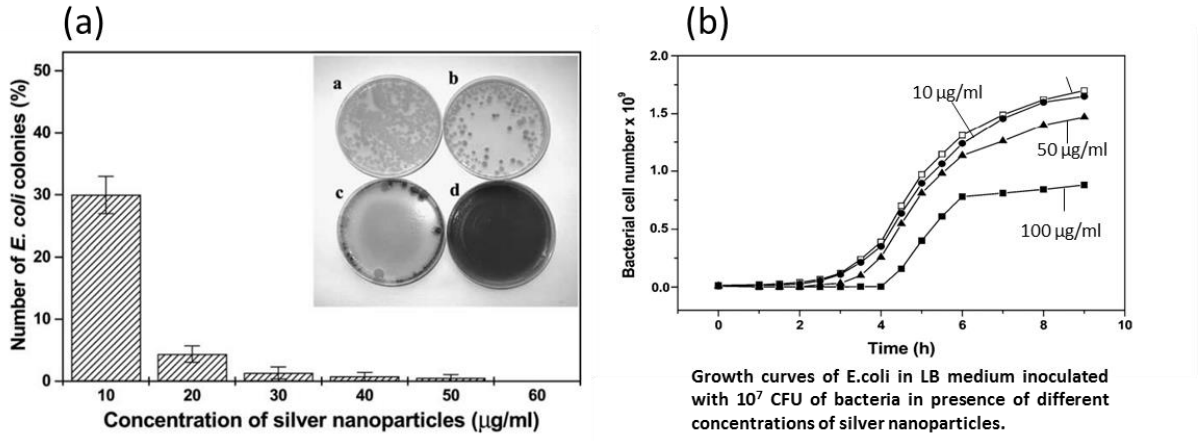

Figure 3 : Experimental results from I. Sondi *et al.* [30] (a) concentration at which of AgNPs inhibited gram negative *E.coli* (b) The length of time gram negative *E.coli* was inhibited in varied solutions of AgNPs.

3.4.1 *Problems Associated with Silver Nanoparticles*

A literature review by N.R. Panyala *et al.* [12] found that AgNPs could bind to proteins, enzymes and the cell walls of mammalian cells. This binding released highly reactive radicals that caused inflammation and the destruction of mitochondria. AgNPs could also cause cell death and necrosis. In addition, it was found that the ingestion of colloidal silver was linked to neurological problems, fatigue, skin irritation and kidney damage.

An interesting study by S. Kittler *et al.* [36] shed some light on the effect of AgNPs on human mesenchymal stem cells (hMSCs). Figure 4 shows that between 1ug/ml (0.01 ppb) and 2.5 ug/ml (0.025 ppb) AgNPs, cell viability remained relatively high for up to one month. However, at above 2.5 ug/ml (0.25 ppb) AgNPs, cell viability reduced to zero after six months' exposure. It must be noted that this test was conducted under static conditions and thus results could vary drastically under flow, because the AgNP concentration in the environment would be more dynamic. But this study did indicate that there were potential risks in AgNPs in the body. These results were significant because they showed that prolonged exposure of human cells to high silver concentrations can be highly detrimental to human cell growth.

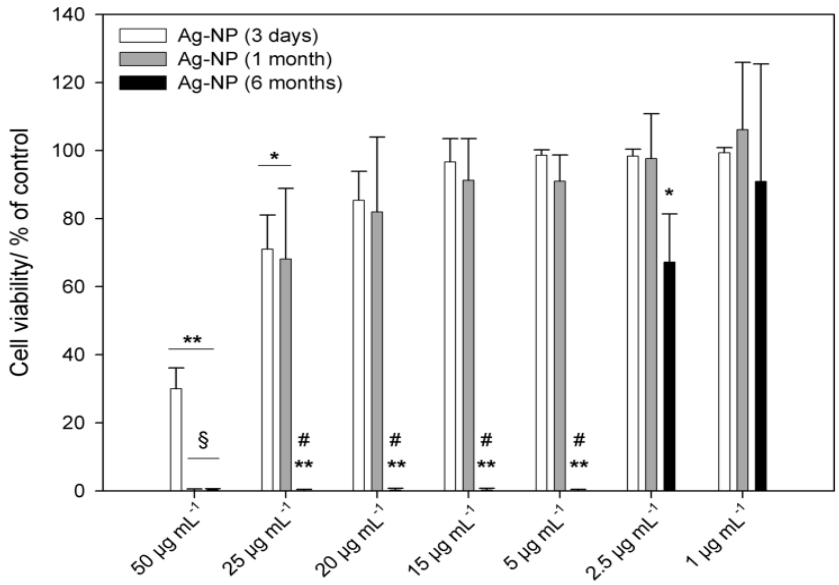

Figure 4 : Effect of the age of silver nanoparticles (AgNPs) after immersion for 3 days, 1 month, and 6 months at 5°C on the viability of hMSCs. The cells were treated with different concentrations of silver nanoparticles for 24h under cell culture conditions [36].

3.5 Staphylococcus Aureus and Staphylococcus Epidermidis

Staphylococci are gram-positive spherical bacteria that are found in the form of microscopic clusters. Staphylococci occur commonly on the skin and in the noses of humans. Of all 20 species of Staphylococci that are known, *S. aureus* and *S. epidermidis* are of greatest concern, owing to their interactions with the human body. *S. aureus* forms yellow/white clusters and *S. epidermidis* forms white clusters. *S. aureus* is mainly found in nasal passages, oral cavities and within the gastrointestinal tract, whereas *S .epidermidis* is almost exclusively found on the skin [37,38].

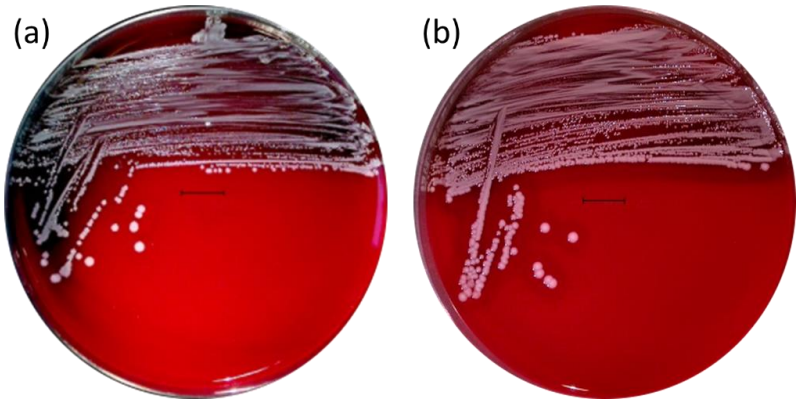

Figure 5 : Colonies of (a) Staphylococcus epidermidis and (b)Staphylococcus aureus, cultivated aerobically on bovine blood agar during 24 h at 37°C [39,40].

S. aureus causes many different kinds of pus-forming infections. Owing to its being such a commonly-occurring bacterium, it creates major problems in hospital environments, as it becomes methicillin resistant [41,42]. *S. epidermidis* infection occurs via an initial attachment step with the formation of a slime-like biofilm on implanted devices, which causes tissue inflammation and immune response [38].

3.6 Bacterial Biofilms

Biofilms can be defined as groups of microorganisms that are attached to a surface, which have grown to such lengths that individual colonies have joined together to form a layer [43]. Studies by A. Gristina *et al.* [44] and C.E. Jim *et al.* [45] refers to the competition between bacteria and tissue integration with respect to same surface attachment as "the race for the surface". If the tissue cells colonise the surface before bacterial cells then the likelihood of bacterial attachment decreases [44].

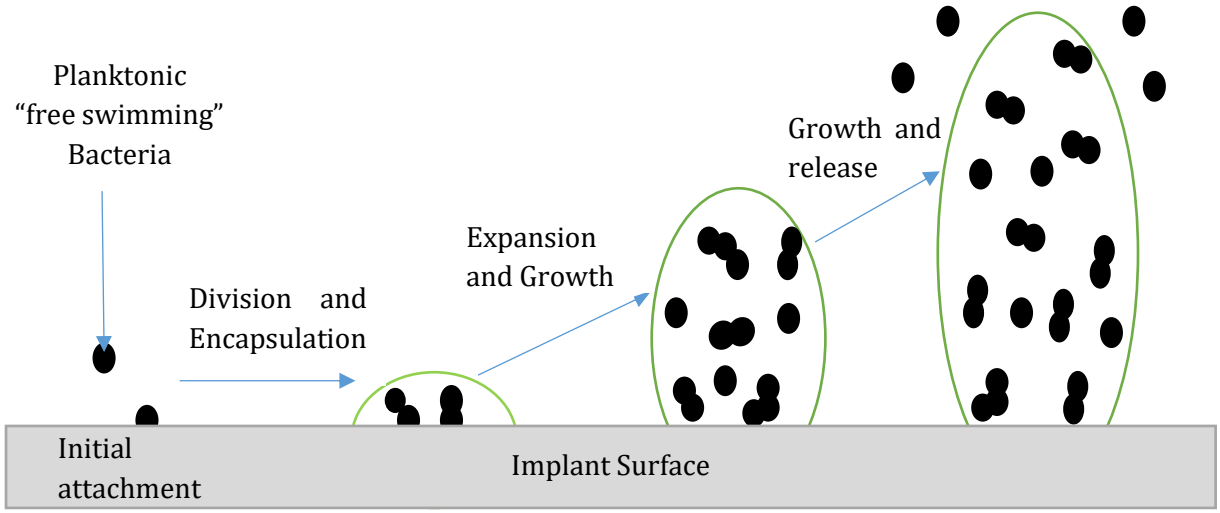

Figure 6 : Illustration of the attachment, growth and release of bacterial cells on implant surfaces [38].

The initial stage of biofilm formation is the attachment of free-swimming bacteria to the implant surface. This is followed by cell division and the growth of a protective matrix polysacceride. This layer provides a barrier against the immune system and provides a level of antibiotic resistance. With continued growth, the density of bacteria within individual colonies increases to a point where the colony will start to release free bacteria which colonise regions surrounding the parent colony. These individual colonies can then group together to form larger colonies on the implant surface. This inhibits tissue integration and causes infection [43–45]. Therefore, a window of opportunity exists during

the initial stages of bacterial adhesion to the surface to swing the race for the surface in the favour of tissue integration.

3.7 Surface Modification Techniques

3.7.1 *Surface of Metallic Materials*

In this review there are two definitions of the surface modification of metallic materials. The more common definition is that a surface treatment achieves a change in surface topography. The less common definition refers to a treatment that achieves a change in surface properties on a molecular level. There are also techniques that affect both surface topography and chemistry [26].

3.7.2 *Surface Oxide Films*

A metal surface such as titanium is usually coated with a thin layer of oxide film. The oxide film surface is covered by hydroxyl groups, on to which water molecules are adsorbed [26]. TiO_2 has been found to be useful as a pigment and as a photocatalyst.

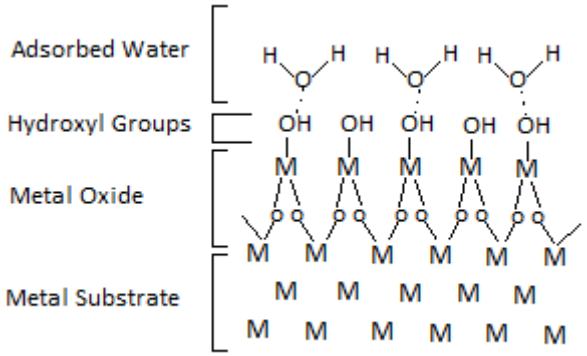

Figure 7 : Illustration of chemical bonding between a base metal and its oxide.

TiO_2 occurs as mainly three minerals, namely anatase, rutile and brookite, the two former having tetragonal crystal systems and the latter having an orthorhombic crystal system, as illustrated in Figure 8. It has been found that the metastable anatase phase exhibits the most photocatalytic activity of the three polymorphs. Anatase has a higher band gap of 3.2 eV relative to rutile, which has a band-gap of 3.0 eV. This increased band gap increases the valence band maximum of anatase, thus increasing its oxidative power. The bulk properties of anatase and rutile are summarised in Table 3 [46–48].

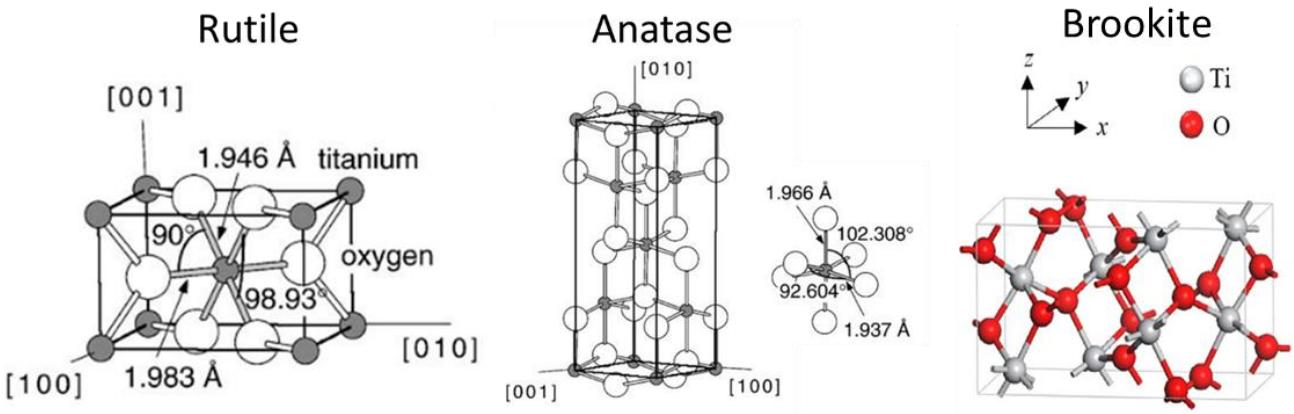

Figure 8 : The primitive cells of rutile, anatase and brookite (from left to right) [46,49].

The oxide on the Ti-6Al-4V alloy surface consists of mostly TiO_2, with small amounts of aluminium oxide also present [26]. The immediate environment around the forming oxide can affect the composition of the formed oxide film. Passive oxide layers, like those on titanium, continually undergo partial dissolution and reprecipitation while in contact with surrounding electrolytes [50]. This means that in a biological environment the properties of the surface oxide can change over time, owing to the incorporation of biological ions from the surrounding environment [26]. This is shown schematically in Figure 9 below.

Table 3 : Bulk Properties of TiO_2 [46].

Crystal Structure	*System*	*Lattice constants(nm)*		*Density(kg/m³)*	*Phase Stability*
Anatase	Tetragonal	a=b=0.4584	c = 0.2953	4240	Metastable
Rutile	Tetragonal	a=b=0.3733	c = 0.9370	3830	Stable
Brookite	Orthorhombic	a = 0.5455 b = 0.9181	c = 0.5142	4110	Metastable

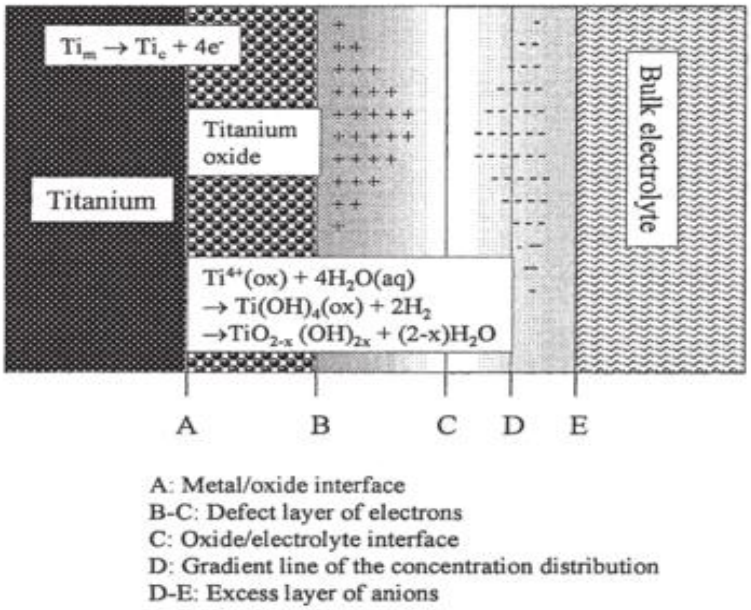

A: Metal/oxide interface
B-C: Defect layer of electrons
C: Oxide/electrolyte interface
D: Gradient line of the concentration distribution
D-E: Excess layer of anions

Figure 9 : Schematic structure of electrical double layer at titanium oxide/electrolyte interface. Subscripts indicate m-metal and c-cation [50].

3.7.3 *Surface Roughening Techniques*

There are a myriad of surface roughening techniques available, which range from acid etching, grinding and polishing procedures to more advanced techniques, such as the use of plasma spray and anodising. Surface roughening can improve the surface area available for silver doping of the titanium alloy surfaces and thus it is important to gain some knowledge of these techniques for possible use in this study. It was found in a study by D.L. Cochran *et al.* [51] that the attachment of soft tissue was slower on the surface of micro-roughened titanium when compared to polished titanium surfaces. Similar conclusions were found in other studies [52,53]. However, it has been shown that higher surface roughness increases the rate of osseointegration [54].

3.7.4 *Dual Acid Etching*

Dual etching involves the immersion of a titanium sample into a combination of HCL and H_2SO_4 for several minutes at up to 100°C. Etching of titanium produces micro-pits with sizes ranging from 0.5 to 2 µm in diameter. The surface that is produced has a micro-rough topography. Figure 10 shows a representation of a surface topography generated by dual acid etching [54].

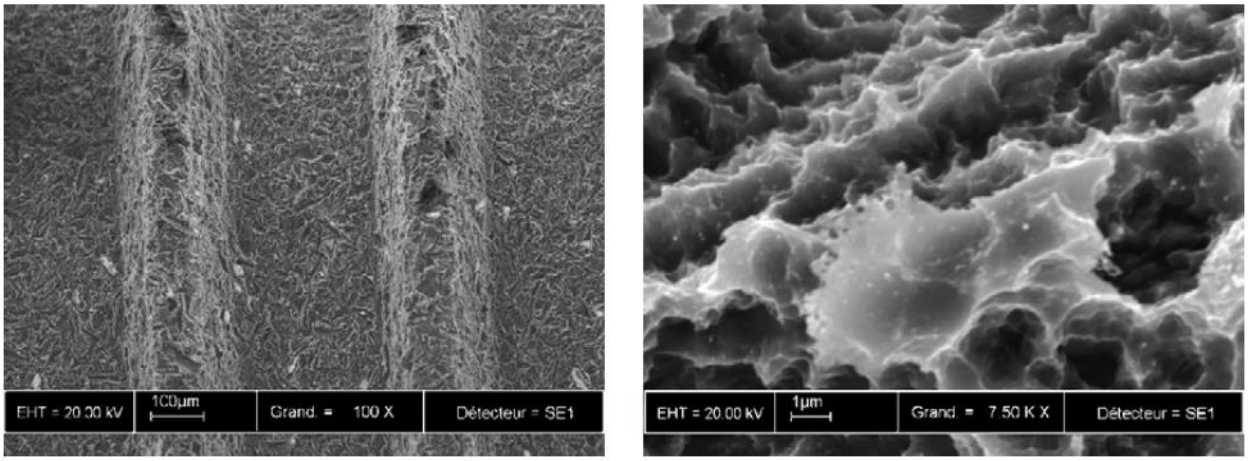

Figure 10 : Scanning electron micrographs of titanium surfaces post dual acid etching treatment [54].

3.7.5 *Piranha Solution*

Another chemical method of surface roughening is to use piranha solution. The solution is made by adding H_2SO_4 (97%) to H_2O_2 (50-30%). The polished titanium sample is then immersed in the piranha solution.

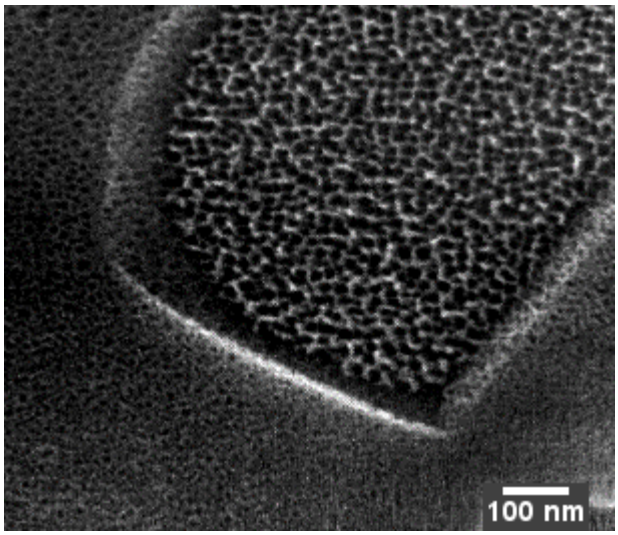

Figure 11 : Scanning elecron micrograph of Ti-6Al-4V after etching in piranha solution.

In the case of Ti-6Al-4V the β-phase is preferentially etched and the formation of nano-pits occurs. Figure 11 shows a surface produced by a 1:1 mixture of H_2SO_4 (97%) to H_2O_2 (50%) [54,55] .

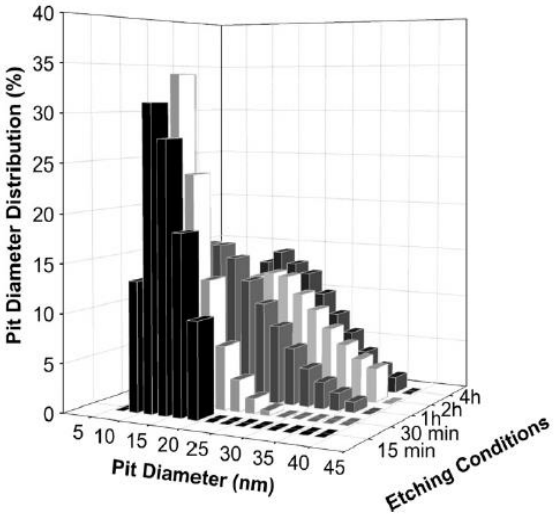

Figure 12 : Evolution of nano-pit diameter as a function of etching time [56].

In a study conducted by Variola *et al*. [56] it was found that piranha solution treatment had no significant effect on fibroblast adhesion. The study also found that the nano-pit diameter distribution on the surface became wider with increased exposure time to piranha solution.

3.7.6 *Anodisation of Titanium*

Anodisation is an electrochemical technique that oxidises the surface of titanium to produce titanium oxide (TiO_2) layers with varied thickness, depending on the electrolyte used, voltage, current density, and temperature [54,57]. Anodisation of titanium is carried out by taking a sample and suspending it in a chosen electrolyte. The titanium sample is attached to the positive terminal (anode) of the voltage source and the counter electrode to the negative terminal (cathode) [2,57]. Figure 13 shows an illustration of the experimental setup for anodisation. The voltage can be increased incrementally or steadily to the desired amount, depending on the thickness of the oxide layer one wants to obtain, and after a predetermined length of time the voltage is decreased to 0. Oxygen can be bubbled through the solution to improve the homogeneity of oxide layer growth [2,57] .

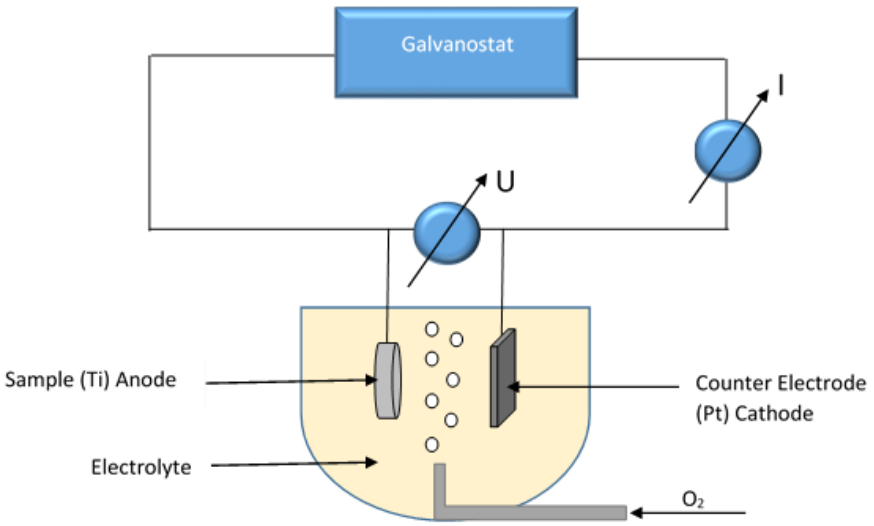

Figure 13 : Illustration of an electrochemical cell used to conduct anodisation [2,56].

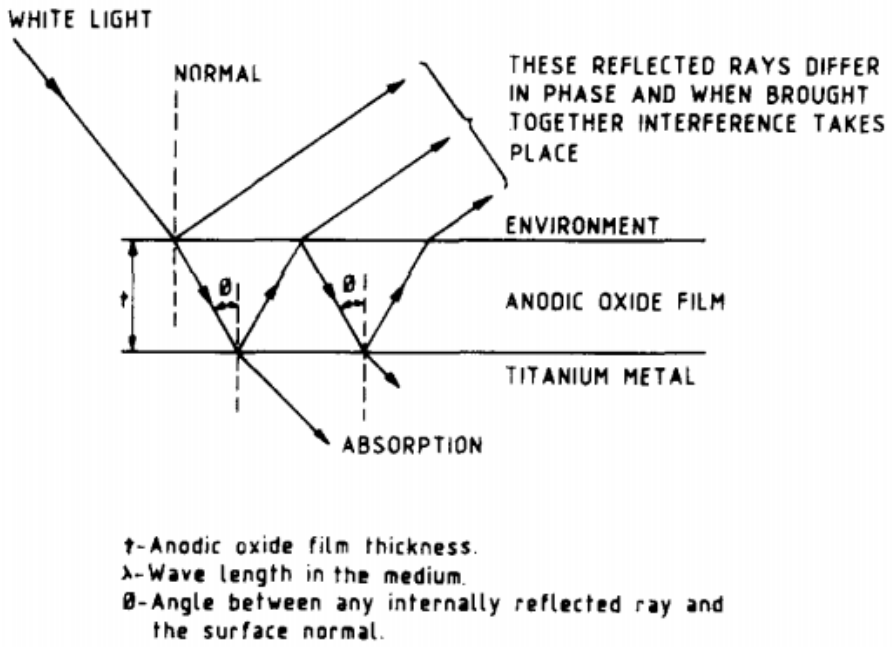

t-Anodic oxide film thickness.
λ-Wave length in the medium.
Ø-Angle between any internally reflected ray and the surface normal.

Figure 14 : Reflection of light at anodic oxide film of titanium [58].

The visual colour of the oxide is related to the thickness of the oxide film and the change in colour occurs owing to interference phenomena when light enters the oxide film. A TiO_2 thin film has the ability to refract, reflect and absorb light. When light falls on to the surface of the oxide film it partly undergoes both reflection and transmission. The light that is transmitted reaches the oxide/titanium interface and some partial absorption takes place. The light is then, once again, reflected towards the oxide/air interface. This process, coupled with multiple reflections, results in a phase shift. Since the phase shift is dependent on the oxide thickness and the number of internal reflections, as well as on the constructive and destructive interactions of the light waves leaving the oxide surface, differences will result in the observed colours for the varying TiO_2 thicknesses [58]. This process is illustrated in Figure 14 above. Table 4 below shows the voltage conditions required to obtain different visual colours of surface oxides on titanium [54,57].

Table 4 : Summary of the interference colours of the titanium oxide layer as a function of applied voltage (DC).

VOLTAGE(DC)	TITANIUM COLOUR
5	Yellow
10	Brass
15	Purple
20	Violet-blue
25	Purple blue
30	light blue
35	Grey blue
40	Pale aqua
45	Green blue
50	Pale Bronze
55	Pale Green
60	Purple
65	Green
70	Rose Gold
75	Red Purple
80	Bronze
85	Gold Purple
90	Rose
95	Dark green
100	Grey
105	Grey
110	-

Anodisation can produce micro-rough and nano-rough surfaces. Common electrolytes used for anodising are H_2SO_4, H_3PO_4, HNO_3 and HF. A study by D. Velten *et al.* [2] showed a near linear relationship between applied voltage and TiO_2 layer thickness, when oxide layer thickness was related to applied voltage at a constant current density of 2mA/cm^2 (See Figure 15 below). D. Velten *et al.* [2] were also able to correlate oxide layer colour to a thickness range (See Table 5).

It can be seen that Table 4 and Table 5 correlate to some degree. The difference in values is that the results in Table 4 are based on pure titanium, whereas D. Velten *et al.* [2] averaged results from both CP-Ti and Ti-6V-4Al samples into Table 5, which would skew results away from those of pure titanium [2,57]. The results of these studies discussed above were important because, when combined, they allow for the prediction of oxide layer thickness via visual/macroscopic inspection.

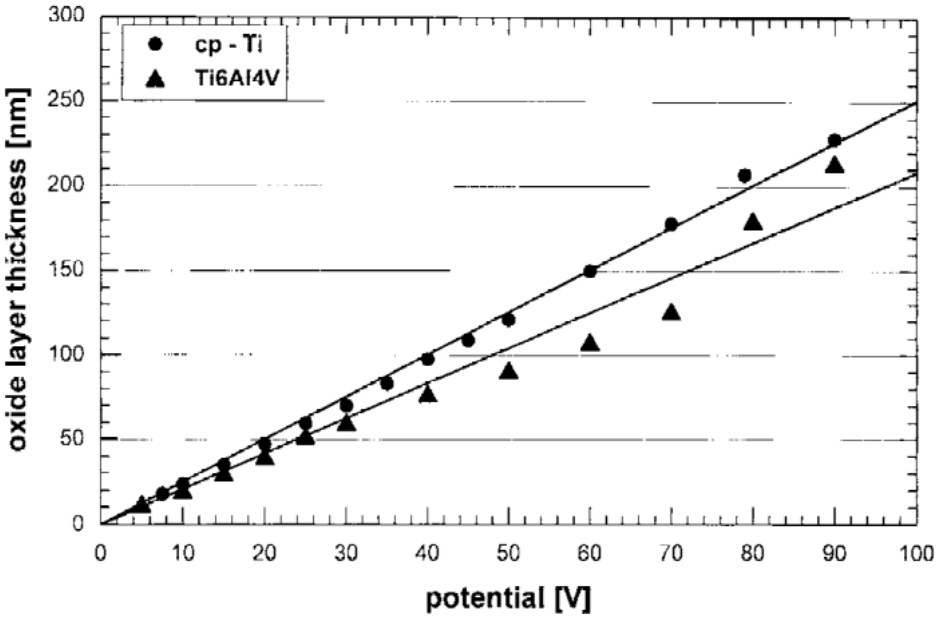

Figure 15 : Correlation between oxide layer thickness and applied potential of oxides produced by 0.5M H_2SO_4 2mA/cm² [2].

Table 5 : Colours of oxide layers after anodic oxidation [2].

COLOURS OF OXIDE LAYERS AFTER ANODIC OXIDATION

LAYER THICKNESS(NM)	10-25	25-40	40-50	50-80	80-120	120-150	150-180	180-210
COLOUR	Golden	Purple	Deep Blue	Light Blue	Yellow	Orange	Purple	Green

Research conducted by D. Gong *et al.* [13] found that nano-tubular TiO_2 could be formed via anodisation in a 0.5-3.5wt% HF solution at 20V for 20 minutes (See Figure 16).

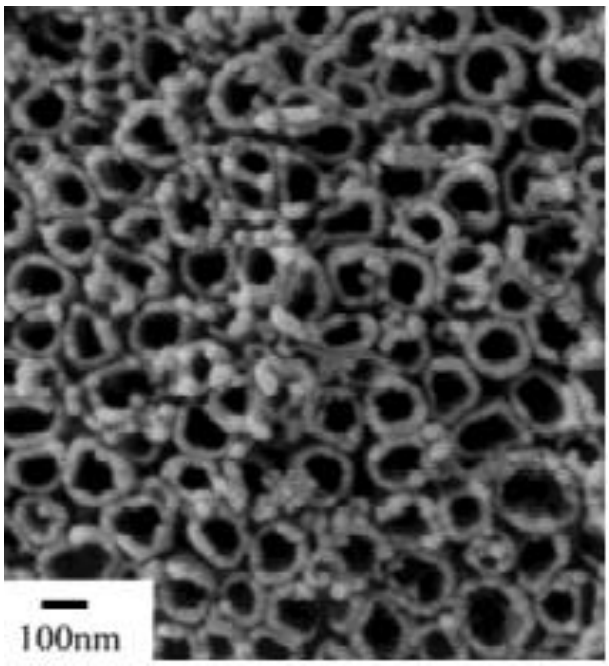

Figure 16 : Nano-tubular oxide layer [13].

There are many parameters that affect TiO_2 layer characteristics during anodisation: electrolyte concentration, pH, temperature, the potential difference applied between the cathode and the anode, and the current density imposed to achieve a specific value of potential difference [19]. In research conducted by Diamanti *et al.* [19], anodisation was conducted at constant current density (20 mA/cm^2) with changing H_2SO_4 electrolyte concentration. It was found in this study that as electrolyte concentration increased the maximum attainable potential decreased (See Table 6). These results are important to this study because a voltage of 100V was planned to be used and thus an electrolyte capable of reaching these potentials could be selected.

Table 6 : Maximum value of cell potential achieved as a function of solution concentration [19].

	MAXIMUM POTENTIAL ATTAINED (V)
H_2SO_4 0.25M	120
H_2SO_4 0.5M	110
H_2SO_4 0.7M	100
H_2SO_4 1.0M	90
H_2SO_4 2.0M	70

During the same study, potential growth rates during the first 10 seconds of reaction were determined for each electrolyte concentration, as well as the time taken to reach 70V potential. Table 7 shows the results [19].

Table 7 : Potential growth rate in first 10s of polarisation (dV/dt) and anodisation to reach 70V (T_{70V}) as a function of solution [19].

	H_2SO_4 0.25M	**H_2SO_4 0.5M**	**H_2SO_4 0.7M**	**H_2SO_4 1.0M**	**H_2SO_4 2.0M**
***DV/DT* [V/S] 1ST 10 SEC**	3.37	3.54	2.97	2.90	1.58
T_{70V}[S]	58	45	44	60	510

Phase analysis by XRD showed that with increasing concentration of electrolyte the potential at which the anatase phase began to appear decreased *i.e.* higher electrolyte concentrations favoured anatase formation [19].

Table 8 : Anatase formation theshold voltages as function of H_2SO_4 solution concentration [19].

CONCENTRATION	THRESHOLD VOLTAGE
0.25M	90V
0.5M	70V
0.7M	Lower
1M	Lower
2M	Lower

Only the threshold values for anatase formation of 0.25M and 0.5M were reported by M.V. Diamanti *et al.* [19]. However, in their findings they reported the trend to decrease with increasing molarity. The group reported that the 0.5M H_2SO_4 electrolyte offered the best compromise between maximum attainable voltage and anatase formation. The formation of anatase phase may be an important factor in the this study, because the greater oxidative power of anatase phase could affect the oxidative dissolution of silver nanoparticles formed during the surface modification techniques investigated.

In a second set of experiments M.V. Diamanti *et al.* [19] kept the electrolyte concentration constant at 0.5M and varied the current density from 10 to 108 mA/cm^2. It was found that, as the current density was increased, the maximum attainable voltage would increase from a minimum at 70V to a maximum at 150V. Phase analysis showed that increasing the current density promoted anatase formation. It was also reported that morphology was affected by anodic spark deposition (ASD) at voltages higher than 100V and current densities above 40 mA/cm^2. This ASD phenomenon gave rise to small craters on the surface [19].

In a study by S. Uttiya *et al.* [20] anodic oxidation of titanium using H_2SO_4 and H_3PO_4 electrolytes were compared. Figure 17 shows their results. The surfaces in images (a) and (c) were produced by anodisation in 1M H_2SO_4 at 100V and 150V respectively, while the surfaces in images (b) and (d) were produced using 1.5M H_3PO_4. It can be seen that in (a) there is formation of isolated pores and in (c) the pores are more of a network surface morphology, owing to the merging of individual pores. When comparing the different results when using H_2SO_4 and H_3PO_4, it can be seen that H_3PO_4 does not have a strong tendency to form a porous surface, even when anodised at 150V. The pore size distributions are shown in (e) for 100V H_2SO_4 and (f) for 150V H_2SO_4.

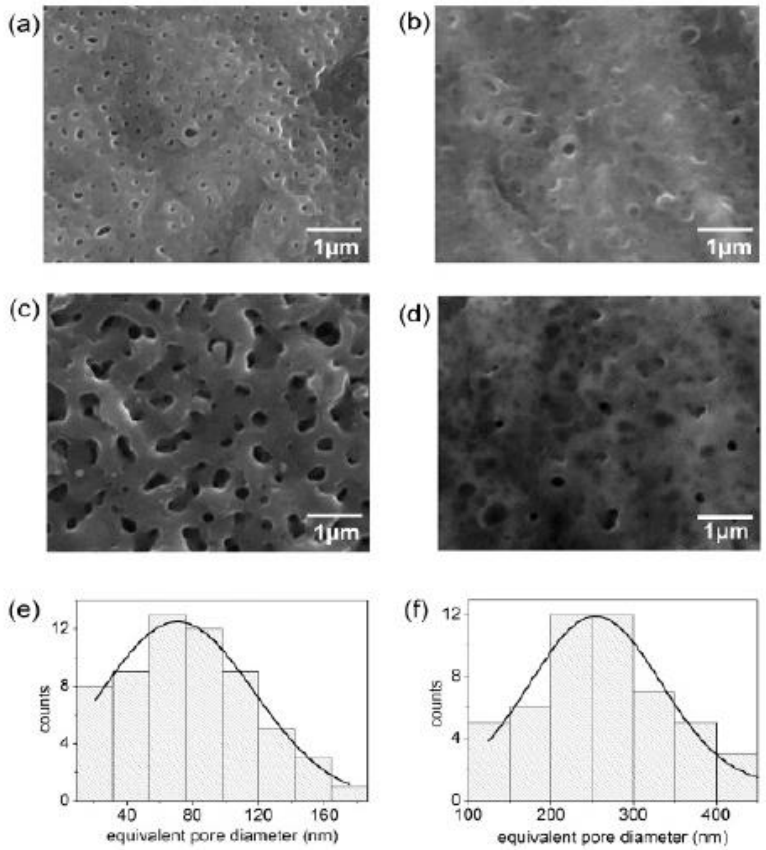

Figure 17 : SEM images of titanium samples after anodisation in (a) H_2SO_4 at 100V, (b) H_3PO_4 at 100V, (c) H_2SO_4 at 150V, (d) H_3PO_4 at 150V, (e) histogram of the equivalent pore diameters of samples anodised in H_2SO_4 at 100V, (f) histogram of the equivalent pore diameters of samples anodised in H_2SO_4 at 150V [20] .

Morphology studies via atomic force microscopy (AFM) found that the pores in 100V H_2SO_4 samples had clearly-defined wall boundaries. It was also found that oxide layers grown in H_2SO_4 were more uniform than those grown in H_3PO_4. This study corroborated the findings of M.V. Diamanti *et al.* [19] with respect to H_2SO_4 facilitating an oxide layer that had a prevalent anatase crystalline phase. S. Uttiya *et al.* [20] found, via XPS analysis, that H_3PO_4 tends to create phosphate inclusions. This is interesting as there are reports that phosphates increase bone attachment rates [45,54,59]. In a study by H.J. Oh *et al.* [60], XPS analysis showed the presence of sulphur and phosphate inclusions post 180V anodisation for 30 minutes in a 1.5M H_2SO_4/ 0.3M H_3PO_4/0.3 M H_2O_2 mixture electrolyte. H.J. Oh *et al.* [60] also found that thicker oxide layers were produced in a 1.5M H_2SO_4/0.3 M H_2O_2 solution without a significant change in the morphology when a purely 1.5M H_2SO_4 electrolyte was used. The morphology was similar to those presented in Figure 17 (c). It was proposed that this phenomenon was due to the reaction between the peroxide and the titanium surface. This study once again confirmed that the major oxide phase present was anatase after anodisation [60] .

In a study by N.K. Kuromoto *et al.* [15] anodisation was carried out on CP-Ti in a 1.4M H_3PO_4 solution. Figure 18 shows the results of the anodisation at voltages ranging from 50 - 250V. It can be seen that a porous structure is observed only at 150V and above. The surface morphology found below 150V resembles the morphology found by S. Uttiya *et al.* [20] for H_3PO_4 anodised samples. Therefore, the study by N.K. Kuromoto *et al.* [15] showed that a surface morphology similar to that produced by a H_2SO_4 electrolyte could be produced, but only at much higher voltages.

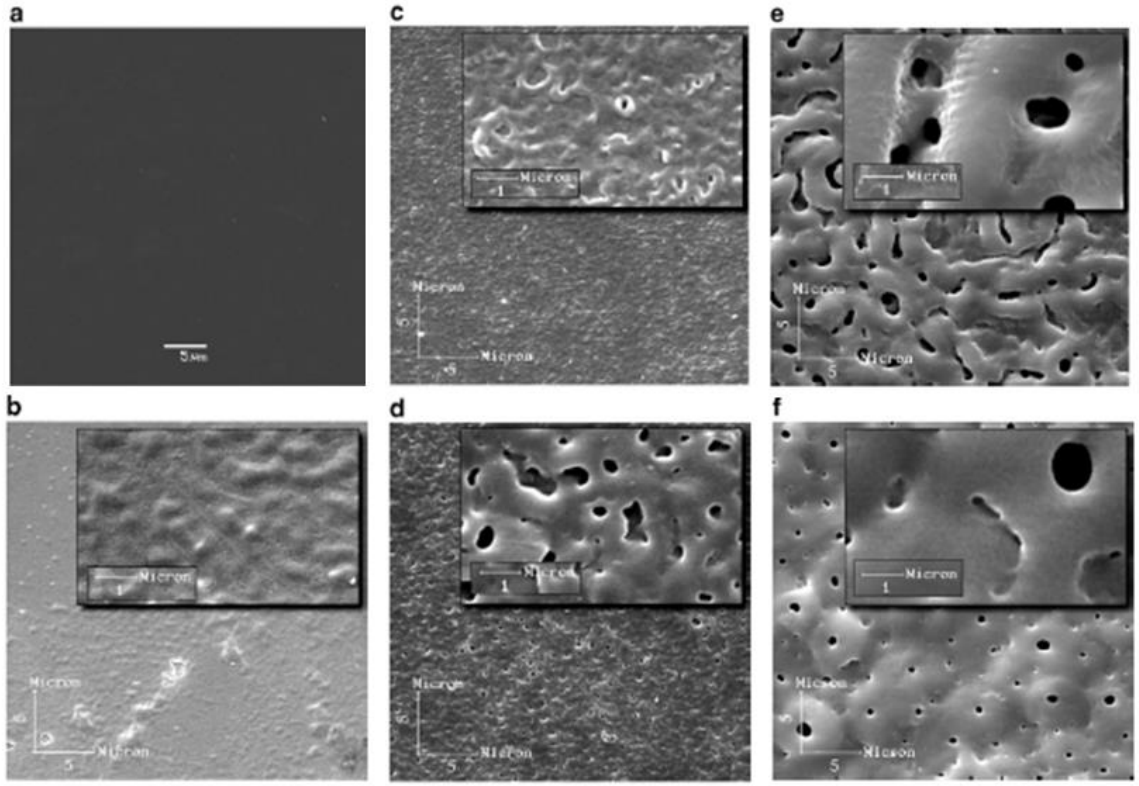

Figure 18 : SEM micrographs of titanium oxide films on cp-ti surfaces: (a) cp-Ti, (b) 50V, (c) 100V, (d) 150V, (e) 200V, (f) 250V [15].

In a Study by H.Z. Abdulla *et al.* [21] it was found that the oxide layer had four stages of development. These stages of development depended on the applied potential:

- Stage 1: At very low potentials (5V), oxidation commenced and the oxide layer formed was incoherent (amorphous).
- Stage 2: At low potentials (10 V), a smooth monolayer of about 3nm thickness formed, which consisted mainly of anatase.
- Stage 3: At intermediate voltages (20-70 V), the film thickness increased but growth was accelerated on surface defects, causing an uneven surface.
- Stage 4: At high voltages (100V) there was pore formation, owing to dielectric breakdown (arching). At voltages higher that 100V these effects were enhanced.

H.Z. Abdulla *et al.* [21] were in agreement with N.K. Kuromoto *et al.* [15] in terms of surface morphology.

In a study by Y.T. Sul *et al.* [61], various electrochemical parameters were investigated and their effect on the interference colour produced was noted (Table 9). The interference colours in this study correlate well with the results found by D. Velten *et al.* [2]. From the data in this study it can be shown that the oxide layer thickness increased linearly for samples anodised in H_3PO_4 at up to 100V. The H_2SO_4 electrolyte oxide grew at a linear rate until 80V and then an increase in the rate of oxide formation was observed between 80 - 120V. The results are summarised in Figure 19 below. These results were similar to those obtained by D. Velten *et al.* [2].

Table 9 : Summary of electrochemical parameters and oxide thickness [61].

VOLTAGE(V)	TIME(S)	OXIDE THICKNESS(NM)	INTERFERENCE COLOUR
SULPHURIC ACID ,1.0 M 15 MA/CM²			
22	2.5	54.3	Dark Purple
50	7.5	93	Bright Blue
80	18.5	147.7	Bright Orange
100	44.5	242.4	Green
130	156	361.5	Gray
PHOSPHORIC ACID 1.0M 5MA/CM²			
20	6.5	45.7	Orange
40	9.5	67.3	Dark Blue(green)
60	12.5	96.7	Blue + Gray
80	17	120	Green
100	23	154	Reddish Yellow

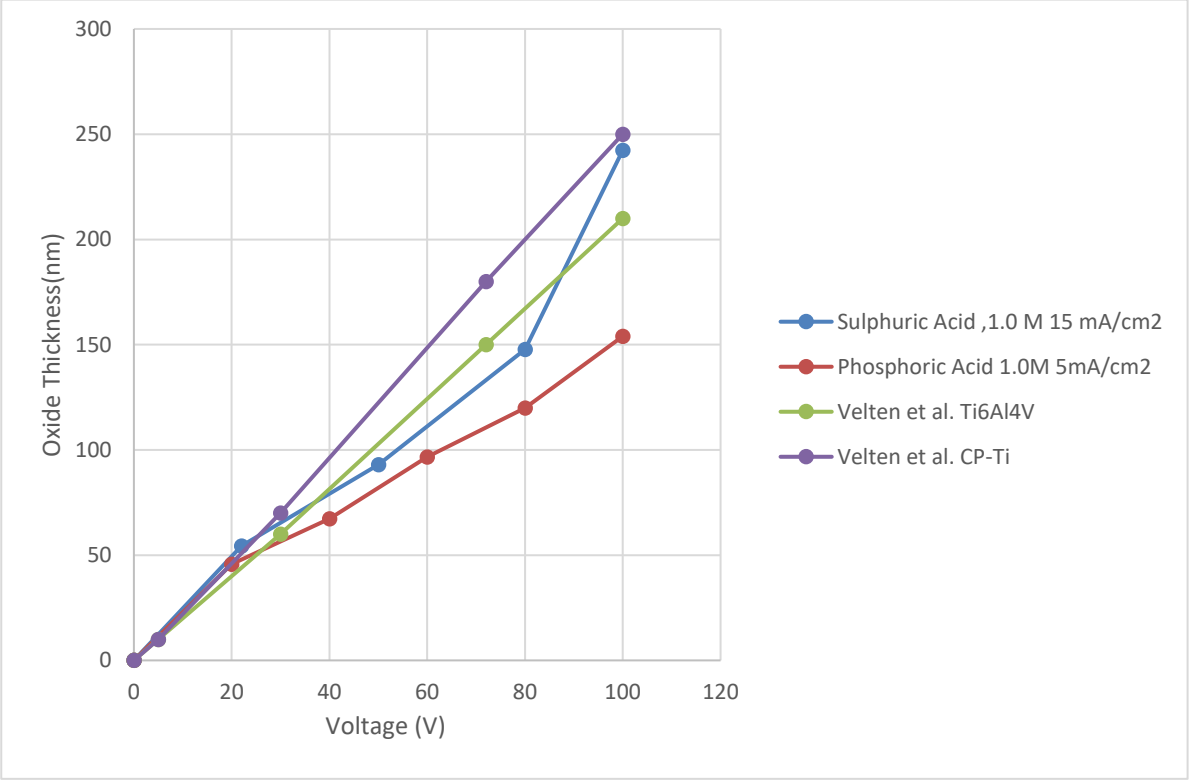

Figure 19 : Line graph showing the linear relationship between oxide thickness and applied voltage [61,2].

In a study by B. Yang *et al.* [22] where a CP-Ti substrate was anodised at DC voltages of 90,155 and 190 with a constant electrolyte concentration of 1M H_2SO_4 for 1min, the microstructural observations (Shown in Figure 20), i.e. the surface porosity, were in agreement with results reported in the previously discussed studies conducted by S. Uttiya *et al.* [20] and M.V. Diamanti *et al.* [19] . Furthermore, it was found that at 90V the CP-Ti showed a complete anatase crystal structure. Increasing the anodising voltage to 150V resulted in a mixed anatase/rutile oxide up to 180V where the oxide was found to be completely rutile [22].

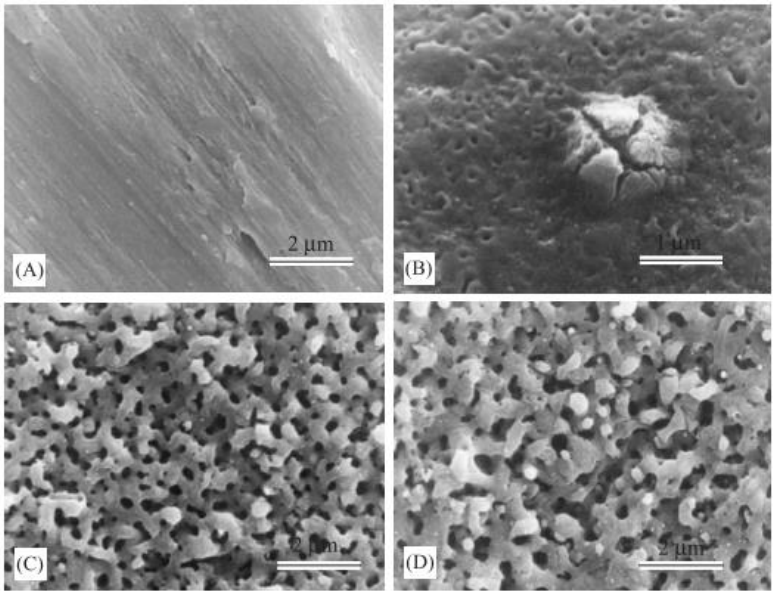

Figure 20 : SEM photographs of (a) titanium metals without treatment and titanium metals anodically oxidised at (b) 90V , (c) 155V, (d) 180V in 1M H_2SO_4 for 1 min [22].

Table 10 : Properties of samples after anodic oxidation and soaking in SBF [22].

Parameters for study	Sample number	Treatment condition	After anodic oxidation		Apatite formation ability in SBF	
			Anatase	Rutile	3 days	6 days
Voltage	1	90 V	+	−−−	−−−	−−−
	2	155 V	++	+++	+	+++
	3	180 V	−−−	++++	++	+++
Heat treatment	4	90 V + HT	++	+	++	+++
	5	155 V + HT	++	+++	++	+++
	6	180 V + HT	−−−	+++	++	+++
Concentration of H_2SO_4	7	0.5 M	+++	++	+	+++
	8	1 M	++	+++	+	+++
	9	3 M	+	+++	++	+++

"+, ++, +++": The ability to form anatase, rutile or apatite on the metal surface, respectively.
"−−−": Without ability to form anatase, rutile or apatite on the metal surface.

Another interesting result was that the apatite formation ability (a measure of bioactivity/compatibility) of the surfaces only occurred in samples where anodic spark deposition had taken place, *i.e.* above 90V. In the same study, the anodised samples were heat treated and it was found that an increase in the oxide layer thickness assisted in the increase in bioactivity relative to the thinner layer that had been produced by anodisation only at 90V. The use of 0.5M H_2SO_4 electrolyte led to the formation of a highly anatase oxide layer with a good ability to form apatite. This is important because it indicates that the sulphuric acid electrolyte concentration used in this study could improve

the bioactivity and biocompatibility of the formed oxide layer. Although biocompatibility studies are not within the scope of this thesis, it is important to aim to use electrolytes that have seen success in other studies. The results are summarised in Table 10 [22]. In a study by H. Song *et al.* [17] the surface characteristics and bioactivity of oxide films formed by high voltage anodisation were investigated. This study also concluded that anodically oxidised samples were more bioactive relative to as-received titanium surfaces.

3.7.7 *Agluna Method*

The Agluna method uses anodisation to grow a titanium oxide film onto a titanium substrate, this is followed by a silver ion exchange reaction to dope the surface oxide with silver. The idea being that the surface would release silver ions over time, which would act as an antimicrobial agent. It was important to test this method as it was already in production and would serve as a good control to compare other silver ion incorporation methods investigated in this study [62].

According to the patent for the Agluna method and related literature discussed previously, a polished sample attached to a positive electrode was placed in a dilute acidic electrolyte, either 2.1M H_3PO_4 or 0.1M H_2SO_4. The next step was to generate a thin passive TiO_2 film on the surface. This was achieved by exposure to 15V for a time period not specified in the patent at a current density of 2.5-10 mA/cm^2. Passivity of the oxide was achieved when current density dropped below 1 mA/cm^2. The voltage was then reduced to 0 and then increased either incrementally or steadily to 100V and once the oxide became passive it was kept at 100V for 1-10 min. During this step water molecules were oxidised to form peroxides via [62]:

$$2H_2O \rightarrow H_2O_2 + 2H^+ + 2e^-$$

The generated peroxides reacted with Ti-O$^+$ to produce a soluble peroxy-titanyl complex via:

$$TiO^{2+} + H_2O_2 \rightarrow TiO_2^{2+} + H_2O$$

The formed peroxy-titanyl complex was held within the pores generated by anodisation. After exposure to 100V the voltage was reduced to 20V for 20 min. (The patent does not state the purpose of this final step.) The sample surface was then exposed to a reducing agent of 0.1M KBr for seven minutes. The reduction step reduced peroxy-titanyl to titanium hydroxide ($Ti(OH)_4$). The sample was then rinsed in deionised (DI) water and then exposed to a 0.1M $AgNO_3$ solution for 60 min in order for ion exchange to occur. This caused an ion exchange reaction between the hydrogen atom of the hydroxide ligand and the silver ions, producing a Ti-O-Ag bond, thereby incorporating ionic silver into the surface [62].

In Section 3.7.6 it was seen that the most common acidic electrolytes used were sulphuric and phosphoric acid. It was shown in that section that H_3PO_4 was not able to produce the surface morphology at the anodisation voltages claimed by the Agluna method (100V), but H_2SO_4 was able to. Furthermore, there was already literature (See Section 3.7.6) that described the effect of H_2SO_4 concentration, applied potential and current density on oxide layer phase composition. A study by H.J. Oh *et al.* [60] reported that the anatase phase was more reactive than the rutile phase of the oxide layer. This further strengthened the choice of using H_2SO_4 as it was reported that anodisation using a H_2SO_4 electrolyte resulted in the anatase phase being the most prevalent phase composition at Agluna method voltages.

3.7.8 *Sol-Gel Technique*

The sol gel process is one of the main processes used to incorporate metal ions such as Ag, Cu and Fe into titanium oxide particles or films [63]. The metal oxide is produced from a metal alkoxide precursor in an alcohol-based solvent. The metal surface to be coated is placed into the solution and stirred at high speeds up to 6000rpm. In a study by D. Velten *et al.* [2] a $Ti(OC_4H_9)_4$ solution was used as the alkoxide and ethanol as the solvent. During stirring the alkoxide coated the surface of the sample and, simultaneously, the solvent evaporated and the alkoxide reacted with atmospheric water to produce a metal hydroxide (titanium hydroxide) and butanol. See Reaction 1[2].

$$Ti(OC_4H_9)_4 + 4\,H_2O \rightarrow Ti(OH)_4 + C_4H_9OH \quad (1)$$

With continued hydrolysis the titanium hydroxide started to form Ti-O-Ti linkages, thus producing three-dimensional TiO_2 particles on the surface. A drying step was then employed at about 130°C for 30 minutes to evaporate any residual solvent. This caused individual TiO_2 particles to agglomerate. A final sintering/annealing step was then employed at 300 - 700°C for one hour in order to remove residual organic compounds and to bind TiO_2 particles together to form a layer [2]. A schematic of the sol-gel process is given in Figure 21.

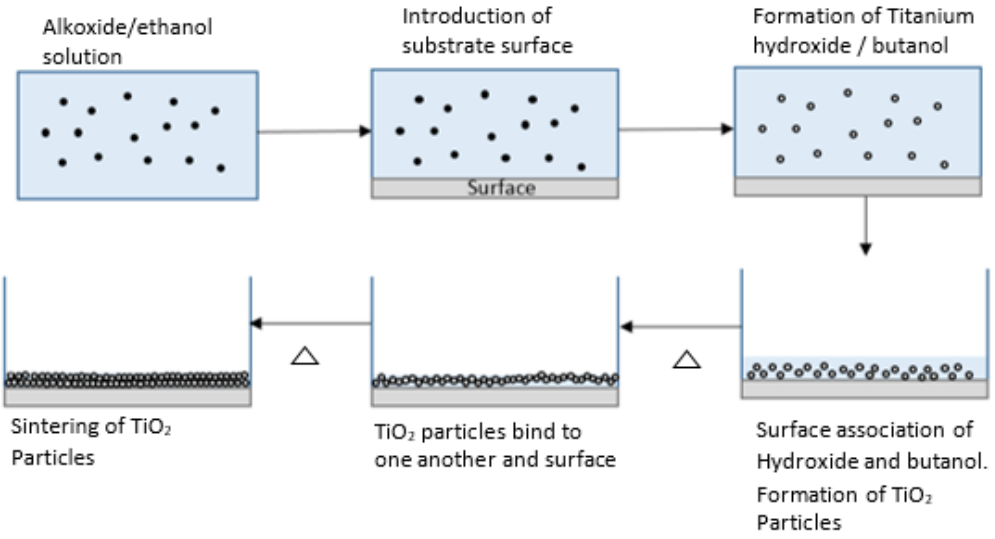

Figure 21 : Illustration of the process of titanium oxide microparticle formation [2].

In an experiment conducted by T. Lopez *et al.* [64], TiO_2 was doped with Pt ions via the following method: A mixture of $Ti(OBu)_4$ and platinum acetyl lacetonate in n-butanol was added drop-wise to a 70°C refluxing solution of ethanol, water and HCl. Once gelation had occurred the mixture was air dried for 24 hours.

In a study by H.E. Chao *et al.* [63], silver doped TiO_2 particles were generated by the addition of a mixture of $Ti(OBu)_4$ and acetyl acetone, drop-wise, into ethanol. This solution was then stirred for 30 minutes, followed by the addition of water and nitric acid. With continued stirring a clear TiO_2 sol was formed. Upon formation of the sol, $AgNO_3$ and HNO_3, the stabiliser, were added. In order to coat the titanium substrate a dip coating process was performed.

A study by J. Thiel *et al.* [24] doped TiO_2 particles with silver by a drop-wise addition of titanium chloride to a silver precursor ($AgNO_3$) that had been dissolved in ethanol. It was observed that the reaction was exothermic and produced gas. Once the solution had returned to room temperature it was placed in an oven for 24 hours at 80°C. This was followed by annealing for one hour at 600°C.

A review by A. Di Paola *et al.* [65] reported that the synthesis of TiO_2 via the Sol-gel method usually resulted in anatase or rutile crystal structures, but there were cases where brookite was observed when sol-gel synthesis was carried out in low temperature acidic conditions.

In this thesis , titanium oxide powders will be doped with silver using silver nitrate. The relevance of the studies by H.E. Chao *et al.* [63] , H.E. Chao *et al.* [63] and J. Thiel *et al.* [24] were thus used as guides for the synthesis of these powders. Since the experimental plan was to conduct the sol-gel synthesis under low temperature acidic conditions, the study by A. Di Paola *et al.* [65] provided information regarding the crystal structures that could be expected to form.

3.7.9 *Ion Implantation*

This thesis investigates the use of ionic implantation to dope titanium alloy and titanium oxide layers with silver, thus it is important to investigate the relevant literature regarding the interaction of implanted silver ions within these crystal structures as well as any literature that investigates the antimicrobial effect of such surfaces.

Ionic implantation works by the selective ionisation and unidirectional acceleration of the dopant atoms in an electric field towards the substrate material. When the ion beam contacts the substrate surface, the ions penetrate the target material and lose energy and these ions come to rest at some depth depending on the nature and chemistry of the substrate material, the initial energy provided (keV) and the dose (ions/cm^2) of the ions [66,67].

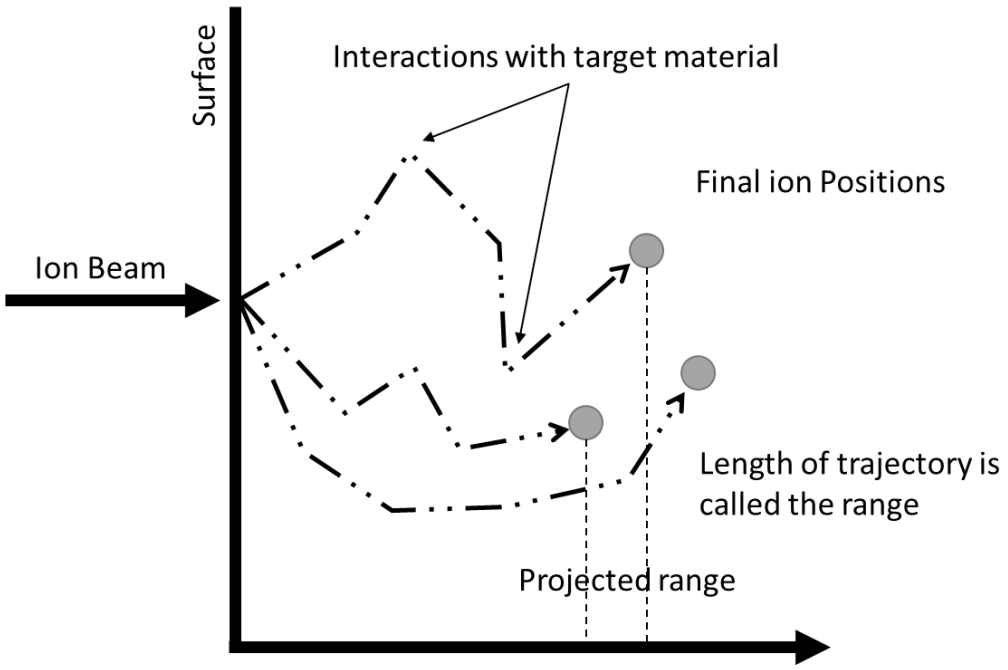

Figure 22 : Illustration of ion implantation [66].

One of the most important parameters of ion implantation is the ion dose. As illustrated in Figure 23, at low ion dose (< 10^{16} ions/cm^2) the implanted ions can become supersaturated in the host matrix. Once the solubility limit of the implanted atom in the host matrix is met, there is nucleation and subsequent growth/coalescence of the implanted ions in the matrix. A threshold dose value for the nucleation nanoparticles can be determined for any material experimentally by altering the ion dose at a constant beam energy. During the formation of Ag nanoparticles in an oxide matrix, it is expected that Ag would have a higher affinity to react with oxygen since the Gibbs free energy of formation of

the Ag-O bond is -2.68 kcal/mol versus the 0 kcal/mol for the Ag-Ag bond at 25 °C. (However, in this dissertation the implantation took place into a TiO_2 substrate. Therefore, the affinity between titanium and oxygen should be considered.)

In order to calculate the Gibbs free energy of formation for Ti-O at 25 °C, the Ellingham diagram and Gibbs free energy formula in Figure 24 can be used. Since the temperature is known, only the equilibrium partial pressure (P_{O2}) for the TiO_2 oxidation reaction is required. In order to obtain the value of the partial pressure from the Ellingham diagram, a vertical line (blue) should first be drawn from 25 °C upward on the x-axis and where this line intercepts with the TiO_2 oxidation line should be marked (red dot). Secondly, a slanted line should be drawn from the "0" in the top left, through the interception point and finally on to the P_{O2} axis. The temperature in Kelvin and obtained P_{O2} (in atm) should then be placed into the Gibbs free energy equation to obtain the Gibbs free energy of formation for Ti-O at 25 °C. Since the P_{O2} for the TiO_2 reaction at 25 °C is < 10^{-100} atm and the experiments in this study would take place at 1 atm, the oxidised state of titanium would thus be stable. The Gibbs free energy of formation for Ti-O at 25 °C was calculated to be -212.20 kcal/mol.

Since the Gibbs free energy of formation for Ti-O at 25 °C is so much lower than that of Ag-O, oxygen atoms prefer to bond to titanium even with the presence of Ag, thus Ag-Ag bonding would be energetically favourable [67]. Various forms of crystal structure damage can occur during ion implantation, such as extended and point defects, local crystallisation, precipitation of new phases and amorphisation. An example of amorphisation of SiO_2 as a consequence of ion implantation is shown in Figure 25 [67].

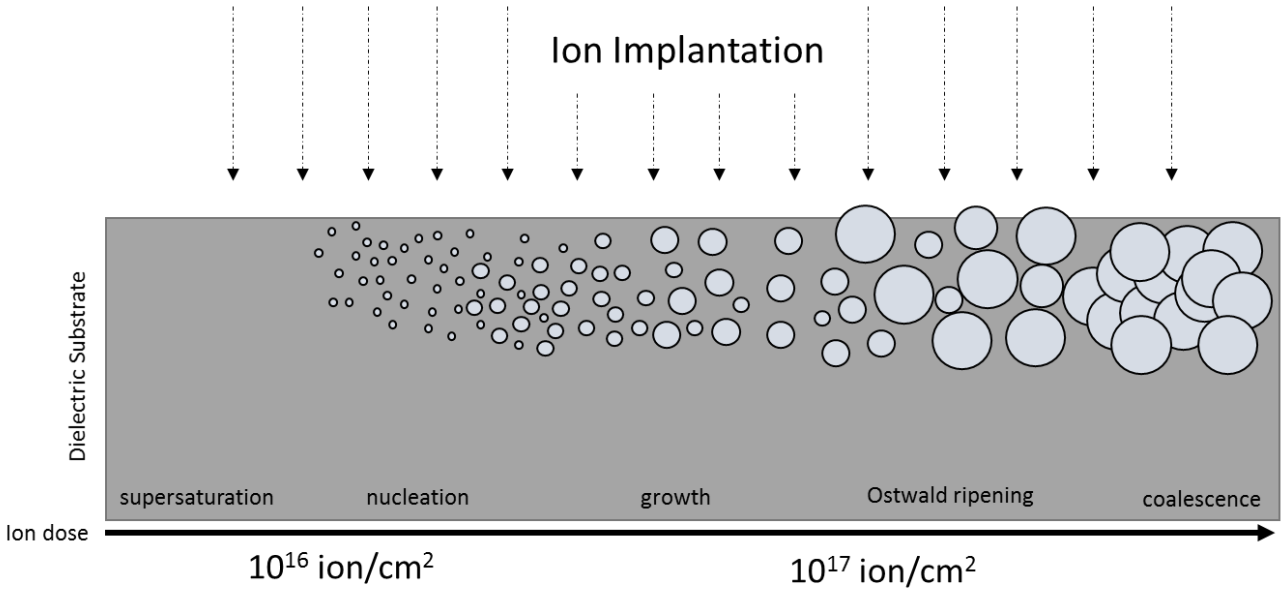

Figure 23 : Illustration of the physical process involved in the formation of nanoparticles during ion implantation as function of ion dose [67].

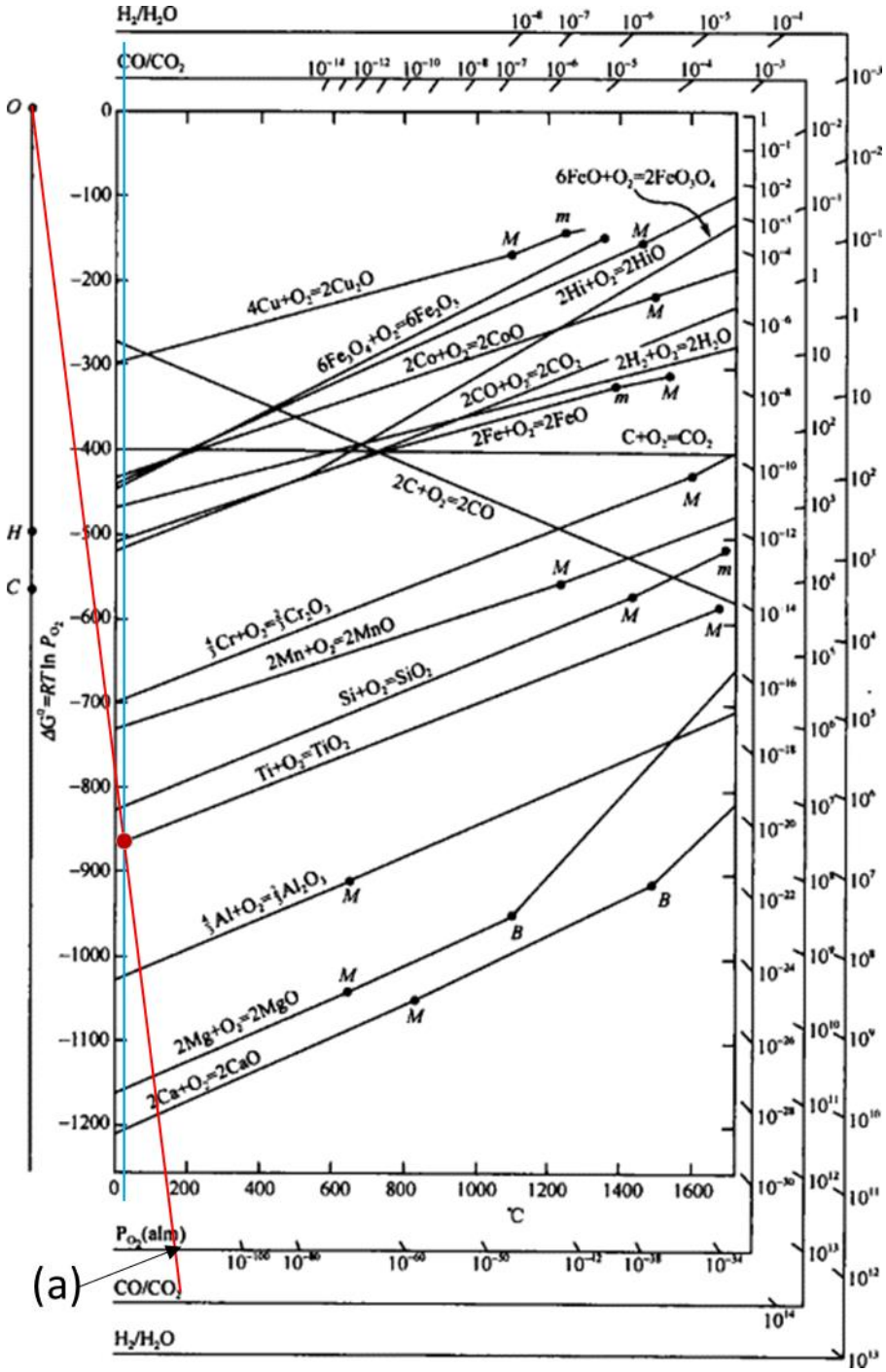

Figure 24 : Ellingham Diagram [68].

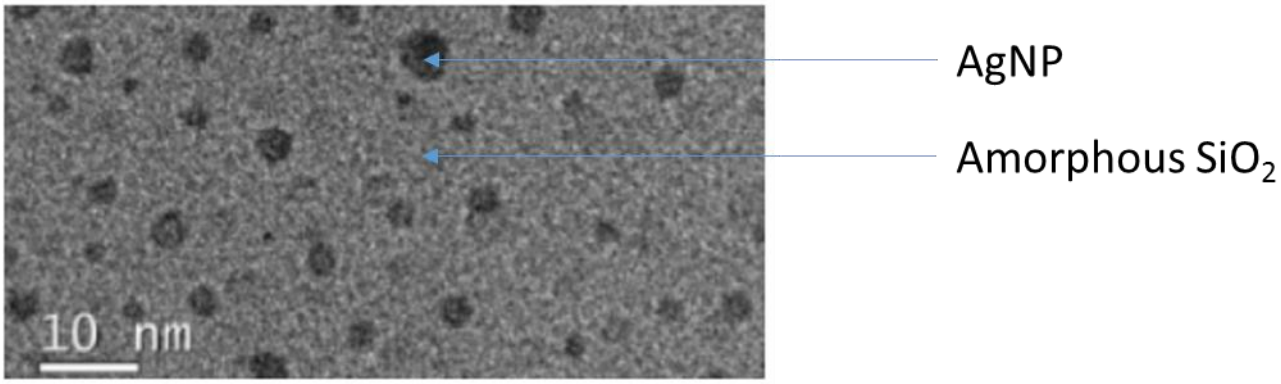

Figure 25 : TEM image of amorphised SiO_2 implanted with Ag ions [67].

In a study conducted by Y.Z. Wan *et al.* [69], ion implantation of titanium metals with silver and copper ions showed positive antimicrobial results against *S. aureus*. The results of the study are shown in Table 11 below. It can be seen from Table 11 that Ag^+ ions are effective when implanted with a dose of $2x10^{17}$ ions/cm^2. It was also found in the study by Y.Z. Wan *et al.* [69] that wear resistance of the implant increased with an increasing dosage of ions and that corrosion resistance was not affected by ion implantation. The limitations of this study are that there are no silver ion release curves presented and that the reason for the increased wear resistance of the surfaces observed post ion implantation was not explained. This thesis aims to fill these knowledge gaps.

Table 11 : Effect of ion dose on the antibacterial effect (%) of various copper ion implanted materials [69].

Samples	Silver ion implantation		Copper ion implantation	
	Ion dose (10^{17} ions/ cm^2)	Antibacterial effect (AE)	Ion dose (10^{17} ions/ cm^2)	Antibacterial effect (AE)
317L	0	0	0	0
	0.5	80	0.5	22
	1	95	1	69
	1.5	99.9	2	83
	2	100	4	99.7
Pure titanium	0	0	0	0
	0.5	83	0.5	31
	1	99.9	1	49
	1.5	100	2	90
	2	100	4	100
Ti–Al–Nb	0	0	0	0
	0.5	67	0.5	28
	1	99	1	42
	1.5	100	2	80
	2	100	4	99.9

In a study by D. Song *et al.* [70] reactive magnetron sputtering was used to form a multilayer nano-composite film where the top layer was a 200nm thick Ag doped TiO_x, as shown in Figure 26. The study investigated the antimicrobial activity of these surfaces as the oxygen partial pressure was changed during sputtering.

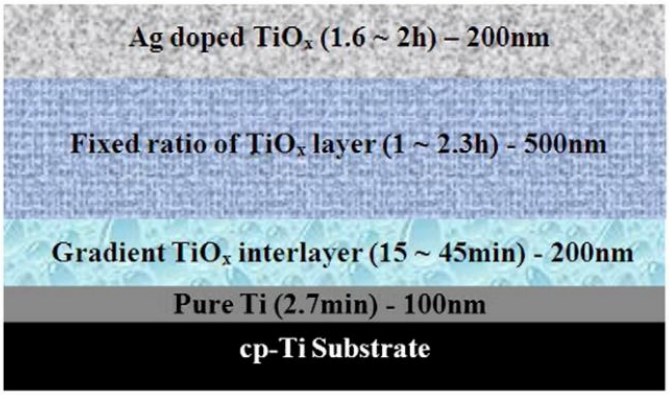

Figure 26 : Illustration of nano-composite film stacking layers [70].

This research also included an interrupted Ag^{+} release profile study, combined with an antimicrobial activity study, with which D. Song *et al.* [70] were able to determine a minimum concentration requirement for a surface to be bacteria repellent. This value is shown Figure 27 as 0.10 ppb. The study by D. Song *et al.* [70] also reported a dramatic reduction in colony forming units (CFUs) from the control CP-Ti sample (a), which had 500 CFU to lower than 12 CFU in (b - e). See Figure 28.

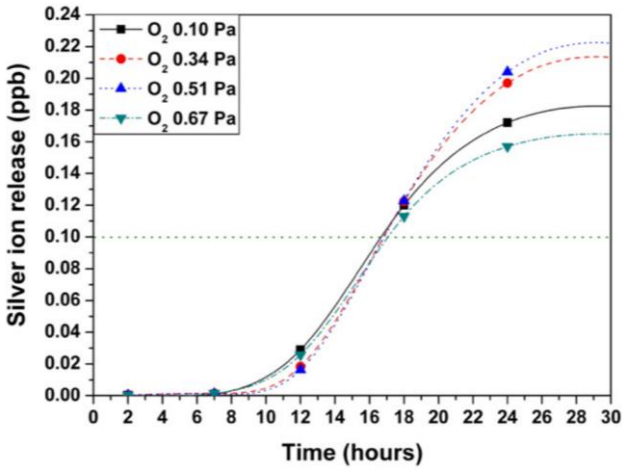

Figure 27 : Ag ion release test in the artificial saliva. Horizontal dotted line represents the minimum requirement for an antibacterial surface [70].

The study by D. Song *et al.* [70] relates to this thesis , because it presents silver ion release data from a silver doped titanium oxide that may ,microstructurally, closely resemble surfaces generated in this study. Thus, this data could be used to infer whether the generated surfaces would be antimicrobial, since actual antimicrobial testing was not within the scope of this study.

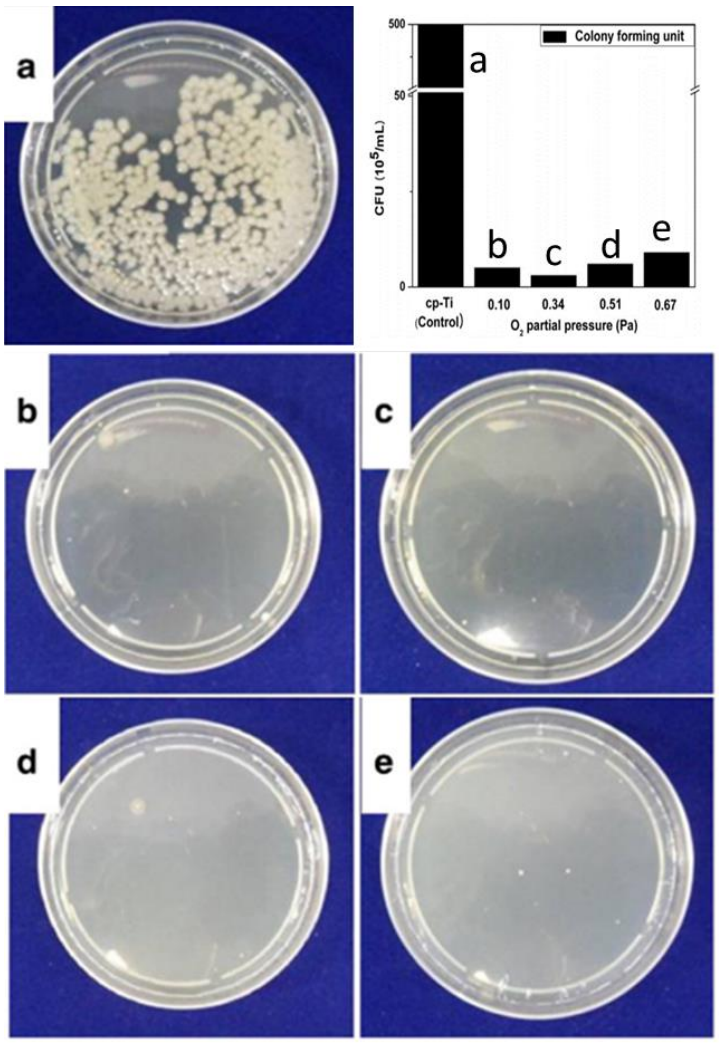

Figure 28 : (a) CP-Ti (control), (b) 0.10 Pa, (c) 0.34 Pa, (d) 0.51 and (e) 0.67 Pa O_2 partial pressure [70].

3.8 Methods of Silver Particle Formation and Application

There are various methods used to produce silver nanoparticles. Many of the techniques to be discussed rely on a silver-containing precursor such as $AgNO_3$, a reducing agent and a protecting molecule that prevents particle agglomeration. These methods are discussed in more detail in the subsequent sections.

3.8.1 *Hydroxyapatite*

Hydroxyapatite (HAP), with respect to orthopaedic implants, is used as an osteoconductive coating, owing to its excellent biocompatibility and bioactivity [45,71]. This calcium phosphate based material simulates the naturally-occurring hydroxyapatite in bone [59]. With respect to HAP nanoparticles, the preferred morphology of the particles is rods or needles as these closely simulate the HAP found in bone [72]. It is also important to note that naturally-occurring HAP has a calcium to phosphate ratio of 1.67(Ca/P =1.67). Thus, it is important to maintain this stoichiometry when synthesis of synthetic HAP is carried out [59,71,73]. HAP functions by a mechanism that releases calcium phosphate into the surroundings of the implant and causes body fluids to concentrate around the implant and precipitate natural biological apatite on to the surface of the implant. This causes an increased rate of healing [54,74]. There are various methods used to apply hydroxyapatite on to the surface of titanium. These methods include nano-particulate coating, dip coating, sputter coating, pulsed laser deposition, hot pressing and electrostatic spraying [45]. Chemical methods of HAP applications are biomimetic precipitation, sol-gel and hydrothermal synthesis [73].

3.8.2 *Biomimetic Precipitation*

Biomimetic precipitation involves the preparation of HAP NPs in conditions that mimic body fluid, body temperature (37°C) and pH (7.4). Table 7 shows the concentration of ionic groups in human body fluid and a biomimetic solution produced by C. Tas *et al.* [75].

Table 12 : Ion concetrations of SBF solutions and human plasma [75].

Ion	Tas *ET AL.* (MM)	Body Fluid (MM)
Na^+	142.0	142.0
Cl^-	125.0	103.0
HCO_3^-	27.0	27.0
K^+	5.0	5.0
Mg^{2+}	1.5	1.5
Ca^{2+}	2.5	2.5
HPO_4^{2-}	1.0	1.0
SO_4^{2-}	0.5	0.5

The solution was prepared by the addition of reagents containing the desired ions to deionised water. Each reagent could be added only once the previous reagent had completely dissolved. Table 13 shows the reagents and the order in which these reagents must be added to 700ml of deionised water in order to produce the biomimetic solution (SBF) [75].

Table 13 : Chemical compositon of SBF solutions [75].

ORDER	REAGENT	AMOUNT (GPL)
1	NaCl	6.547
2	$NaHCO_3$	2.268
3	KCL	0.373
4	$Na_2HPO_4 . 2H^2O$	0.178
5	$MgCl_2. 6 H_2O$	0.305
6	HCL (37%)	15ml
7	$CaCl_2 . 2H_2O$	0.368
8	Na_2SO_4	0.071
9	$(CH_2OH)_3CNH_2$	6.057

As evident in Table 13, a 15ml of HCL (37%) was added before the addition of $CaCl_2$ in Step 6. This was due to some turbulence observed in the solution. This additional HCL was the reason for the increased chloride ion concentration in Table 12. The solution temperature was then raised to 37°C and titrated with 25ml of 1M HCL solution to a pH of 7.4. During the titration the SBF solution was diluted to 1L. Correct proportions of $Ca(NO_3)_2.4H_2O$ (99%) and $(NH_4)_2HPO_4$ were then added to two separate beakers of SBF solution. An ammonia solution was added to the $Ca(NO_3)_2.4H_2O$ solution (both at 37°C). The $(NH_4)_2HPO_4$ was then added at 4ml/min under stirring conditions. The NPs formed were then centrifuged and calcinated to produce nano-powder (See Figure 29) [75].

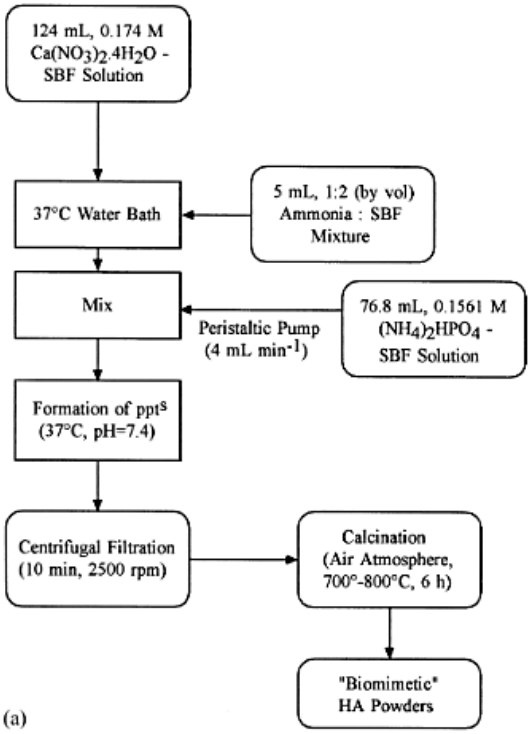

Figure 29: (a) Process flowchart for HA synthesis by the 'initial addition' technique [75].

The advantages of the biomimetic procedure over wet chemical precipitation were smaller particle sizes, higher crystallinity and narrower particle size distribution. However, the biomimetic process produced spherical particles that were not the preferred needle or rod-like shapes that mimicked natural HAP more effectively [76].

3.8.3 *Wet Chemical Method*

This method involves the addition of 0.3M H_3PO_4 solution to an equal volume of 0.5M $Ca(OH)_2$ solution at a 2 drops per second rate at RT. The reaction takes place under alkaline conditions and thus the pH is kept above 10 by the addition of NH_4OH. The precipitate ages in solution for five days. The precipitate is then washed with deionised water and dried in an oven at 110°C for two hours [76]. However, this method produced particles of lower crystallinity, greater particle size and HAP particle size distribution relative to the biomimetic process. This is summarised in Table 14.

Table 14 : Characteristics of the HAP powders [76].

SAMPLE	PARTICLE SIZE(NM)	CRYSTALLINITY (%)	RANGE(NM)
BIOMIMETIC	27	67	15-40
WET CHEMICAL	62	42	28-120

3.8.4 *Surfactant Assisted Hydrothermal Hydroxyapatite Particles Synthesis*

Hydrothermal processing is a method used to produce crystal particles with a unique morphology. The morphology of hydroxyapatite particles produced by hydrothermal processing is affected by temperature, solvent pH and solvent additives [77,78].

In a study by Y. Wang *et al.* [72] on the effect pH had on hydroxyapatite morphology it was found that a pH of between 6 and 9 produced whisker morphology in the micron range, shown in Figure 30 (a) and (b) respectively. Their study also found that at a high pH of 14 the crystallinity of the particles decreased significantly.

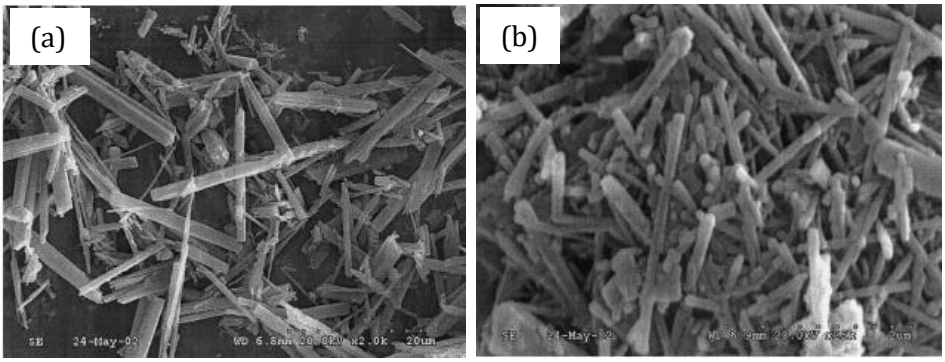

Figure 30 : SEM micrographs of HA whiskers and crystals with a different pH value at the same temperature 140°C: (a) pH=6, (b) pH=9 [72].

In the same study the effect of temperature was also investigated. It was found that, at all synthesis temperatures between 60 and 140°C, a needle-like morphology was present. It was found that at lower temperatures a second, undesired phase, monetite, was present. However, this phase decreased to negligible levels at 120°C [72]. See XRD in Figure 31 where monetite is indicated by the vertical blue lines.

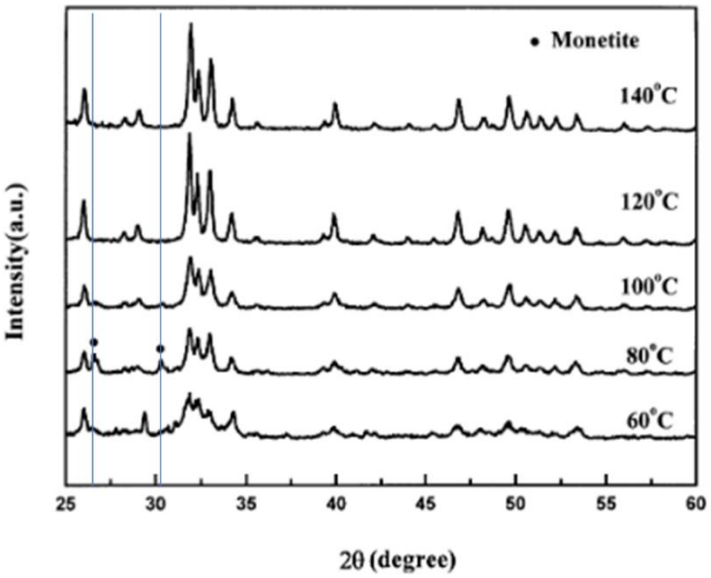

Figure 31 : The XRD pattern of HA powders synthesised at a different temperature with the same pH = 9 [72].

The hydrothermal process itself involves the reaction of acid, usually H_3PO_4, with a calcium-containing molecule such as calcium chloride or calcium hydroxide. The reactants are then placed in a Teflon vessel and heated to the desired temperature, typically between 80 - 150°C [72,78]. In a study by Y. Wang *et al.* [72], surfactant cetyltrimethylammonium bromide(CTAB) was added to the hydrothermal process. It was found that in the presence of CTAB, by increasing the reaction temperature at a constant pH and reaction time, the length and diameter of HAP crystals increased [72] .

Table 15 : Summary of results found by Y. Wang *et al.* [72].

REACTION TEMP(°C)	PH	TIME(H)	DIAMETER(NM)	LENGTH(NM)	MORPHOLOGY
90	13	20	27		Nearly round
120	13	20	74		Nearly round
150	13	20	85		Nearly round
90	9	20	27	255	Needles
120	9	20	34	840	Fibres
150	9	20	60	1125	Fibres

In this study it was shown that the addition of CTAB assisted in the control of HAP morphology by promoting growth of the crystals along one axis, creating an elongated needle or fibre morphology. In addition, the CTAB was effective at pH values where hydroxide concentrations were low enough not to interfere with the interaction of CTAB. Thus, at a higher pH round crystals were formed, since CTAB interactions were inhibited by high hydroxide concentration [72].

3.8.5 *Hydroxyapatite Silver Ion Exchanged Particles*

In order for Ag^+ to be incorporated into the chemical structure of HAP an ion exchange reaction between calcium and silver must take place in solution. Thus, for example in a study by N. Rameshbabu *et al.* [79] $AgNO_3$ and $Ca(OH)_2$ solutions were mixed.

$$2\ AgNO_{3(aq)} + Ca(OH)_{2(aq)} = 2\ AgOH_{(s)} + Ca(NO3)_{2(aq)}$$

This was followed by the addition of a H_3PO_4 solution and microwaving at 800W for 30min. This study showed positive results with a calcium/silver substitution percentage of 15%, resulting in 100% inhibition of *E. coli* formation and 50% and higher substitutions showing 100% inhibition of *S. aureus*. A zone of bacterial inhibition was reported at silver substitution levels above 20% [79].

In another study by V. Stanic *et al.* [71], silver oxide was dissolved in a solution of H_3PO_4. This solution was then added dropwise into a solution of calcium hydroxide. The produced particles were collected and filtered after 24 hours. This study also showed positive results with complete inhibition of *E. coli* and *S. aureus* at a Ag/ (Ca + Ag) ratio of 0.004. A zone of inhibition was also reported [71].

3.8.6 *Poly (lactic-co-glycolic acid)*

Research into the applications of synthetic polymers in the medical field have gained increased attention in the last 20 years. Some synthetic polymers, such as co-polymers of lactic and glycolide, are known have no toxicity and good mechanical properties [80].

Poly (lactic-co-glycolic acid) (PLGA) has shown a great amount of potential as a drug delivery carrier. There are many PLGA-based implant devices that approved by the FDA. PLGA is biocompatible and biodegradable. In the human body the PLGA molecule is hydrolysed via the ester linkages and this produces lactic acid and glycolic acid. These products can be eliminated by natural metabolic pathways [80].

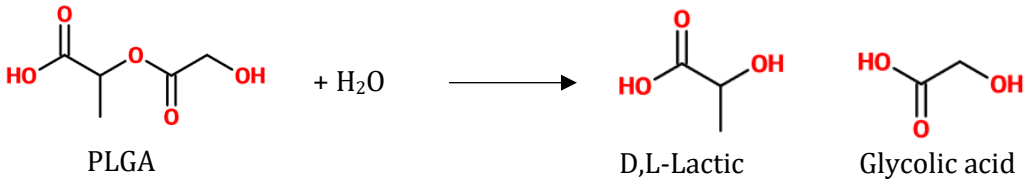

Figure 32 : Illustration of the hydrolysis reaction of PLGA polymer to produce D,L-lactic and glycolic acid.

PLGA can be processed into many different shapes and sizes and is able to encapsulate molecules of almost any size. PLGA is soluble in various solvents such as dichloromethane (DCM), acetone and ethyl acetate [80].

There are various factors that influence the degradation rate of PLGA, such as initial molecular weight, surface exposure to water and composition of the co-polymer. The composition of the co-polymer is said to be one of the major factors in determining degradation rate. See Figure 33.

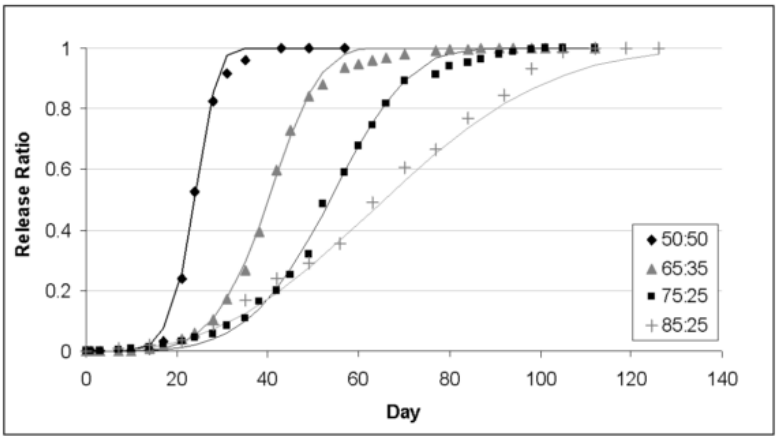

Figure 33 : Modeled *in vivo* release profiles for 50:50 , 65:35, 75:25 and 85:15 poly lactic-co-glycolic acid [80].

A rule of thumb is that a higher glycolic acid content leads to a more hydrophilic polymer and thus a quicker degradation rate. The only exception to this rule is the 50:50 co-polymer, which has been shown to have the fastest degradation rate. Figure 33 above shows a model of degradation rates of different co-polymer ratios [80]. For example, the notation 65:35 means that the PGLA polymer is comprised of 65% lactic acid and 35% glycolic acid monomers. Table 16 shows *in vivo* degradation times for lactide-based polymers, as well as PLGA co-polymers [81]. The biodegradation mechanism that primarily determines the release characteristics of these polymers is via bulk erosion (hydrolysis).

Table 16: Biodegradation of Lactide/Glycolide polymers [81].

POLYMER	APPROX. TIME FOR BIODEGRADATION (MONTHS)[A]
POLY(L-LACTIDE)	18-24
POLY(DL-LACTIDE)	12-16
POLY(GLYCOLIDE)	2-4
50:50 (DL-LACTIDE-CO-GLYCOLIDE)	2
85:15 (DL-LACTIDE-CO-GLYCOLIDE)	5
90:10 (DL-LACTIDE-CO-CAPROLACTONE)	2
[A] ***biodegradation times vary depending on implant surface area, porosity and molecular weight***	

3.9 Electrospinning/Spraying

3.9.1 *Introduction*

Electrospinning is a technique that is capable of producing a non-woven layer of polymeric fibres of nanometres in diameter [82]. These non-wovens can be spun on to surfaces to create unique surface properties. Electrospinning is a relatively easy technique that has a high potential for use on a large scale. The main uses of electrospinning in the biomedical field are tissue engineering, drug release and wound dressings [82]. Spinning of fibre and spraying of polymeric particles are both possible using the electrospinning technique setup. Whether a polymer is spun or sprayed is dependent on the viscosity of the polymer melt/solution, on the volatility of the polymer solvent, on the molecular weight of the polymer and on the applied electric field [82].

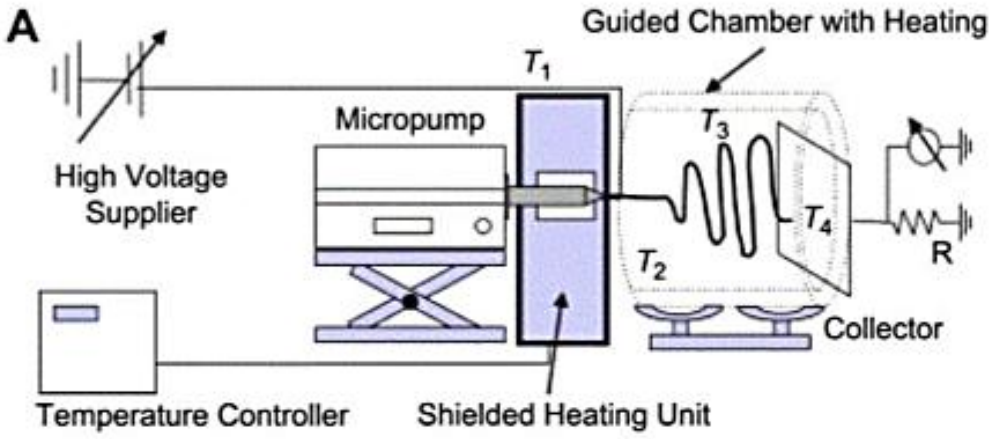

Figure 34 : Schematic of a typical electrospinning setup [82].

The steps to take in order to conduct successful electrospinning experiments are to:

1) Choose a Polymer (*e.g.* PGLA).
2) Identify a substrate to spin on to (*e.g. t*itanium).
3) Approximate the critical entanglement concentration.
4) Adjust the spinning parameters until a steady stream of nanofibers is obtained.

Collector plates can be stationary or rotating. Fibres spun on to a stationary plate have poor directionality, whereas fibres spun on to rotating collectors are more aligned. In order to approximate the critical entanglement concentration, a series of polymer solutions of different concentrations must be prepared. The polymer solution that is most likely to spin will be viscous but will still "pour" well. If the solution is too dilute, electrospraying may take place and if the solution is too viscous, beaded fibres will be spun [83].

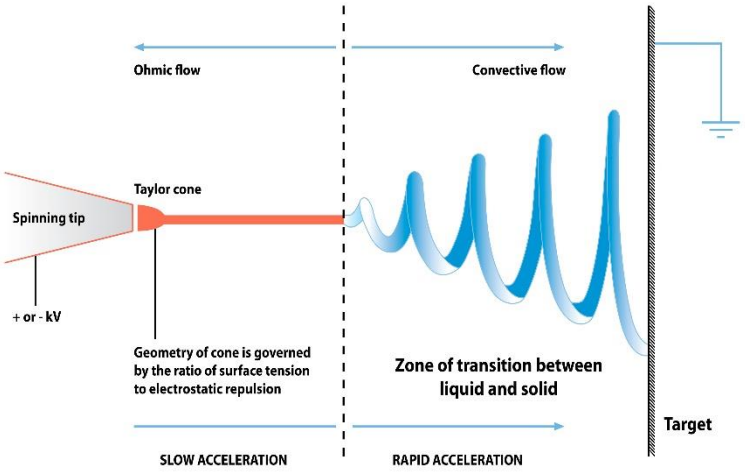

Figure 35 : Illustration of the formation of electrospun nanofibres [83].

As stated previously the electrospinning parameters are crucial to successfully spinning nano-fibres. Initially, the flow rate must be set so that when a polymer drop at the syringe tip is wiped away, it is immediately replaced by a new drop. The standard starting distance between the tip and collector is 20cm. The voltage is applied across the system and is slowly increased until a stable Taylor cone develops. If a stable stream of polymer does not develop, the collector can be moved closer or the polymer solution concentration must be increased.

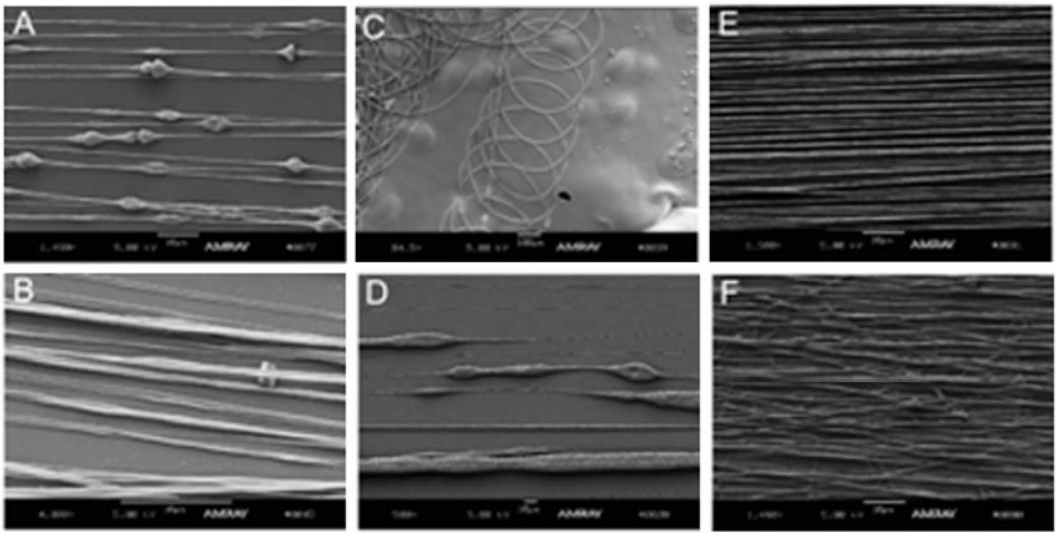

Figure 36: Electrospun fibres can exhibit a variety of morphologies: (a) beading, (b) ribbons, (c) curlicues, (d) porous globs, (e) good alignment, and (f) poor alignment [83].

Once the polymer has been spun, morphological analysis via SEM/TEM studies can also give indications as to what spinning parameters to change in order to get well-spun fibres. When fibres are beaded or form ribbons, the polymer solution concentration must be decreased [83]. If fibers have a wavy morphology, the distance between the syringe tip and collector must be increased.

3.9.2 *Uses of Electrospinning in Tissue Engineering*

Tissue engineering is a field that, in part, focuses on the production of synthetic scaffolds that promote the growth of cells on to and into their structures. The scaffolds produced must, as with all biomaterials, not induce an immune response. Electrospinning produces scaffolds that can be tailored to simulate the structure of extracellular matrices (porosity and surface area), which, in turn, promotes cell growth into its structure. The types of polymers used to produce these scaffolds are Poly (Lactic Acid) and Poly (Glycolic Acid) and their co-polymers (PLGA), as well as Poly (Caprolactone). These polymers are all biocompatible and biodegradable [82]. As discussed earlier, many biodegradable polymers such as PLGA are used in drug delivery systems. These developed drug delivery systems are of great importance to the tissue engineering field, because the slow release of drugs can assist with tissue integration into the scaffolds [84]. A relevant example is the use of electrospinning a wound dressing made of PVA fibres containing AgNPs.

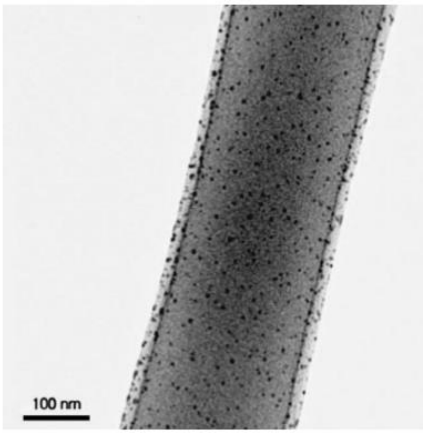

Figure 37 : TEM image of post-UV treated electrospun PVA/$AgNO_3$ fiber web [84].

This was produced by spinning a PVA solution containing aqueous $AgNO_3$, followed by a heat treatment/UV treatment. This produced the fibre in Figure 37. It was found that this fibre was 99% antibacterial. However, skin discoloration was an issue, owing to the high silver concentrations. Constant moisture was required to produce the bioactive Ag^+ [82]. A more recent study by F.N. Almajhdi *et al.* [25] produced PLGA fibres containing silver nanoparticles for use as anticancer and antimicrobial agents.

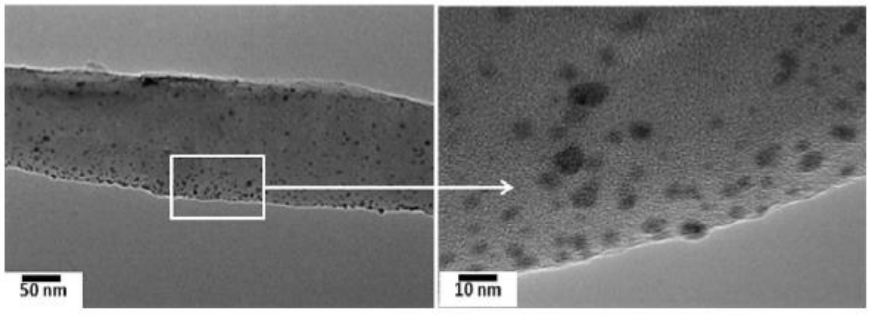

Figure 38 : TEM images of PLGA nanofibers containing 7% AgNPs [25].

The difference in producing nanoparticles within this fibre using this method was that a reducing agent was added to the polymer spin solution. It was found that a 7% AgNP containing PLGA fibre successfully inhibited Staphylococcus aureus, Bacillus cereus, Listeria monocytogenes and Salmonella typhimurium via inhibition zone studies. However, this study was only conducted *in vitro* and reported no results regarding skin discoloration [25].

3.10 Characterisation Techniques

3.10.1 *Electron Microscopy*

Electron Microscopy was developed owing to the inherent limitations of optical microscopy and the need to see finer structural details. The Transmission Electron Microscope (TEM) was the first electron imaging tool, developed by Max Knoll and Ernst Ruska in 1931. Scanning Electron Microscopy (SEM) was first commercially available in 1965 [85]. Electron microscopes function similarly to optical microscopes except, instead of using reflected light to generate images, they use a focused beam of electrons under high vacuum. All electron microscopes work via the same principle. Initially, a beam of focused electrons is accelerated toward the specimen. When the electron beam comes into contact with the sample surface, this leads to various electron/sample interactions (Figure 39).

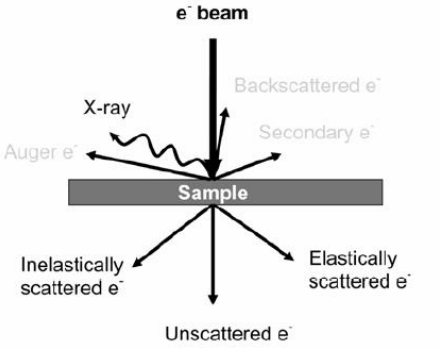

Figure 39 : Illustration of electron and sample interactions [85].

SEM uses secondary and backscattered electrons (each with their own corresponding detector) to generate images. Secondary electrons can only escape the sample surface if they are within the top 10nm of the surface and the images generated are appropriate for surface imaging and characterisation, such as morphology and porosity studies. Thus, images generated by these electrons are topographic in nature. Backscattered electrons are high energy electrons that originate from deeper within the interaction volume. (See Figure 40.) Since the number of backscattered electrons is directly related to the atomic number of the elements contained in the sample, higher average atomic weight atoms (regions) appear brighter. One limitation of the backscatter detector is that when atomic weights of elements are similar, contrast difference are difficult to determine. When combined with EDS, SEM can also take advantage of X-rays produced by electrons that relax back to ground state after excitation. The energy of the X-rays produced in this manner is characteristic of the specific elements. Thus SEM/EDS can be used to qualitatively detect the presence of specific atoms. Quantitative data can be obtained using calibration standards. A limitation of EDS in this relating to this study are that due to the relatively thin oxide film formed relative to the bulk and the high sample volume of the EDS it became difficult to detect silver due to the masking of the data by the bulk titanium signal.

Some modern-day scanning electron microscopes have the capability to perform focused ion beam milling (FIB milling). These FIB/SEM machines are equipped with two columns, one column accelerates ions (usually Gallium) and the other electrons (for imaging). The process of FIB milling beings by deposition of a protective carbon coating on the surface of the area to be analysed. The angle of incidence for the 1st milling step is usually between 0^0 and 5^0 . At the angle a beam of high energy gallium ions are accelerated towards the surface of the material and is slowly eroded away. This is conducted from both sides {see Figure 40(b}. Once successfully milled, the sample is attached to a needle and then detached from the surface of the material by milling away the base and thereafter

carried to a TEM grid [86,87]. After attachment to the TEM grid the sample undergoes a further "thinning" process which reduces the cross-sectional thickness until the sample becomes electron transparent for later TEM analysis. Since the thinning process also involves the high energy ions, it can cause damage to the sample such as delamination of layers from one-another and create unintended holes and short pathways in the sample if overly thinned[87].

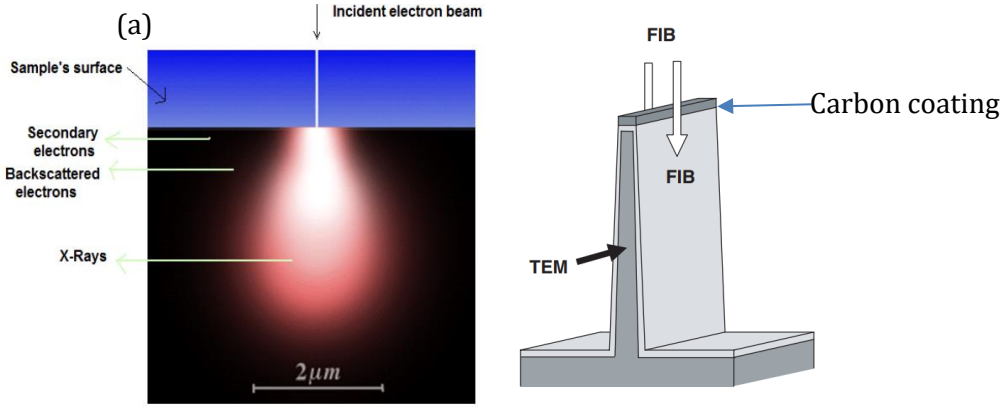

Figure 40 : (a) Illustraton of (a) electron beam interaction volume [88] and (b) FIB milling[87]

Electrons interact with the specimen within a certain "interaction volume". Figure 40 shows the interaction volume for the various types of electrons produced. TEM is able to use the unscattered (transmitted) electrons and both elastically and inelastically scattered electrons to image samples. TEM samples must be made thin enough so that unscattered electrons can penetrate through the sample. The image is generated by contrast differences caused by sample thickness, atomic number, crystal orientation and phase contrast [88].

3.10.2 *Atomic Force Microscopy*

Atomic force microscopy (AFM) is a form of scanning probe microscopy (SPM). The first SPM method required conductive samples to give accurate results. With the invention of the Atomic Force Microscope, non-conductive materials, such as polymers and ceramics, could also be analysed [89]. AFM provides three major advantages over other microscopy techniques [90]:

- the ability to image in three dimensions (x,y,z)
- does not require a vacuum environment
- can be used in liquid environments

The AFM has three modes of function:

- contact mode
- tapping mode
- lift mode and/or non-contact mode.

Contact mode operates by scanning a sharp-tipped cantilever across the sample. The image is obtained by measuring the tip deflection or the repulsive forces between the tip and the measured surface. Due to drag forces, contact mode can damage the sample when soft samples are imaged. Tip dragging can be avoided in tapping mode. During tapping mode operation the cantilever oscillates and "taps" the surface at defined intervals [90].

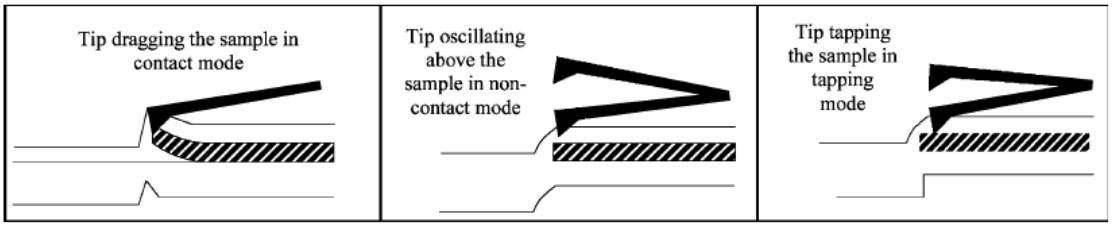

Figure 41 : Contact mode(left), non-contact mode(middle) and tapping mode(right) [90].

Lift mode is used to distinguish the magnetic/electric contribution from the topographical one. In this mode a line scan is completed in tapping mode (acquisition of the topographical data), followed by a non-contact scan near the surface (magnetic/electric field data are captured). In order for this mode to work, a ferromagnetic tip is required [90].

3.10.3 *Rutherford Backscatter Spectroscopy (RBS)*

Rutherford Backscatter Spectrometry (RBS) is a widely-used technique for the analysis of thin films. Typically, the sample surface is bombarded with ions with an energy in the Mega-electron Volt (MeV) range of 0.5 - 4 MeV. The ions used for bombardment are typically helium or lithium. The advantage of RBS is that it is able to determine film thickness with resolution in the nanometre scale. RBS is also able to quantitatively depth profile individual elements without the need of calibration standards. The sensitivity of this technique to heavy elements is in the parts-per-million (ppm) range [91]. The drawbacks of RBS are that it is not sensitive to light elements and it is not able to effectively resolve atoms of similar molecular mass. For the purposes of this study, where Ti-6Al-4V was used, these drawbacks did not come into play since the atomic masses of Ag, Ti, V, Al and O are vastly different.

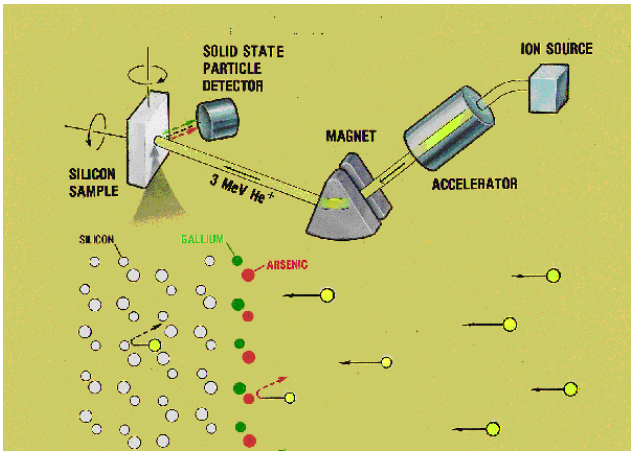

Figure 42 : Illustration of the process of RBS measurement [91].

Figure 42 illustrates the process by which RBS takes its measurements. Ions are released from an ion source and accelerated towards the sample surface. The ions make contact with the substrate atoms and are backscattered on to a solid-state detector. The peak intensity of the detected element is related to the area density or film thickness [92].

3.10.4 *X-ray Diffraction*

Diffraction occurs when electromagnetic radiation is scattered by a periodic array of long-range order. This scattering of electromagnetic radiation leads to constructive interference at specific angles (θ). X-ray radiation has a wavelength that is similar in magnitude to interatomic bonds. When a crystalline sample is irradiated with x-rays, each atom acts as a scatter point. The strength with which an atom scatters the x-ray light is directly proportional to the number of electrons around the atom. The scattering of the X-ray light results in a diffraction pattern that is representative of the atomic arrangement within the crystalline material. Since amorphous materials have no long-range atomic order, they do not produce diffraction patterns [93].

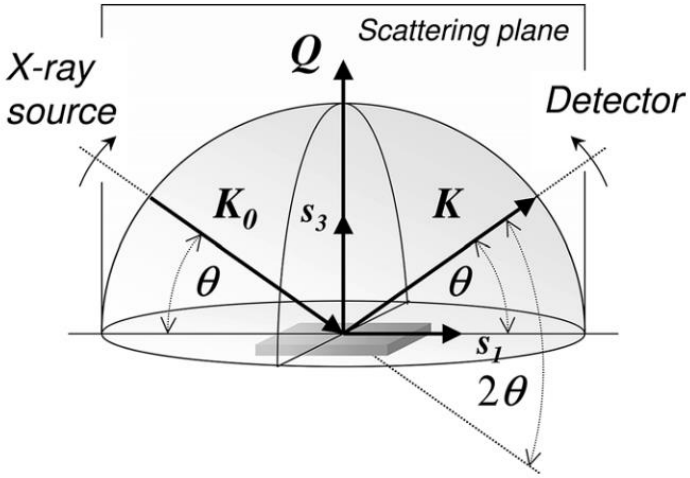

Figure 43: Schematic representation of a θ/2θ scan [93].

Generally, diffraction experiments are conducted by positioning the sample in the centre of the diffraction instrument and then exposing the sample to an x-ray beam at various angles (θ). The

detector, which measures the scattered radiation, is placed at the same angle from the surface of the sample as the incident beam [93] (See Figure 43).

The diffraction peaks produced in x-ray diffraction experiments are associated with planes of atoms that are identified via their Miller indices (hkl). The interplanar spacing vector d_{hkl} that is normal to the (hkl) plane can be used to determine where diffraction peaks will be observed via Bragg's Law. (See equation below.) The calculation of the interplanar spacing for various crystal systems is given in Table 17 [93].

$$\lambda = 2\, d_{hkl} \sin\theta \text{ – Bragg's Law}$$

Figure 44, Figure 45 and Figure 46 show reference XRD spectra for anatase, rutile and brookite TiO_2 respectively. It can be seen that, for example, the (101) plane for anatase was expected to have a peak around $2\theta = 25°$, the (110) plane for rutile was expected at $2\theta = 27\text{-}28°$ and for brookite the (121) plane at $2\theta = 31°$.

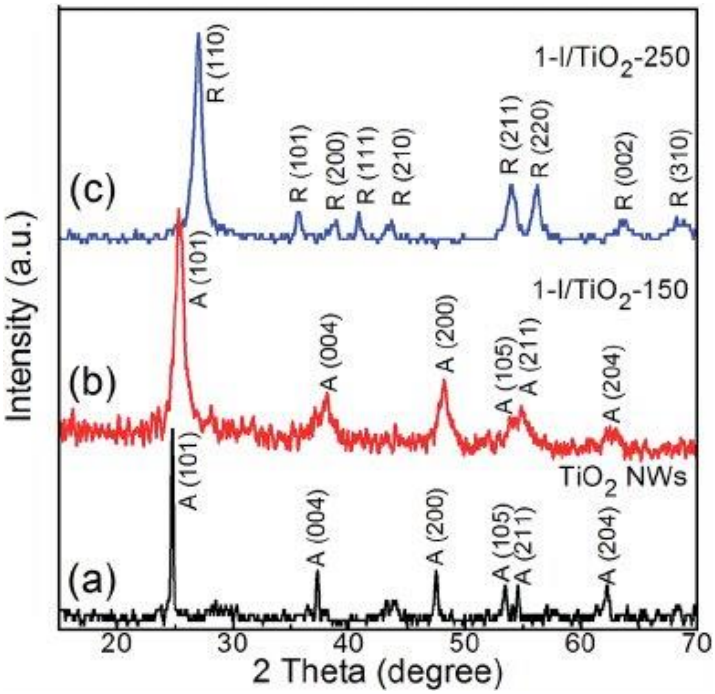

Figure 44 : Reference XRD spectrum for anatase TiO_2 (a) [94] **.**

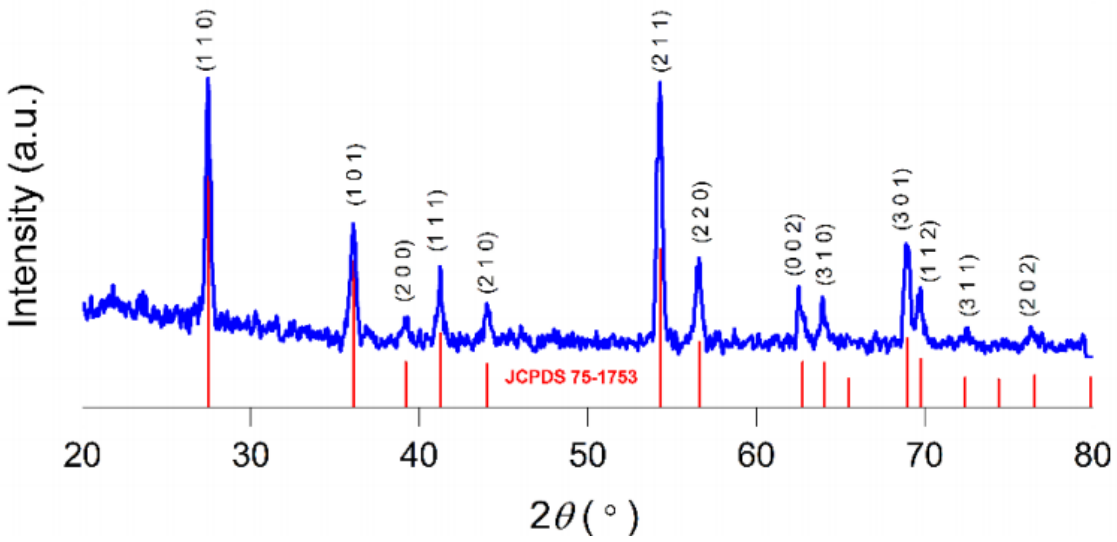

Figure 45 : Reference XRD spectrum for rutile TiO_2 [95].

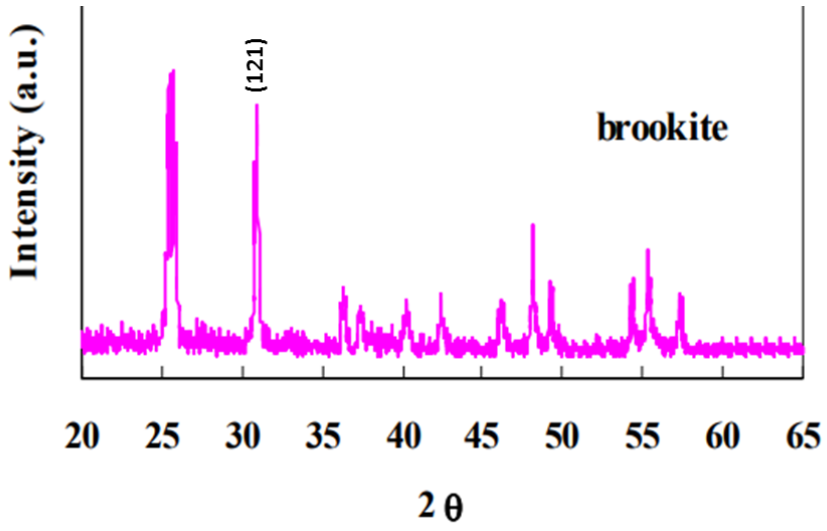

Figure 46 : Reference XRD spectrum for brookite TiO_2 [65].

Table 17 : Interplanar spacings d_{hkl} for different crystal systems and their dependency on Miller indices (hkl). Parameters a, b and c give the lengths of the crystallographic unit cell, while α , β and γ specify angles between them [93].

Crystal system	Constraints	$\frac{1}{d_{hkl}^2} =$
Cubic	$a = b = c$ $\alpha = \beta = \gamma = 90°$	$\frac{h^2 + k^2 + l^2}{a^2}$
Tetragonal	$a = b$ $\alpha = \beta = \gamma = 90°$	$\frac{h^2 + k^2}{a^2} + \frac{l^2}{c^2}$
Orthorhombic	$\alpha = \beta = \gamma = 90°$	$\frac{h^2}{a^2} + \frac{k^2}{b^2} + \frac{l^2}{c^2}$
Hexagonal	$a = b$ $\alpha = \beta = 90°$ $\gamma = 120°$	$\frac{4}{3}\frac{h^2 + hk + k^2}{a^2} + \frac{l^2}{c^2}$
Trigonal/ Rhombohedral	$a = b = c$ $\alpha = \beta = \gamma$	$\frac{(h^2 + k^2 + l^2)\sin^2\alpha + 2(hk + hl + kl)(\cos^2\alpha - \cos\alpha)}{a^2(1 - 3\cos^2\alpha + 2\cos^3\alpha)}$
Monoclinic	$\alpha = \gamma = 90°$	$\frac{h^2}{a^2\sin^2\beta} + \frac{k^2}{b^2} + \frac{l^2}{c^2\sin^2\beta} - \frac{2hl\cos\beta}{ac\sin^2\beta}$

3.10.5 *ICP-MS*

Inductively Coupled Plasma Mass Spectrometry (ICP-MS) is a method that is used for trace elemental analysis. In the field of geological sciences ICP-MS has been particularly widely implemented because of the sensitivity of the equipment to rare earth elements [96,97]. The advantages that ICP-MS has over similar techniques, such as ICP-Atomic Absorption Spectroscopy (ICP-AAS) and ICP-Optical Emission Spectroscopy (ICP-OES) are as follows:

- Increased detection limits for most elements
- Faster analysis times
- ICP-MS has the ability to minimise matrix interferences because it uses a high temperature.
- Inductively coupled plasma source
- Increased detection capability as compared to ICP-AES for the sample sampling rate
- Owing to Mass spectrometer coupling, isotopic information is also obtained.

The basic operation of ICP-MS is as follows:

The sample is pumped from a sample vial into the nebuliser, where it is mixed with argon gas to form an aerosol. The aerosol is then sprayed into the plasma. As the sample travels through the high temperature argon plasma, the aerosol droplets go through a process of drying, decomposition, atomisation and, finally, ionisation. The positive and neutral ions are extracted from the plasma in the sampling orifice and pass through the skimmer cone into a region that contains electrostatic lenses that focus the ion beam and remove unwanted neutral species. The positive ions are separated by bending the positive ion beam away into the reaction cell. The positive ions enter a quardapole/octopole ion guide, which can be tuned to further isolate analyte elements. From here, the analyte elements enter the mass analyser, which separates elements according to their mass:charge ratio. The end result is a mass spectrum, where intensity at a given mass is proportional to the concentration of the isotope at that mass [96,97].

4. Methodology

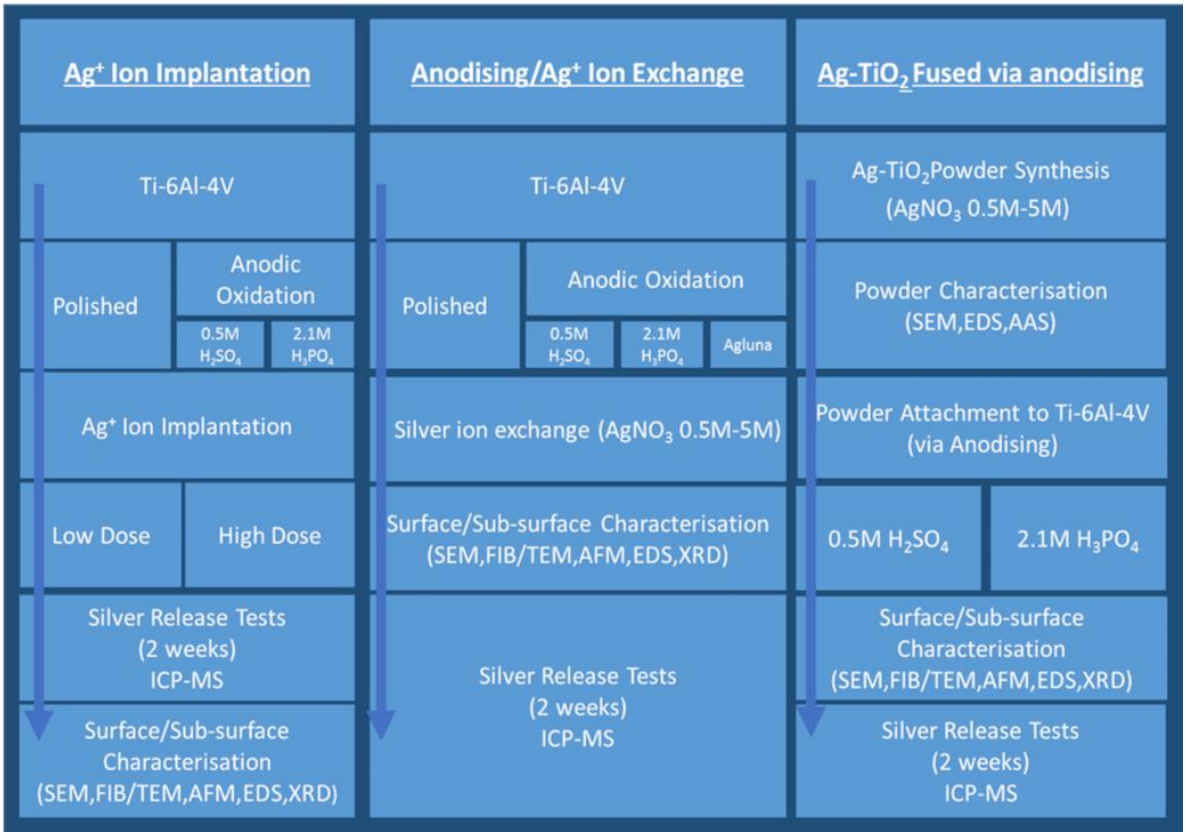

Figure 47: Summarised experimental procedure.

4.1 Surface Preparation

Samples were cut into 15mm diameter discs of 3 - 4mm thickness from Ti-6Al-4V rods provided by LRS implants. The samples were cut using the wire-cutting facilities at the Mechanical Engineering Department of the University of Cape Town.

4.1.1 *Polishing*

Samples were polished on an automatic polisher, according to the procedure in Table 18:

Table 18 : Automatic polisher: the procedure

STEP	SURFACE	FORCE(N)	ROTATION SPEED OF PAD(RPM)	ROTATION SPEED OF HEAD(RPM)	ROTATION OF HEAD	TIME(S)
1	1200 Grit	20	300	150	Counter rot	60
2	2400 Grit	10	300	150	Counter rot	30
3	MD-Chem	20	300	n/a	Co-Rotation	300

4.1.2 *Dual Acid Etching*

Dual acid etching was performed by heating a 70% w/w HCL/H_2SO_4 solution to 80°C for five minutes. The final dual acid etched surface is illustrated in Figure 49. Only the Samples to be coated in Ag-TiO_2 were dual acid etched.

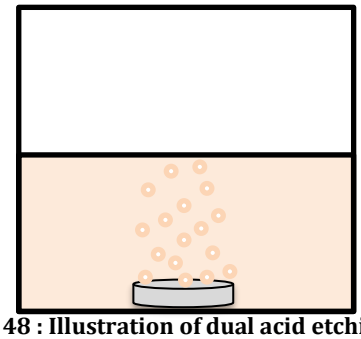

Figure 48 : Illustration of dual acid etching experiment.

Figure 49 : Illustration of a dual acid etched surface.

4.2 Particle preparation

4.2.1 *Ag-TiO_2 Particle Synthesis via Sol-Gel*

The powder synthesis was conducted via the sol-gel method, in which titanium butoxide was hydrolysed in a flask containing a stirring mixture (1500rpm) of H_2O and HNO_3 at pH 1. One each of 0M, 0.05M, 0.5M and 5.0M stock solutions of $AgNO_3$ were made. 10 ml of each $AgNO_3$ solution were placed into separate vials, which were then covered in foil to minimise light exposure and stirred at 1500 rpm, using a stirrer bar and magnetic plate. It was ensured that the pH of the solution in each vial was 1 prior to stirring via the addition of c.HNO_3 in a drop-wise manner. Titanium butoxide (3.0g) was then added drop-wise to the stirring solution. In each case, a white precipitate was observed. The mixture was allowed to stir for 24hrs, after which it was dried at 100°C for 24 hrs and further dried at 200°C for 20 minutes. Each of the four powders was then transferred into a clean vial and the vials were stored in a cool, dark place. Samples of the powders (*ca.* 0.2g) were taken from each vial and calcinated at 600°C for 2 hours, this to remove any residue present in the powders. The powders were digested in hot concentrated sulphuric acid using a MARS-5 Microwave Digester, belonging to the Department of Chemical Engineering at the University of Cape Town. After digestion, the resultant solution was analysed using AAS to determine the percentage of silver present in each powder.

4.3 Surface Modification

4.3.1 *Anodising followed by Ag Ion Exchange*

The polished disc sample was placed inside a corrosion probe (Figure 50(a)). The corrosion probe was then placed into a 2-neck round bottomed flask containing either the 2.1M H_3PO_4 or 0.5M H_2SO_4 electrolytes and a stirrer bar. The entire setup was placed on a magnetic stirrer plate.

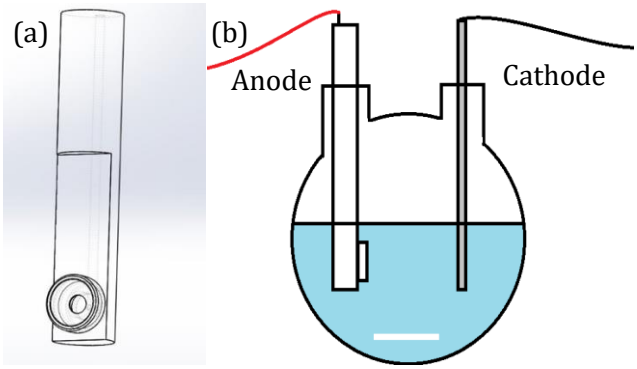

Figure 50 : (a) corrosion probe, (b) illustration of electrochemical cell.

A piece of titanium metal was used as the counter electrode to the anodic sample (Figure 50(b)). Initially, the stirring was set to 200 rpm. A DC voltage of 15V with a current of 10mA was passed through the circuit for three minutes to initialise oxide growth. It was noted that the titanium polished surface turned a shiny golden colour. After this initial passivation stage, the voltage was decreased to 0V and slowly increased to 100V without allowing the current to exceed 50mA. Once 100V was reached, stirring was stopped and the voltage was applied for one minute and then decreased to 0V. The oxide layer morphologies were analysed using SEM and AFM. Oxide layer thickness was determined using FIB and TEM. Samples anodised via the Agluna patent method were initially anodised at 15V for three minutes and then at 100V for one minute. The voltage was then reduced to 20V for 20 minutes. The resultant oxidised titanium alloy disc samples that had been anodised by the above procedure in either the 2.1M H_3PO_4 or the 0.5M H_2SO_4 electrolytes were then reduced by placing the oxidised samples into a 0.1M KBr solution at RT for seven minutes, after which the samples were quickly rinsed in distilled water. In order for silver to be incorporated into the reduced-oxide surface via Ag ion exchange, the reduced-oxidised discs were then transferred into 0.05M, 0.5M and 5.0M AgNO3 solutions. The samples were soaked in these solutions for 60 minutes at RT. Samples anodised via the Agluna method were soaked in a 0.1M AgNO3 solution for 60 minutes at RT.

4.3.2 *Attachment of the Four Ag-TiO_2 powders via Anodising*

In order to attach the Ag-TiO_2 particles to the DAE titanium surface, 0.1g of each of the powder particles was first suspended in 5ml ethanol and then 300uL of the suspension was pipetted on to eight separate titanium discs *i.e.* two discs were coated with each powder. The solvent was then allowed to evaporate (Figure 51) and this step was repeated three times *i.e.* 3 x 300uL in order to achieve a even coating across the surface of the titanium subtrate.

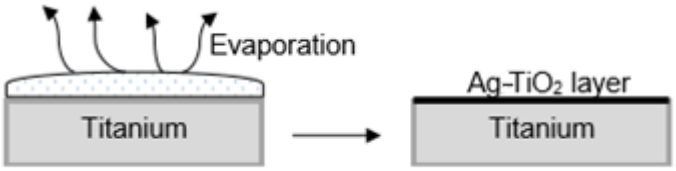

Figure 51 : Illustration of powder coating process.

Once the 3 x coating was completed (illustrated in Figure 52), four of the eight coated titanium disc surfaces were anodised in the 0.5M H_2SO_4 electrolyte and the remaining four were anodised in the 2.1M H_3PO_4 electrolyte. The anodising was conducted at 100V for 60 seconds. The process above was repeated five times.

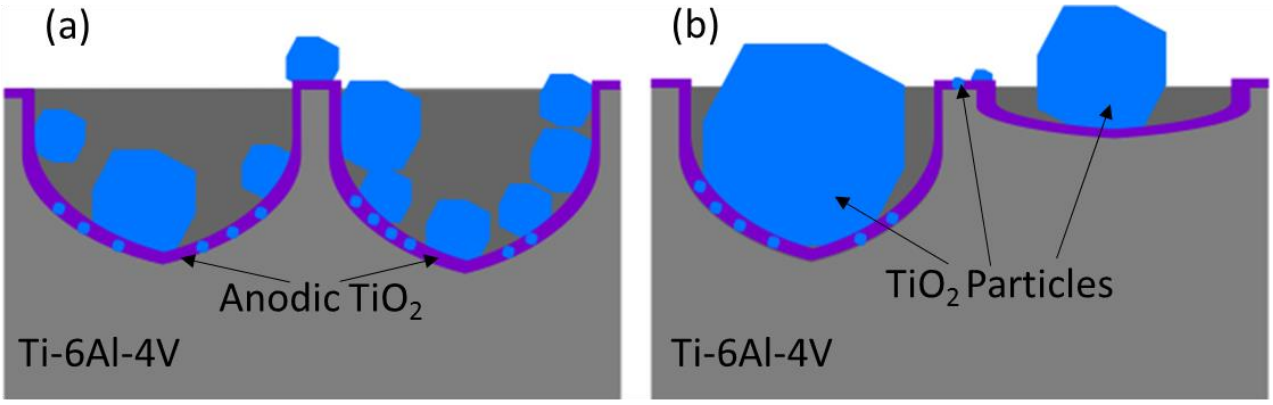

Figure 52 : Illustration of the possible outcome of DAE surfaces with deposited Ag-TiO_2 particles attached via anodic oxidation. (a) Small to medium Ag-TiO_2 sized particles, (b) Larger Ag-TiO_2 Particles.

4.3.3 *Silver Ion Implantation*

Ten samples were left in the polished condition. Ten polished Ti-6Al-4V discs were anodically oxidised using 2.1M H_3PO_4 and a further ten using 0.5M H_2SO_4, according to the method in Section 4.3.1. Five of the 2.1M H_3PO_4 anodised samples, five of the 0.5M H_2SO_4 anodised samples and five of the polished samples were ion implanted at 0.4 x 10^{17} ions/cm^2 and the remaining five of each group were ion implanted at 1.2 x 10^{17} ions/cm^2. The acceleration energy used was 84 keV and ion beam current density of 1 to 1.5 µA/cm^2.

Table 19 : Ion implantation conditions.

SAMPLE ID	SAMPLE PRE-IMPLANTATION CONDITION	IMPLANTATION DOSE REALISED(ION/CM^2)	IMPLANTATION TEMPERATURE
I1	Anodised 2.1M H_3PO_4 100V 1min	0.4 x 10^{17}	RT
I2	Anodised 2.1M H_3PO_4 100V 1min	0.4 x 10^{17}	RT
I3	Anodised 2.1M H_3PO_4 100V 1min	1.2 x 10^{17}	RT
I4	Anodised 2.1M H_3PO_4 100V 1min	1.2 x 10^{17}	RT
I5	Anodised 0.5M H_2SO_4 100V 1min	0.4 x 10^{17}	RT
I6	Anodised 0.5M H_2SO_4 100V 1min	0.4 x 10^{17}	RT
I7	Anodised 0.5M H_2SO_4 100V 1min	1.2 x 10^{17}	RT
I8	Anodised 0.5M H_2SO_4 100V 1min	1.2 x 10^{17}	RT
I9	Polished	0.4 x 10^{17}	RT
I10	Polished	0.4 x 10^{17}	RT
I11	Polished	1.2 x 10^{17}	RT
I12	Polished	1.2 x 10^{17}	RT
ACCELERATION ENERGY(KEV)	84		
ION BEAM CURRENT DENSITY (µA/CM^2)	1 to 1.5		

4.4 Surface Characterisation

After the preparation of the various sample surfaces, the samples were imaged using Scanning Electron Microscopy. The images gathered for the anodised and ion exchanged samples (hereafter referred to as Ag Ion exchanged anodic TiO_2 layers) in Section 4.3.1 were analysed with ImageJ software to determine the equivalent pore diameter of the pores that had formed during ASD at 100V. In the presented EDS data, Ag could be detected. However, its presence could not be evaluated quantitatively, because the thicknesses of the oxide films were in the 200nm range and the EDS was not sensitive enough to quantitatively detect Ag through all the background noise.

This procedure was followed by X-ray diffraction to determine any crystal structure differences between the two different sample types. Atomic Force Microscopy (AFM) was then conducted to highlight any differences in topography between the two sample types. Rutherford Backscatter Spectroscopy (RBS) was then used to quantify the Ag within the Ag Ion exchanged anodic TiO_2 layers. Thereafter, FIB was used to cross-section the oxide layers. Finally, TEM images of the cross-sections were taken and analysed via EDS analysis.

For the Ag-doped TiO_2 particles attached via anodising in Section 4.3.2, the powder particles themselves were first characterised via SEM, EDS and AAS. SEM images were used to determine the average particle size via ImageJ. EDS point and mapping data were used to confirm the presence of silver. The particles were then digested in hot concentrated H_2SO_4 using the MARS-5 Microwave Digester. After digestion the resultant solutions were analysed using AAS to quantify the Ag present in each of the four powders.

After powder attachment via anodising, the surfaces were imaged in SEM and further EDS analysis was conducted. This was followed by X-ray Diffraction to determine any crystal structure differences between the different samples. Rutherford Backscatter Spectroscopy was then used to quantify the Ag within the surface oxide. Finally, FIB was employed to cross-section the oxides and TEM images of the cross-sections were taken. Thereafter, an EDS analysis was conducted on the cross-sections.

The Ag ion implanted samples were imaged using SEM. Images gained from SEM were analysed using ImageJ depending on the images obtained. This was followed by X-ray Diffraction to determine any crystal structure differences between the different samples before and after ion implantation (Refer to Section 4.3.3). Atomic Force Microscopy was conducted to highlight any differences in topography between sample types. Rutherford Backscatter Spectroscopy was then used to quantify the Ag within the surface oxide. Finally, FIB was employed to cross-section the oxides and TEM images of the cross-sections were taken. Thereafter, an EDS analysis was conducted on the cross-sections.

When all of the above procedures had been followed, samples were placed within a 25ml SBF at 37°C for two weeks. 1ml aliquots of solution were taken at 24 hours (To observes initial burst release of silver), 72 and 336 hours (in order to observe how the silver release rate changes over this time frame). These aliquots were stabilised with diluted nitric acid and analysed using ICP-MS to quantify the silver released from the samples.

5. Results and discussion of the surface and sub-surface characterisation of surface modified Ti-6Al-4V

5.1 Ag Ion Exchanged Anodic TiO_2 Layers

5.1.1 *Surface Morphology*

Ti-6Al-4V surfaces were anodised using two electrolytes, namely, 0.5M H_2SO_4 and 2.1M H_3PO_4. The procedure during anodisation was initially:

- To hold the voltage at 15V for three minutes in order to initiate oxide growth and allow for the passivation of the oxide.
- Decrease the voltage briefly to 0V and then gradually raise to 100V, at which voltage it was maintained for 60 seconds.

During both steps the current was not allowed to exceed 50 mA. Figure 53 shows images of the resultant surfaces, (a) and (b), obtained after their respective anodisation procedures. For Sample (c), a third step was added by decreasing the voltage from 100V down to 20V for 20 minutes, as per the Agluna method, which was discussed in Section 3.7.7. It was seen that the anodising conditions of (a) produced a green oxide, whereas (b) and (c) produced similar pinkish-lilac coloured oxides, which was expected as both of these samples used the same electrolyte (2.1M H_3PO_4). According to Figure 15 in Section 3.7.6, anodisation at 100V corresponds to an oxide film thickness in the 200nm range, thus it was expected that all the samples would have oxide film thicknesses in this range. Table 5 in the same section related surface colour to thickness. This correlation also placed these surfaces in the 150-210nm range in terms of oxide thickness.

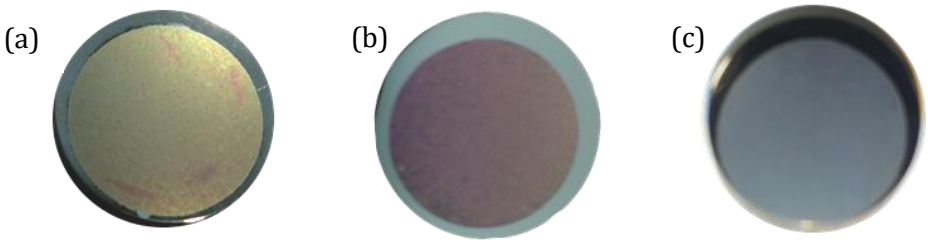

Figure 53 : Macroscopic images of oxide films produced via (a) 0.5M H_2SO_4 @100V 1min, (b) 2.1M H_3PO_4 @100V 1min and (c) the Agluna method.

The SEM results shown in Figure 54 (a) and (b) below, indicate that the surface pore morphology changed when the anodising electrolyte was changed from 0.5M H_2SO_4 to 2.1M H_3PO_4 *i.e.* The pore shape, size and homogeneity across the respective surface were different. Although not within the scope of this work, correct pore morphology is important for bone to tissue bonding after a medical implant is placed within the body. The samples anodised in 0.5M H_2SO_4 confirmed the results of S. Uttiya *et al.* [14]: Anodising in a H_2SO_4 electrolyte caused the formation of well-defined and isolated surface pores, relative to the ill-defined pore morphology generated by the 2.1M H_3PO_4 electrolyte. However, there was increased pore formation along the grain boundaries in the case of (a), owing to pore coalescence, and this had not been reported by S. Uttiya *et al.* [14]. In contrast, there was no pore coalescence along the grain boundaries in Figure 54 (b) and (c). The findings here further corroborated those of S. Uttiya *et al.* [14], in that in the case of the 2.1M H_3PO_4 there were a greater

number of pores on the surface that appeared to be linked together. However, S. Uttiya *et al.* [14] were premature in assuming a network morphology throughout the cross-section, as no cross-sectional data were present in their study. When comparing the surfaces obtained via the Agluna method {See Figure 54 (c)} and the anodised surface {See Figure 54 (b)}, both of which were generated by using the 2.1M H_3PO_4 electrolyte, there was no visual difference, despite the additional 20V step employed during anodisation via the Agluna method. Both had areas of high and low porosity with undefined pores. In other words, (b) and (c) were similar in their surface morphology.

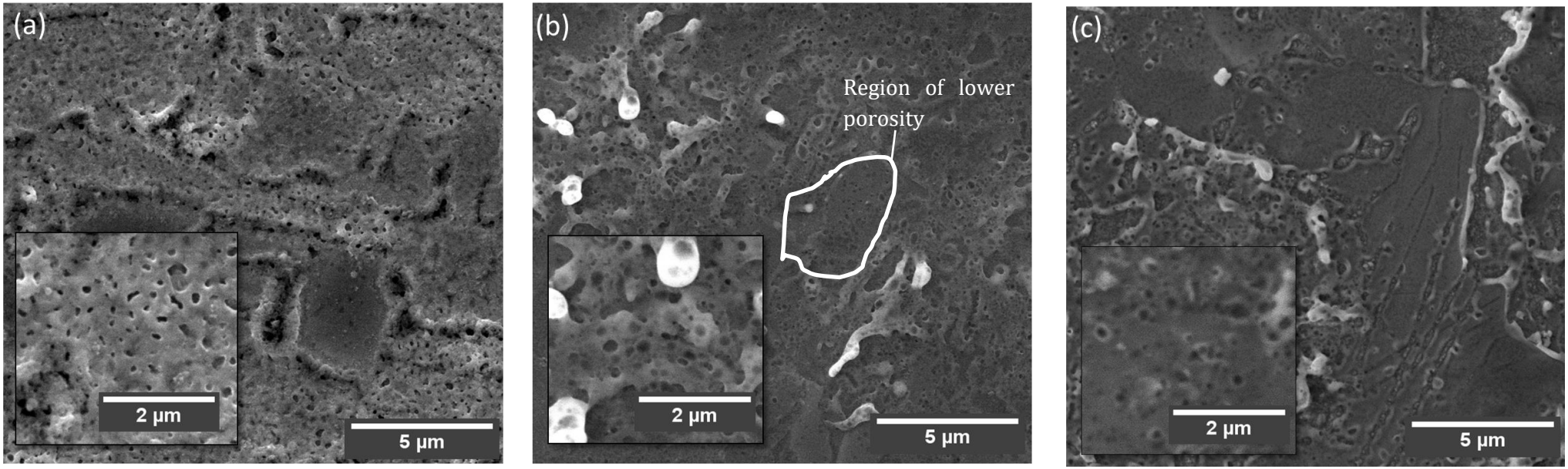

Figure 54 : Secondary electron SEM images of anodic TiO_2 layers formed using: (a) 0.5M H_2SO_4 (3 min @ 15V and 1 min @ 100V), (b) 2.1M H_3PO_4 as anodising electrolyte (3 min @ 15V and 1 min @ 100V) and (c) anodised via the Agluna method (2.1M H_3PO_4, 3 min @ 15V , 1 min @ 100V and 20min @ 20V).

5.1.2 *Surface roughness of oxide film*

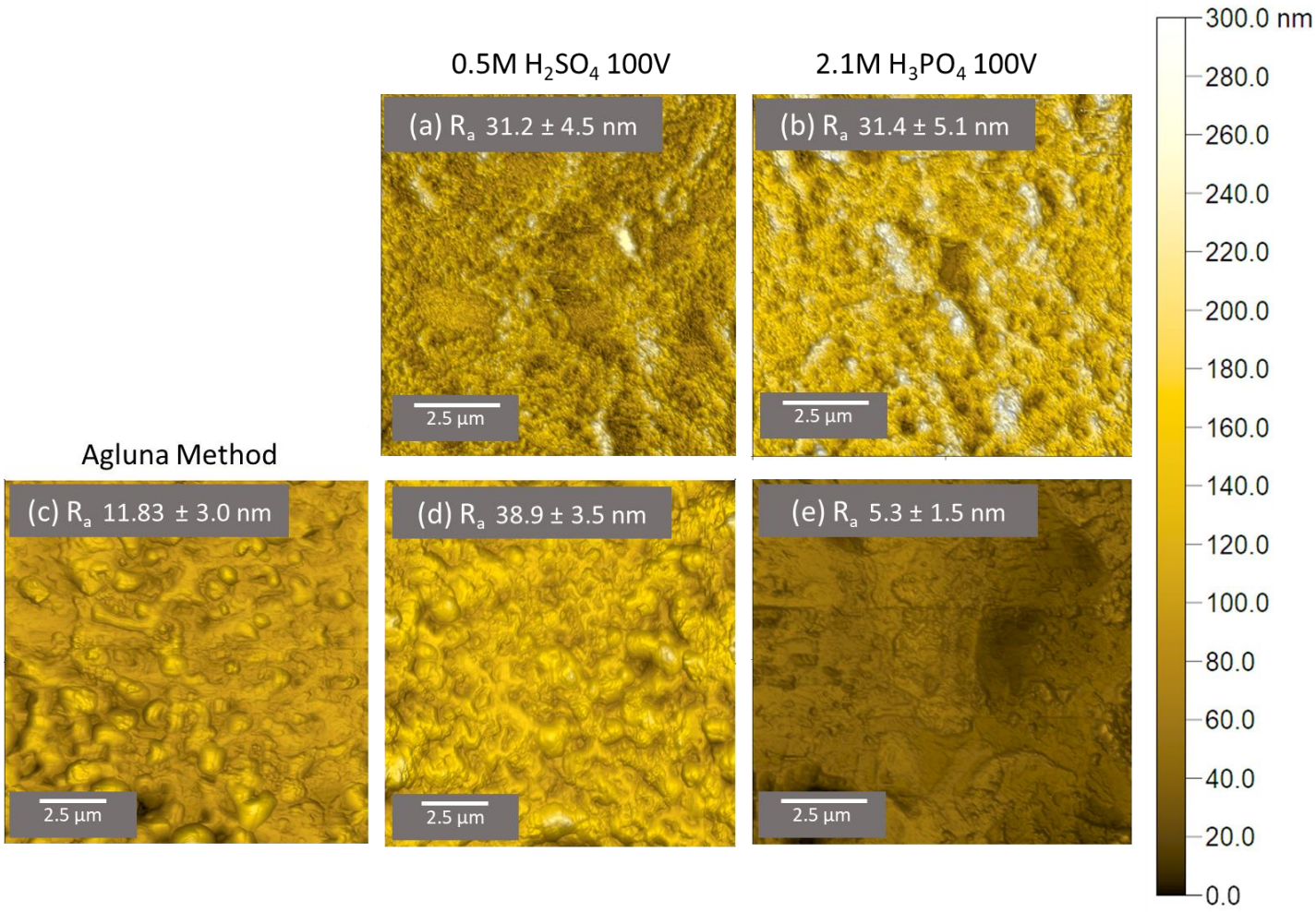

Figure 55: contact mode AFM images of TiO_2 films produced at 100V.

AFM results further confirmed that pores formed using the 0.5M H_2SO_4 electrolyte, as depicted in Figure 55 (a) and (d), had well-defined walls, in contrast to those in Figure 55 (b) and (e), which were anodised in the 2.1M H_3PO_4 electrolyte. Surface R_a data obtained from the AFM showed that the oxide produced by the 0.5 M H_2SO_4 electrolyte, as shown in Figure 55, had similar R_a in the different fields of view where (a) had 31.2nm and (d) had 38.9nm, whereas the oxide layer produced by the 2.1M H_3PO_4 electrolyte in (b) and (e) had vastly different R_a of 31.4 and 5.3nm respectively. This again suggested that the oxide produced by the 0.5M H_2SO_4 electrolyte was homogeneous in terms of porosity across the surface, relative to the significantly less homogeneous porosity of the oxide layer produced by the 2.1M H_3PO_4 electrolyte. The oxide layer generated via the Agluna method (See Figure 55 (c)) lay within the same average roughness range as the surfaces produced by the 2.1M H_3PO_4 electrolyte at 100V, namely 11.8nm. Thus, it was again shown that the extra step when anodising via the of Agluna method had no appreciable effect on the surface topography.

5.1.3 *Surface Oxide Film Porosity Distribution*

As shown in Figure 56 below, there was no significant difference in the average pore diameter between samples anodised via the 0.5M H_2SO_4 and 2.1M H_3PO_4 electrolytes. The average surface pore diameter results for the oxides produced by the 0.5M H_2SO_4 and 2.1M H_3PO_4 electrolytes, as well as by the Agluna method, were found to be 118.0 ± 70.4 nm, 121.0 ± 68.0 nm and 127.3 ± 91.3 nm respectively. It must be noted that these data did not include the areas of low porosity, as seen in

Figure 54 (b). The histograms in Figure 56 (a - c) were all very similar in shape. The maximum pore for (%) of (a), (b) and (c) were 22.9 %, 23.0 % and 21.7 % respectively, these pore (%) values all corresponding to an 80nm pore diameter. Thus, it was shown that the pore diameters for all the studied samples were predominantly within the range of 80 to 120nm. Thereafter, the pore (%) markedly decreased for 160 – 320nm pores in all cases.

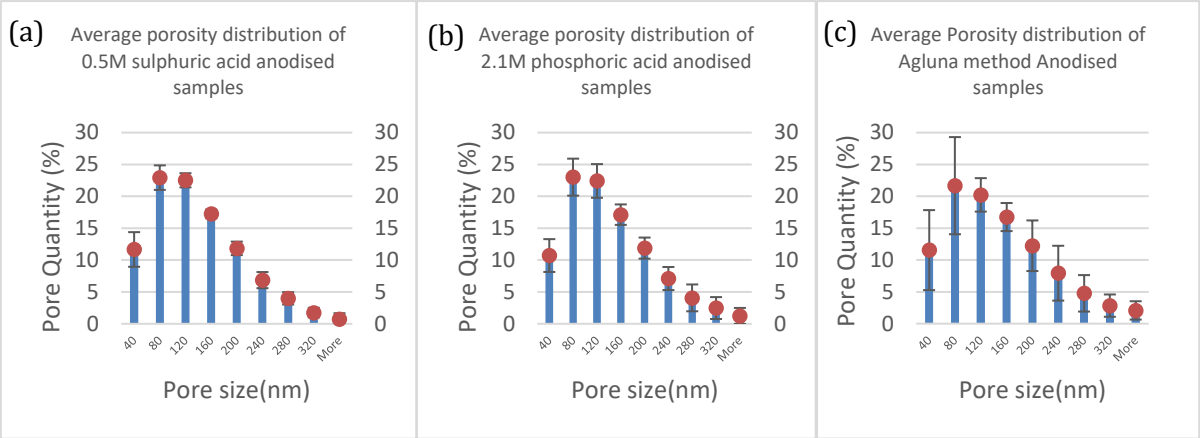

Figure 56 : Pore size distribution histograms of (a) 0.5M H_2SO_4 100V, (b) 2.1M H_3PO_4 100V, and (c) the Agluna method. *Ca.*100000 pores analysed per sample type across many fields of views.

When comparing the porosity produced via the 2.1M H_3PO_4 electrolyte at 100V, as seen in Figure 56(b) above, to the Agluna method {Figure 56 (c)}, it is shown that the additional 20V step during the Agluna method slightly increased the average pore diameters, as well as increasing the standard deviation from 68.0nm to 91.3nm, meaning that there is more inhomogeneity in terms of pore sizes on the surface.

5.1.4 *Surface RBS Analysis*

The RBS data, shown in Figure 57, revealed the atomic % (at%) of Ag present within the first 50nm of the two studied oxides. For the samples anodised in the 0.5M H_2SO_4 electrolyte at 100V, shown in Figure 57 (a) and (b), the results were 1.9 at% Ag and 0.8 at% Ag and for samples anodised in the 2.1M H_3PO_4 electrolyte at 100V, shown in Figure 57 (c) and (d), were 0.9 at% Ag and 5.0 at% Ag. For the samples anodised in the 0.5M H_2SO_4 electrolyte there was an unexpected decrease in the Ag content within the first 50nm of the surface as the $AgNO_3$ anodising electrolyte was increased. However, the samples anodised in the 2.1M H_3PO_4 electrolyte showed the expected trend of increasing Ag content within the first 50nm as the $AgNO_3$ concentration was increased. In Sample (d) there was an additional peak present, this peak being identified as bromine, which was used to reduce the surface after anodising before the Ag ion exchange step. This peak was not always present as it depended on the area that was analysed via RBS, This peak was excluded when calculating the at% Ag within the surface when present.

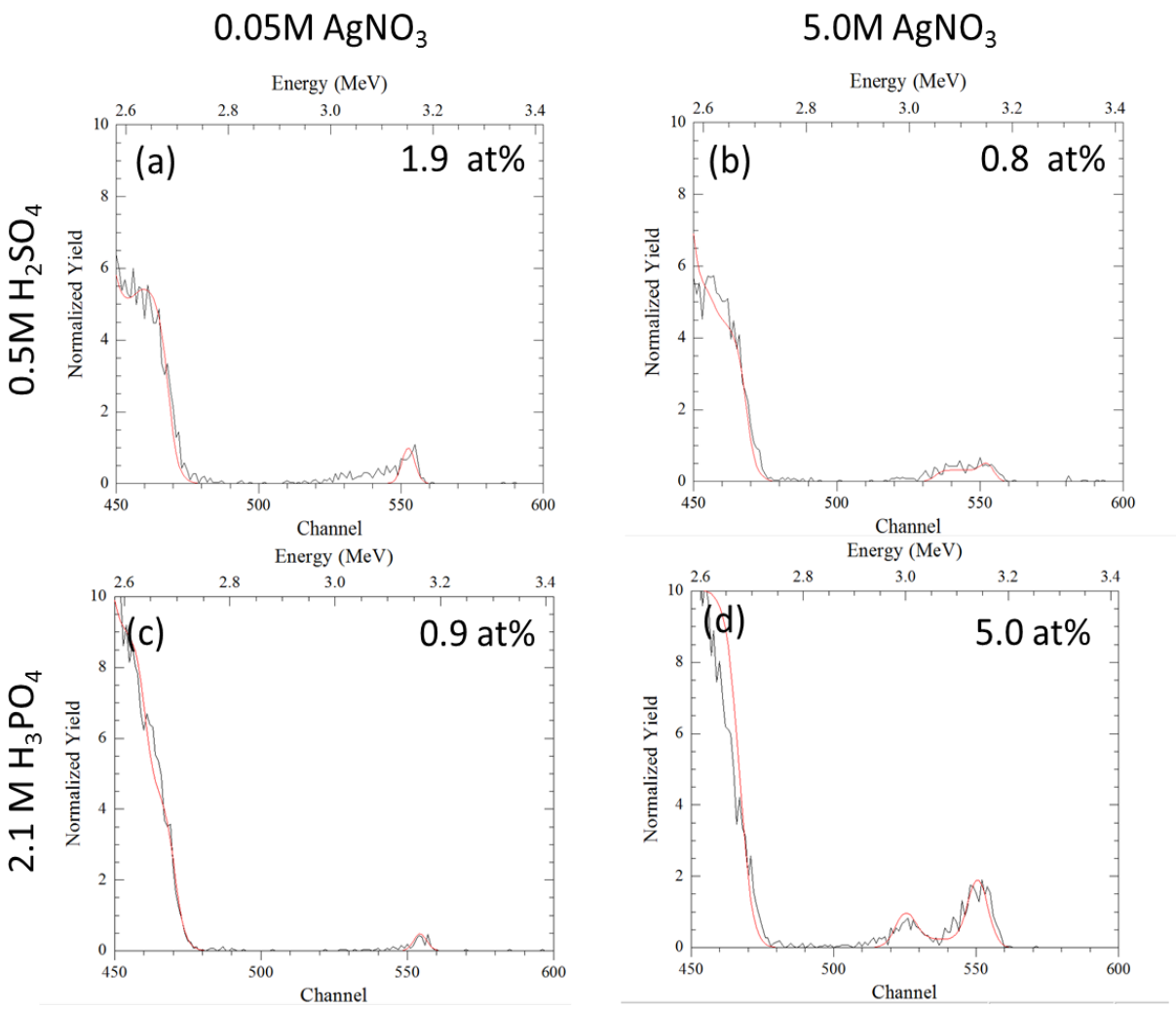

Figure 57 : Rutherford Backscatter results of Ag ion exchanged surfaces (a) Anodised in 0.5M H_2SO_4 and ion exchanged in 0.05M $AgNO_3$, (b) Anodised in 0.5M H_2SO_4 and ion exchanged 5.0 M $AgNO_3$, (c) Anodised in 2.1M H_3PO_4 and ion exchanged 0.05M $AgNO_3$ and (d) Anodised in 2.1M H_3PO_4 and ion exchanged 5.0 M $AgNO_3$.

RBS confirmed the presence of silver within the surface layer, but did not give an indication as to whether this silver would release from the surface and act as a desired antimicrobial agent. Therefore, in order to effectively draw conclusions from the RBS data, silver release rate curves would be required to clarify the relationship between the stored silver in the surface and the corresponding silver release, which will be further discussed in a chapter 6.1.

5.1.5 *Surface X-ray Diffraction*

When comparing the XRD spectra of the oxides generated by the 0.5M H_2SO_4 electrolyte and the 2.1M H_3PO_4 electrolyte, as seen in Figure 58 (a) and (b) respectively, to the spectrum in Figure 60 of Ti-6Al-4V, it is apparent that there was an additional peak for both (a) and (b) in the 25 - 30 theta range. Upon comparison to relevant reference spectra for TiO_2, these peaks in the 25 - 30 theta range could be identified as the anatase (101) and rutile (110) in Figure 58 (a) and (b) respectively.

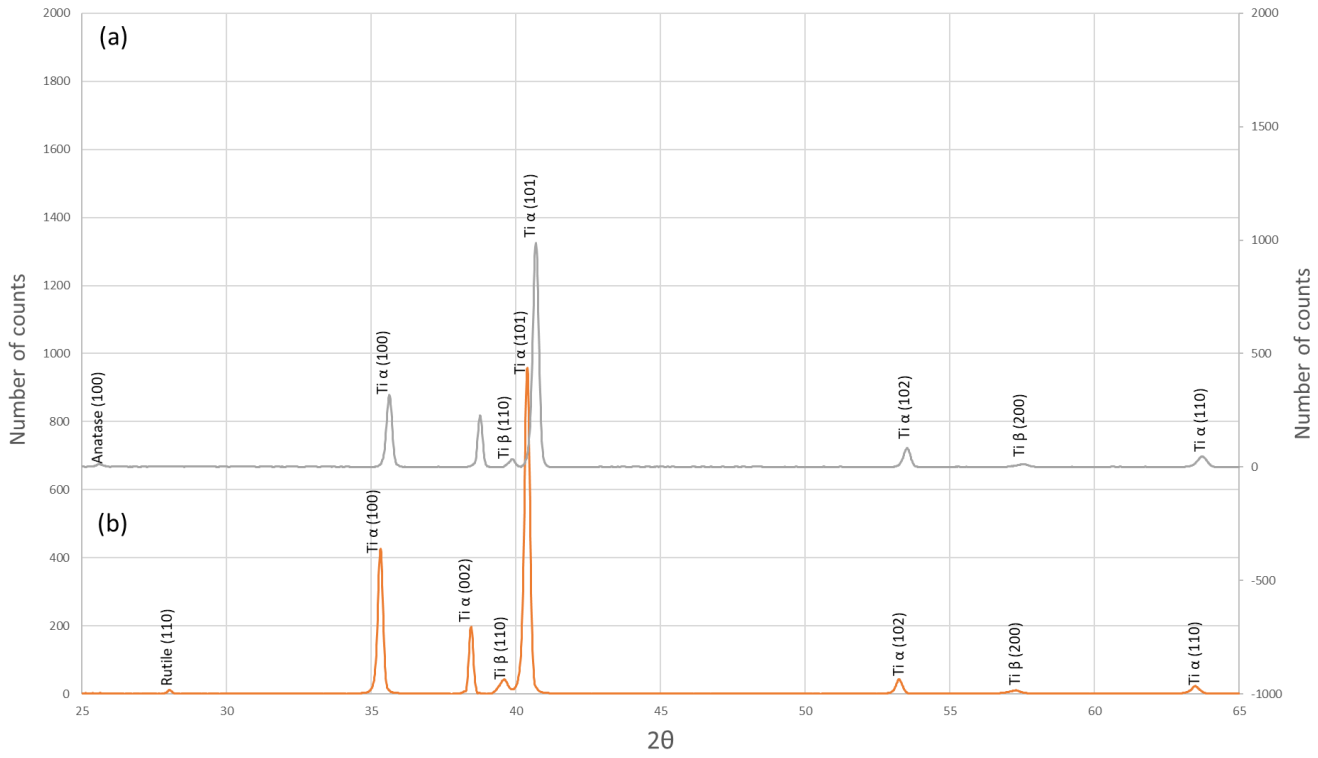

Figure 58 : XRD spectra of anodic TiO_2 formed via anodising in (a) 0.5M H_2SO_4 100V and (b) 2.1M H_3PO_4 at 100V.

Figure 58 (a) shows that the oxide film produced by the 0.5M H_2SO_4 electrolyte produced a surface that contained the predominantly anatase phase oxide film, while the XRD spectrum of the oxide generated by the 2.1M H_3PO_4 electrolyte, shown in 58 (b), had a predominantly rutile crystal structure. These results correlated with those reported in previous research [19,60].

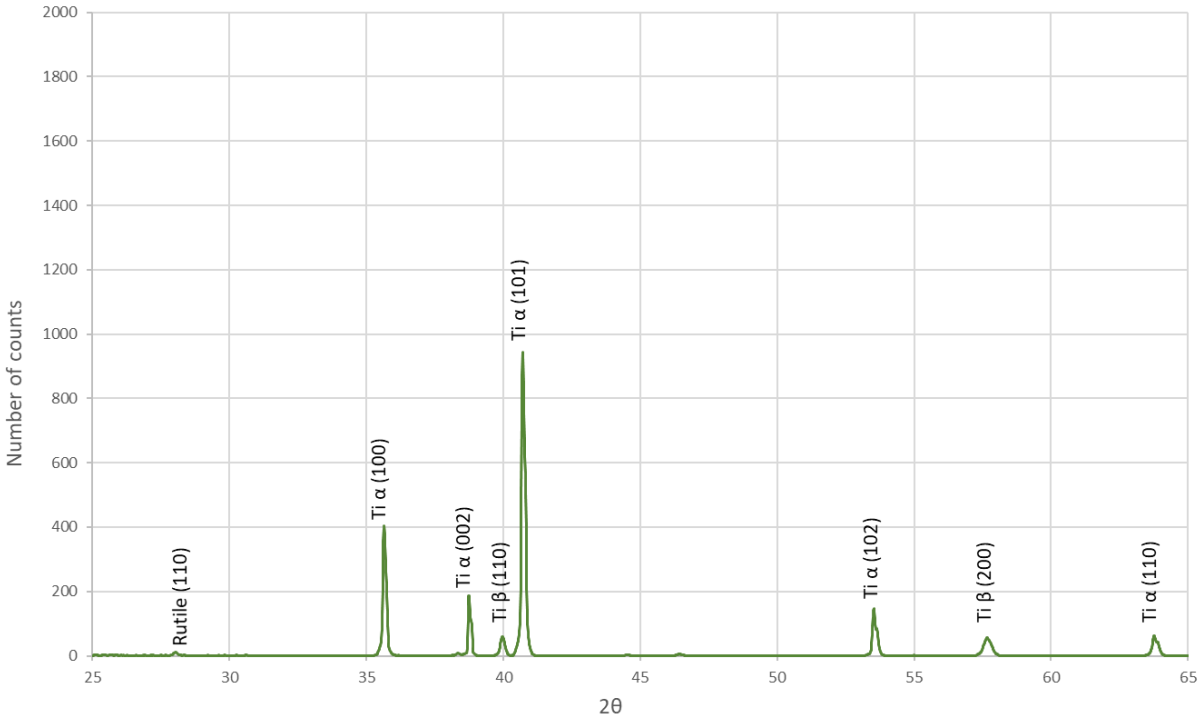

Figure 59 : XRD of sample anodised via the Agluna method.

When comparing the XRD results in Figure 58 (b) with those obtained for the Agluna method in Figure 59, the results were found to be nearly identical to those of the Agluna method, which also produced a predominantly rutile oxide. This was to be expected, since both these methods used 2.1M H_3PO_4 as their respective electrolytes.

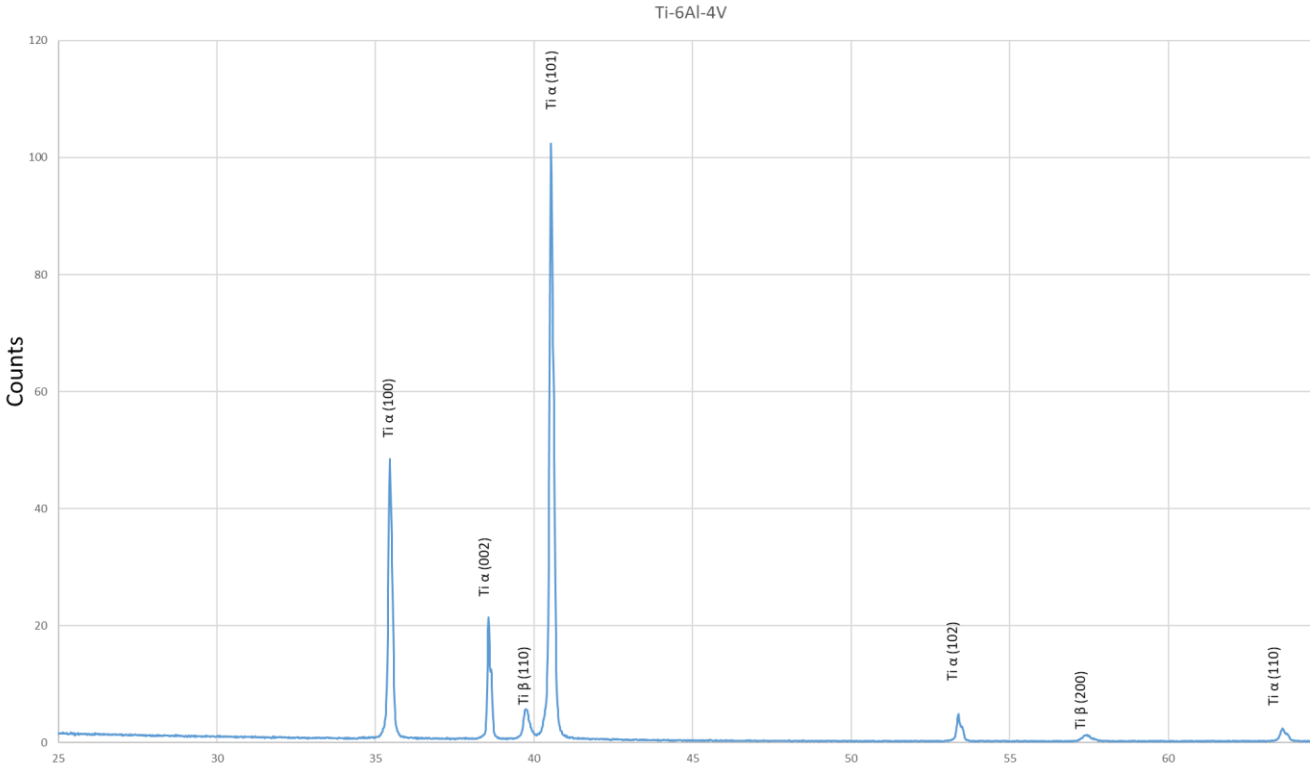

Figure 60 : XRD spectrum of Ti-6Al-4V.

However, there were a few instances where samples did not show any crystalline structure in their XRD spectra. There were two plausible explanations for these anomalies. Either the samples were completely amorphous or, more likely, the oxide layer that had formed in each case was too thin relative to the base metal, with the result that the signal from the oxide film was masked by the underlying titanium base metal. In literature, these studies were usually conducted using titanium foils, which, after anodisation, had significantly less base metal remaining and thus less interference. Therefore, in this study the XRD data could only be used qualitatively to determine the most prevalent phases present after anodisation under the different studied conditions.

5.1.6 *Sub-Surface Morphology*

Figure 61 (a) and (d) show the titanium oxide film produced via anodisation in the 0.5M H_2SO_4 and 2.1M H_3PO_4 electrolytes respectively, before ion exchange with $AgNO_3$. Both oxides were internally porous, the layers both showing isolated pores, rather than an internal network of pores. On the other hand, pore coalescence was visible to a greater degree in Sample (a) relative to Sample (d). Image analysis of the oxide films produced by the 0.5M H_2SO_4 electrolyte revealed that the average internal pore diameters were 39.3 ± 39.8 nm, whereas the oxide films produced by the 2.1M H_3PO_4 electrolyte had a slightly smaller average pore diameter of 20.1 ± 30.8 nm. The standard deviations from the mean for both oxide types were relatively high compared to their respective means. This indicated that there was a large spread in the porosity data, which correlated with a visual inspection, where the pore sizes could be identified as highly varied.

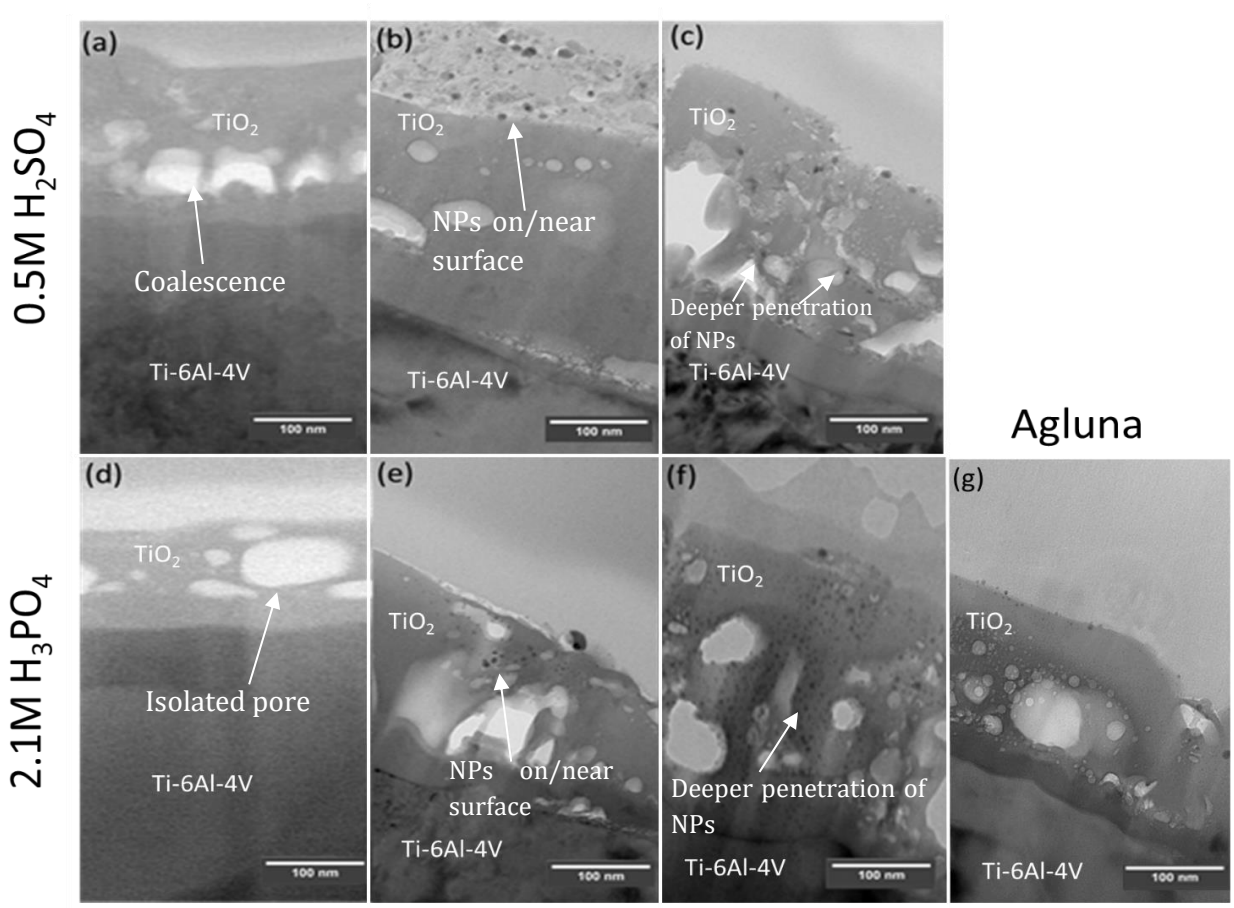

Figure 61 : Bright-field TEM images of oxide layer cross-sections produced by (a) 0.5M H_2SO_4, (b) 0.5M H_2SO_4 followed by Ag ion exchange in 0.05M $AgNO_3$, (c) 0.5M H_2SO_4 followed by Ag ion exchange in 5.0M $AgNO_3$, (d) 2.1M H_3PO_4 as anodising electrolyte at 100V, (e) 2.1 M H_3PO_4 followed by Ag ion exchange in 0.05M $AgNO_3$, (f) 2.1 M H_3PO_4 followed by Ag ion exchange in 5.0M $AgNO_3$ and (g) the Agluna method.

After the Ag ion exchange of the oxide films that had been generated using the 0.5M H_2SO_4 and 2.1M H_3PO_4 electrolytes in a 0.05M $AgNO_3$ solution, as shown in Figure 61 (b) and (e), the images revealed the presence in both cases of nanoparticles (NPs) on the surface, as well as slightly within the oxide surface. When the $AgNO_3$ concentration was increased to 5.0M, it was evident that the AgNPs had penetrated even more deeply within the oxide films, as shown in Figure 61(c) and (f). Therefore, through comparison of these micrographs it could be determined that a higher $AgNO_3$ concentration led to deeper formation of the AgNPs within the oxide films. Samples treated according to the Agluna method showed similar AgNP formation and sub-surface morphological features to those anodised in the 2.1M H_3PO_4 electrolyte.

When these oxide films were studied in cross-section it became apparent that, although the surface porosity in the case of the film produced by 2.1M H_3PO_4 appeared to produce a network-like structure on the surface, this did not necessarily translate into a fully-developed network formation internally.

The average thickness of the oxide films produced by anodisation in the 0.5M H_2SO_4 and 2.1M H_3PO_4 electrolytes, as well as those generated using the Agluna method, are summarised in Table 20 below. On average, the oxide films produced when using the 0.5M H_2SO_4 electrolyte were thicker than those generated when using the 2.1M H_3PO_4 electrolyte. In contrast, when the oxide film thickness obtained via anodisation of the samples in the 2.1M H_3PO_4 electrolyte and via the Agluna method were compared, there was no significant difference in oxide film thickness. This indicated that the additional

20V step employed during the Agluna method anodising procedure had no effect on the oxide film thickness.

Table 20 : Summary of the average oxide thickness results obtained from TEM cross-section image analysis.

	0.5M H_2SO_4	**2.1M H_3PO_4**	**AGLUNA**
THICKNESS (NM)	259.5 ± 35.3	206.0 ± 24.2	193.9 ± 27.7

The EDS mapping of oxygen and titanium in the oxide films, as depicted in Figure 62, showed the expected results, with the base metal consisting of mainly titanium and the oxide region (TiO_2) showing a mixture of oxygen and titanium. This confirmed that the base material was titanium with a titanium oxide layer (TiO_2) bonded to the surface.

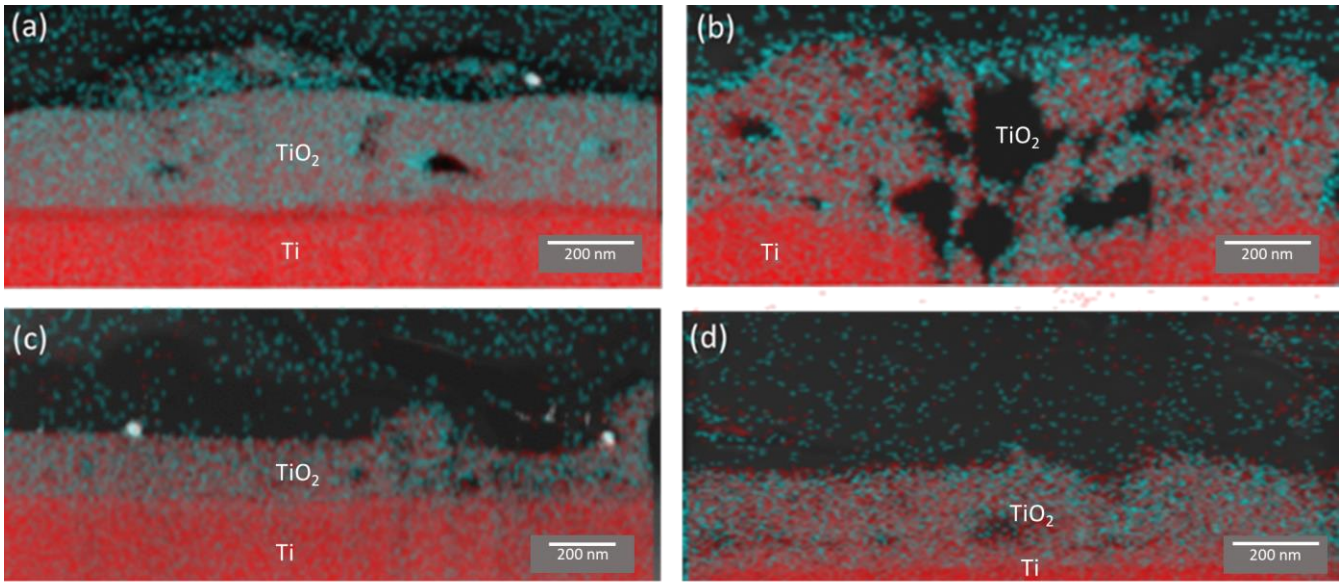

Figure 62 : Bright-field TEM, EDS maps of oxygen (blue) and titanium (red) of samples, (a) anodised in 0.5M H_2SO_4 electrolyte, followed by ion exchange in 0.05M $AgNO_3$, (b) anodised in 0.5M H_2SO_4 electrolyte, followed by ion exchange in 5.0M $AgNO_3$, (c) anodised in 2.1M H_3PO_4 electrlyte, followed by ion exchange in 0.05M $AgNO_3$, and (d) anodised in 2.1M H_3PO_4 electrolyte, followed by ion exchange in 5.0M $AgNO_3$.

Figure 63 below shows the EDS mapping and point ID data for the various cross-sectioned TiO_2 samples that had been produced by anodisation in either the 0.5M H_2SO_4 or 2.1M H_3PO_4 electrolytes, followed by Ag ion exchange in either 0.05M or 5.0M $AgNO_3$ solutions.

The EDS mapping (shown in blue) of the cross-sectioned oxide films presented in Figure 63 below showed lower sensitivity towards silver relative to the EDS point ID data collected, and thus the EDS mapping of the silver was not as helpful in gaining additional information regarding the chemical make-up of the oxide films. This inability of the EDS mapping to detect the silver may have been due to the higher amount of bulk oxide relative to the silver leading to less than satisfactory counts, thus resulting in the silver signals during EDS mapping becoming low and/or undetectable.

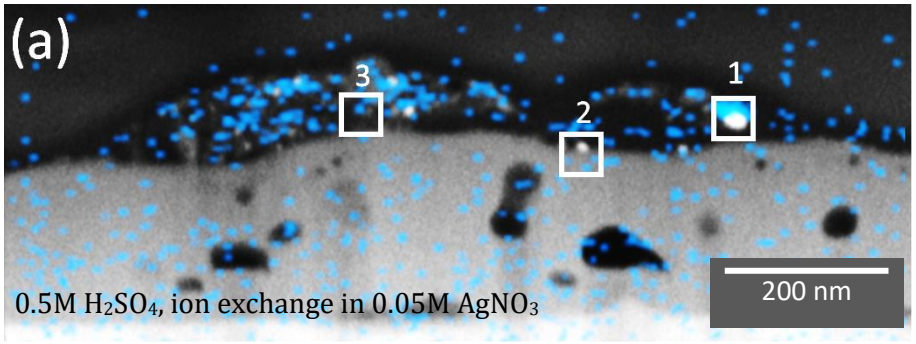

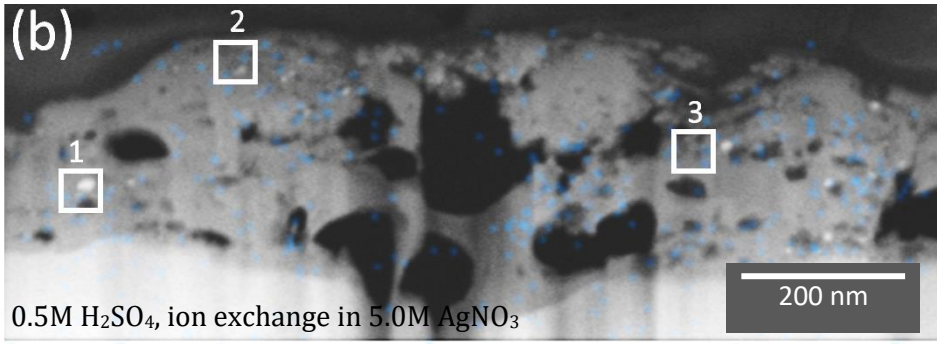

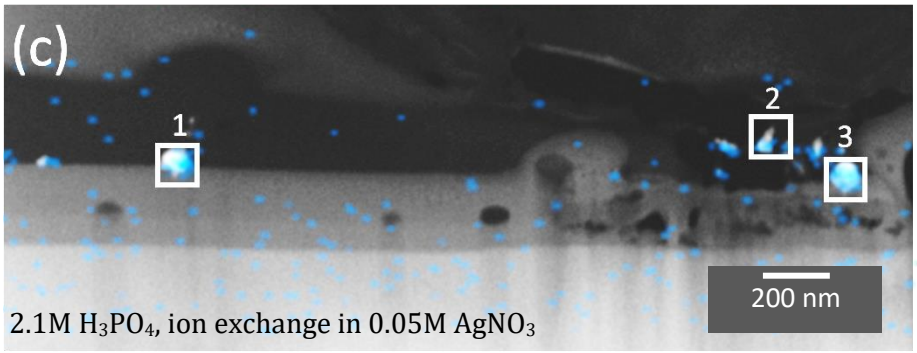

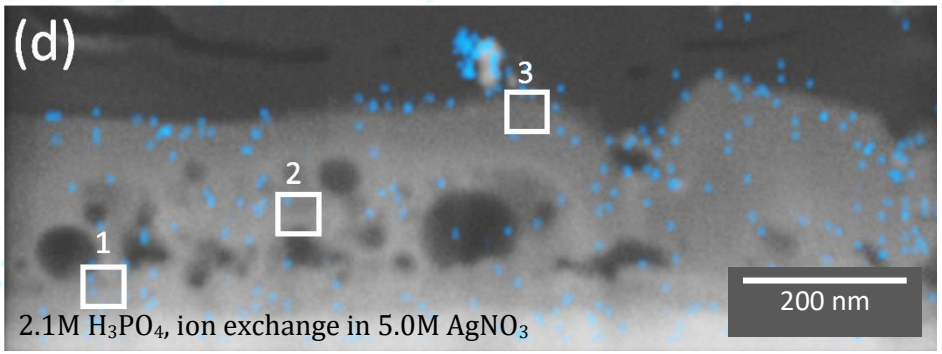

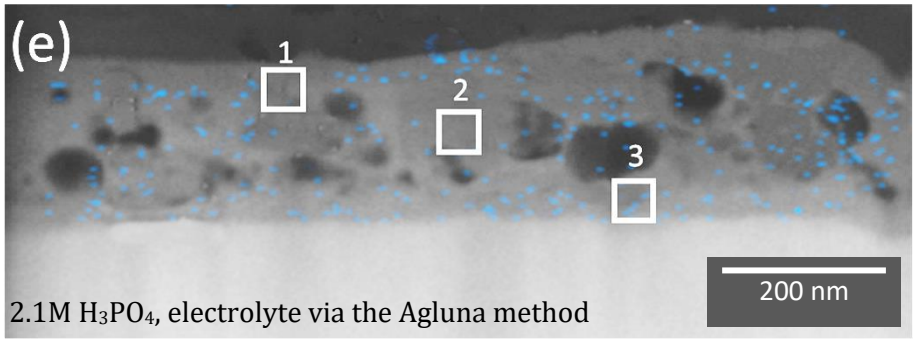

	a			b			c			d			e		
	1	2	3	1	2	3	1	2	3	1	2	3	1	2	3
Ag (wt%)	70	18	23	13	9	14	11	80	73	-	-	2	5	1	23
Ti (wt%)	<1	4	13	31	31	33	9	-	<1	50	38	5	31	5	13
O (wt%)	2.5	13	22	40	38	34	12	-	2	41	50	18	40	18	22

Figure 63: Dark-field TEM, EDS mapping (blue) and point ID data (white squares) of Ag for Samples (a) anodised in 0.5M H_2SO_4 electrolyte, followed by ion exchange in 0.05M $AgNO_3$, (b) anodised in 0.5M H_2SO_4 electrolyte, followed by ion exchange in 5.0M $AgNO_3$, (c) anodised in 2.1M H_3PO_4 electrolyte, followed by ion exchange in 0.05M $AgNO_3$, (d) anodised in 2.1M H_3PO_4 electrolyte, followed by ion exchange in 5.0M $AgNO_3$, and (e) anodised in 2.1M H_3PO_4 electrolyte via the Agluna method.

The EDS point ID and mapping data gathered from samples in this section will now be discussed. In Figure 63 (a) the Ag detected within the oxide film by EDS point ID and mapping (See Areas 1, 2 and 3) was in the same location as the NPs depicted in Figure 61 (b). This was confirmation that the NPs were silver, *i.e.* AgNPs.

Figure 63 (b) shows that the use of EDS mapping did not facilitate a conclusive identification of areas that contained silver. This was because the signal for silver in the anodic oxide and the base titanium were similar and thus most of the mapping data could be considered noise. In contrast, EDS point ID analysis, as seen in Areas 1, 2 and 3, detected 9 - 14 wt% of silver. The locations of the EDS point ID analysis and the locations of the AgNPs depicted in the corresponding TEM image of this sample, shown in Figure 61(c), were in agreement. This reinforced the observation that the detected NPs were AgNPs .

In Figure 63 (c), both EDS point ID analysis and EDS mapping detected silver near and on the surface of the oxide film, while the TEM image in Figure 61(e) showed NP formation deeper beneath the oxide film surface. Point ID data in Figure 63 (d) detected silver on the surface of the oxide film in Area 3. Deeper within the oxide film, *i.e.* in Areas 1 and 2, no silver was detected. The corresponding TEM image of this sample in Figure 61(f) showed the presence of AgNPs near the surface, which corroborated the EDS point ID data. However, the same TEM image {Figure 61(f)} also showed silver nanoparticle formation deeper into the oxide film cross-section, which was not detected by the EDS point ID data or EDS mapping.

Figure 63 (e) shows the EDS Mapping and EDS point ID analysis of samples anodised via the Agluna method, using a 0.1M $AgNO_3$ concentration during the Ag ion exchange. The point ID analysis detected silver near the surface (Area 1) and beneath the surface (Area 2). Deeper within the oxide film (Area 3) no silver was detected. The corresponding TEM image for this sample, depicted in Figure 61(g), coincided with the point ID data, as visually there were AgNPs present on and slightly within the surface.

As stated above and in previous sections, it was anticipated that EDS data would be somewhat unreliable during this study, owing to the relatively low amounts of silver penetration into some of the oxide films and the low sensitivity of the EDS to silver in the presence of relatively large amounts of bulk oxide.

5.1.7 *Summary Discussion of Silver ion Exchanged Surfaces*

In summary, there were few significant differences with regards to the surface and sub-surface morphologies in samples anodised in the 2.1M H_3PO_4 electrolyte *versus* the Agluna method (where an additional 20V 20min anodising step was utilised). In terms of the crystal structure phases of the oxide films, both were found to be predominantly rutile. Likewise, both of these sample conditions exhibited almost identical pore distribution across the surface, the only difference being a higher standard deviation of pores for samples produced via the Agluna method, which was attributed to the longer anodising time from the additional 20V step, which allowed for a greater degree of pore coalescence to take place. The surface roughness of the samples produced via the Agluna method also fell into the same range as those anodised in the 2.1M H_3PO_4 electrolyte. In terms of sub-surface morphologies and AgNP distribution within the oxide films, the two were comparable, as were the oxide film thicknesses.

Upon comparison of the samples anodised in the 0.5M H_2SO_4 electrolyte with those anodised in the 2.1M H_3PO_4 electrolyte, under otherwise identical anodising conditions, it was found that the porosity across the surface of the samples produced via the 0.5M H_2SO_4 electrolyte was more homogeneous relative to the porosity produced in the 2.1M H_3PO_4 electrolyte. In addition, the pore diameter and the pore diameter distributions were near-identical. The pores formed as a consequence of using the 0.5M H_2SO_4 electrolyte were shown to have defined pore walls, whereas those pores formed using the 2.1M H_3PO_4 electrolyte did not have defined pore walls.

With reference to the crystal structure phases, the oxide films formed by anodising in the 0.5M H_2SO_4 electrolyte were predominantly anatase, whereas rutile was the dominant phase when samples had been anodised in the 2.1M H_3PO_4 electrolyte. The average oxide film thickness of samples produced via the 0.5M H_2SO_4 electrolyte was thicker than that produced via the 2.1M H_3PO_4 electrolyte. The locations of AgNPs in the oxide films were similar in both cases, showing silver concentrations near the surface of the oxide film and to a lesser extent within the bulk of the oxide. Increasing the $AgNO_3$ ion exchange concentration in turn increased the depth of penetration of Ag into both the anodic oxides, which was confirmed by the deeper AgNPs formation of AgNPs within the oxide films.

It was concluded that anodising electrolyte selection played a major role in changing the surface and sub-surface morphology, as well as the crystal structure phases present after anodic oxidation of Ti-6V-4Al. The electrolyte selection for the anodising procedures investigated in this research had no effect on the location of silver within the oxide films. Furthermore, RBS data showed that increasing the Ag ion exchange concentration for samples anodised in the 0.5M H_2SO_4 electrolyte seemed to reduce the amount of Ag absorbed by the TiO_2, whereas samples anodised in the 2.1M H_3PO_4 electrolyte demonstrated an increase in the absorption of silver. The additional 20V step in the Agluna method had no significant effect on the oxide film with respect to thickness, morphology, silver absorption and crystal structure.

5.2 Ag-TiO_2 Fused via High Voltage Anodising

5.2.1 *Ag-Doped Powder Characterisation*

Figure 64 shows the results obtained from SEM imaging of the TiO_2 powders. It can be seen in (a), where no $AgNO_3$ was added in the powder synthesis process, that the powder particles remained relatively small, with an average equivalent circular diameter of 2.6 µm. As the concentration of the $AgNO_3$ was increased in the powder synthesis process, the average diameter of the TiO_2 particles increased to a maximum of 5.5 µm (d). The reason for this increase in particle diameter becomes evident when the diameter distributions, shown in Figure 64, (a) to (d), are compared. When the $AgNO_3$ concentration was increased the distribution incrementally changed from a relatively normal distribution in (a) to one that had become positively skewed in (d). This skewed distribution was indicative of TiO_2 particle agglomeration during synthesis, which resulted in a larger average particle diameter, as well as more significant standard deviations from the mean.

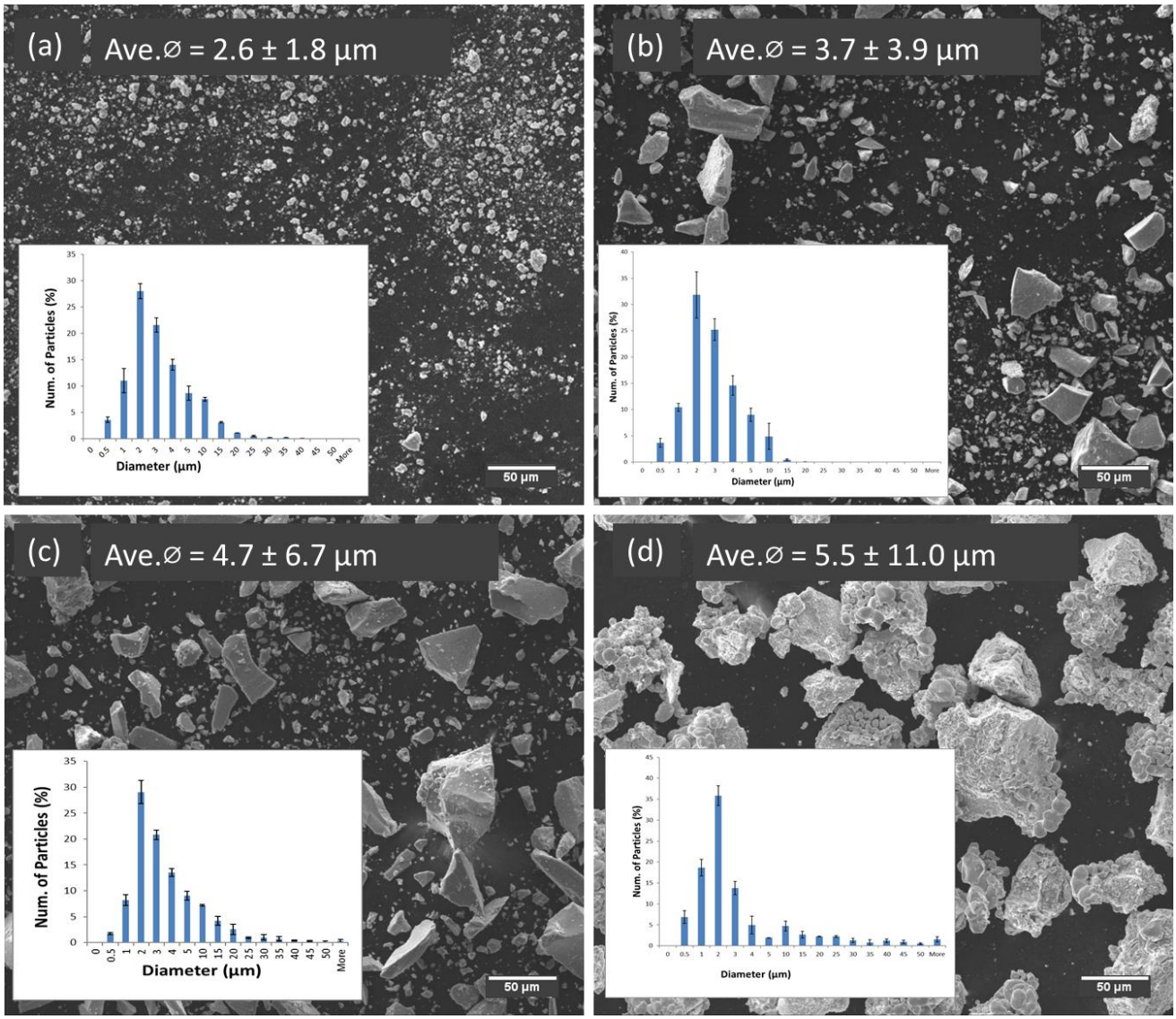

Figure 64 : Secondary electron SEM Images of TiO_2 powder synthesised in (a) 0 M, (b) 0.05 M, (c) 0.5 M and (d) 5.0 M $AgNO_3$ solution. Size distributions obtained via ImageJ software.

The EDS mapping results of the TiO_2 particles observed in Figure 64 are shown in Figure 65. The EDS mapping results showed an inverse relationship between Ag and Ti. This is illustrated in Figure 66. When the silver concentration within the powder samples increased, the titanium concentration decreased, while the oxygen content remained relatively constant. This result showed that the Ag atoms preferred to displace the Ti atoms within the TiO_2 crystal lattice during particle synthesis. Since EDS is not considered a strongly quantitative technique, elemental silver within the powder particles was also measured via the digestion of TiO_2 powder in hot concentrated H_2SO_4, followed by Atomic Absorption Spectroscopy (AAS). These results are shown in Table 21 and are also graphically displayed in Figure 66. As the $AgNO_3$ concentration during powder synthesis was increased, so did the Ag wt% within the resultant powders. The resultant silver-containing TiO_2 powders will from here on be referred to as Ag-TiO_2 powders.

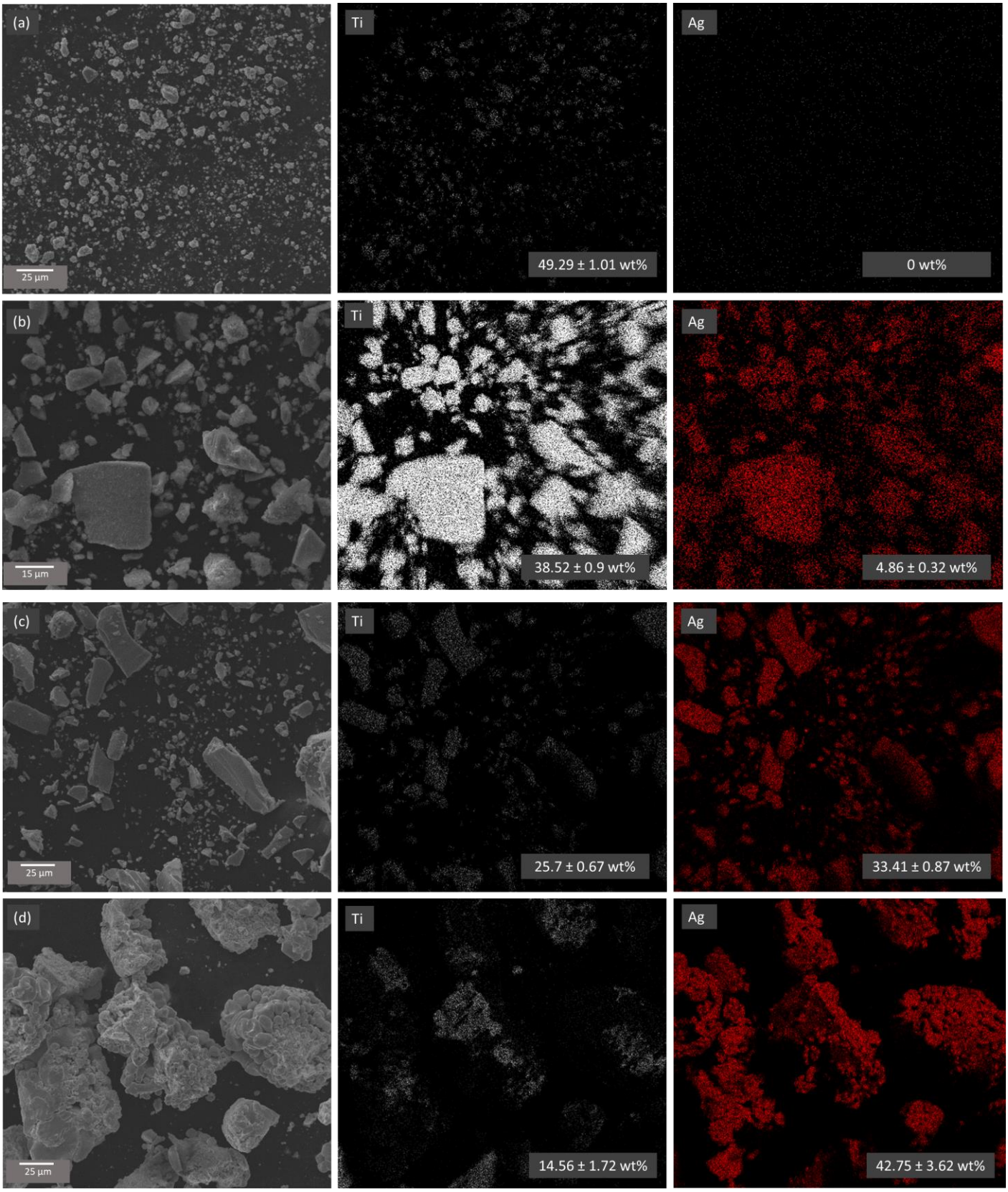

Figure 65 : EDS Mapping of TiO_2 powder doped with (a) 0 M, b) 0.05M, (c) 0.5M and (d) 5.0M $AgNO_3$ solutions.

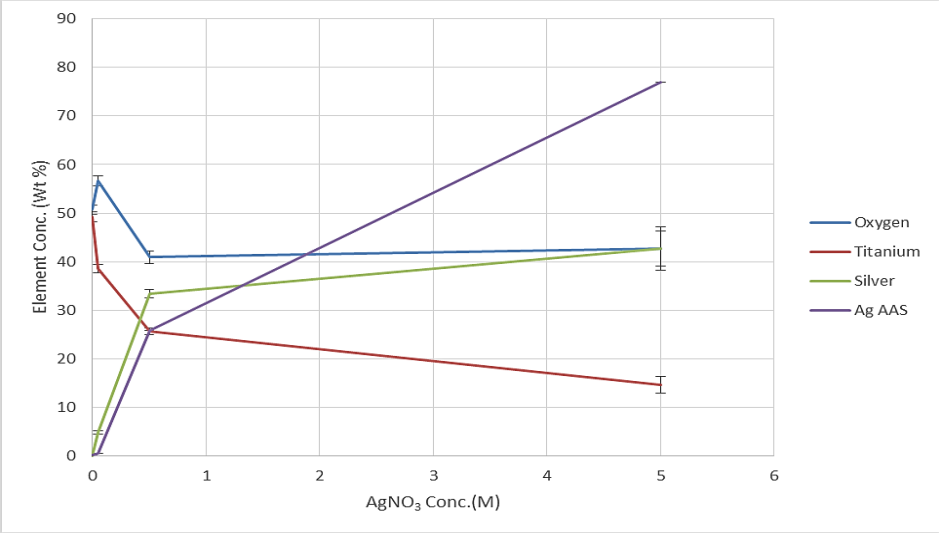

Figure 66 : Graphic representation of the elemental composition of Ag-doped TiO_2 powder after synthesis in 0 – 5.0M $AgNO_3$ solution.

Table 21: Ag (wt%) in titanium oxide powder synthesised using various concentrations of $AgNO_3$.

$AgNO_3$ (Molar)	Final powder Ag (wt %)
0 M	<0.10
0.05M	0.48
0.5M	25.77
5.0M	76,93

Upon comparison of the Ag wt% data obtained via EDS (green) with the data obtained via AAS (purple), as shown in Figure 66, it was found that at lower Ag concentrations, EDS analysis would overestimate the silver content within the Ag-TiO_2 powders relative to AAS analysis, while at high silver concentrations EDS would significantly underestimate the silver content. However, the trends produced by both techniques were similar, *i.e.* there was an increasing Ag wt% within the powders as the $AgNO_3$ concentration during powder synthesis was increased. It was found that as the wt% Ag within the Ag-TiO_2 powder samples was increased, so did the average particle diameter increase (See Figure 67 below).

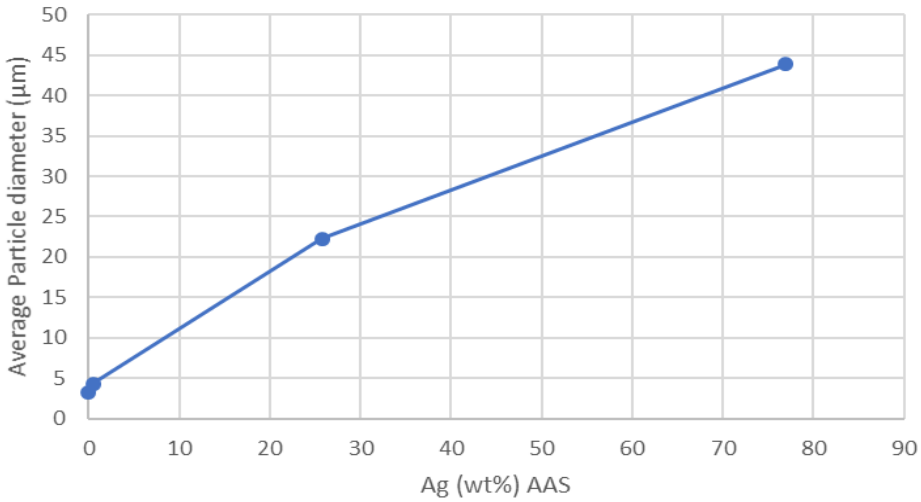

Figure 67: Relationship between the wt% Ag (measured by AAS) and the average powder particle diameter.

5.2.2 *Macroscopic Surface Morphology of Samples Post Ag-TiO_2 Attachment via Anodisation*

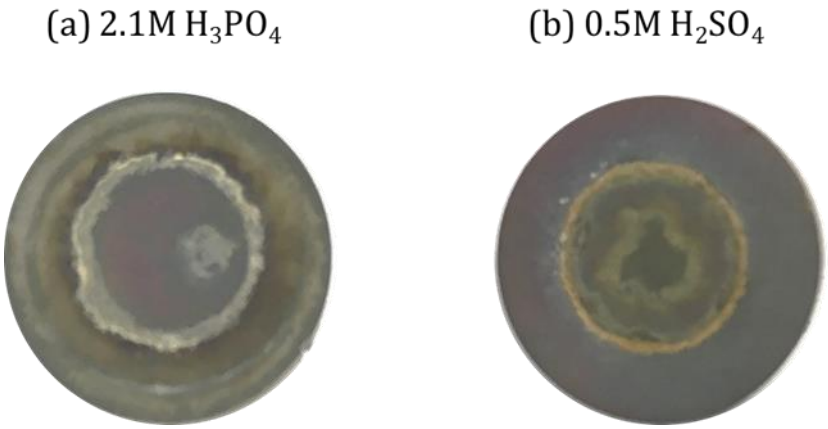

Figure 68 : Macroscopic images of Ag-TiO_2 particle coated surfaces. Particles fused via (a) 2.1M H_3PO_4 @ 100V and (b) 0.5M H_2SO_4 @ 100V.

Figure 68 above shows examples of the surfaces obtained after the coating of Dual Acid Etched (DAE) Ti-6Al-4V discs with Ag-TiO_2 powder and then subsequent anodising in the relevant electrolyte to facilitate Ag-TiO_2 powder attachment to the titanium alloy surface. It was visually apparent that, after anodisation, there was some residual powder remaining on the surfaces. The coated Ti-6Al-4V disc samples were placed in an ultrasonic bath after anodisation in order to determine whether the powder had been fused to the surface. During ultrasonication, it was observed that the unbound powder left the sample surface, but the fused powder was retained, as shown in Figure 68. It was further observed that most powder remained fused in areas where sufficient downward pressure was exerted, *i.e.* around the edges where a Viton O-ring was present. In order to scale up this method of Ag-TiO_2 powder attachment around a shaft, in order to provide a proof of concept, it was proposed that a Viton mesh be tightened around the shaft during the anodising procedure. Since a Viton mesh was not freely available, further Viton O-rings were instead placed around the circumference of the Ag-TiO_2 dip-coated titanium alloy shaft and then the shaft was anodised. The result of this procedure is shown in Figure 69. It was observed that Ag-TiO_2 powder did attach to the surface of the titanium alloy where pressure was exerted by the Viton O-rings. Although the coating is not uniform, this is not a requirement for the surface as the silver ions would be released into the environment immediately around the implant which should prevent bacterial adhesion. Additionally it is envisaged that a "raster" type pattern would be imprinted onto the implant if a mesh was used.

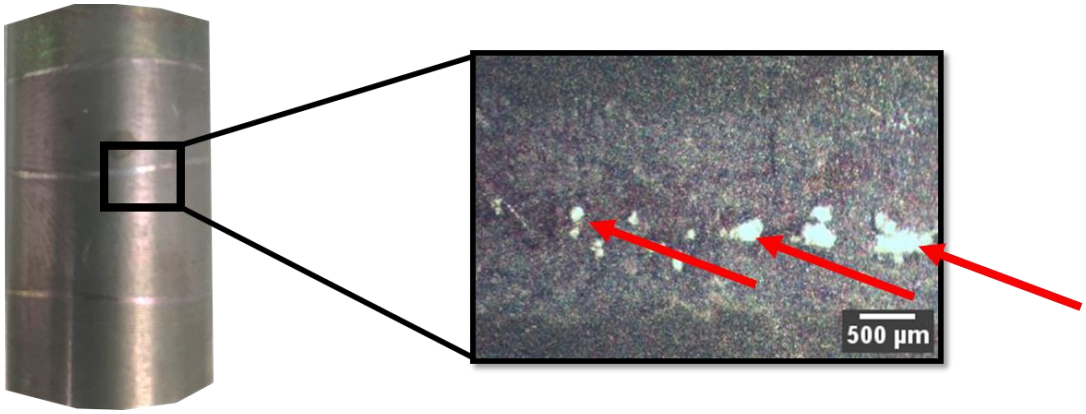

Figure 69 : Anodised TiO_2 dip coated Ti-6Al-4V rod. Red arrows indicate attached powder particles.

5.2.3 *Fused Ag-TiO_2 Surface morphology and EDS analysis*

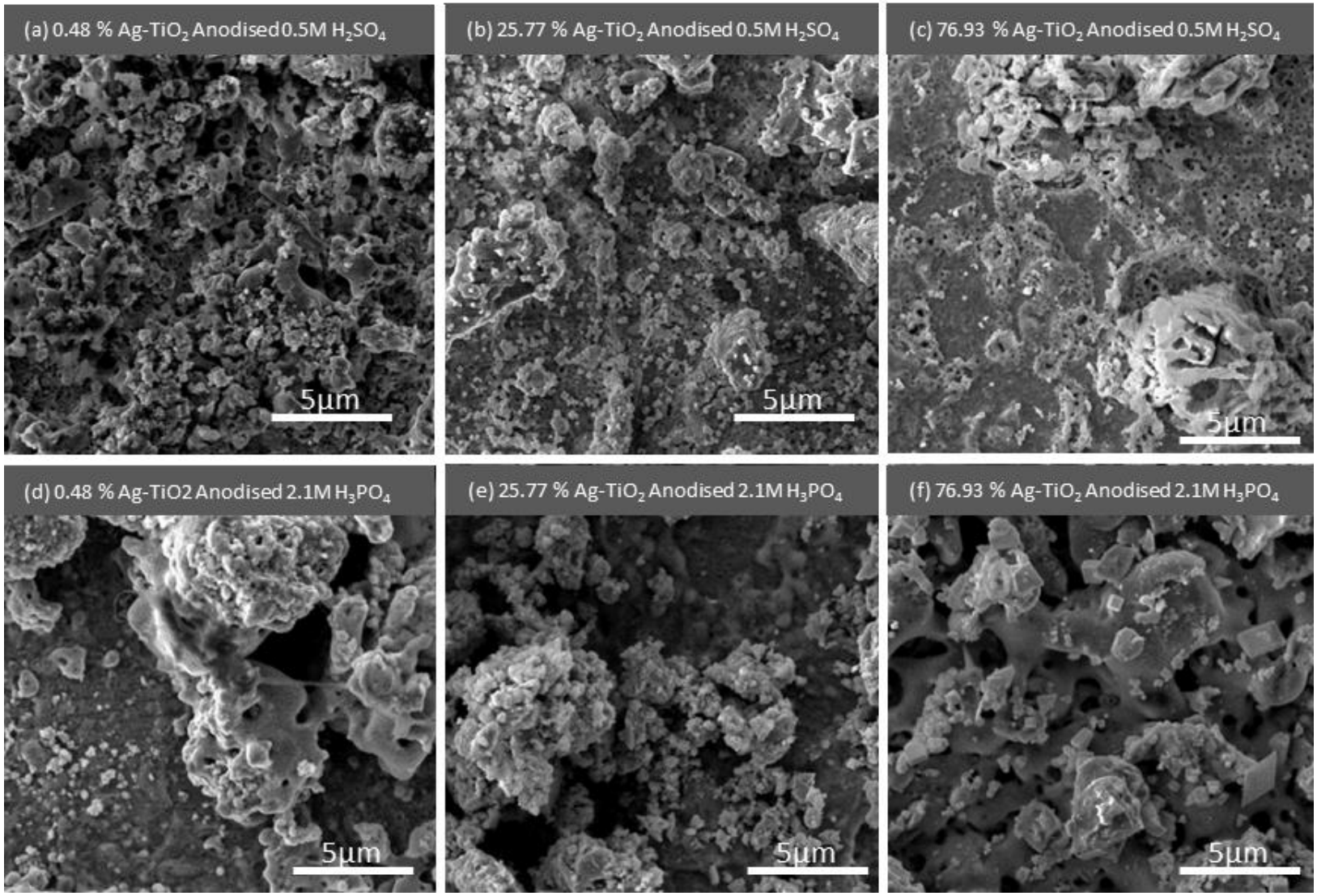

Figure 70 : Secondary electron SEM of 0.05M, 0.5M and 5.0M Ag-TiO_2 fixated via anodising in (a) 0.5M H_2SO_4, (b) 0.5M H_2SO_4, (c) 0.5M H_2SO_4, (d) 2.1M H_3PO_4, (e) 2.1M H_3PO_4 and (f) 2.1M H_3PO_4 electrolyte.

In this section, the three Ag-TiO_2 powders synthesised using 0.05M, 0.5M and 5.0M $AgNO_3$ will from here on, be referred to as 0.48% Ag-TiO_2, 25.77% Ag-TiO_2 and 76.93% Ag-TiO_2 respectively. The SEM images of the surfaces obtained after the attachment of the 0.48, 25.77 and 76.93 wt% Ag-TiO_2 powders via anodising at 100V when using either the 0.5M H_2SO_4 or the 2.1M H_3PO_4 electrolyte are shown in Figure 70. It was observed that in all sample conditions, as shown in Figure 70, the surfaces had become more irregular, owing to the presence of the powders after attachment via the anodising process. AFM data obtained via this method were not useful, as the AFM had difficulty measuring within the many crevasses present on the sample surfaces, as shown in Figure 70 above.

Figure 71 - Figure 76 below show further SEM imaging of the Ag-TiO_2 fused titanium alloy surfaces, which had been overlaid with EDS point ID results (shown as "+" symbols in the SEM images). It can be seen that, in all the sample conditions presented in Figure 71 - Figure 76, Ag was present in areas where the Ag-TiO_2 particles were visibly present. The red circles in Figure 71 - Figure 76 identify areas where visible attachment between Ag-TiO_2 particles and the underlying anodic oxide film had occurred. Figure 72 shows an interesting area where particle pull-out may have occurred, which is shown by the visible holes within the base oxide. Interestingly, within these holes there are visible Ag-TiO_2 particles (confirmed by EDS). This indicated that smaller particles may have been encapsulated by the oxide film grown during anodising, while larger Ag-TiO_2 particles were attached near their base, as indicated by the red circles in Figure 71, Figure 73, Figure 75 and Figure 76.

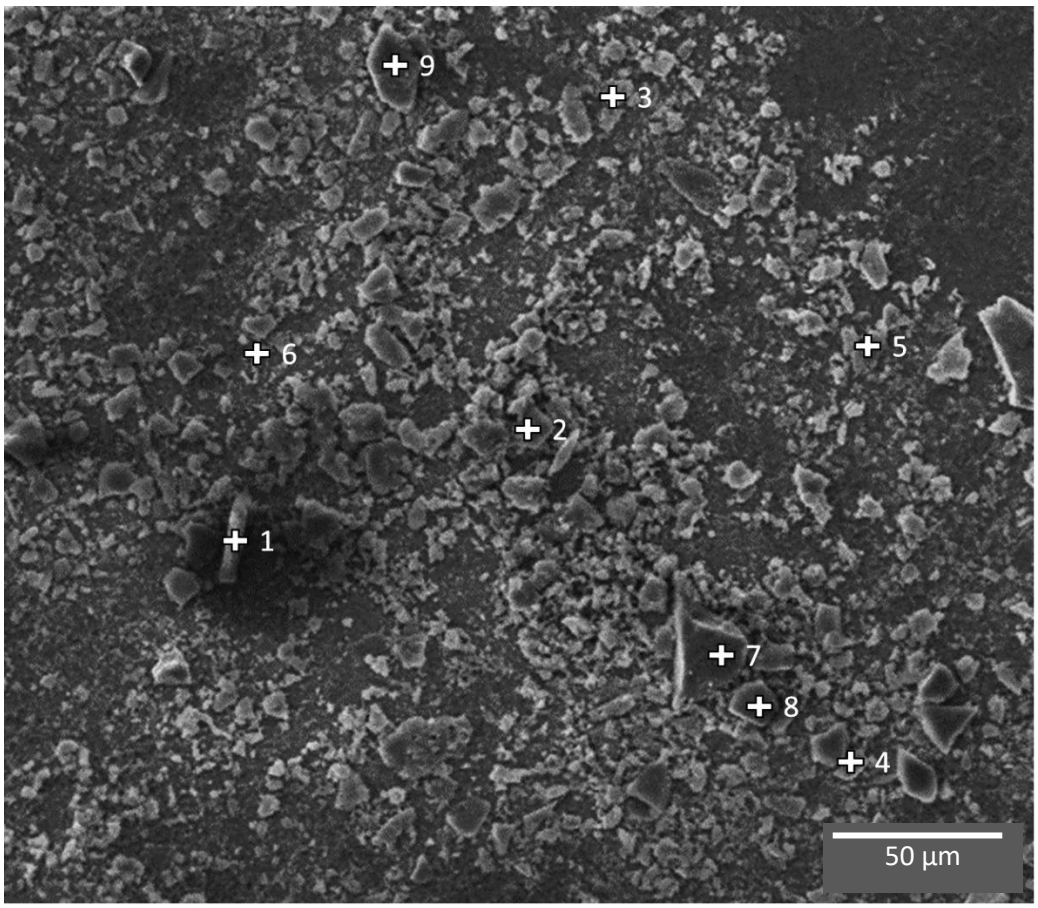

Point	Ag (wt%)
1	-
2	1.21
3	0.79
4	2.82
5	0.86
6	0.31
7	2.92
8	1.41
9	3.12

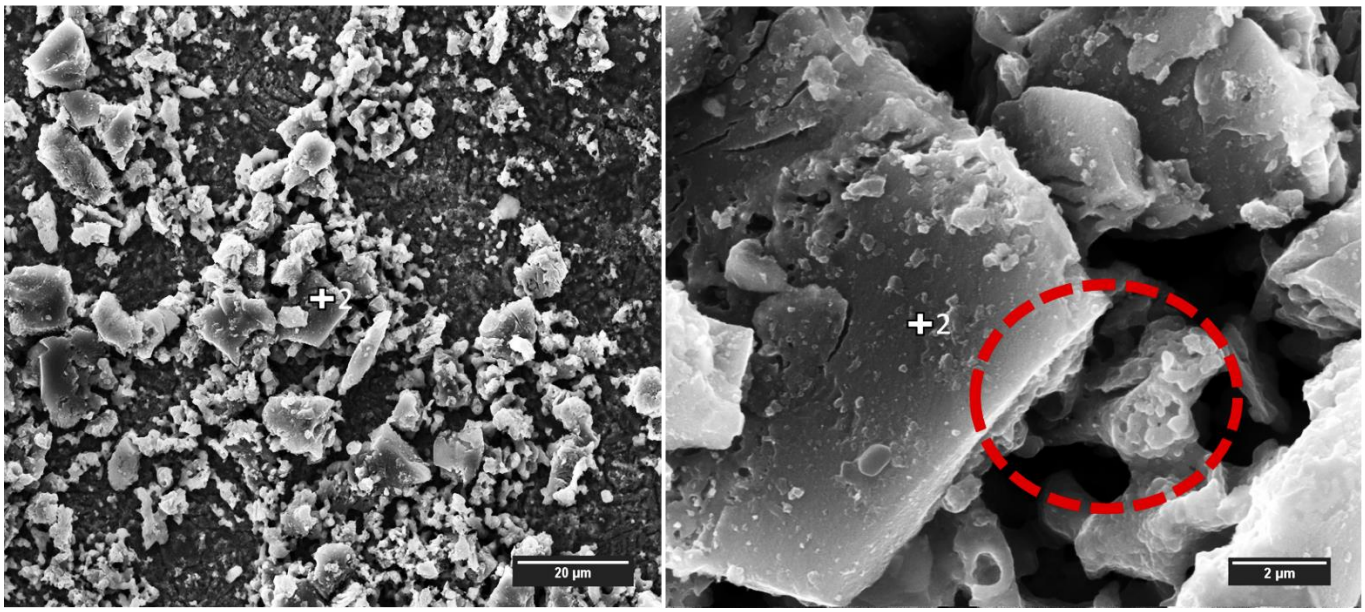

Figure 71 : Secondary electron SEM/EDS of 0.45 wt% Ag doped TiO_2 bound via anodising, while using a 0.5M H_2SO_4 electrolyte. The red circle indicates visible attachment of particles.

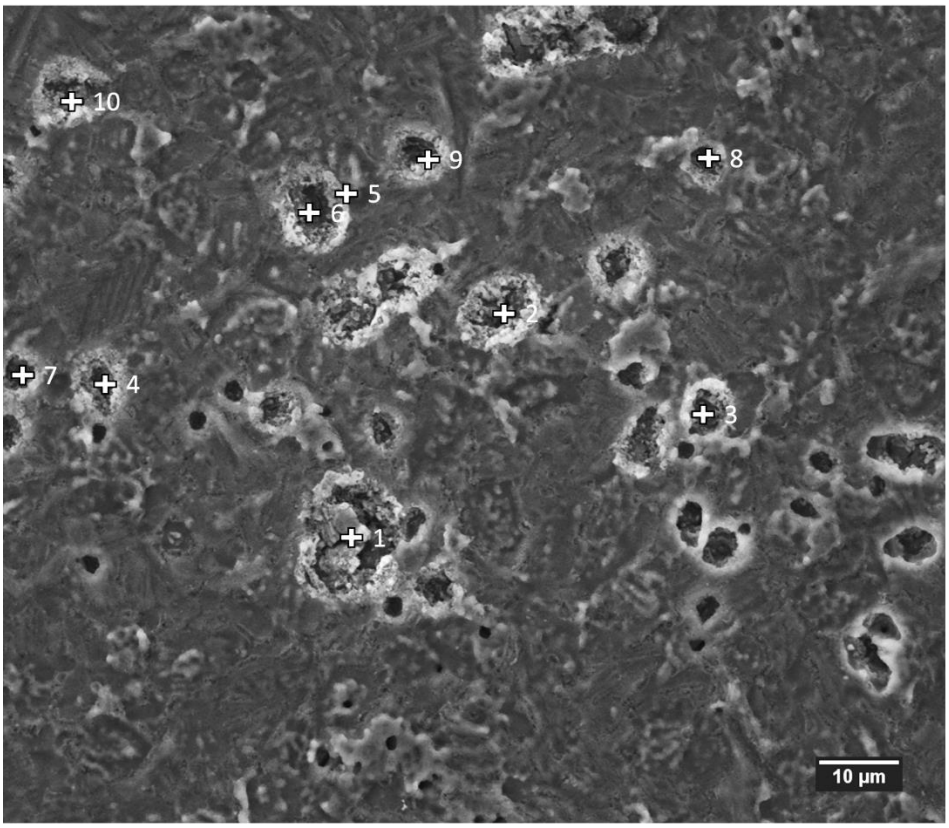

Point	Ag (wt%)
1	2.52
2	2.21
3	2.62
4	3.18
5	-
6	3.54
7	1.95
8	1.06
9	1.29
10	1.43

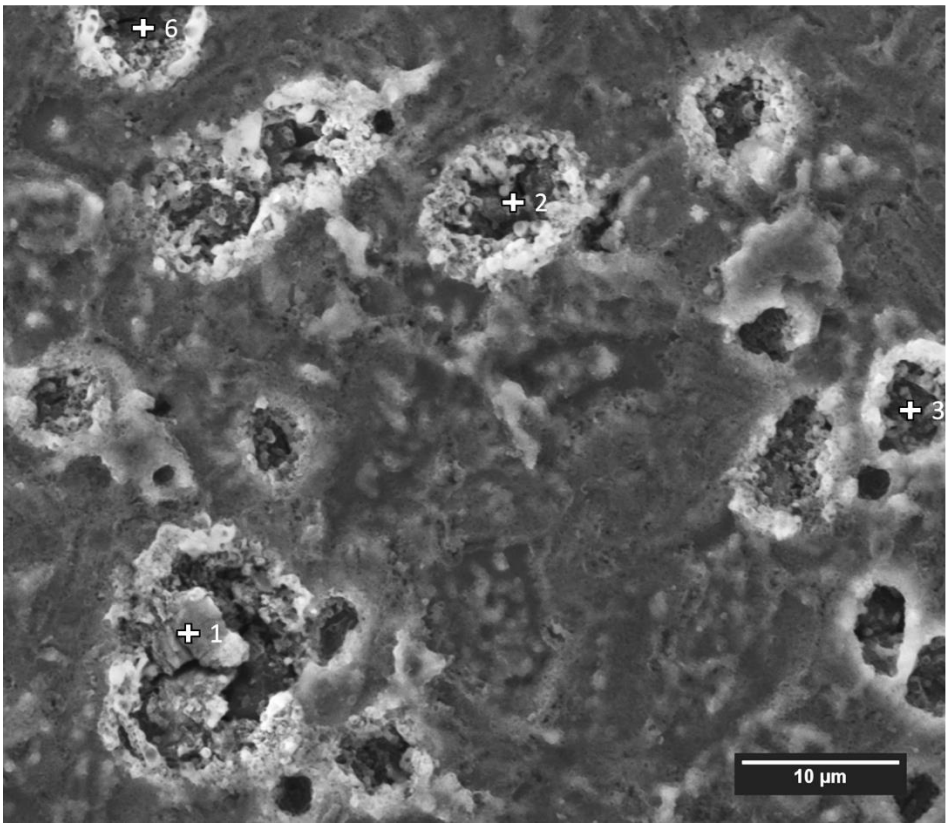

Figure 72 : Secondary electron SEM/EDS of 76.93 wt% Ag doped TiO_2 bound via anodising, whilst using a 0.5M H_2SO_4 electrolyte.

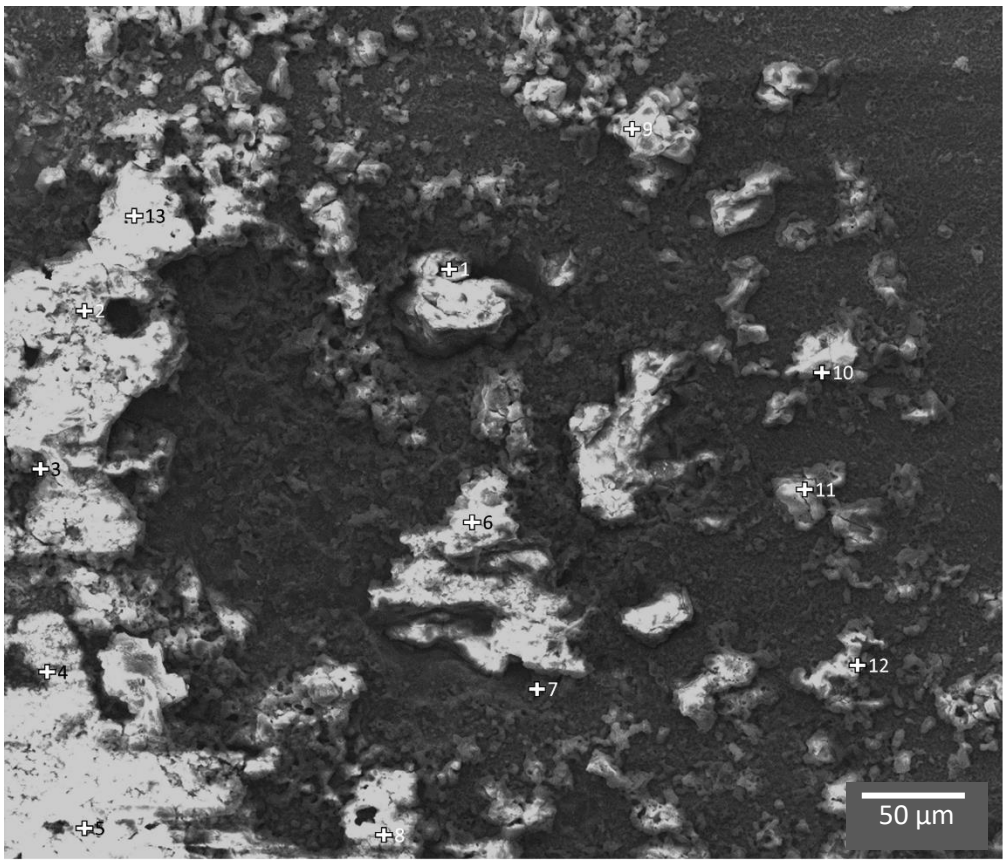

Point	Ag (wt%)
1	-
2	4.33
3	3.94
4	1.47
5	5.83
6	0.93
7	-
8	2.6
9	3.88
10	6.48
11	1.64
12	5.13
13	1.75

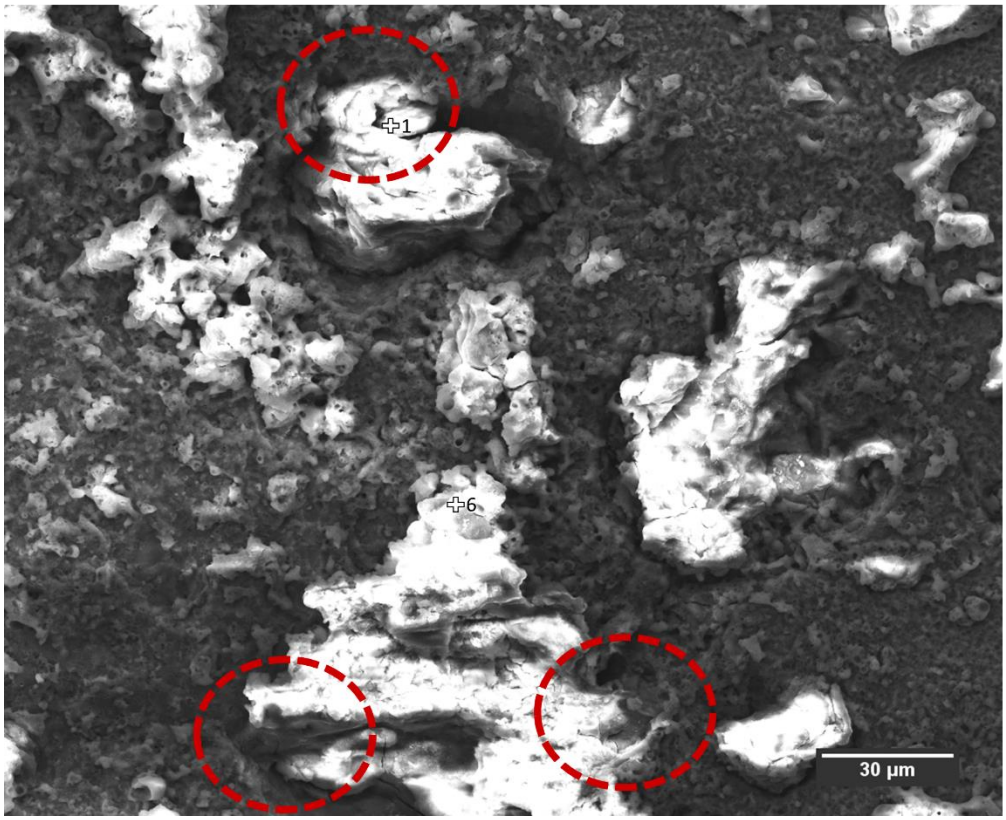

Figure 73 : Secondary electron SEM/EDS of 25.77 wt% Ag doped TiO_2 bound via anodising, while using a 2.1M H_3PO_4 electrolyte. Red circles indicate visible attachment of particles.

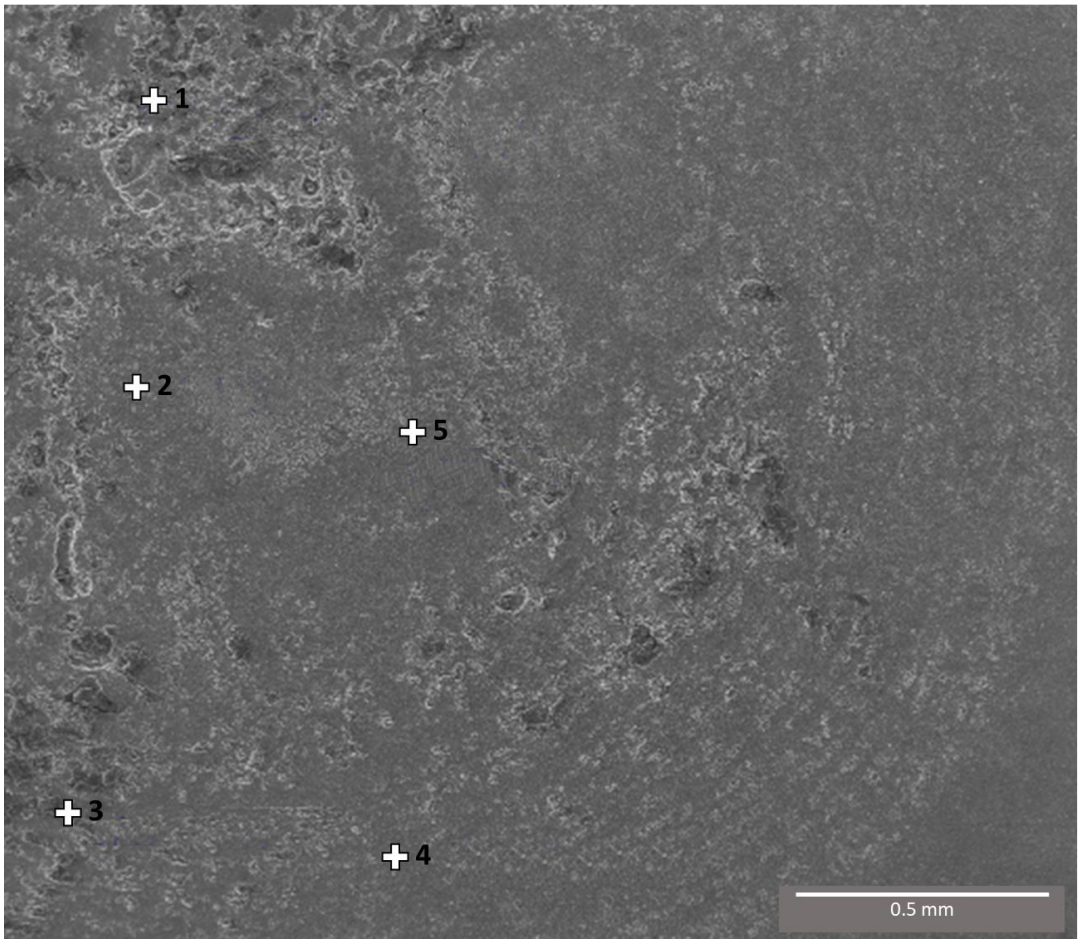

Point	Ag (wt%)
1	0.47
2	0.72
3	0.24
4	0.51
5	0.55

Figure 74 : Secondary electron SEM/EDS of 25.77 wt% Ag doped TiO_2 bound via anodising, while using a 2.1M H_3PO_4 electrolyte.

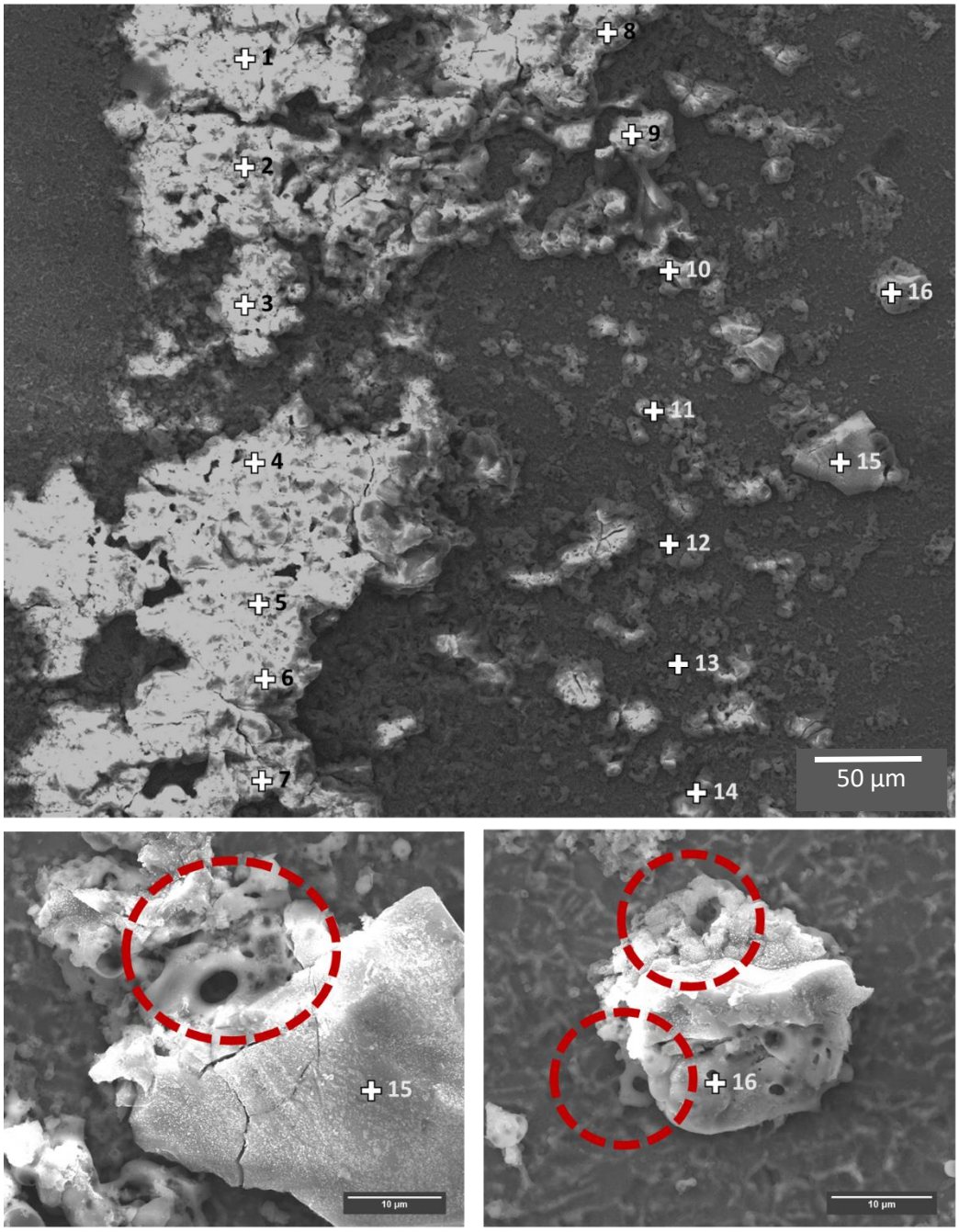

Point	Ag (wt%)
1	1.72
2	1.42
3	-
4	3.26
5	1.58
6	2.29
7	1.15
8	1.45
9	3.28
10	1.43
11	2.89
12	-
13	0.63
14	-
15	3.56
16	2.93

Figure 75 : Secondary electron SEM/EDS of 76.93 wt% Ag doped TiO_2 bound via anodising, while using a 2.1M H_3PO_4 electrolyte. Red circles indicate visible attachment of particles.

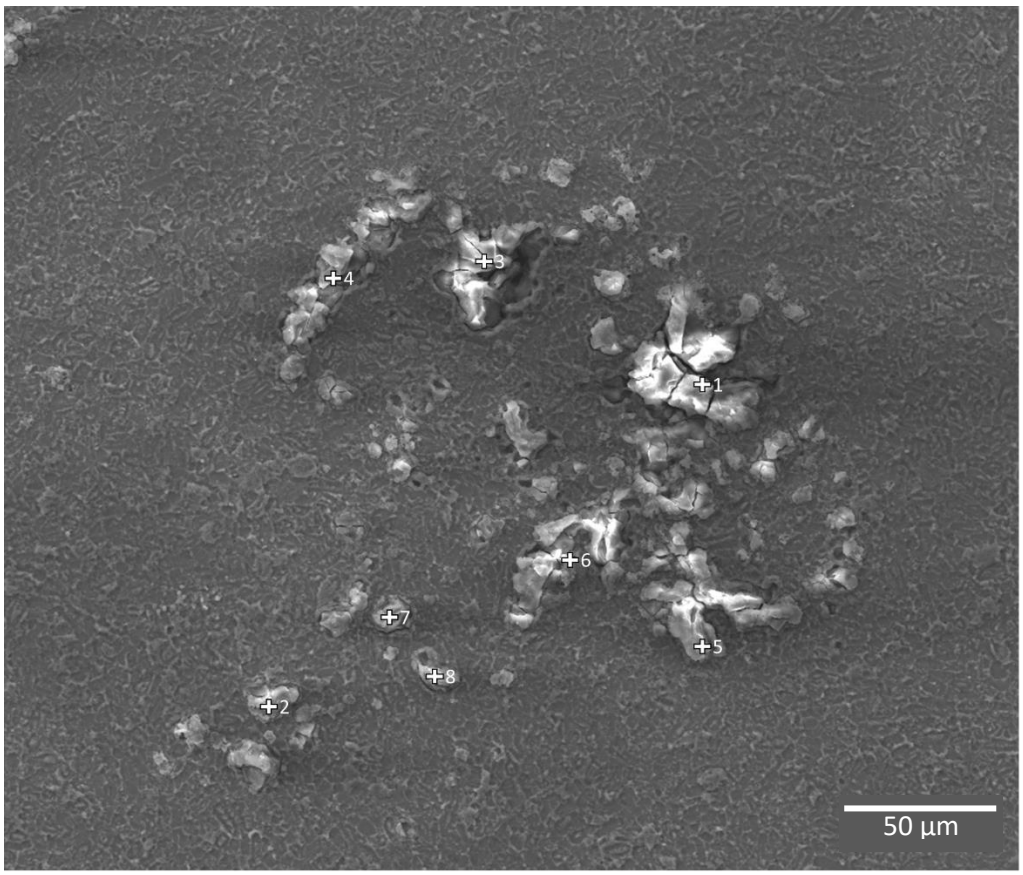

Point	Ag (wt%)
1	0.41
2	0.59
3	0.97
4	-
5	0.79
6	-
7	-
8	-

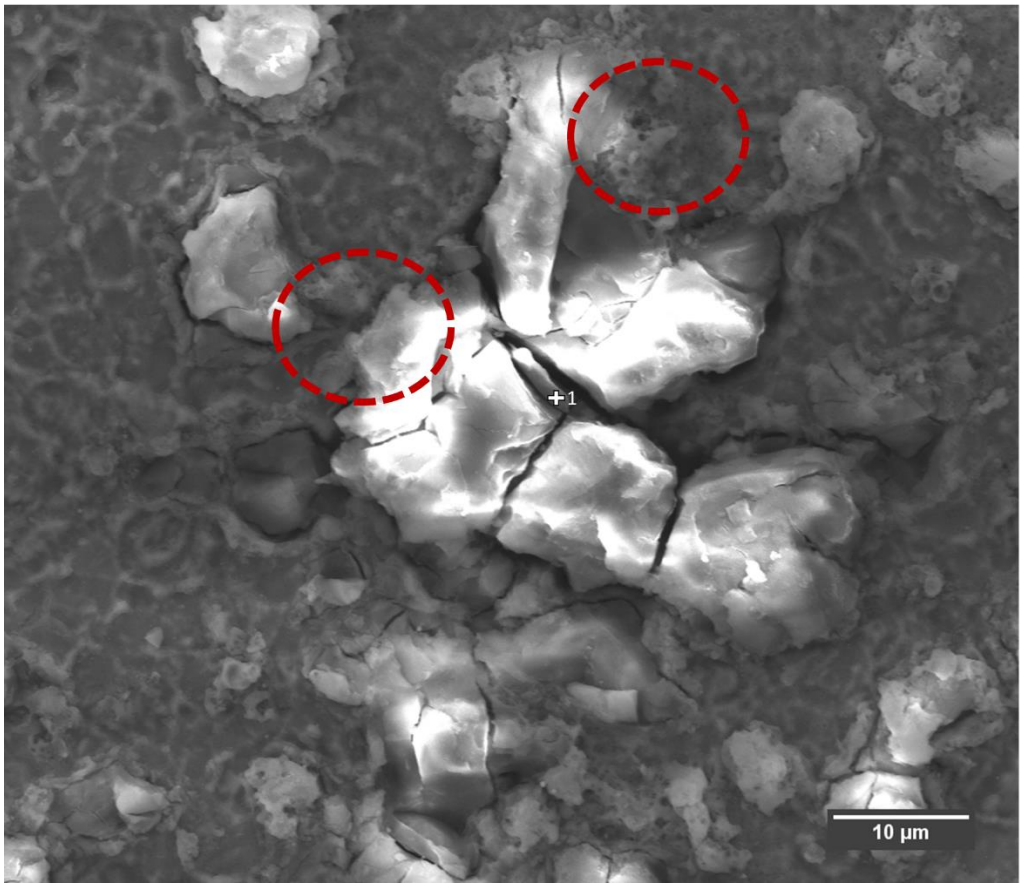

Figure 76 : Secondary electron SEM/EDS of 76.93 wt% Ag doped TiO_2 bound via anodising, while using a 2.1M H_3PO_4 electrolyte. Red circles indicate visible attachment of particles.

5.2.4 *Surface RBS Analysis of Fused Ag-TiO_2 Surfaces*

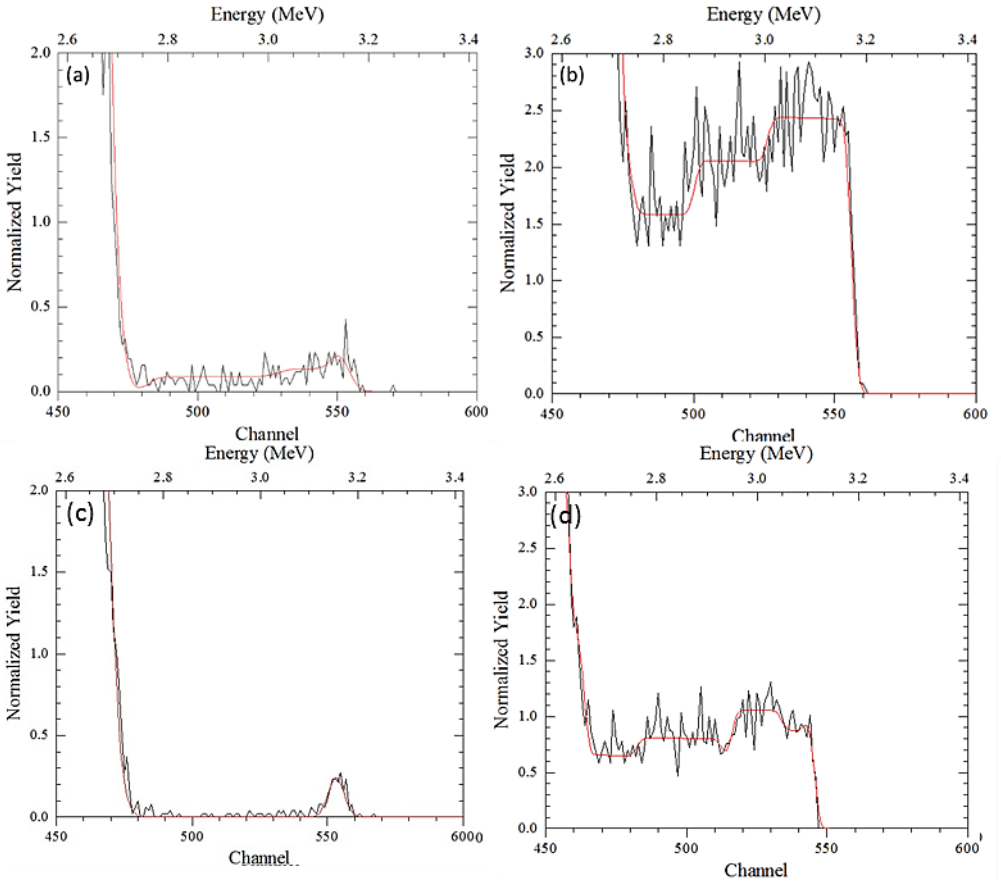

Figure 77 : Rutherford Backscatter results of Ag-TiO_2 powder bound via anodising in (a) 0.5M H_2SO_4 0.48% Ag, (b) 0.5M H_2SO_4 76.93% Ag, (c) 2.1M H_3PO_4 0.48% Ag and (d) 2.1M H_3PO_4 76.93% Ag.

Figure 77 shows the results obtained from RBS analysis of samples that had been coated in Ag-TiO_2 powder and attached via anodising in two different electrolytes, namely, 0.5M H_2SO_4 {(a) and (b)} and 2.1M H_3PO_4 {(c) and (d)}. When Figure 77 (a) and (b) are compared, the expected trend is observed: Increasing the Ag wt% (from 0.48 wt% to 76.93 wt%) within the Ag-TiO_2 powder, on a surface produced using H_2SO_4, results in a large increase of the at% Ag (from *ca.* 0.7 at% to *ca.* 4 at%). The same trend, but with a difference in the at% Ag, is observable in Figure 77 (c) and (d): Increasing the Ag wt% (from 0.48 wt% to 76.93 wt%) within the Ag-TiO_2 powder, on a surface produced using H_3PO_4, results in a smaller increase of the at% Ag (from *ca.* 0.6 at% to *ca.* 1.3 at%). This smaller increase associated with the H_3PO_4 surface was unexpected in that it had been anticipated that the at% Ag would be the same in both surfaces for the 76.93 wt% samples. The discrepancy in the at% Ag values could be attributed to the unavoidably uneven coating of the titanium with Ag-TiO_2 during the preparation of the samples. This led to varied at% Ag results from the RBS analysis conducted at different points on the surface.

5.2.5 *Surface X-ray diffraction*

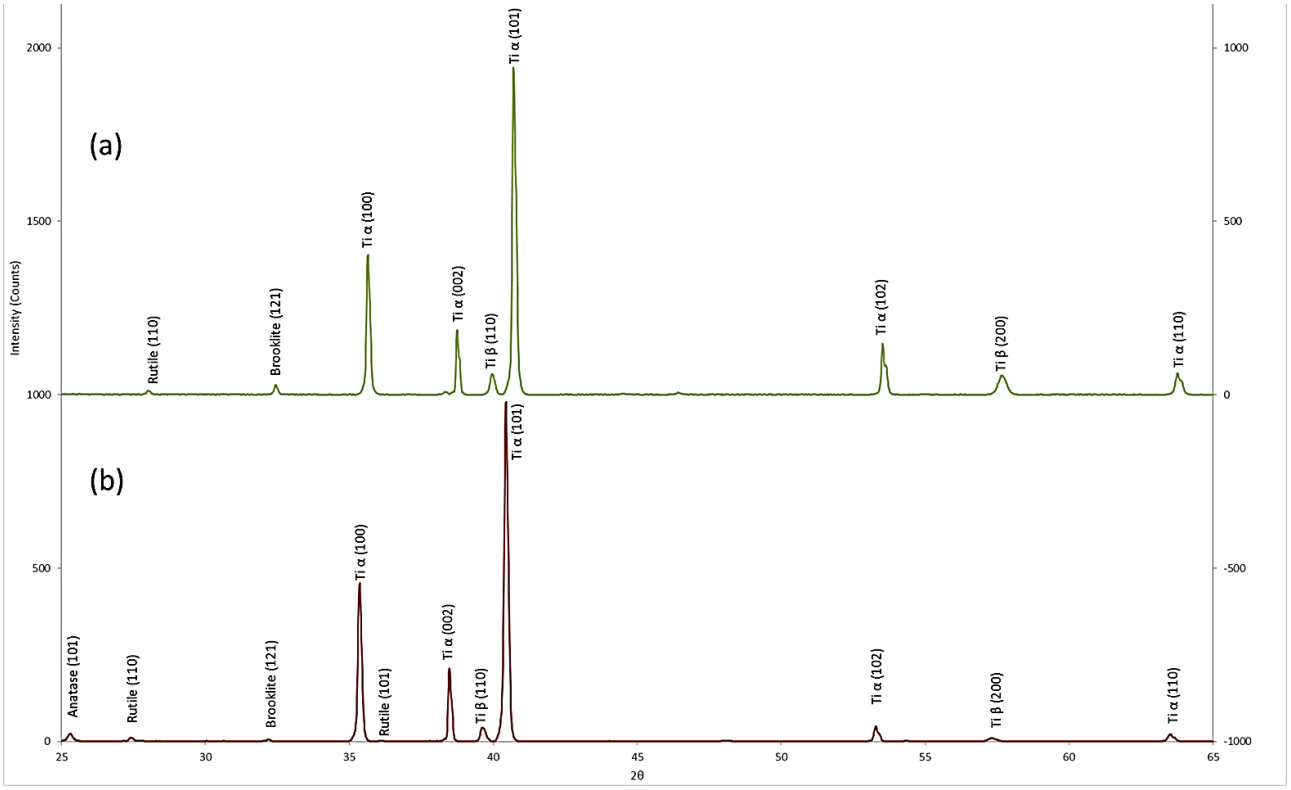

Figure 78 : XRD spectra of surfaces coated in Ag-TiO_2 attached via anodising in (a) 2.1M H_3PO_4 and (b) 0.5M H_2SO_4 at 100V.

Figure 78 shows the XRD results obtained from surfaces to which Ag-TiO_2 powder was attached using anodising. For the sample anodised in the 2.1M H_3PO_4 electrolyte {See Figure 78 (a)}, it was found that the crystal structure phase was predominantly brookite (121), with smaller amounts of rutile (110) also detected. With Sample (b), anodised in the 0.5M H_2SO_4 electrolyte, it was found that the predominant crystal structure was anatase (101), with smaller amounts of rutile (110) and brookite (121) also detected. The presence of rutile in (a) and anatase in (b) indicates that the anodic oxide film growth occurred in a process similar to that of the the anodised samples in Section 5.1: the same crystal structure phases were present (rutile and anatase), correlating with their respective anodising electrolytes.

In both XRD spectra, the samples showed the presence of brookite (121). Since brookite was not a crystal generated via the anodic oxidation of Ti-6Al-4V in either of the two electrolytes utilised in this research, it must be concluded that the brookite (121) peaks were associated with the incorporated TiO_2 powders. A review by A. Di Paola *et al.* [65] reported that brookite was observable in sol-gel powders synthesised in acid conditions at low temperatures. Since, in this research, the sol-gel was synthesised at a pH of 1 at RT, there was a high likelihood that the brookite (121) peaks present in the XRD data above were due to the formation of a brookite crystal structure phase during the synthesis of the Ag-TiO_2 powders.

5.2.6 *Sub-Surface Morphology*

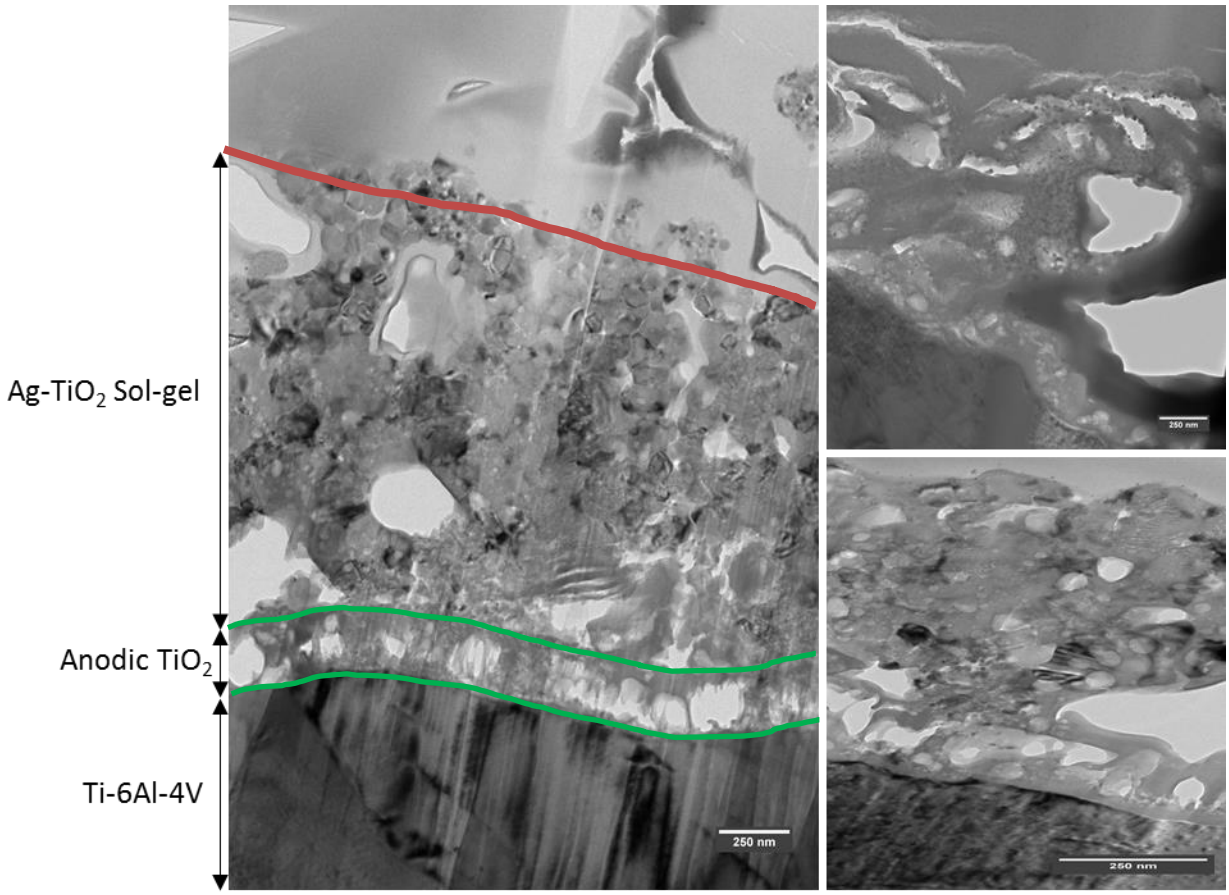

Figure 79 : Bright-field TEM of the Sub-Surface Morphology of Ag-TiO_2 sol gel particles fused to surface using anodic oxidation.

Figure 79 above is a representation of the sub-surface morphology obtained during the study of the FIB-TEM cross-sections of the Ag-TiO_2 coated titanium samples in Figure 80 to Figure 89, which will be discussed later in this section.

In Section 5.1.6. an oxide layer *ca.* 200 - 250nm thick was observed to form after the anodising process. A distinct oxide layer that had a layer thickness in the same range is shown in Figure 79 above (between the green lines). Thus, it could be concluded that this anodic TiO_2 layer was also formed owing to the anodising process. As will be observed later in this section, the anodic oxide layer was AgNPs deficient, thus further confirmation that the formation of this anodic oxide layer was due to anodic oxidation of the base titanium alloy and not as a consequence of the Ag-TiO_2 particles on the surface.

The second Ag-TiO_2 sol-gel layer (between the green and red lines) was attached to the top of the anodic oxide. The formation of this distinct layer appears to have been due to the presence of the Ag-TiO_2 particles on the surface during the attachment process, which had acted to catalyse the formation of this very thick oxide layer. The Ag-TiO_2 sol-gel layer had large variations in layer thickness across the surface. This was due to the fact that the thickness of the formed layer depended on the amount of particle deposition in the observed field of view, as well as on the size of the particles present prior to the anodisation step.

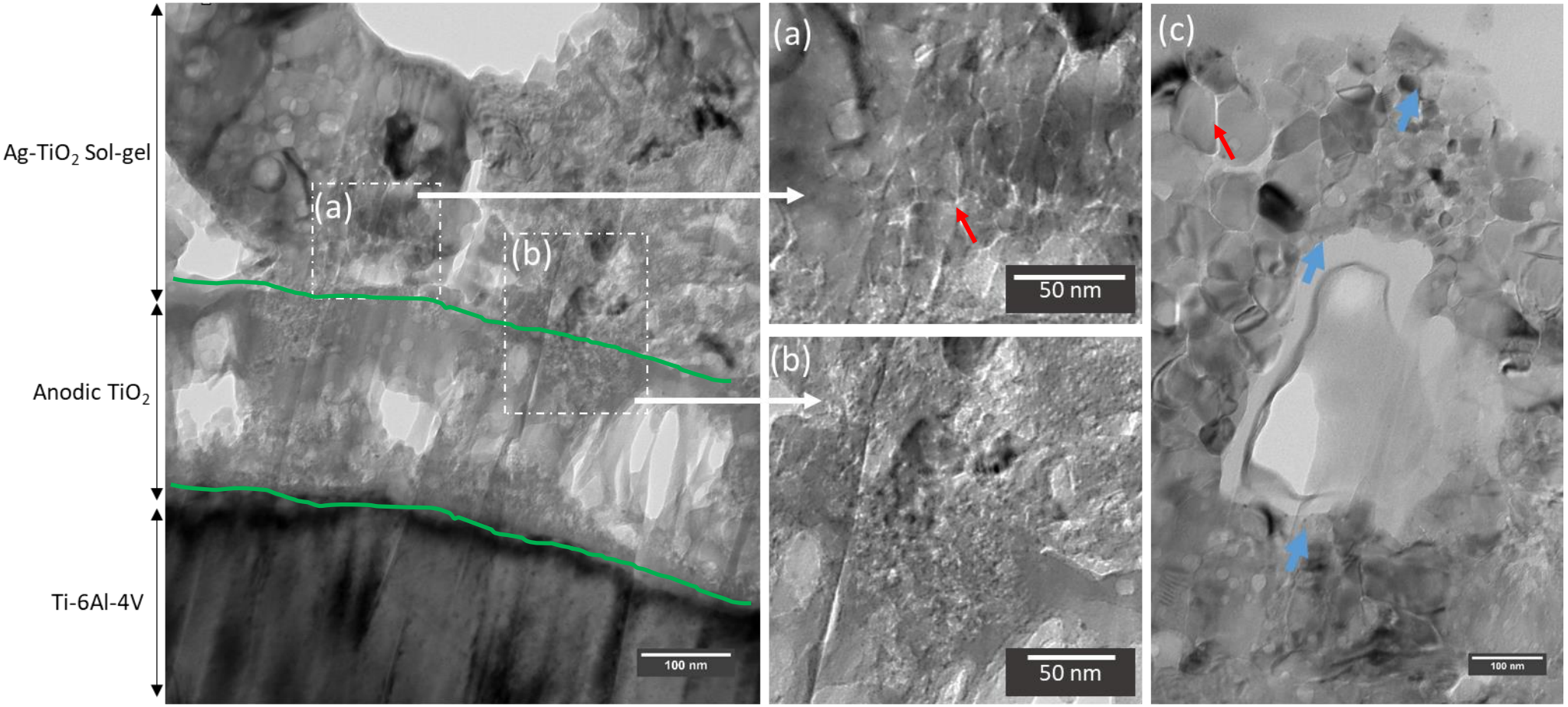

Figure 80 : Cross-sectional Bright-Field TEM of a sample coated in the 0.45wt% Ag-TiO_2 powder, fused via anodising in 0.5 M H_2SO_4 at 100V showing in (a) and (b) areas of bonding between the anodic oxide and Ag-TiO_2 and in (c) nm-sized TiO_2 particles. Blue arrows indicate AgNPs. Smaller boundaries (red arrows)

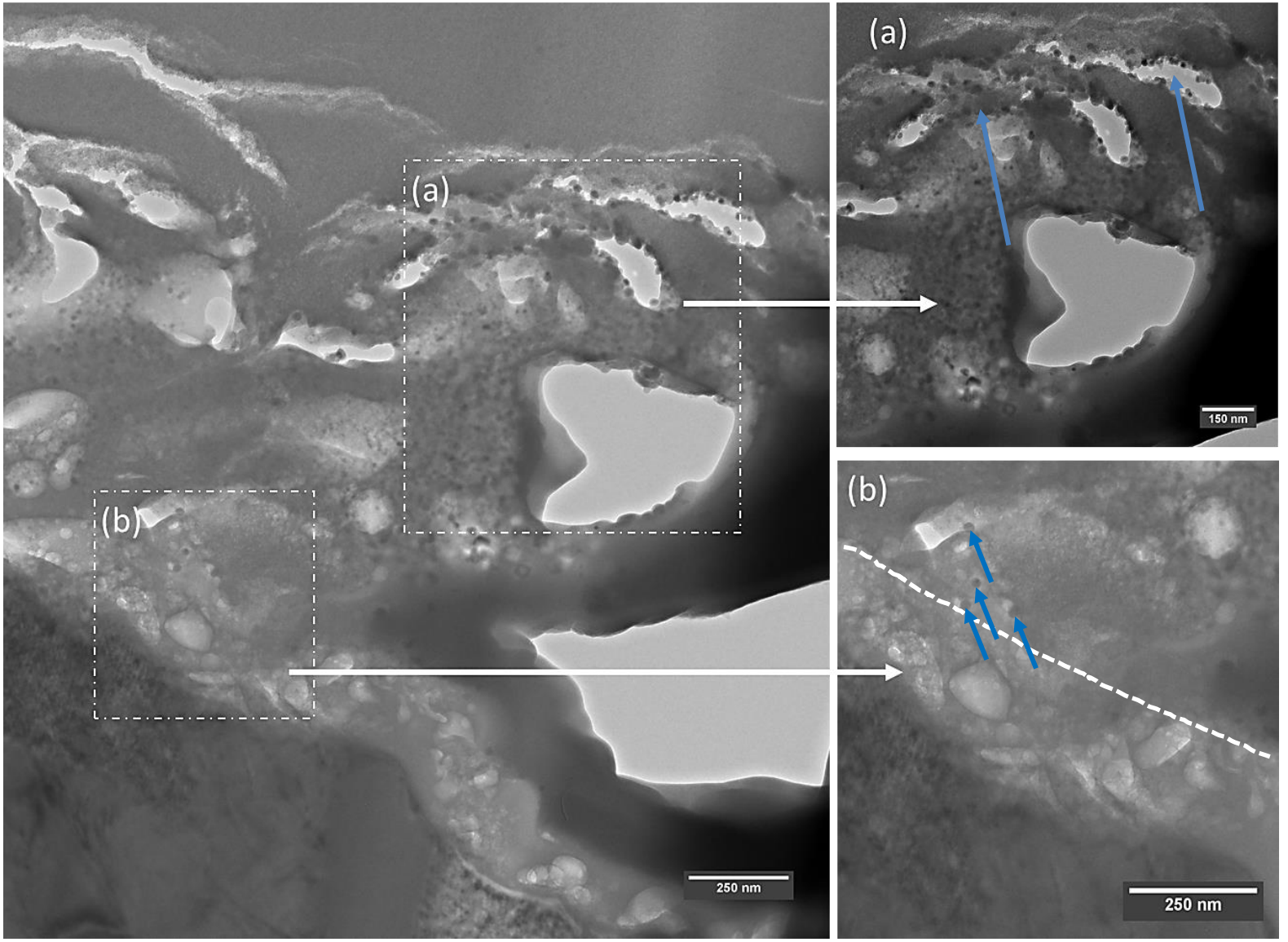

Figure 81 : Cross-sectional Bright-Field TEM of a sample coated in the 0.45wt% Ag-TiO_2 powder, fused via anodising in 2.1 M H_3PO_4 at 100V, showing in (a) AgNPs and in (b) area of bonding between the anodic oxide and Ag-TiO_2 (white dotted line). Blue arrows indicating AgNPs.

Figure 80 shows the cross-section of a Ti-6Al-4V surface that had been coated with 0.45wt % Ag-TiO_2 particles. Fusion of the Ag-TiO_2 particles was carried out via anodisation in the 0.5M H_2SO_4 electrolyte at 100V. The resultant cross-sectional microstructure was similar to the representative structure shown in Figure 79. Upon inspection of Figure 80(a) and (b), it was observed that these showed the areas of bonding between the base anodic oxide layer and the Ag-TiO_2 sol-gel layer. Upon closer inspection of (a) it was noticed that there were smaller boundaries within the oxide layer (red arrows). The same boundaries were visible in (c). These boundaries were most likely due to the close packing of smaller Ag-TiO_2 sol-gel particles that had become encapsulated within the larger oxide layer during the anodising process. This encapsulation of the Ag-TiO_2 particles was also mentioned and observed during the SEM imaging in Figure 72 (Section 5.2.3). This encapsulation of these smaller particles indicated that the presence of the Ag-TiO_2 particles at the surface, when anodising was commenced, could be acting as a catalyst for the rapid growth of a thick oxide film around the smaller particles. In Figure 80(c), the blue arrows indicate the location of NPs within and on the surface of these smaller TiO_2 particles. The EDS analysis in Figure 90(h) confirmed that these were AgNPs. It was noticed that there was a lack of AgNPs within the base anodic oxide, which indicated that the growth of the base anodic oxide layer had not been not catalysed by the presence of TiO_2 particles, *i.e.* the anodic oxide layer was generated by the traditional mechanism of anodic oxidation of the base Ti-6Al-4V metal. A representative EDS analysis in Figure 90(c), Areas 8 and 10, confirmed that there was no Ag detected in the anodic oxide region.

Figure 81 shows the cross-section of the Ti-6Al-4V surface that had been coated with 0.45wt % Ag-TiO_2 particles. The 2.1M H_3PO_4 electrolyte was used instead of the 0.5M H_2SO_4 electrolyte during the anodic oxidation process. It was noticed that, once again, a base anodic oxide layer formed that contained no AgNPs within its bulk. Figure 80, Area (b) shows AgNPs (blue arrows) near the interface between the anodic oxide and the Ag-TiO_2 layer, owing to the presence of Ag-TiO_2 particles near the interface. The EDS analysis of an area near (b) confirmed the presence of silver in the Ag-TiO_2 layer {See Figure 90 (i) Areas 28 to 30}. Figure 80(b) also showed an area where bonding between the anodic oxide layer and the Ag-TiO_2 layer had occurred. It was noticed that in the case of this sample there were no small TiO_2 particles encapsulated within the Ag-TiO_2 layer. However, the presence of AgNPs was observed in Area (a). The reason for the lack of small TiO_2 particles in the Ag-TiO_2 layer could have been due to two factors, either the thick Ag-TiO_2 layer in this field of view had formed owing to a micron-sized Ag-TiO_2 particle bonded to the surface of the anodic oxide or the smaller particles had been more cohesively fused.

A second field of view of Figure 82 will now be discussed. It can be seen in this field of view that, on the surface of the base titanium metal, an anodic oxide layer had formed. Attached to the anodic oxide layer was the Ag-TiO_2 layer. Of interest were the facts that this sample exhibited less porous oxide above the TiO_2 layer and the presence of a dense oxide layer containing AgNPs (See Figure 83). The EDS confirmed the presence of AgNPs in the dense oxide layer {Figure 90 (a)}. Therefore, the dense layer must also have originated from the attached TiO_2 particles, because this was the only method used to introduce silver on to the surface of the sample. Area (a) of Figure 82 shows numerous dimples on the oxide layer cross-section. This was most likely due to the presence of a high concentration of AgNPs that had become dislodged during the FIB milling process. Area (b) shows a close-up view of an attachment point between the anodic oxide layer and the Ag-TiO_2 layer. This area also shows the presence of AgNPs, which is an indication that Ag-TiO_2 particles must have been present in this region prior to anodising. Area (c) shows a very thin surface oxide layer that contained AgNPs at regular intervals.

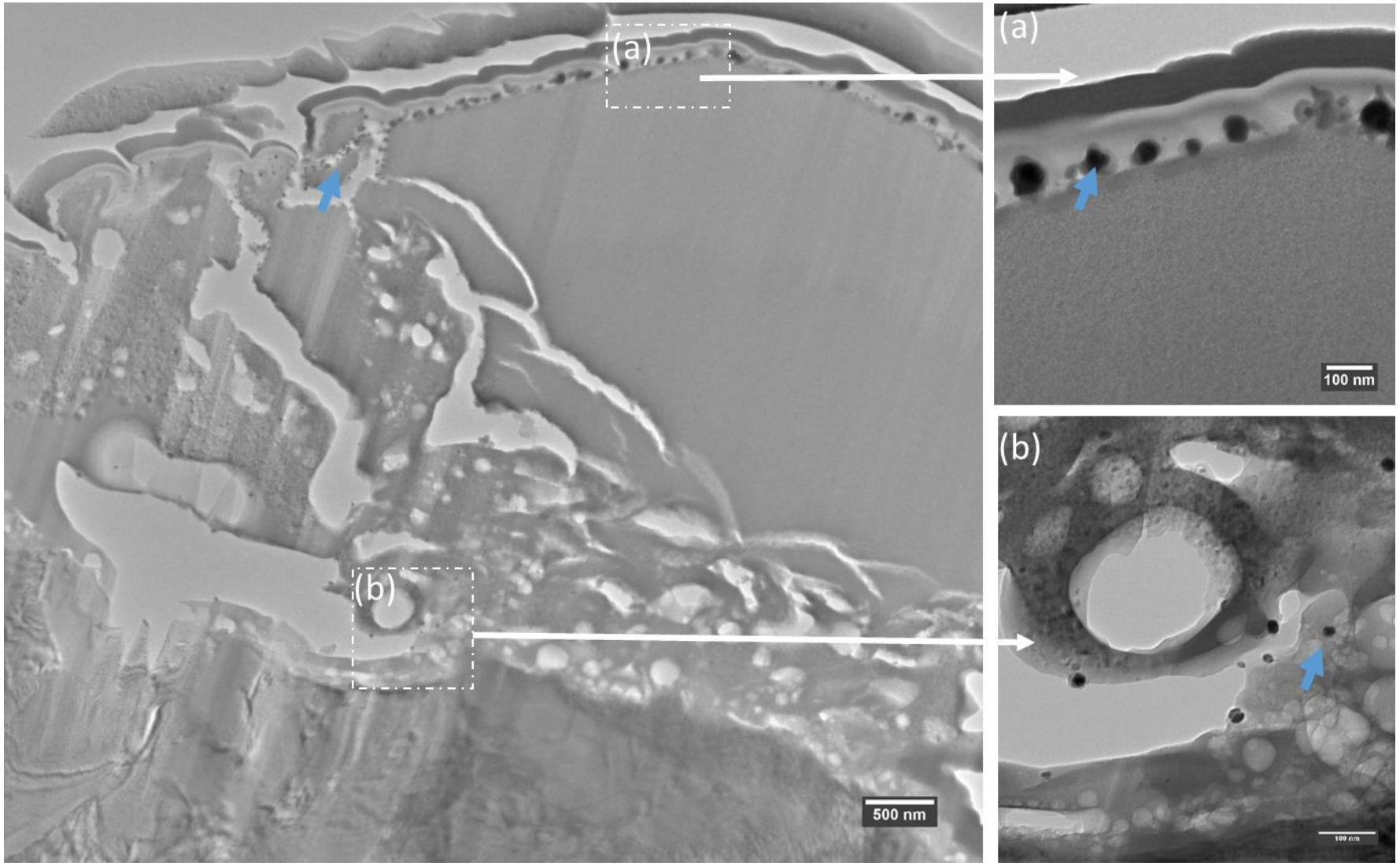

Figure 82 : Cross-sectional Bright-Field TEM of a sample coated in the 0.45wt% Ag-TiO_2 powder, fused via anodising in 2.1 M H_3PO_4 at 100V showing (a) dimpled surface, (b) area of bonding between the anodic oxide and Ag-TiO_2, and (c) thin TiO_2 that contains AgNPs. Blue arrows showing AgNPs.

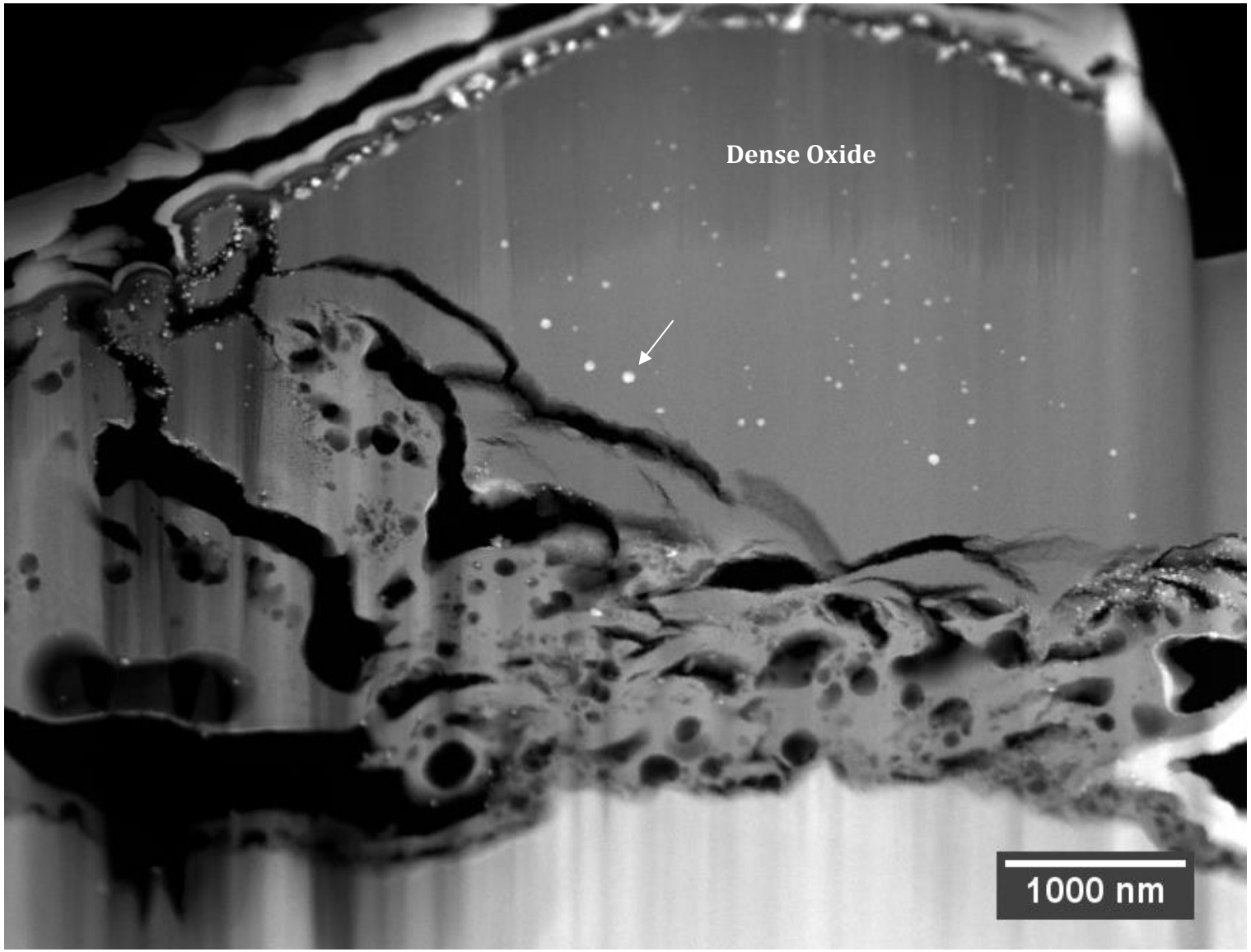

Figure 83 : Annular dark field STEM image of a sample coated in the 0.45wt% Ag-TiO_2 powder, fused via anodising in 2.1 M H_3PO_4 at 100V. Bright areas within the oxide indicate Ag concentrations. White arrow indicating AgNP.

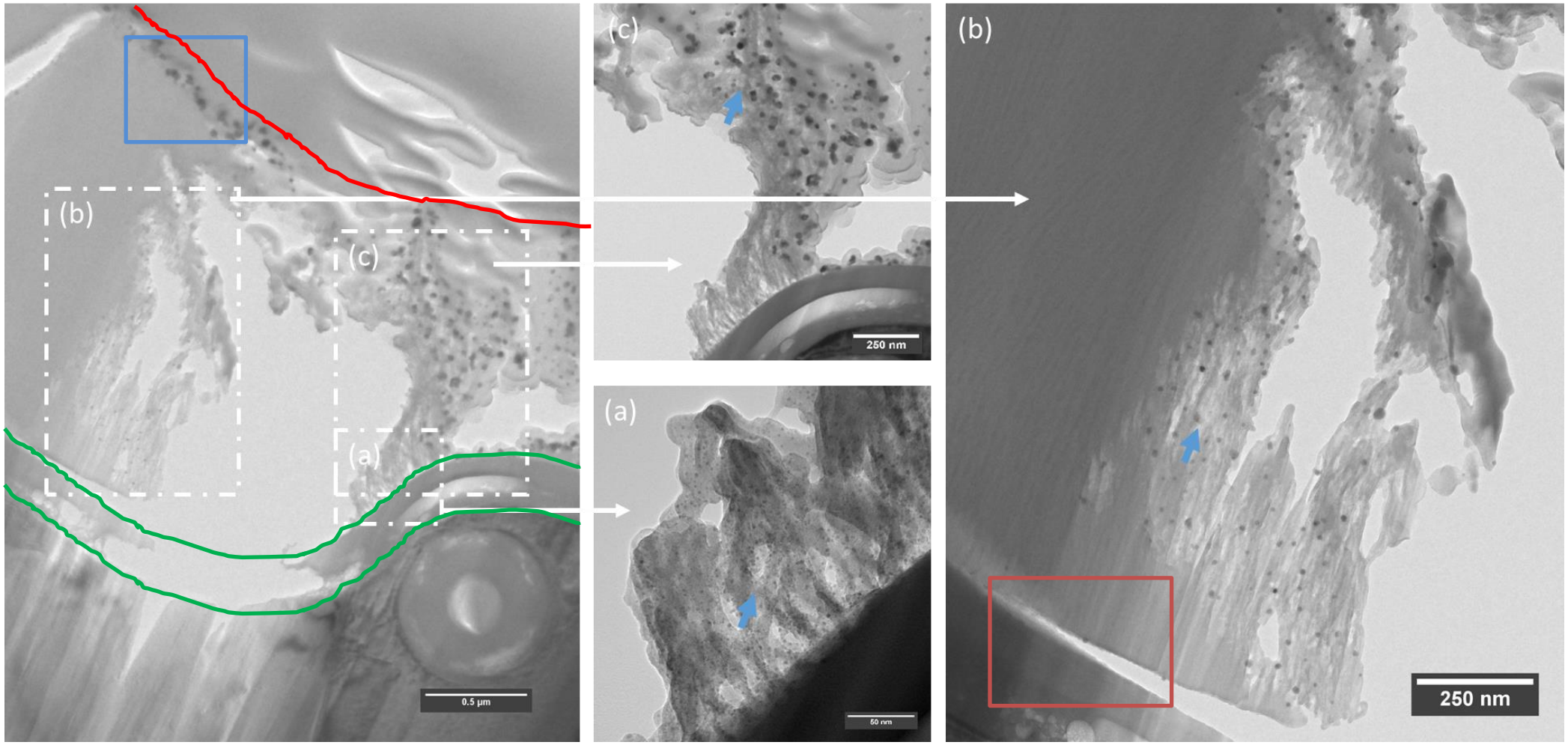

Figure 84 : Cross-sectional Bright-field TEM of a sample coated in the 25.77 wt% Ag-TiO_2 powder, fused via anodising in 2.1 M H_3PO_4 at 100V, showing (a) area of bonding between the anodic oxide and Ag-TiO_2, (b) damaged dense TiO_2 and (c) AgNPs. Blue arrows indicating AgNPs. Red box indicated delamination.

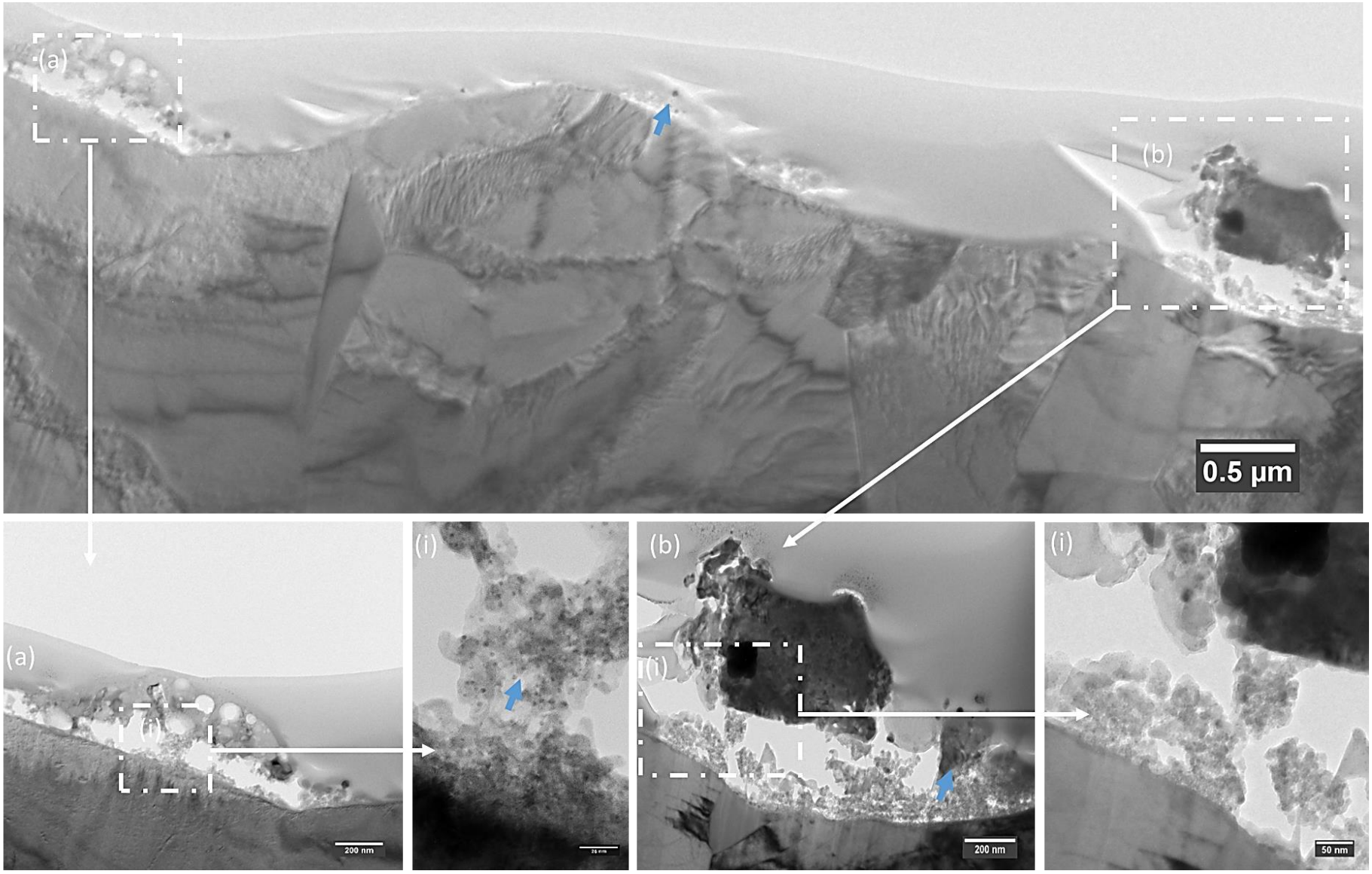

Figure 85 : Cross-sectional Bright-field TEM of a sample coated in the 25.77 wt% Ag-TiO_2 powder, fused via anodising in 0.5 M H_2SO_4 at 100V, showing in {a(i)} AgNPs and in {b(i)} area of bonding between the anodic oxide and Ag-TiO_2 particle. Blue arrows indicate AgNPs. Blue arrows indicating AgNPs.

Figure 86 : Cross-sectional Bright-Field TEM of a sample coated in the 25.77 wt% Ag-TiO2 powder, fused via anodising in 0.5 M H_2SO_4 at 100V.

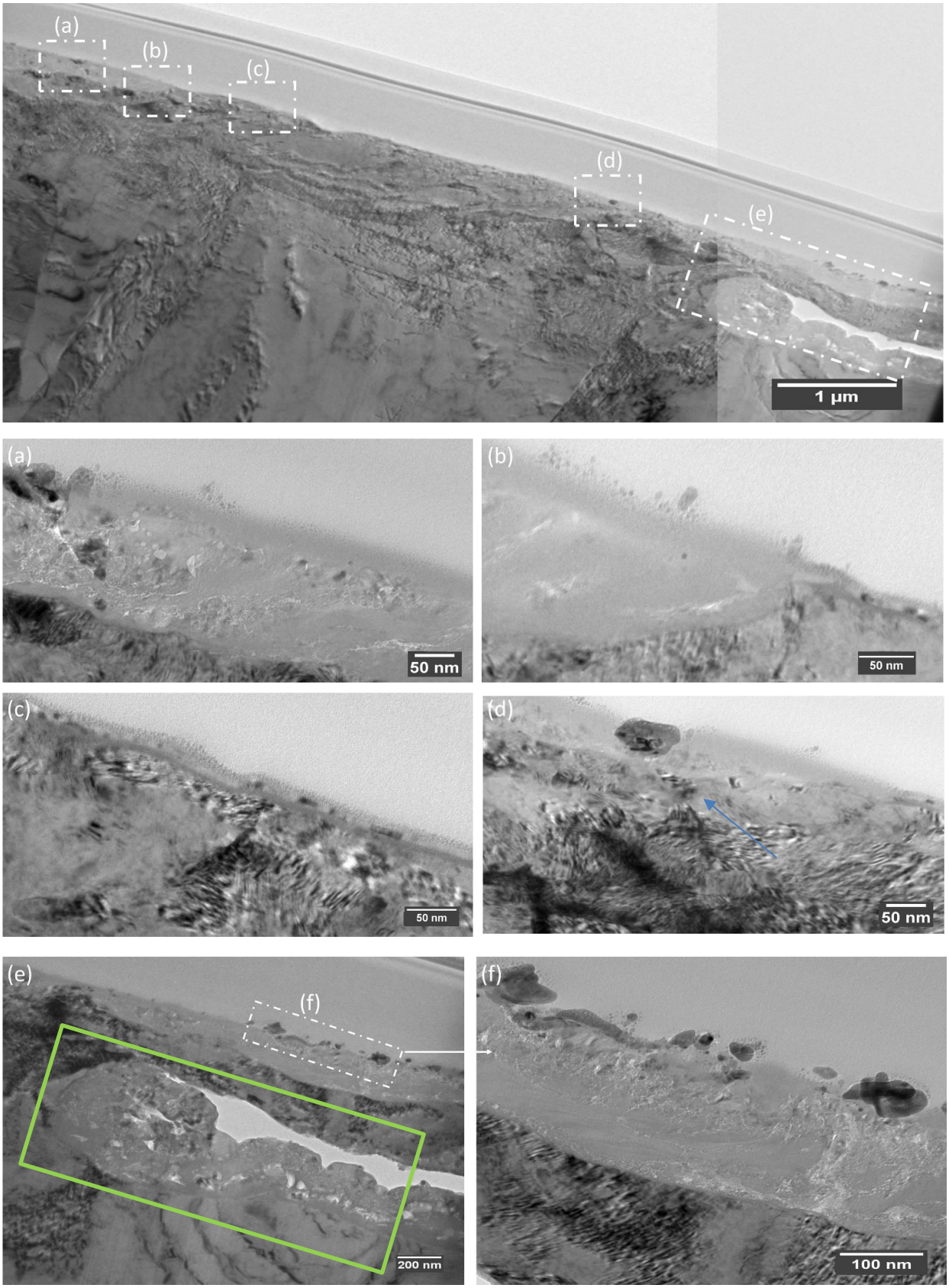

Figure 87 : Cross-sectional Bright-Field TEM of a sample coated in the 76.93 wt% Ag-TiO_2 powder, fused via anodising in 0.5 M H_2SO_4 at 100V, showing in (a) and (b) thick AgNP containing oxide, in (c) thin AgNP containing oxide, in (d) large AgNP stuck in oxide surface, in (e) crevasse filled with TiO_2 and in (f) large AgNPs stuck in oxide surface.

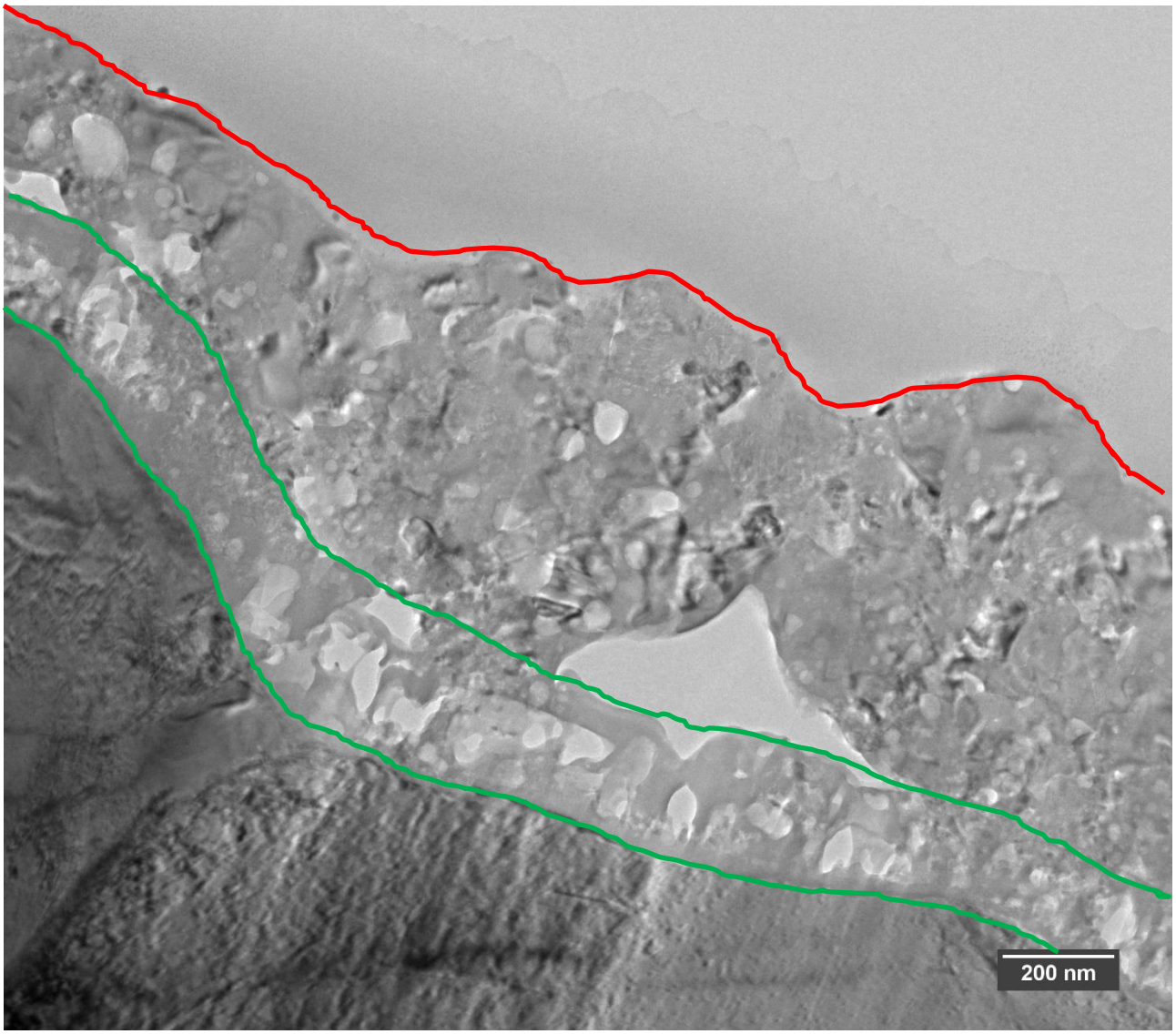

Figure 88 : Cross-sectional Bright-Field TEM of a sample coated in the 76.93 wt% Ag-TiO_2 powder, fused via anodising in 0.5 M H_2SO_4 at 100V.

Figure 84 shows the cross-section of the Ti-6Al-4V sample surface that had the 25.77wt % Ag-TiO_2 powder fused on to it, using the 2.1M H_3PO_4 anodising electolyte. It must be noted that the central region had previously been occupied by an oxide that was significantly damaged by the FIB milling process. Of significance is the fact that this damage assisted in the revealing of certain surface features and these will be discussed below. Once again, the base anodic oxide generated by the anodising process was present and this had no AgNP formation within its bulk. A study of the Ag-TiO_2 and the anodic oxide layer interface at Site (a) shows continuity between the anodic oxide and Ag-TiO_2 layers, indicating that there was significant bonding between these oxide layers. A fine AgNP dispersion within the Ag-TiO_2 layer was also observed. A study of the FIB-damaged region (b) reveals the AgNPs within the Ag-TiO_2 layer.

At the lower side of Figure 84, Site (b) at the red rectangle, the interface between the two oxides is shown. Delamination of the Ag-TiO_2 layer from the anodic oxide layer had occurred owing to the FIB damage. The delamination confirmed that these two layers were distinct from each other. Site (c) also showed numerous AgNPs within the Ag-TiO_2 layer. As in the sample shown in Figure 82, this sample also had AgNPs present along the surface (indicated by the blue square in Figure 84). The EDS analysis of the AgNP-containing surface (blue square - Figure 84) is shown in Figure 90(c), Area 6. This

confirmed the presence of silver. The EDS analysis of the dense oxide in 84(b) is shown in Figure 90(c) and Areas 7 and 11 in this figure confirm the presence of silver within the dense oxide.

Figure 85 shows a cross-section of a Ti-6Al-4V sample surface that had the 25.77wt % Ag-TiO_2 powder fused on to it, using the 0.5M H_2SO_4 electrolyte. The cross-section of this sample had a thin anodic oxide layer present at the surface. There was evidence of $AgTiO_2$ particle attachment in Areas (a) and (b). In Area {a(i)} there was a clearly visible dispersion of AgNPs within the oxide and at Site {b(i)} there was the attachment of a large Ag-TiO_2 particle to the surface via the anodic oxide layer. Silver was confirmed to be part of the composition of this particle by the EDS analysis data shown in Figure 90(b) Area 4. It must be noted that the area indicated in Figure 85(b) was significantly damaged by the FIB milling and attachment points were more numerous before the FIB thinning process was performed. There are also AgNPs present within the oxide at (b). Because Figure 85 did not fully exhibit the typical three-layered structure as found in the samples described previously (See Figure 79), another FIB cross-section was cut from a sample created under identical conditions (See Figure 86) and in that cross-section the resultant microstructure was similar to the representative structure. (Figure 79).

Figure 87 shows a cross-section of a Ti-6Al-4V sample surface that had the 76.93 wt% Ag-TiO_2 powder fused on to it, using the 0.5M H_2SO_4 electrolyte. It was apparent that the area being sampled in this case did not entirely conform to the expected cross-sectional microstructure evident in most previously-discussed sample conditions, in that there was not the formation of a three-layered oxide structure (See Figure 79). It was evident in Areas (a) and (b) that the oxide layer was thick (on average *ca.* 169.4nm), relative to Areas (c) {*ca.* 9.6nm thick} and (d) {*ca.* 65.7nm thick}, and contained small numbers of AgNPs near the surface. This was confirmed using EDS analysis, as shown in Figure 90(e) Area 17. The EDS analysis also confirmed {See Figure 90(e), Area 16} the presence of small amounts of Ag within the bulk of the oxide shown in Figure 87, Area (a). Shifting the field of view across the sample to Area (c) in Figure 87, the oxide layer becomes very thin, but it still contains AgNPs within the surface. Figure 87(d) shows a large Ag-TiO_2 particle attached to the base oxide (blue arrow). Area (e) in Figure 87 is noteworthy as it shows oxide formation under the surface of the Ti-6Al-4V metal. The reason for this is that during the dual acid etching process the grains themselves were eroded. In the case of this sample, the grain is at a very specific orientation to the surface and thus, during the etching process, a crevasse was created in the sub-surface of the Ti-6Al-4V sample. During the dip-coating of the sample with Ag-TiO_2 particles, some of the particles may have penetrated into the crevasse. The EDS analysis, presented in Figure 90(d) Area 15, did show small amounts of silver present in the crevasse, indicating that there had been some Ag-TiO_2 particle penetration into this area. During the anodising step, the electrolyte would have penetrated into the Ag-TiO_2 particle-containing crevasse. Thus, the anodic oxide layer and the Ag-TiO_2 layer would have formed owing to the presence of Ag-TiO_2 particles in the crevasse, as shown by the green rectangle. Area (f) in Figure 87 shows Ag-TiO_2 particles attached to the surface of the base oxide. The fact that these particles contained silver was confirmed by the EDS analysis, shown in Figure 90(d), Areas 12 and 13. Because Figure 87 did not exhibit the typical three-layered structure observed in other samples, another FIB cross-section was cut from a sample created under identical conditions and in this cross-section the expected microstructure was observed (See Figure 88).

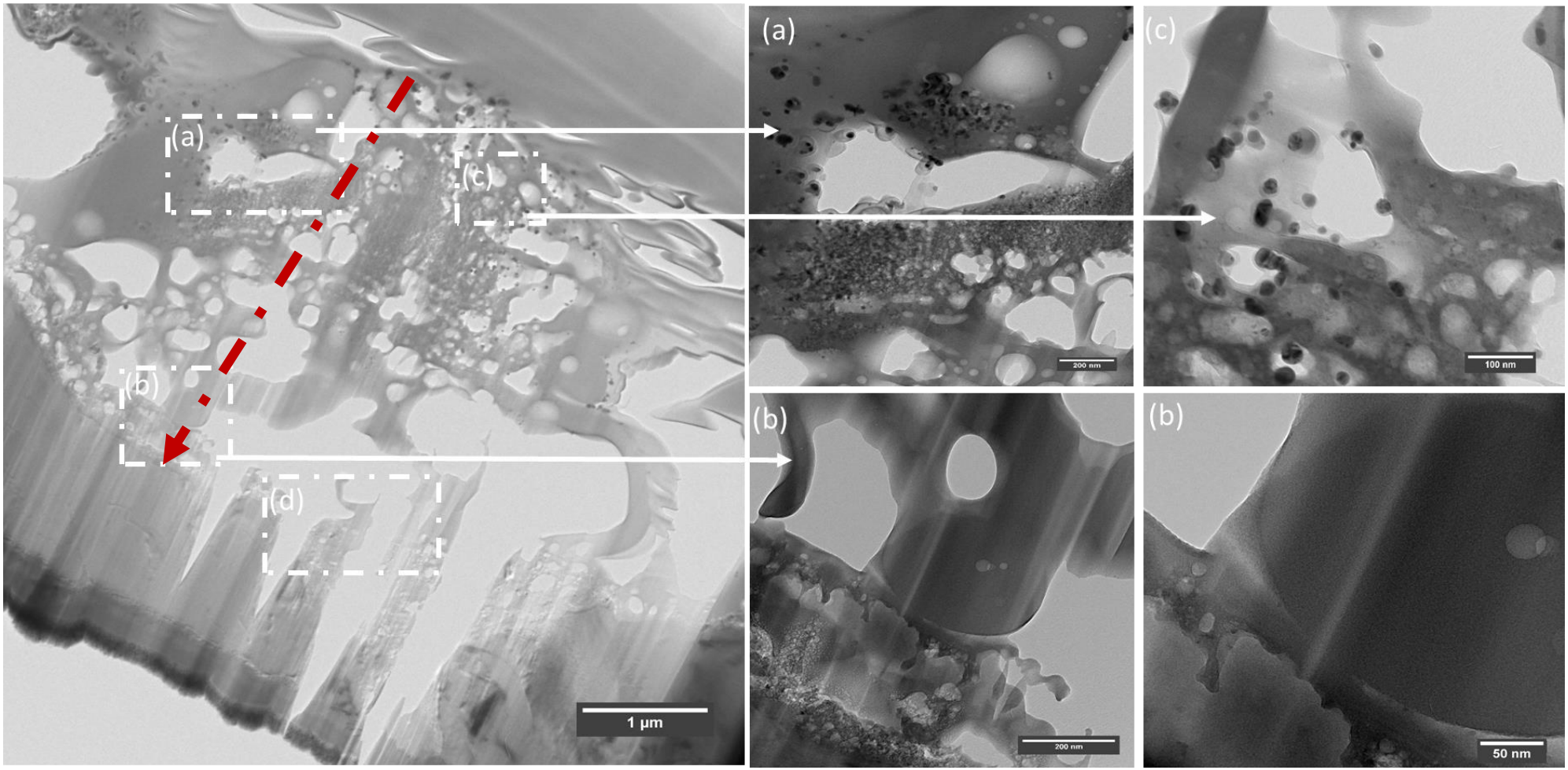

Figure 89 : Cross-sectional Bright-Field TEM of a sample coated in the 76.93 wt% Ag-TiO_2 powder, fused via anodising in 2.1 M H_3PO_4 at 100V, showing in (a) and (c) AgNPs and in (b) area of bonding between the anodic oxide and Ag-TiO_2. Red arrow indicating the direction of decrease in AgNP s.

The cross-sectional microstructure shown in Figure 89 had the expected morphology, *i.e.* an anodic oxide layer with the Ag-TiO_2 layer fused to its surface. The attachment points of the Ag-TiO_2 layer to the anodic oxide layer are shown in (b) and (d). It can be seen in (d) that the two oxide layers had been significantly damaged during the FIB milling process. In Figure 89(a), the presence of AgNPs within the Ag-TiO_2 layer was confirmed by the EDS analysis, which is shown in Figure 90(f). Progressively fewer concentrations of AgNPs were observed closer to the anodic oxide layer (direction indicated by the red arrow in Figure 89). This decrease in silver content with surface depth is shown in Figure 90(g), Areas 21 and 22. In addition, the EDS illustrated in Figure 90(c), Areas 8 and 10, confirmed that the anodic oxide layer was Ag-deficient and, therefore, AgNP-deficient.

5.2.7 *EDS analysis*

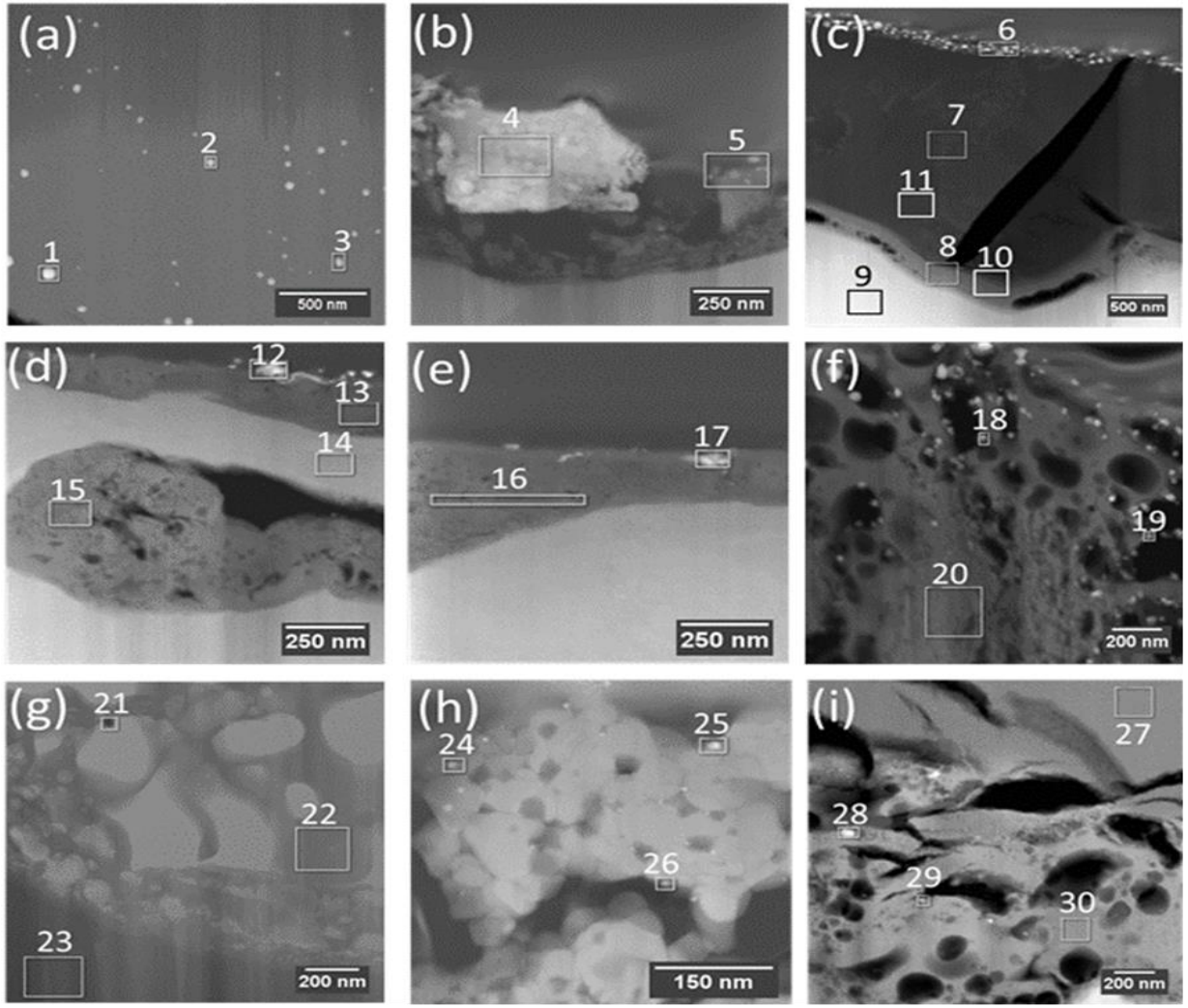

Area	Ti (wt%)	O (wt%)	Ag (wt%)
1 (Dense Oxide)	41.7	32.6	18.2
2 (Dense Oxide)	43.8	32.8	16.7
3 (Dense Oxide)	49.6	35.8	7.9
4 (Large AgNP)	-	-	85.5
5	25.9	17.9	12.4
6	5.7	11.3	21.1
7 (Dense Oxide)	28.4	52.0	1.3
8 (Anodic Oxide)	60.8	28.5	-
9 (Base Metal)	87.9	-	-
10(Anodic Oxide)	58.7	29.7	-
11 (Dense Oxide)	28.3	51.6	1.0
12	13	9.1	45.2
13	43.2	43.6	0.9
14 (Base Metal)	84.1	-	-
15	47.1	45.5	0.7
16	10.9	14.8	5.9
17	48.9	43.7	1.3
18	7.6	16.1	51.7
19	15.7	19.4	46.5
20	48.6	38.4	-
21	5.1	13.8	67.9
22	31.2	49.6	-
23 (Base Metal)	87.3	-	-
24	26.7	25.5	4.0
25	41.3	35.1	10.0
26	33.1	33.8	4.7
27	53.5	40.7	-
28	37.1	28.8	24.7
29	45.2	36.6	11.3
30	48.1	41.7	1.6

Figure 90 : Bright-Field TEM : EDS analysis areas of TiO_2 layers from FIB samples shown in Figure 79 to Figure 89, with corresponding EDS data.

5.2.8 *Summary Discussion of Ag-TiO_2 Fused Surfaces*

In summary, as the silver content within the synthesised TiO_2 powders was increased, so there was an increase in the average diameter of the Ag-TiO_2 particles. This was due to a greater degree of particle agglomeration, owing to the progressively higher Ag wt% within the Ag-TiO_2 particles, which was a consequence of the increase in the $AgNO_3$ concentration during the Ag-TiO_2 powder synthesis. The EDS and AAS analyses confirmed the presence of Ag within the Ag-TiO_2 powders and reflected the expected trend that, as the $AgNO_3$ concentration during the TiO_2 synthesis was increased, so would the Ag content within the resultant Ag-TiO_2 powders. Macroscopically, the powders were observed to attach to areas where downward pressure had been exerted during the anodising process.

The surface morphology was consistent in all the samples that had the Ag-TiO_2 powders fused on to the Ti-6Al-4V surfaces via the anodising process, irrespective of which electrolyte was used, 0.5M H_2SO_4 or 2.1M H_3PO_4. The surface morphology included an anodic oxide layer with the Ag-TiO_2 layer fused to its surface.

The Ti-6Al-4V surfaces of the samples that had Ag-TiO_2 powders (with progressively higher Ag wt%s) fused on to them, using the 0.5M H_2SO_4 electrolyte, were analysed via RBS. The RBS analysis of the resultant surfaces that used the extreme values of the Ag wt%s (*i.e.* 0.48 Ag wt% and 76.93 Ag wt%) showed that these surfaces increased in Ag content from 0.7 at% to 4 at% respectively, as a result of this increase in the Ag wt% in the Ag-TiO_2 powders.

The Ti-6Al-4V surfaces of the samples that had Ag-TiO_2 powders (with progressively higher Ag wt%s) fused on to them, using the 2.1M H_2SO_4 electrolyte, were also analysed via RBS. The RBS analysis of the resultant surfaces that used the extreme values of the Ag wt%s (*i.e.* 0.48 Ag wt% and 76.93 Ag wt%) showed that these surfaces increased in Ag content from 0.6 at% to 1.3 at% respectively, as a result of this increase in the Ag wt% in the Ag-TiO_2 powders.

The XRD analysis of the Ti-6Al-4V surfaces that had been anodised in the 0.5M H_2SO_4 and 2.1M H_3PO_4 electrolytes, as described in Section 5.1.5, resulted in crystal structure phases that were predominantly anatase and rutile respectively, depending on which electrolyte was used. In contrast, in samples that underwent the same anodising process as above but with the addition of Ag-TiO_2 powders prior to anodisation, the same anatase and rutile crystal structure phases were present, but an additional brookite phase could be observed. It could be concluded that, since brookite was not a crystal structure phase generated via the anodic oxidation of Ti-6Al-4V (Section 5.1.5), the brookite phase was attributable to the incorporated Ag-TiO_2 powders.

Study of the sub-surface morphology in cross-section revealed that the oxide layers exhibited a characteristic structure: The base was a 4mm thick disc of Ti-6Al-4V alloy, on to which a second Ag-deficient anodic oxide layer, approximately 200nm thick, was grown. The third AgNP-containing oxide layer, which was shown to be attached to the surface of the anodic oxide layer, was significantly thicker than the second layer. However, there were certain areas observed in some of the samples that deviated from the characteristic structure described above, in that they did not exhibit the three-layered structure. In these cases, the third thicker TiO_2 layer was not present. However, all samples were shown to contain AgNPs. The detection of Ag, implying the presence of AgNPs, in areas of the samples that had a third (thicker) layer was further confirmed by EDS analysis. In areas where the third layer had not developed, silver (and thus AgNPs) was found in the second layer.

It was concluded that the development of the third oxide layer (the Ag-TiO_2 layer) could be attributed to the presence of the TiO_2 powder, which acted as the catalyst in the development of this layer. The sub-surface analysis provided by the FIB-TEM images, confirmed that the Ag-TiO_2 particles had been successfully attached to the surfaces of the Ti-6Al-4V samples via the anodic oxidation in both the 0.5M H_2SO_4 and 2.1M H_3PO_4 electrolytes.

In literature there was no indication of the method of anodisation being used to attach TiO_2 particles to the surface of titanium. The method in this section successfully presented a novel method to attach TiO_2 particles to the surface of titanium without the need for high temperature sintering. This would assist in applications where mechanical properties of the base titanium would like to be retained whilst altering the surface properties.

5.3 Silver Ion Implanted Surfaces

5.3.1 *Surface Morphology*

Figure 91 depicts the surfaces obtained after the polished Ti-6Al-4V discs had undergone anodisation in the 2.1M H_3PO_4 {See (a)} and 0.5M H_2SO_4 {See (b)} electrolytes, with subsequent silver ion implantation (Ag^+ implantation). In addition, Figure 91(c) depicts the surfaces obtained of the polished Ti-6Al-4V discs that had undergone only the Ag^+ implantation process. During Ag^+ implantation the sample holder masked a region of the sample surface, preventing Ag^+ implantation, thus keeping the anodised surface intact {Refer to the unaffected regions shown in Figure 53(a) and (b)}.

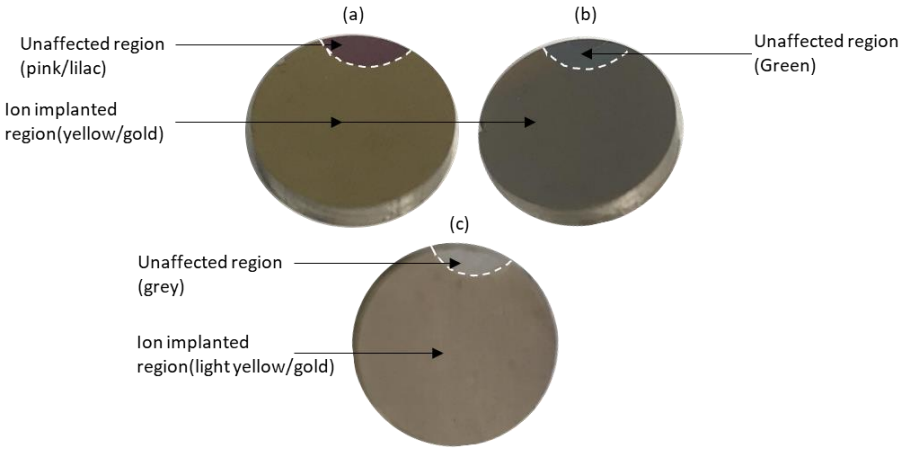

Figure 91 : Surfaces after polishing and Ag^+ implantation: (a) anodised in 2.1M H_3PO_4, (b) anodised in 0.5M H_2SO_4 and (c) polished (not anodised).

It was observed that all the surfaces depicted in Figure 91 experienced a change in colour in consequence of the Ag^+ implantation process. Samples in Figure 91(a) and (b) changed from a pink/lilac and green colour respectively, to a yellow/gold colour. The polished samples (c) changed from a grey surface to a lighter shade of yellow/gold when compared to (a) and (b). The change in the colour of the surfaces that had been anodised and then Ag^+ implanted {See Figure 91(a) and (b)}, may have been due to the reduction of the oxide layer thickness to 10 - 20nm during ion implantation. This possible explanation was suggested by the observed yellow/gold colour, since according to Figure 15 and Table 5, an oxide layer thickness in the 10 - 20nm range corresponded with the observation of a gold colour.

The light yellow/gold surface colour observed in the case of the polished and subsequent Ag^+ implanted Ti-6Al-4V sample {Figure 91(c)}, may have been due to the heat generated during the ion implantation process that caused the growth of a 10 - 20nm thick oxide layer. A 10 - 20nm thick oxide layer would, according to Figure 15 and Table 5, correspond with the observation of a light yellow/gold colour. However, as will be discussed later in this section, it was found that the Ag ion implantation process had no measurable effect on the oxide layer thickness. In addition, no oxide growth was observed on the polished Ti-6Al-4V samples after ion implantation.

It is widely recognised that silver nanoparticles (AgNPs) in aqueous solutions tend to have a yellow to orange colour [98], thus the most feasible explanation for the colour change of both the Ag^+ implanted anodised surfaces {Figure 91(a) and (b)} and the polished surfaces {Figure 91 (c)} would be that the

colour change was attributable to the presence of Ag or AgNPs within the surfaces, thus having nothing to do with the surface oxide thickness.

In this section, the 0.4 x 10^{17} ions/cm^2 and 1.2 x 10^{17} ions/cm^2 ion implantation dosages will be referred to as the "low" and "high" dosages respectively.

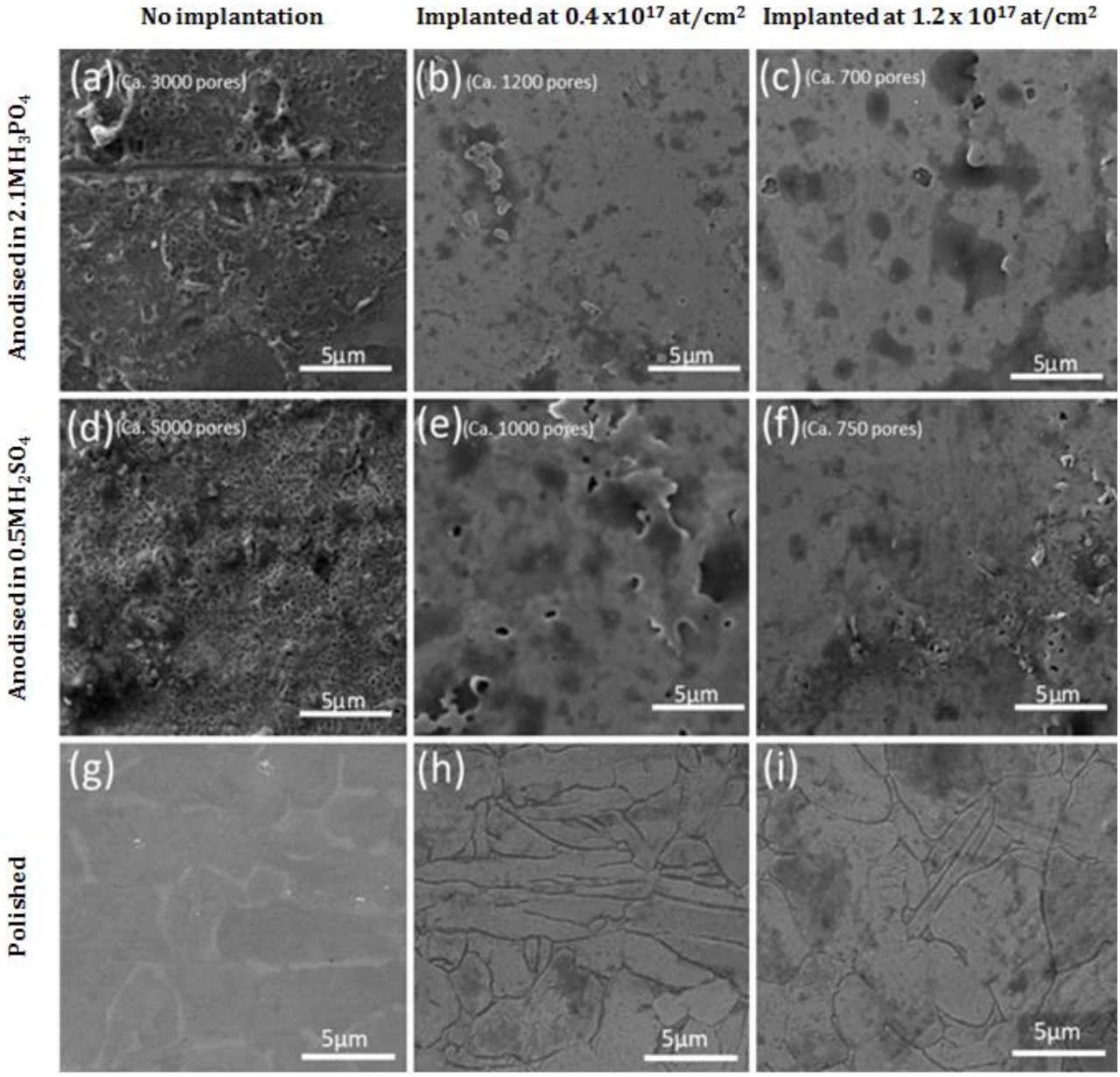

Figure 92 : Secondary electron SEM Images of Ti-6Al-4V after anodising and ion implantation conditions: (a) anodised in 2.1M H_3PO_4 (no ion implantation); (b) anodised in 2.1M H_3PO_4 and Ag^+ implanted at 0.4 x10^{17} at/cm^2; (c) anodised in 2.1M H_3PO_4 and Ag^+ implanted at 1.2 x 10^{17} at/cm^2; (d) anodised in 0.5M H_2SO_4 (no ion implantation); (e) anodised in 0.5M H_2SO_4 and Ag^+ implanted at 0.4 x10^{17} at/cm^2; (f)) anodised in 0.5M H_2SO_4 and Ag^+ implanted at 1.2 x 10^{17} at/cm^2; (g) polished (no ion implantation); (h) polished and Ag^+ implanted at 0.4 x10^{17} at/cm^2; (i) polished and Ag^+ implanted at 1.2 x 10^{17} at/cm^2.

Figure 92 (a) and (d) respectively show the Ti-6Al-4V surfaces that were anodised in the 2.1M H_3PO_4 and 0.5M H_2SO_4 electrolytes before the Ag^+ implantation. The surface morphology of (a) and (d) were in line with the results in Section 5.1, *i.e.* in terms of pore distribution and pore morphology. After the Ag^+ implantation of surfaces (a) and (d) at low {(b) and (e) respectively} and high {(c) and (f) respectively} dosages, both the oxide layers were found to have been eroded by the ion beam. This is confirmed by a marked decrease in the number of surface pores, as shown in Figure 92 {(b) and (c)}

and Figure 92 {(e) and (f)}, relative to their respective starting conditions, as shown in Figure 92 {(a) and (d)}.

Figure 92 (g) shows the polished Ti-6Al-4V samples that were not anodised. It can be observed that, after Ag^+ implantation, the polished starting condition surface (g) had been eroded away at the grain boundaries, creating an etched effect {Shown in Figure 92 (h) and (i)}.

Table 22 : Average Vickers' hardness pre and post ion implantation.

SAMPLE CONDITIONS	**HARDNESS $HV_{0.1}$**		
DOSAGE (X 10^{17} IONS/CM^2)	**Before implantation**	**0.4**	**1.2**
POLISHED	303.6 ± 16.8	292.9 ± 11.2	321.4 ± 9.7
ANODISED 0.5M H_2SO_4	338.4 ± 48.2	328.7 ± 24.8	334.2 ± 25.7
ANODISED 2.1M H_3PO_4	332.5 ± 33.7	351.8 ± 29.0	327.3 ± 17.8

The results in Table 22 show the average hardness obtained via Vickers' Hardness testing of the polished and anodised titanium surfaces before and after Ag^+ implantation. All the tested surfaces exhibited no significant change in hardness after Ag^+ implantation. This suggested that there was no significant formation of "harder" secondary phases, such as second phase ceramic particles, within the oxide layers or titanium alloy metal surfaces. Another possibility for the lack of change in the hardness measurements before and after ion implantation is that the micro-hardness testing technique is not sensitive enough to resolve hardness changes owing to lattice distortion, as a result of the presence of the newly implanted Ag.

5.3.2 *Surface Roughness of the Polished and Anodically-Oxidised Ion Implanted Surfaces*

The Atomic Force Microscopy (AFM) results, shown in Figure 93, indicated that the average roughness (R_a) of the polished samples increased from 13.10nm in (a) to 14.26nm in (b) and finally to 18.99nm in (c). This trend is displayed graphically in Figure 96. These incremental increases were due to the grain boundaries being preferentially etched during the ion implantation process. The grain boundary depths were also measured and were found to be 31.31 ± 8.3 nm and 71.03 ± 21.39 nm, as shown in Figure 93 (b) and (c) respectively. Thus, the incremental surface roughness increases observed from (a) through to (c) were due to the grain boundary etching, caused by the ion implantation beam.

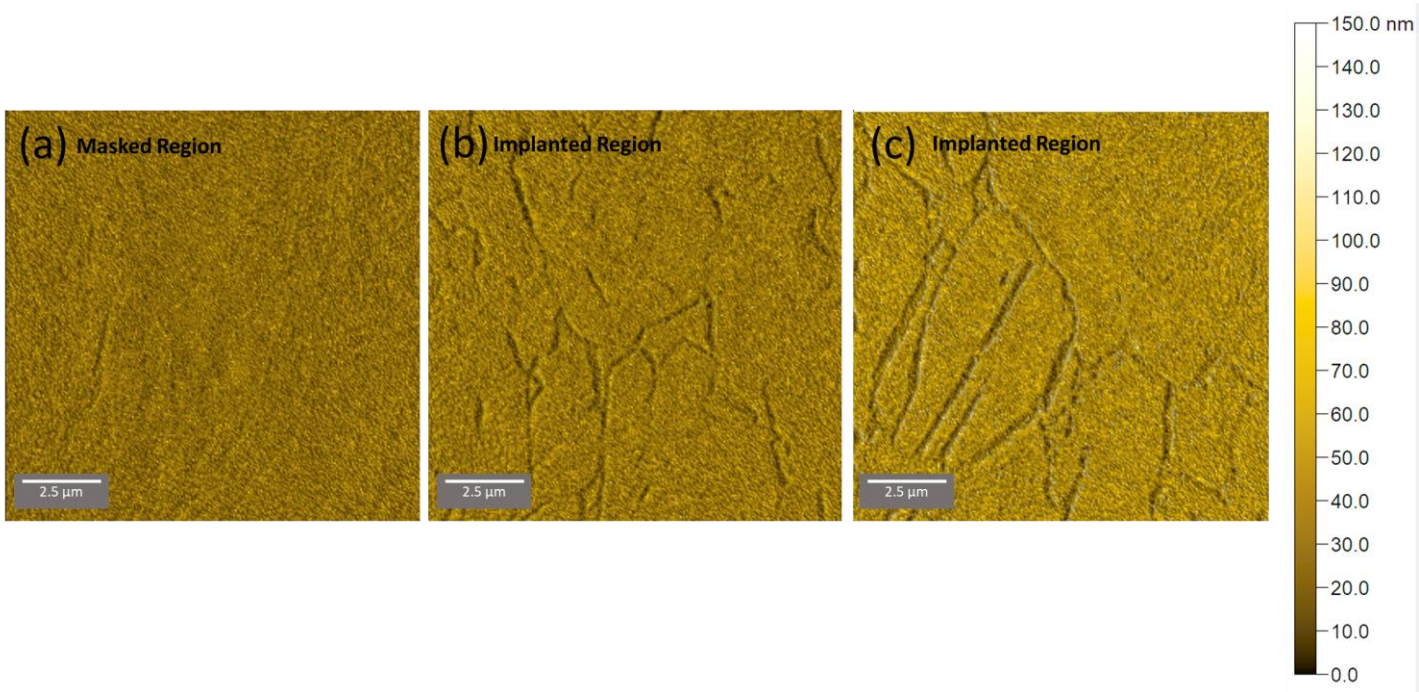

Figure 93 : AFM images of polished Ti-6Al-4V surfaces at ion dosage of (a) 0 (b) 0.4 x 10^{17} and (c) 1.2 x 10^{17} ion/cm2.

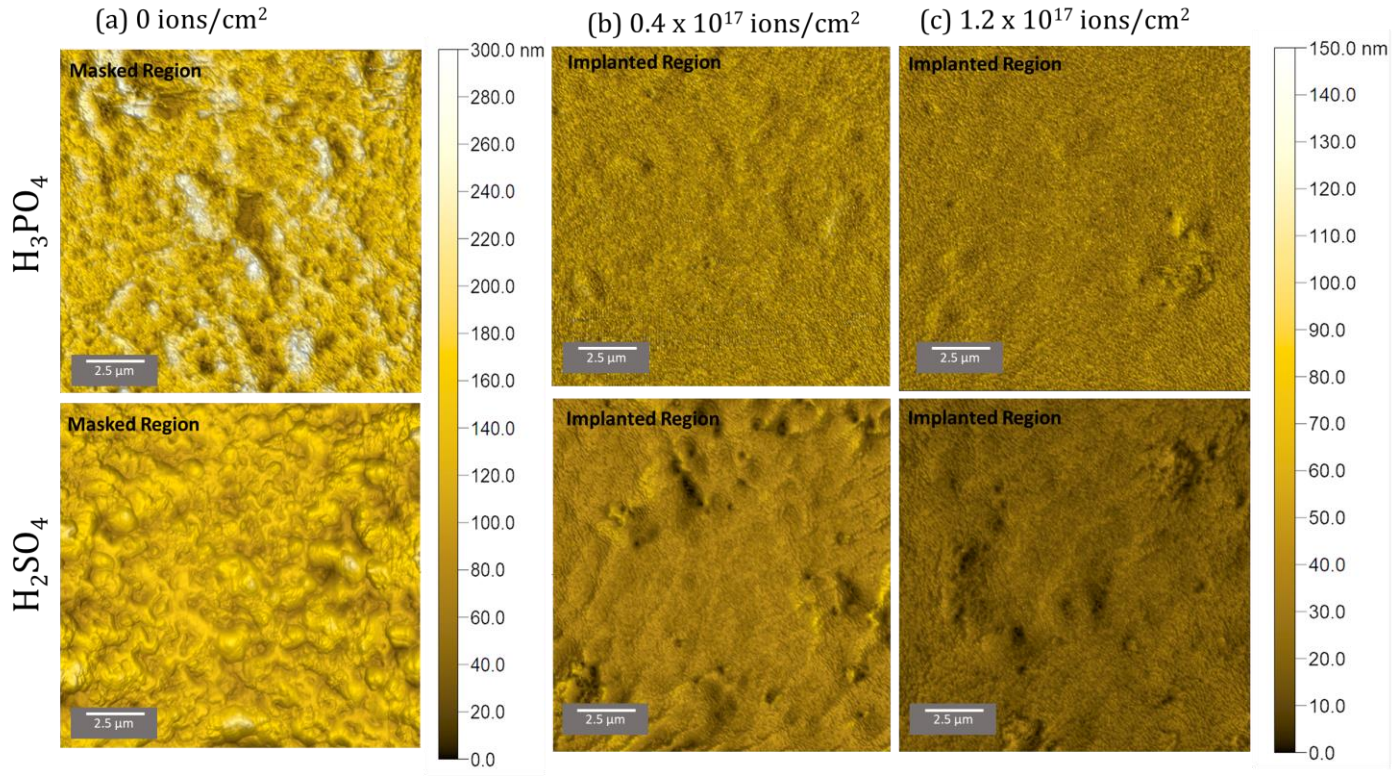

Figure 94 : Central AFM images of anodised Ti-6Al-4V surfaces at ion dosage of (a) 0, (b) 0.4 x 10^{17} and (c) 1.2 x 10^{17} ion/cm² in the 0.5M H_2SO_4 and 2.1M H_3PO_4 electrolytes.

The Atomic Force Microscopy (AFM) results for the titanium samples anodised in the 2.1M H_3PO_4 and 0.5M H_2SO_4 electrolytes before Ag^+ implantation are shown in Figure 94, Column (a). A sharp decrease in R_a was observed after Ag^+ implantation at the low dosage in both the oxide surfaces generated by anodisation in the 2.1M H_3PO_4 and 0.5M H_2SO_4 electrolytes. However, increasing the dosage to 1.2 x10^{17} ions/cm² (the high dosage) did not result in any further reduction of R_a after the Ag^+

implantation. This trend is shown graphically in Figure 96. In order to explain this trend, the areas of high tip deflection (θ) before and after Ag^+ implantation had to be compared. By limiting the AFM tip deflection data to where the deflection was at its highest (highlighted by the yellow circle on the right hand side of Figure 96) , areas of high free surface energy could be highlighted in red (See Figure 95 below). It was observed that in the area masked from ion implantation {See Figure 95(a)} there were a greater number of highlighted areas relative to the area that had been ion implanted, as seen in Figure 95(b). This demonstrated that during the ion implantation process, the ion beam eroded areas of high free surface energy and, as a consequence of this erosion, the R_a had been reduced. This explanation could be extended to the polished titanium samples that had been ion implanted {shown in Figure 93(b) and (c)}. However, since it is widely accepted that grain boundaries are areas of high free surface energy, it could be concluded that the grain boundaries had been preferentially eroded by the ion beam during ion implantation, creating the etched effect that resulted in the increase in R_a.

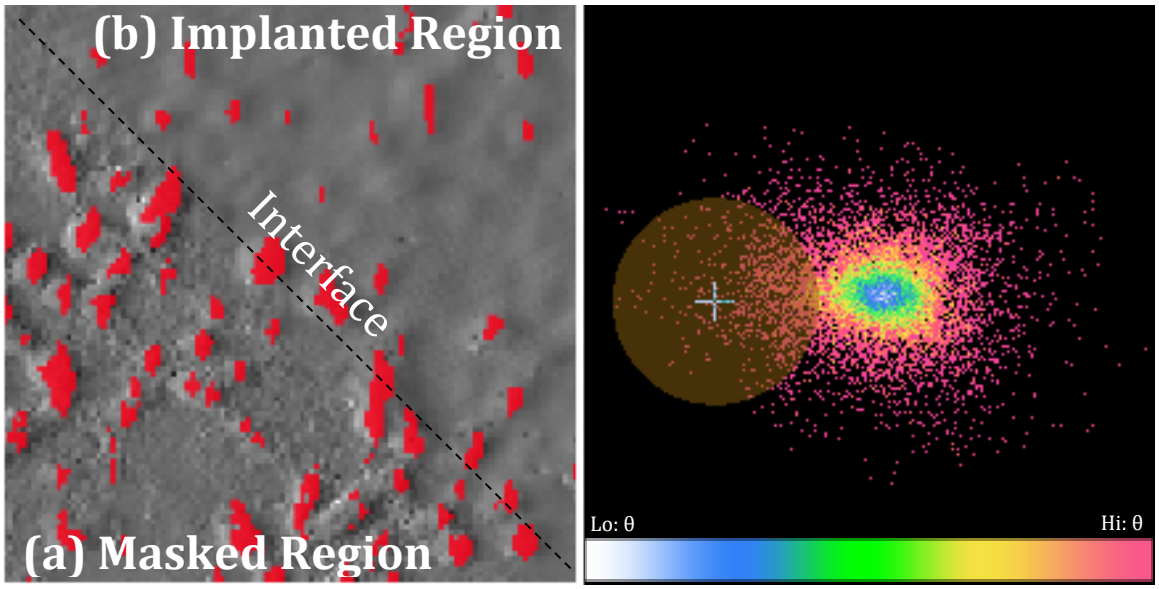

Figure 95 : Left: Contact AFM Tip deflection (θ) analysis of an area (a) masked from Ag^+ implantation and (b) area eroded via Ag^+ implantation. Right: Selected tip deflection data.

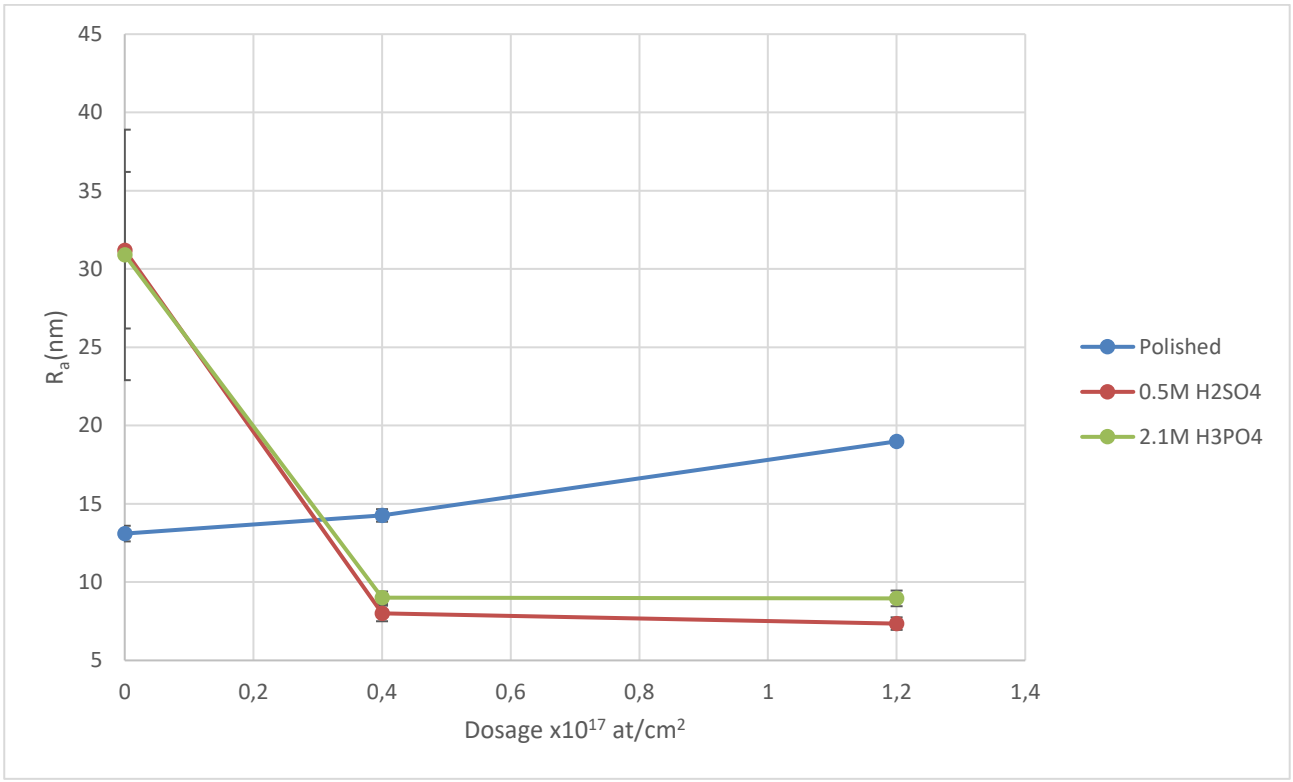

Figure 96 : R_a as a function of Ag ion implantation dosage.

5.3.3 *Surface RBS analysis*

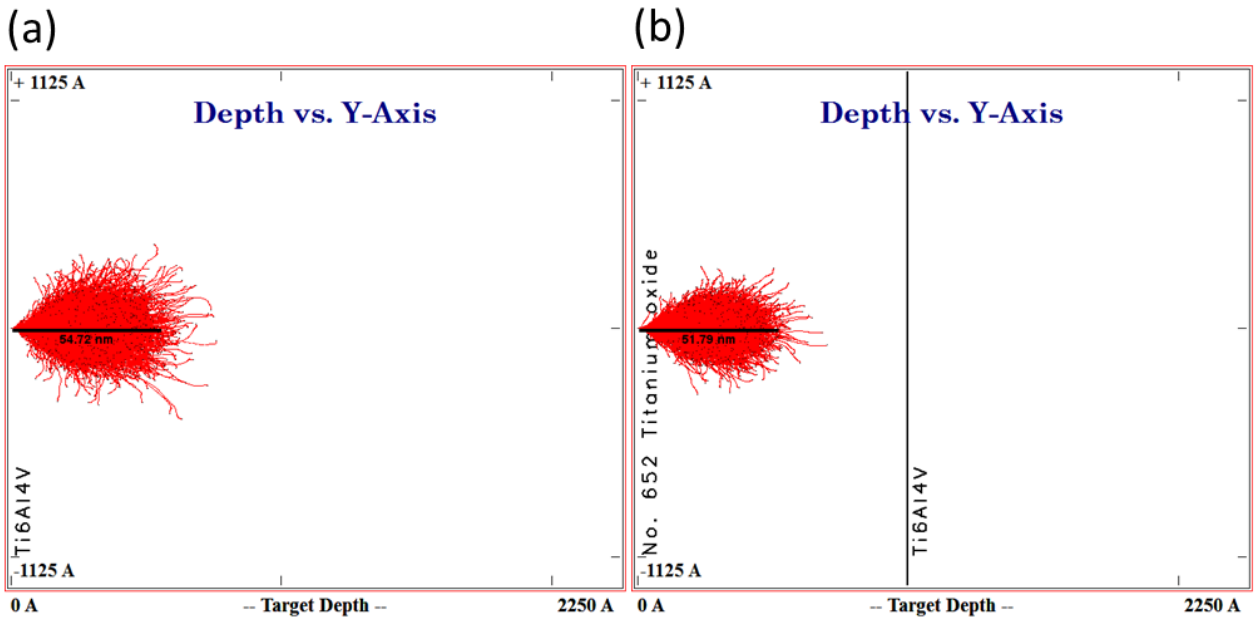

Figure 97 : SRIM simulation of Ag ion implantation at 84keV into (a) Ti-6Al-4V and (b) TiO_2.

The simulated Ag^+ implantation data in Figure 97 showed that the penetration of Ag into the polished Ti-6Al-4V surfaces and the anodic oxide surfaces were predicted to be *ca.* 54 and 51nm respectively. {EDS mapping results, presented later, show that Ag is detected within the first 50nm of both the polished and anodised sample surfaces (See Figure 105), which would be in agreement with the simulated data shown above.} Because the silver did not penetrate deeper than 50nm into the oxide layer and polished titanium surfaces, the RBS data were limited to quantifying the at% Ag present within the first 50nm of each sample. These results are summarised in Table 23 below.

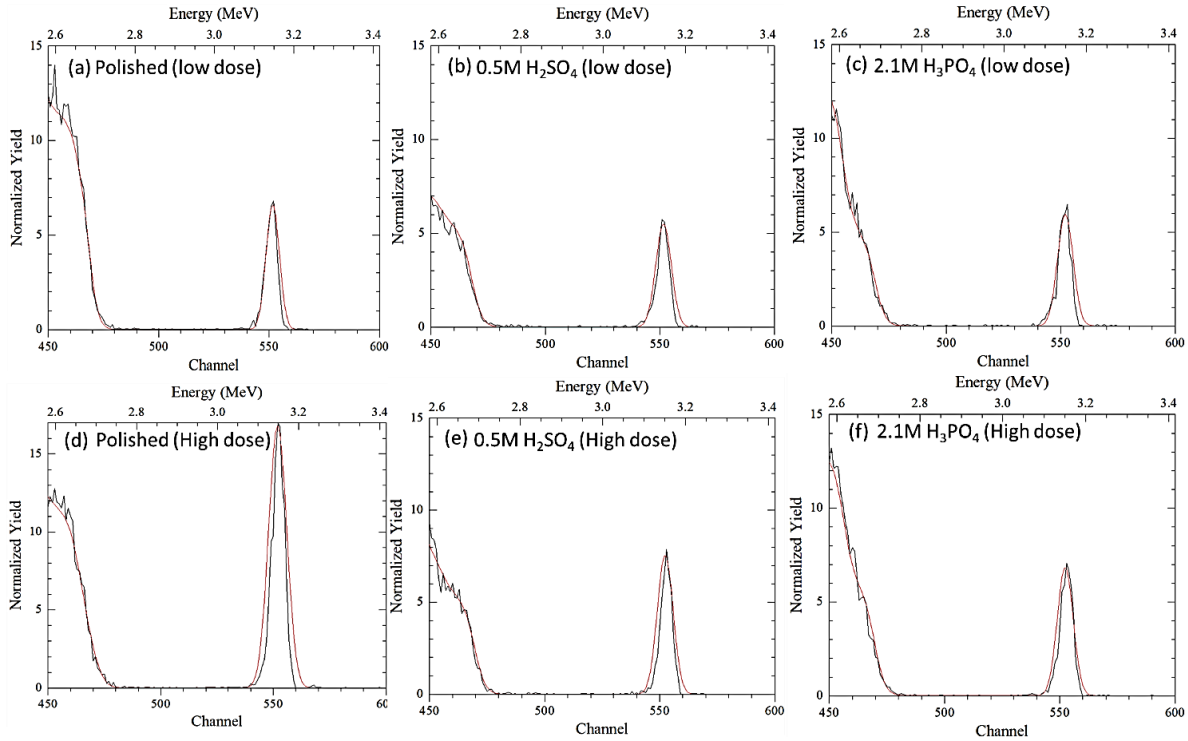

Figure 98 : Rutherford backscatter results of Ag^+ implanted surfaces (a and d) polished, (b and e) 0.5M H_2SO_4 anodised and (c and f) 2.1M H_3PO_4 anodised at low and high Ag^+ dosages.

Table 23 : Summary of Ag content of various ion implanted samples.

	Polished		**2.1M H_3PO_4**		**0.5M H_2SO_4**	
Dose (10^{17} ions/cm^2)	0.4	1.2	0.4	1.2	0.4	1.2
At% Ag	16.5 ± 1.3	40.6 ± 6.3	13.9 ± 1.4	14.7 ± 2.3	16.3 ± 2.6	16.1 ± 2.6

As is shown in Table 23, there was a significant increase in the at% Ag when the ion dosage was increased from low to high in the polished Ti-6Al-4V samples. In contrast, the at% Ag in the anodically oxidised samples remained relatively constant, in spite of increasing the ion dosage from low to high. The plausible explanation as to why the at% Ag remained constant in the latter case of the Ag^+ implanted anodic oxide layers is that the the titanium oxide layer matrix had already been super-saturated with Ag ions at the low dosage, causing the formation of AgNPs (See Section 3.7.9), with the result that, at the high dosage, there was no space available for further Ag ion penetration. Therefore, within the first 50nm of the titanium oxide layer, during ion implantation, a physical barrier to further Ag ion penetration had developed. Thus, it can be deduced that the low dosage level was sufficient to maximise the at% Ag and that a higher dosage was not, in fact, necessary.

Figure 99 corroborates the above rationale, where a SRIM simulation was performed to show that, if a silver layer were added to the anodic oxide layer, further silver penetration would be blocked. It can be seen in this figure that, as the thickness of the Ag layer was increased from 25nm in (c) to 50nm in (d), the penetration of the Ag ions into the titanium oxide layer was inhibited. At 25nm thickness the penetration into the TiO_2 layer was *ca.* 18nm and at a Ag thickness of 50nm it became impossible for newly-implanted Ag ions to penetrate deeper than said 50nm, which meant that they could not reach the oxide layer.

The significant increase in the at% Ag when the ion dosage was increased from low to high in the polished Ti-6Al-4V samples (See Table 23) was likely to have been due to the intermetallic bonding

that occurred in the crystal structure of the polished Ti-6Al-4V sample. There would have been a greater capability to accommodate Ag ions within the Ti-6Al-4V crystal structure of the samples through charge distribution, relative to the lesser capability of the covalently-bonded crystal structure of TiO_2. {TEM imaging would later show (See Figure 102) that the formation of AgNPs was not observeable after ion implantation in the polished samples at either the low or the high dosage of Ag ions and it could be concluded that the Ti-6Al-4V structure had not reached the supersaturation point of Ag and thus nucleation and the growth of AgNPs could not occur.} Therefore, because the physical barrier caused by the formation of of AgNPs was not present, the higher concentration of Ag ions could be implanted within the polished surfaces.

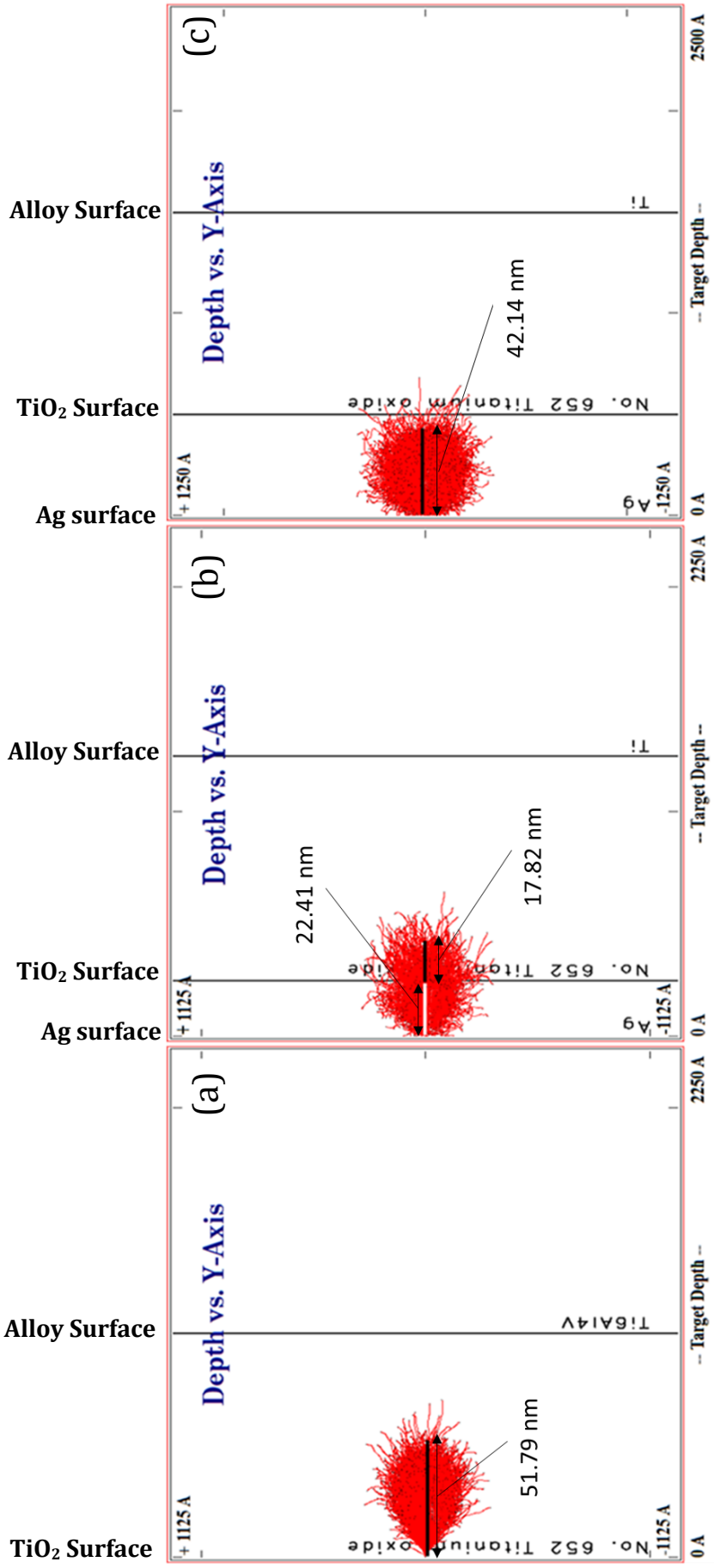

Figure 99 : SRIM simulation of Ag ion implantation at 84keV into (a) TiO_2, (b) 25nm Ag layer on TiO_2 and(c) 50nm Ag layer on TiO_2.

5.3.4 *Surface X-Ray Diffraction*

Contrary to what had been anticipated, the X-Ray Diffraction (XRD) results (See Figure 100) of all the Ag ion implanted oxides showed no anatase (101) or rutile (110) peaks at *ca.* 25 and 27 θ respectively. These findings were irrespective of the anodising electrolyte used or the level of the Ag ion dosage. There were two possible explanations for this. Firstly, the oxide layer thickness might have reduced to a point where the signals from the anatase and/or rutile peaks were being masked by the signals from the base titanium. (Reference to Figure 102 will later show that Ag ion implantation did not significantly change the anodic oxide layer thicknesses, which discredits the first hypothesis.)

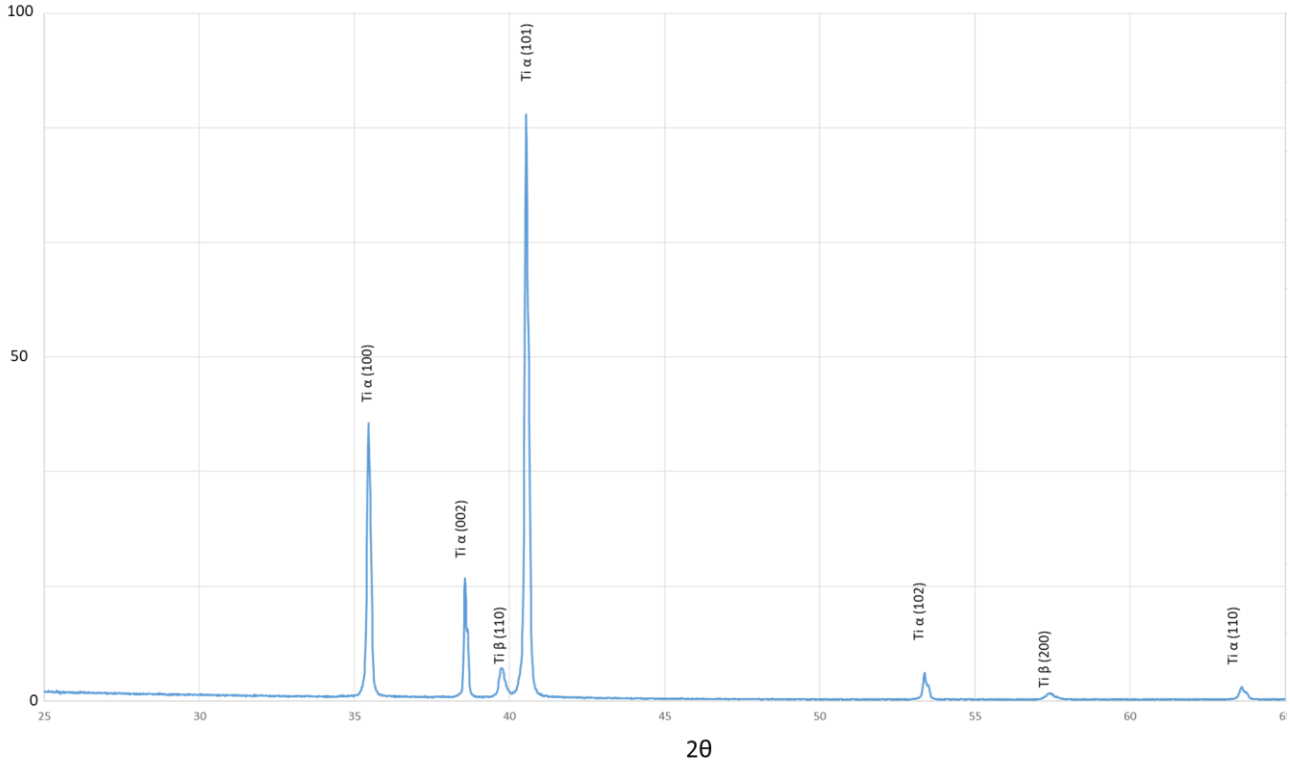

Figure 100 : XRD Spectrum of all ion implanted samples.

Secondly, as a consequence of the Ag ion implantation, the oxide layers could be amorphised. Since amorphous materials have no defined crystal structure, the XRD analysis would not be able to detect any rutile or anatase phases. After ion implantation, it was observed that the TiO_2 layers had, in fact, amorphised {See Figure 101(b)}, thus confirming the veracity of the second hypothesis.

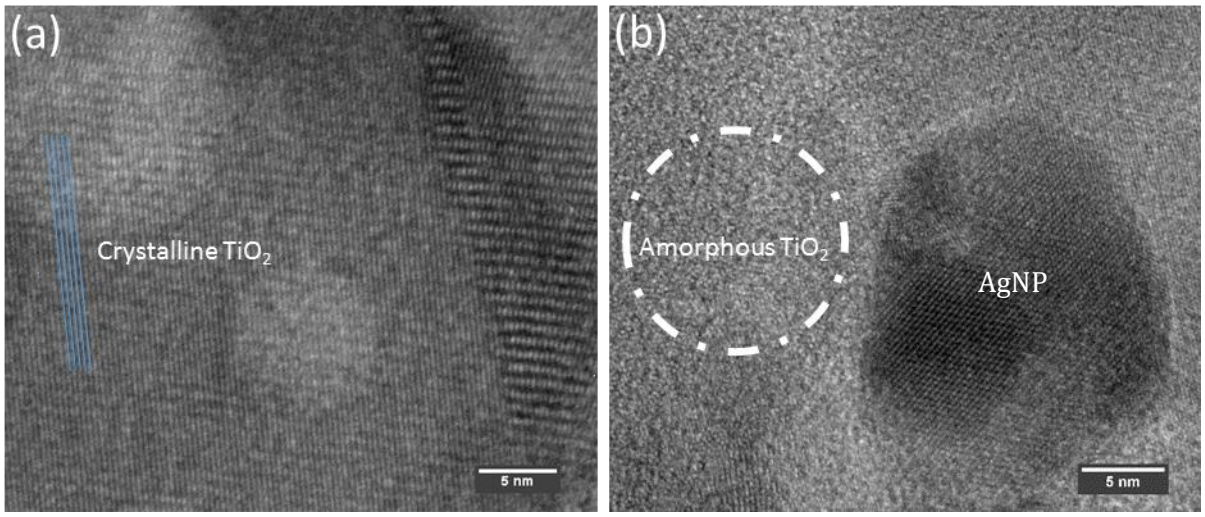

Figure 101 : HR-TEM image of oxide (a) before Ag ion Implantation and (b) after Ag ion implantation.

5.3.5 *Sub-Surface Morphology*

Cross-sectional imaging of the polished Ti-6Al-4V samples via TEM, as shown in Figure 102 (a) and (d), demonstrated that there had been no AgNP formation in the case of the polished samples after the Ag ion implantation process. However, there was a clearly-defined deformation zone showing on each of the images, which was *ca.*100nm wide for both the low and the high Ag ion dosage. Because it is widely accepted that surface deformation improves the wear resistance of materials, the increased wear resistance reported by Y.Z. Wan *et al.* [69], but without explanation, of similar Ag ion implanted titanium alloys was found in this study to be attributable to the deformation of the titanium alloy surface during Ag ion implantation.

The TiO_2 layers generated via anodising in the 2.1M H_3PO_4 and 0.5M H_2SO_4 electrolytes, and subsequently the Ag ions implanted at low and high doses, are shown in Figure 102 {low dose (b) and high dose (e)} and Figure 102 {low dose (c) and high dose (f)}. All the oxide films depicted in this figure showed that there was AgNP formation within the first 50nm of the oxide layer surface, irrespective of the ion dosage or the anodising electrolyte used. The reason for the formation of the AgNPs within the TiO_2 layers was described in detail in Section 3.7.9, which stated that when the Ag ion dosage during ion implantation reached a certain threshold value, the Ag atoms became supersaturated in the TiO_2 crystal structure, and since Ag-Ag bonds are more energetically favourable than Ag-O bonds, nucleation of the AgNPs occurred.

Additionally, it was observed that the average AgNP diameter increased when the Ag ion dose was increased. This was attributed to the Ag ion implantation at the higher dosage increasing the driving force for further AgNP particle growth (as described in Section 3.7.9). The average diameter distributions of the AgNPs formed in the TiO_2 layers that had been generated via anodising in the 2.1M H_3PO_4 and 0.5M H_2SO_4 electrolytes and, subsequently, Ag ion implanted at a low and high dose are shown in Figure 104. These distributions further confirm the observation that Ag ion implantation at higher Ag ion implantation dosages results in an increased driving force for the growth of AgNPs.

The lack of AgNPs within the polished Ti-6Al-4V surfaces that had been Ag ion implanted at both the low and the high dose was due to the capability of the intermetallic bonds of the titanium alloy crystal structure to accommodate the extra electrons brought into the structure by the additional Ag atoms incorporated during ion implantation. Thus, the Ag supersaturation point of the Ti-6Al-4V lattice may be higher than the Ag supersaturation point of TiO_2. This assumption corroborates what was previously observed in Figure 102, (a) and (d), that if the supersaturation point of Ag within the Ti-6Al-4V crystal lattice had not been reached there would have been no AgNP formation. Thus it can be confidently concluded that the Ag is in an ionic state within the Ti-6Al-4V lattice and that the supersaturation point of Ag is higher than the supersaturation point of TiO_2.

While, in the case of the polished Ti-6Al-4V surfaces, the intermetallic bonds of the lattice did accommodate the extra electrons, the Ag ion implantation into the covalently-bonded TiO_2 lattice had the opposite effect: Since covalent bonds cannot accommodate extra electrons, the only possible energetically-favourable positions for the Ag ions would have been to share their electrons with either other Ag atoms or O atoms. Since oxygen atoms have a much higher affinity to bond with Ti atoms than do Ag atoms, Ag-Ag bonding was preferred and this Ag-Ag bonding led to the nucleation of AgNPs when the Ag concentration reached supersaturation point within the TiO_2 matrix.

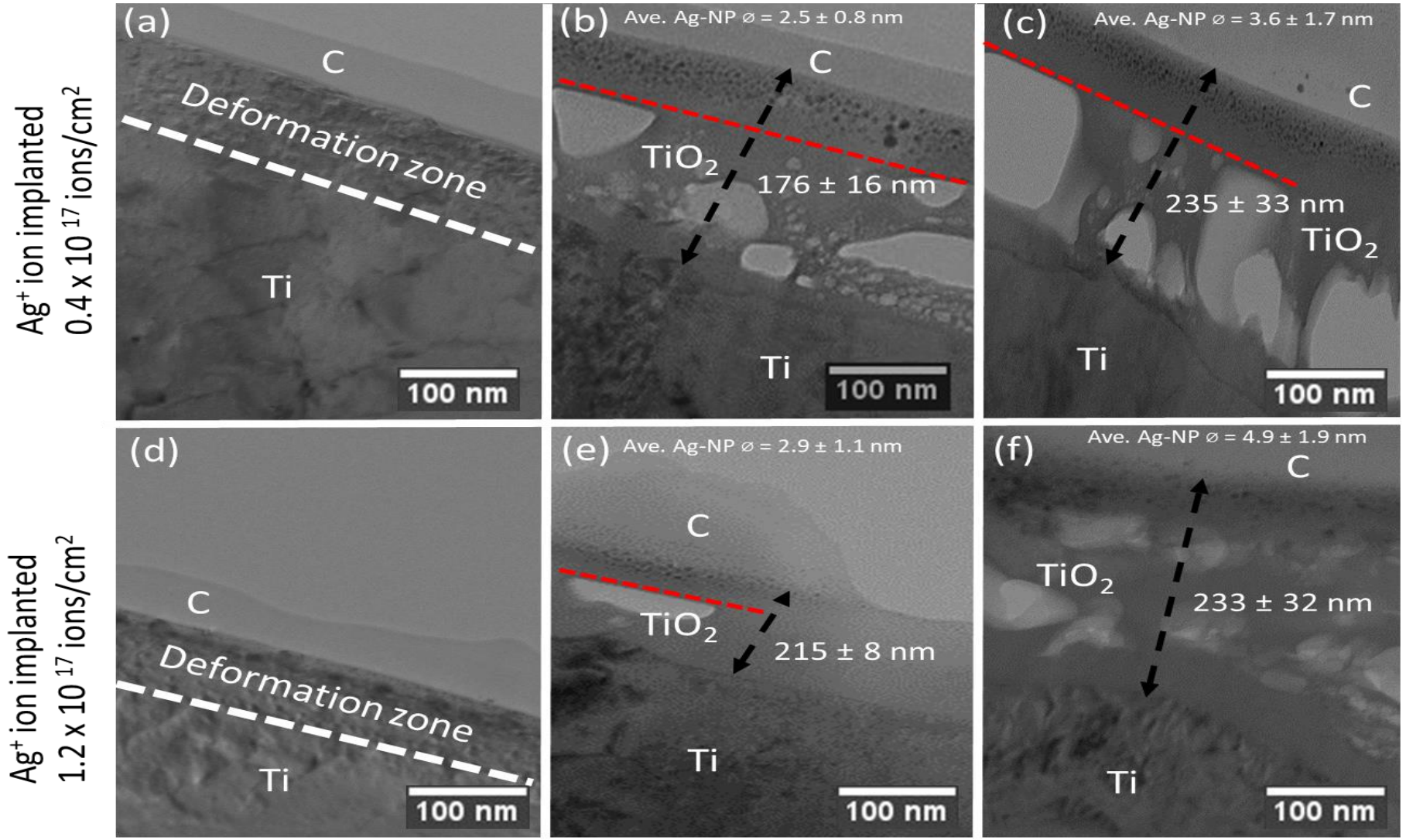

Figure 102 : Bright-Field TEM: Ag ion implanted surfaces: (a and d) polished, (b and e) 2.1M H_3PO_4 anodised and (c and f) 0.5M H_2SO_4 anodised, ion implanted at low and high Ag^+ dosages.

It was observed in the images in Figure 102 and indicated by red-dotted lines that the pores close to the surface had become flattened. This flattening was due to the Ag ion implantation, showing that the oxide layer had been slightly compressed during this process. Since the anodic oxides became golden after silver ion implantation, if Table 5 was used to predict the oxide layer thickness from colour the expected oxide layer thickness result would have been *ca.* 10 - 25nm. However, the anodic oxide layers shown in Figure 102 had thicknesses of *ca.* 200nm. In addition, the thicknesses of the oxide layers were relatively unchanged as compared to those in Figure 61 and Table 20 (the thicknesses before ion implantation). Thus, the only viable explanation was that the presence of the Ag was influencing the refraction of light within the oxide and light reflected off the polished surfaces. Thus, the reason for XRD analysis in Section 5.3.4 lacking in data was not in fact thickness-related, but solely attributable to the amorphous nature of these oxide layers post-ion implantation.

The HR-TEM imaging of the atomic planes, indicated by the blue lines in Figure 103 below, confirmed that the AgNPs were crystalline. It is known that the atomic radius of a silver atom is 144.5 pm. An estimate of the predicted Ag-Ag bond would be twice the Ag atomic radius, which would be 289 pm. Upon measurement of the bond length using ImageJ (the image analysis software used), it was found that the average experimental Ag-Ag bond length was 291.5 pm, which was within acceptable limits to confirm that the observed NPs within the oxide layer discussed in this section were indeed AgNPs.

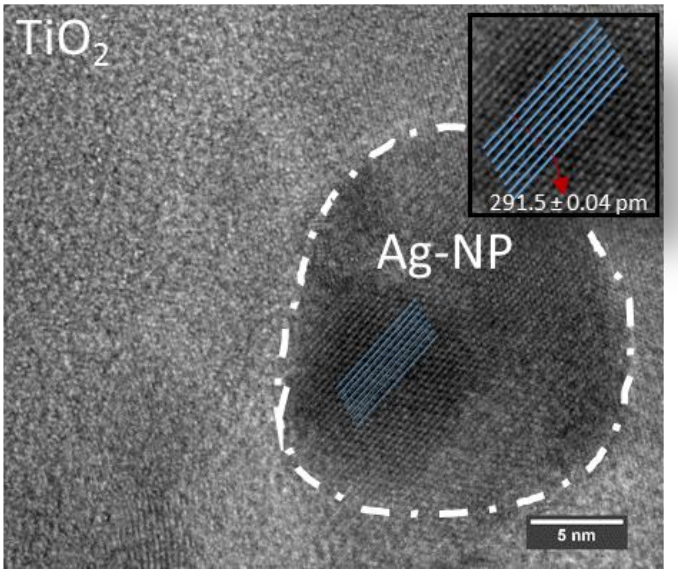

Figure 103 : HR-TEM of oxide after implantation.

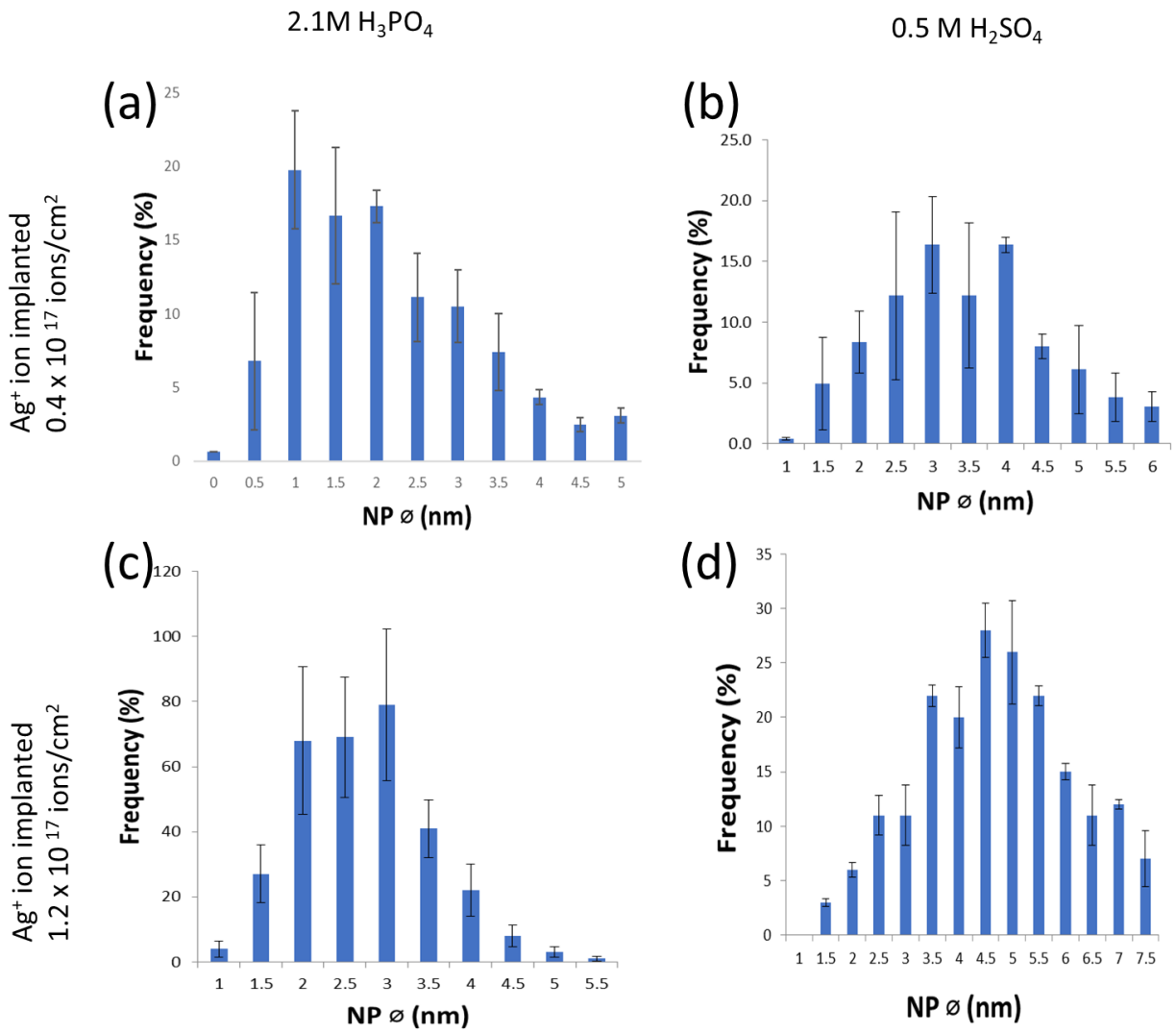

Figure 104 : Ag NP distribution of (a and c) 2.1M H_3PO_4 anodised and (b and d) 0.5M H_2SO_4 anodised samples, ion implanted at low and high Ag^+ dosages.

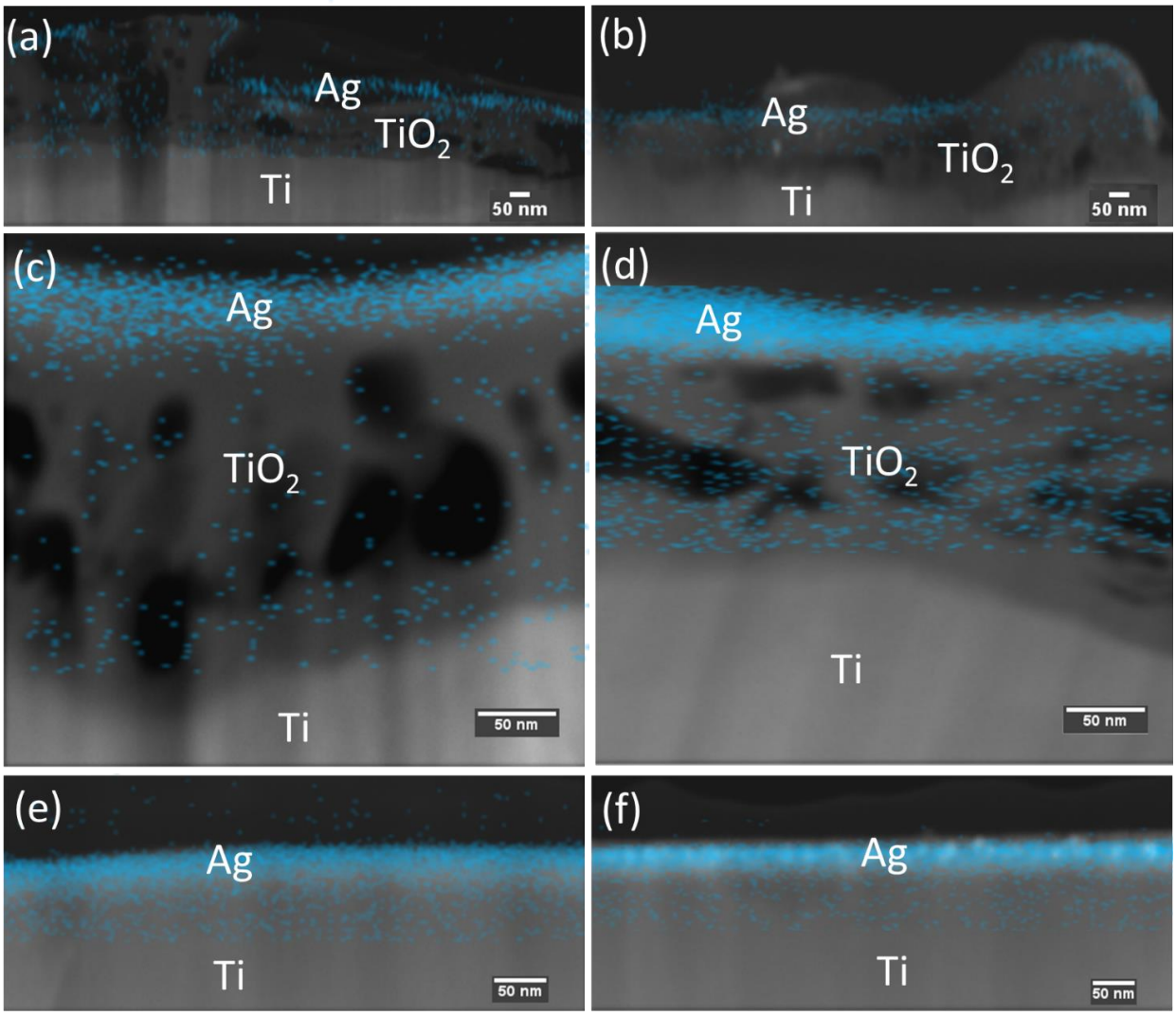

Figure 105 : Bright-Field TEM : EDS Mapping of (a) anodised 2.1M H_3PO_4 and ion implanted at 0.4 x 10^{17} ions/cm^2, (b) anodised 2.1M H_3PO_4 and ion implanted at 1.2 x 10^{17} ions/cm^2, (c) anodised 0.5M H_3PO_4 and ion implanted at 0.4 x 10^{17} ions/cm^2, (d) anodised 0.5M H_3PO_4 and ion implanted at 1.2 x 10^{17} ions/cm^2, (e) polished and ion implanted at 0.4 x 10^{17} ions/cm^2 and (f) polished and ion implanted at 1.2 x 10^{17} ions/cm^2.

The EDS mapping data presented in Figure 105 above further qualitatively confirmed the presence of silver within the first 50nm of all the investigated polished Ti-6Al-4V surfaces and anodic oxide surfaces. Since the silver was detected in the same region as the NPs observed in the titanium oxide layers shown in Figure 102 (b),(c),(e) and (f), it could further be confirmed that the observed NPs were indeed AgNPs.

5.3.6 *Summary Discussion of Silver ion Implanted Surfaces*

A colour change in the surfaces was observed in both polished and anodised Ti-6Al-4V samples. Ti-6Al-4V samples that had been anodised in the 2.1M H_3PO_4 electrolyte changed from lilac to gold and Ti-6Al-4V samples that had been anodised in the 0.5M H_2SO_4 electrolyte changed from green to gold after Ag^+ implantation. Furthermore, the surfaces of the Ti-6Al-4V samples that had first been polished and then ion implanted changed from a metallic grey to a light yellow/golden colour.

Initially, it appeared that the colour changes observed on the anodised sample surfaces after the Ag ion implantation process were due to the erosion of the surface of the titanium oxide layers to *ca.* 10 - 25nm in thickness from their original *ca.* 200 - 250nm thickness. The gold colour supported this supposition. In the case of the polished Ti-6Al-4V samples, it appeared that the colour change was due to the formation of a thin oxide layer (a thickness of *ca.* 10 - 25nm), owing to the heat generated by the ion implantation process. However, upon the cross-sectioning of the TiO_2 surfaces, it was found that the oxide layer thickness had not significantly changed. Furthermore, the cross-sectioning of the Ag ion implanted polished Ti-6Al-4V samples showed no visible oxide growth. Therefore, the colour changes observed in the above samples could not be attributed to either the erosion or the growth of the oxide layer thicknesses.

Within the surface of the oxide layers of the anodised samples, NPs were present. These NPs were confirmed to be AgNPs via EDS, HR-TEM and RBS. Because the colour changes of the anodic oxide layers were not the consequence of oxide layer erosion by the ion beam (See above), it can be concluded that the AgNPs had interfered with the light refraction within the titanium oxide layer and this had resulted in the visually-observed colour change to gold. In the case of the polished Ti-6Al-4V samples that had been ion implanted, the reason for the colour change was more difficult to determine. Since the colour change was very slight, this could have been due to a thin oxide layer formation on the surface containing a small quantity of silver, but this was not observed in the cross-sectional TEM analysis. Alternatively, the colour change might have been attributable to the presence of ionic silver in the first 50nm of the surface. Further research is required to clarify this point.

It was observed that the average diameters of the AgNPs within the surfaces of the anodic oxide layers, generated using both the 2.1M H_3PO_4 and 0.5M H_2SO_4 electrolytes, increased with the higher Ag ion dosage after Ag ion implantation. This was due to the Ag ion implantation dosage being high enough (1.2×10^{17} ions/cm^2) to induce AgNP growth (See the "growth region" in Figure 23). The high dosage led to a greater driving-force for AgNP growth, as opposed to the application of the low dosage (0.4×10^{17} ions/cm^2), which would have had a significantly lower driving force, leading to smaller AgNP diameters. Therefore, it can be concluded that the higher the dosage of Ag ions in the ion implantation process, the greater the average diameter of the AgNPs.

It was also observed that the Ag ion implantation beam had preferentially eroded the areas of high free surface energy on the anodic titanium oxide surfaces (at the high points shown in Figure 95) and on the grain boundaries on the polished Ti-6Al-4V surfaces (See Figure 93). Therefore, two conclusions can be drawn: firstly, the erosion of the anodic titanium oxide surfaces, generated using the 2.1M H_3PO_4 and 0.5M H_2SO_4 electrolytes respectively, led to decreases in R_a, from 30.9nm to 9.0nm and from 31.2nm to 8.0nm respectively, when exposed to the lower Ag ion dose. In contrast, no further reduction in R_a was observed when the anodic titanium oxide surfaces were exposed to the higher Ag ion dose. Secondly, the erosion of the grain boundaries on the polished Ti-6Al-4V surfaces led to an increase in R_a from 13.1nm to 14.3nm when they were exposed to the lower Ag ion dose. However, a

marked increase in R_a, from 14.3nm to 18.9nm, was observed when the grain boundaries on the polished Ti-6Al-4V surfaces were exposed to the higher dose.

RBS analysis of the titanium oxide layers showed that the at% of Ag stored within the layers for samples prepared with the two different electrolytes appeared to be constant, irrespective of the Ag ion implantation dosage. This was because Ag ion implantation into the TiO_2 crystal lattice led to the stable formation of Ag-Ag bonds, *i.e.* AgNPs. Furthermore, the TiO_2 crystal lattice was supersaturated with Ag ions at the low ion dosage and any further increase in the ion dosage had no measureable effect. In addition, the SRIM simulation confirmed that the formation of the AgNPs within the anodic oxide layers during ion implantation could also be a factor in the prevention of further Ag ions penetrating into the anodic oxide layer surfaces, *i.e*, the formed AgNPs would act as physical barriers to further implantation of silver.

The titanium oxide layers produced via the 0.5M H_2SO_4 electrolyte, which were primarily anatase prior to amorphisation by the Ag ion implantation process, at both the high and low Ag ion dose had a higher at% Ag (*ca*. 16 at%) after implantation, relative to the titanium oxide layer generated using the 2.1M H_3PO_4 electrolyte, which was primarily rutile in crystal structure prior to amorphisation by the Ag ion implantation process and, at both the high and low Ag ion dose, had a lower at% Ag (from 13.9 – 14.7 at%). Thus, electrolyte selection was an important parameter with regard to the Ag ion implantation of the titanium oxide layers in order to optimise the amount of stored Ag,

The polished Ti-6Al-4V samples had an increase from 16.5 to 40.6 at % Ag stored within their surfaces as the Ag ion implantation dosage was increased from low to high. This indicated that the Ti-6Al-4V lattice had a significantly greater capability to store silver, relative to the titanium oxide layers discussed above. Furthermore, the lack of AgNPs in the cross-sectional TEM images of the polished Ti-6Al-4V samples that had been Ag ion implanted at the high dose indicated that the Ag saturation point had yet to be reached within the Ti-6Al-4V lattice. In other words, an even higher Ag ion dose could lead to a further increase in the at% Ag within the Ti-6Al-4V lattice if the supersaturation point had not been reached. (This warrants further research.)

At the lower Ag ion implantation dose, the titanium oxide layers and the polished Ti-6Al-4V stored Ag in similar amounts (*ca*. 16 at%). However, at the higher Ag ion implantation dose, the Ti-6Al-4V lattice stored 2.4 times more Ag, relative to the titanium oxide layers. The reason for the higher Ag storage capacity of the polished Ti-6Al-4V samples, relative to that of the titanium oxide layers, was attributed to the intermetallic bonding that had occurred in the Ti-6Al-4V lattice having a greater capability (relative to the covalently bonded TiO_2 lattice) to accommodate the extra electrons brought into the lattice by the Ag ions. Furthermore, because the supersaturation point of the polished Ti-6Al-4V lattice was higher than that of the titanium oxide lattice, there was no AgNP formation in the polished Ti-6Al-4V surfaces and thus less inhibition to newly implanted Ag ions during the ion implantation process.

There were two further observations that might prove to be of significance: firstly, after the Ag ion implantation, the anodic oxide layers became completely amorphous, a recognised consequence of ion implantation, which was confirmed by the HR-TEM imaging and the XRD analysis. Secondly, FIB-TEM cross-sectioning of the anodic oxide layers and of the Ti-6Al-4V surfaces revealed that both the anodic oxide layers and the Ti-6Al-4V surfaces experienced compression during the ion implantation process, but the compression manifested differently: The Ti-6Al-4V surfaces showed a clear deformation band, whereas in the anodic oxide layers the compression took the form of a flattening of the pores near to the surface.

The data collected in this section primarily built upon the study by Y.Z. Wan *et al*. [99] . It provided a reason for the improvement of wear resistance via the cross-sectional TEM results. It also extended this study to the ion implantation of anodic oxides, which had not been reported elsewhere.

6. Silver Ion Integrated Surfaces and Kinetics Discussion

6.1 Silver Ion Release Curves for the Anodised - Ag Ion Exchanged Samples

The experimental setup to determine silver ion release in this research involved the release of ionic silver under static conditions where there was sufficient time for the surfaces to continually release and re-absorb the silver in the SBF solution. Aliquots of solution were taken at 24, 72 and 336 hours. Owing to the experimental set-up, it was difficult to compare the silver release data points obtained during the silver release tests in the in-between stages, *i.e.* at 48h, at 72h and at 168h. Additionally, there was the possibility that Ag ions could agglomerate to form AgNPs during the Ag ion release tests and these AgNPs would not be detectable via ICP-MS. Therefore, it was only of value to consider the initial release rate and the final amount of silver released (in ppb), as well as the Ag release curves as a whole, *i.e.* where the curves were lying relative to one another.

Comparing the initial Ag ion release rates of the samples anodised in the 2.1M H_3PO_4 electrolyte (shown in Table 24), when three $AgNO_3$ concentrations were used (*i.e.* 0.05M, 0.5M and 5M) during the Ag ion exchange step, it was observed that, as the $AgNO_3$ concentration was increased from 0.05M to 5.0M, so did the initial Ag^+ release rates increase, from 5.3 ppb/h to 11.4 ppb/h. However, there appeared to be diminishing returns in the initial Ag ion release rates when the $AgNO_3$ concentration was increased, firstly, from 0.05M to 0.5M (showing a 52.8% increase) and, secondly, from 0.5M to 5M (showing a smaller increase of 40.7%).

The samples produced via the Agluna method, where 0.1M $AgNO_3$ was the silver ion exchange solution, exhibited an initial Ag^+ release rate of 5.6 ppb/h (See Table 24). Since this release rate was close in numerical value to that of the samples that had been anodised in the 2.1M H_3PO_4 electrolyte, followed by Ag ion exchange in a 0.1M $AgNO_3$ solution (5.9 ppb/h), it could be concluded that the additional step employed during the Agluna method (20V for 20 minutes) did not offer any advantage in terms of Ag^+ release over the conventional anodising procedure. Given that in Section 5 it was found that the crystal structure surface and sub-surface morphologies of the samples anodised in the 2.1M H_3PO_4 electrolyte were similar to samples produced by the Agluna method, this result was as expected.

Table 24 : 24h silver release rate for samples anodised in various conditions and Ag ion exchanged in different $AgNO_3$ concentrations. 5 replicates per condition.

Anodising Conditions	**Anodised in 2.1M H_3PO_4 at 100V**				**Anodised in 0.5M H_2SO_4 at 100V**				**Agluna method**
AgNO3 Conc. (M)	0.05	0.1	0.5	5.0	0.05	0.1	0.5	5.0	0.1
Initial Ag+ release rate after 24h(ppb/h)	5.3	5.9	8.1	11.4	7.7	7.8	7.3	4.37	5.6

The trend in the RBS data for the Ti-6Al-4V samples that had been anodised in the 2.1M H_3PO_4 electrolyte and then Ag^+ exchanged (as shown in Section 5.1.4) correlated with the increasing overall Ag^+ release of 150 ppb to 350 ppb {as shown in Figure 106 (a) and (c)} and the increasing initial release rate trend of 5.3 ppb/h to 11.4 ppb/h (as shown in Table 24). Thus, it can be concluded that the initial Ag^+ release rate, the overall Ag^+ release and the at% of stored Ag (via RBS, from 0.9 at% to 5 at%) all increased when the $AgNO_3$ concentration was increased from 0.05M to 5.0M.

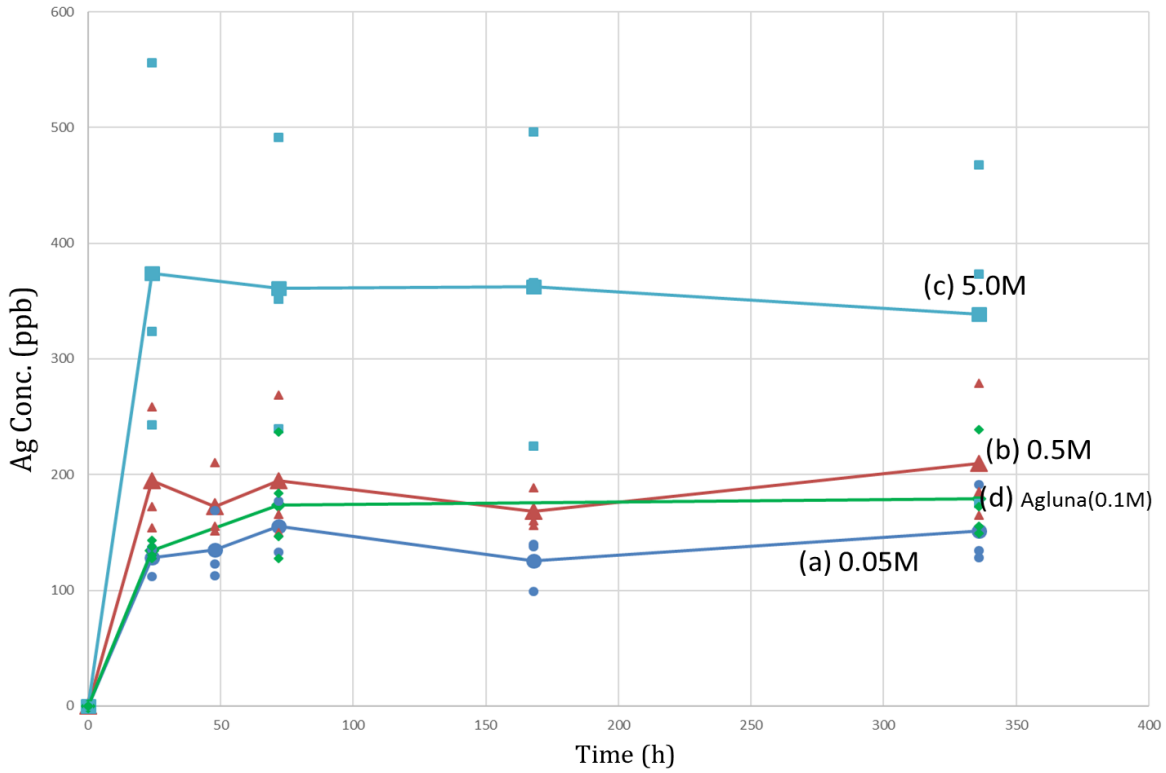

Figure 106 : Average Ag^+ release profile for samples anodised using 2.1M H_3PO_4 @ 100 V followed by ion exchange in a concentration of (a) 0.05M, (b) 0.5M, (c) Agluna, (0.1M) and (d) 5.0M $AgNO_3$.

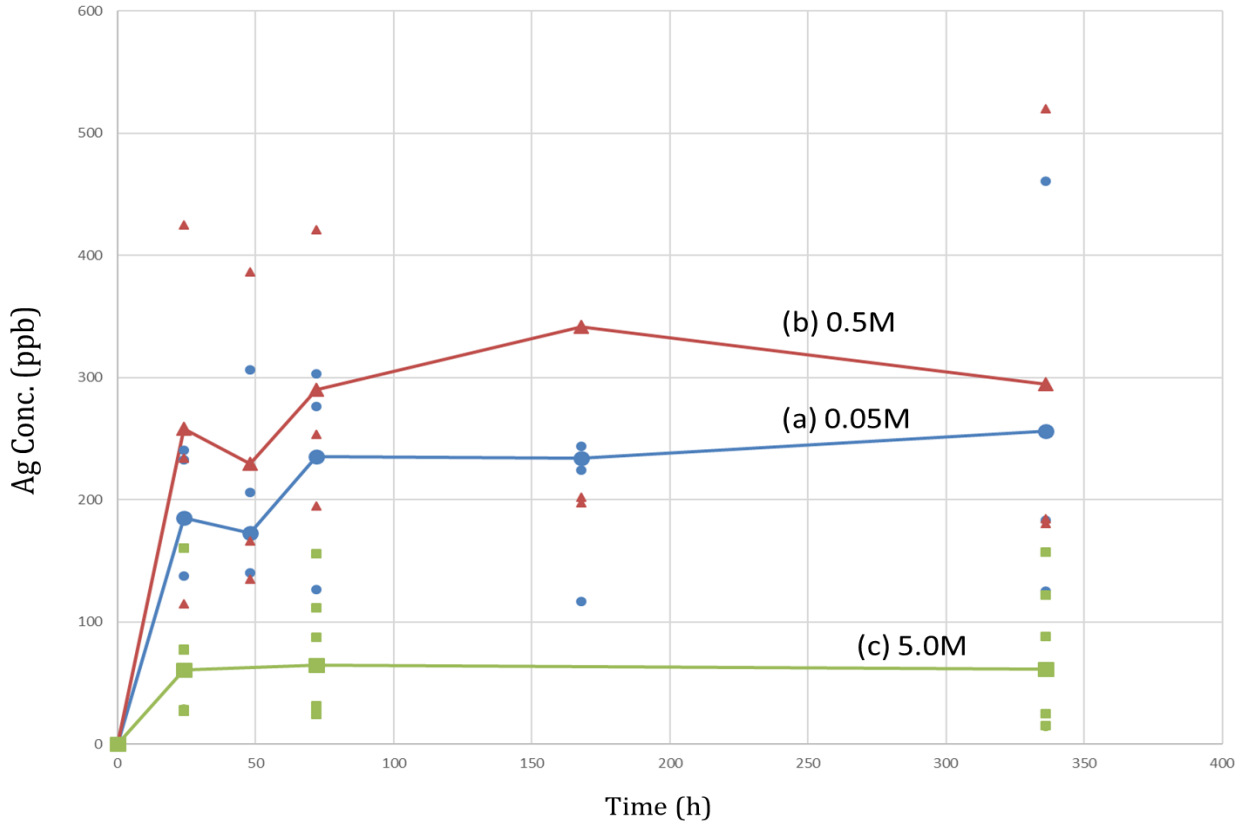

Figure 107 : Average Ag^+ rate profile for samples anodised using 0.5M H_2SO_4 @ 100 V followed by ion exchange in a concentration of (a) 0.05M, (b) 0.5M and (c) 5.0M $AgNO_3$.

It was also noted that after approximately 72 hours there was a plateauing of the Ag^+ release rate in all the samples studied. This is shown logarithmically in Figure 110, in the second row of columns, (i) to (iii). This plateauing could have been the consequence of the static conditions of the Ag^+ release test, because under static conditions there would be a local Ag^+ concentration build-up at the surface of the tested samples, which would in turn cause a localised equilibrium that would result in the stagnation of the Ag^+ release over long periods of time *i.e.* a local solubility limit may have been reached near the surface due to the static release conditions.

When comparing the initial Ag^+ release rates of the samples that had been anodised in the 0.5M H_2SO_4 electrolyte (as shown in Table 24), it was found that there was no significant difference in the initial Ag^+ release rates when the $AgNO_3$ concentration was increased from 0.05M to 0.5M, with the corresponding Ag^+ release rates of 7.7 ppb/h and 7.3 ppb/h respectively. An unexpected result was that, when the $AgNO_3$ ion exchange solution concentration was further increased to 5.0M {See Figure 107 (c)}, the initial Ag^+ release rate was found to be significantly lower (at 4.37 ppb/h) than that of the previously-mentioned samples. This is shown in Table 24. This result was consistent in all five repeats of the testing. The highest obtained initial Ag^+ release rate (for the 5M $AgNO_3$ ion exchanged samples) was lower than the results obtained when the $AgNO_3$ ion exchange solution concentration was 0.05M {See the data points of Figure 107 (a)}.

There are two possible explanations for this apparent anomaly:

Regarding the first explanation, Figure 108 illustrates the diffusion gradients that may form during the Ag^+ exchange step after anodisation. When the anodised sample is placed in a solution containing a low Ag^+ concentration (See "Low Ag Conc." in Figure 108), the process is mostly diffusion-driven, *i.e.* the rate of diffusion of the Ag atoms on the surface into the TiO_2 lattice is faster or at the same rate as the rate at which Ag atoms in the $AgNO_3$ solution can diffuse to the surface. However, if the sample is placed in a highly concentrated Ag^+ solution (See "High Ag Conc." in Figure 108), the rate of Ag atom diffusion from the surface into the TiO_2 lattice remains the same but, in this case, the surface is oversaturated with Ag ions, creating a bottleneck effect, *i.e* the silver atoms that are one atomic spacing away from the surface must "wait for" the silver atoms on the surface to diffuse into the TiO_2 lattice before they themselves can diffuse, first on to the surface and then into the TiO_2 lattice. This bottleneck becomes even greater over time because as the positively-charged Ag ions build up near the surface they repel other nearby Ag ions away from the surface, causing a lower-than-expected Ag^+ absorption rate and consequently a lower-than-expected Ag+ release.

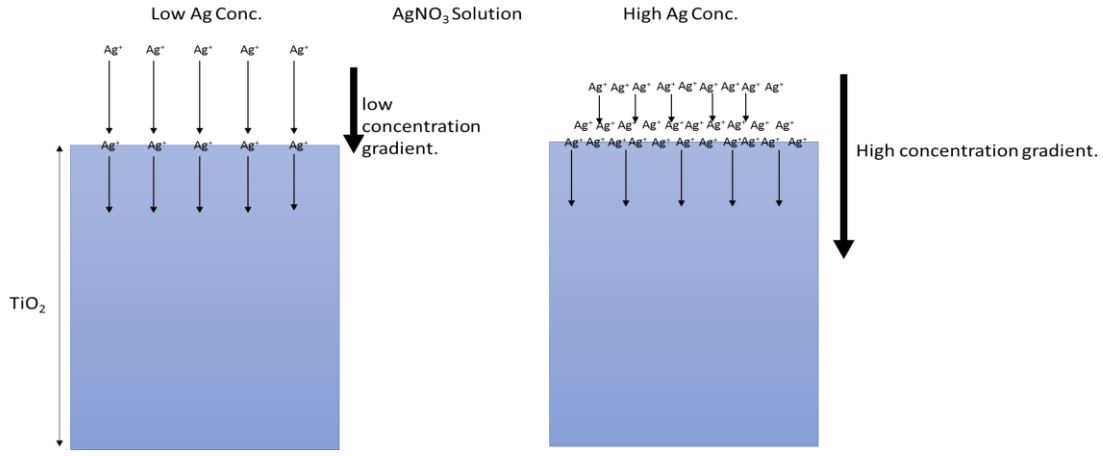

Figure 108 : Illustration of the diffusion gradient at high and low Ag^+ concentrations.

However, according to the hypothesis above, this effect should be present in both the oxide layers formed via either the 0.5M H_2SO_4 or 2.1M H_3PO_4 electrolytes and this is not the case. Therefore, the crystal structure of the respective oxide layers should also be considered as a factor.

This leads to the second possible explanation. As revealed in previous XRD data, Ti-6Al-4V anodised in the 0.5M H_2SO_4 and 2.1M H_3PO_4 electrolytes produced TiO_2 layers with anatase and rutile crystal structures respectively. Anatase is a metastable phase, while rutile is a stable phase and it is generally accepted that anatase has, relative to rutile, a higher activity with regard to photocatalysis, oxidative power and general reactivity. With reference to the illustration of the high Ag^+ concentration shown in Figure 108, it is likely that this high concentration of Ag ions is causing bottlenecking that inhibits the diffusion of Ag near the surface of the anatase TiO_2 layer. This bottlenecking creates time for the anatase TiO_2 either to reduce the Ag ions at the surface into $Ag_{(s)}$ or to oxidise the Ag ions into AgO. If these reactions occur at the surface, the silver will be in solid form and thus will be unable to penetrate the TiO_2 oxide lattice. In addition, if these silver solids build up on the surface of the anatase TiO_2 layer, they would act to reduce the concentration gradient of Ag ions, thereby further inhibiting the penetration of these Ag ions into the oxide lattice. (Owing to the stability of the rutile phase, the above reactions may not occur at a rate that prevents Ag^+ absorption.) Thus, in the case of the anatase TiO_2 layer, the lower-than-expected Ag^+ release observed in the Ti-6Al-4V samples that had been anodised in the 0.5M H_2SO_4 electrolyte and Ag ion exchanged in 5.0M $AgNO_3$ {see Figure 107 (c)} can be explained.

When comparing the Ti-6Al-4V samples anodised in the 0.5M H_2SO_4 electrolyte and ion exchanged in the 0.1M $AgNO_3$ solution to those anodised in the 2.1M H_3PO_4 electrolyte and those anodised via the Agluna method (where all three sample groups were ion exchanged in the same $AgNO_3$ solution concentration of 0.1M), it was observed that the initial Ag^+ release for the anodic oxide layer formed via the 0.5M H_2SO_4 electrolyte was significantly higher at 7.8 ppb/h, relative to the 5.6 ppb/h and 5.9ppb/h Ag^+ release rates observed in the 2.1M H_3PO_4 electrolyte samples and Agluna method samples respectively. This showed that using the 0.5M H_2SO_4 electrolyte resulted in an improved initial rate of Ag^+ release, relative to the rate of Ag^+ release in the latter two cases.

When comparing the initial Ag^+ release rates between samples that had been anodised in the 0.5M H_2SO_4 and 2.1M H_3PO_4 electrolytes and Ag ion exchanged in a 0.5M $AgNO_3$ solution, it was found that the Ag^+ release rates were similar, *i.e.* at 7.3 ppb/h and 8.1 ppb/h respectively.

It was only at $AgNO_3$ ion exchange concentrations higher than 0.5M, that the crystal structure differences between the oxide layers, produced via anodising in the 0.5M H_2SO_4 electrolye (anatase) and the 2.1M H_3PO_4 electrolyte (rutile), began to play a role in the Ag^+ uptake and release rates, as described earlier in this section. The less reactive oxide (rutile) released higher amounts of Ag at > 0.5M $AgNO_3$ ion exchange concentrations relative to those released by the anatase oxide at the same concentrations. This trend comparison is shown graphically in Figure 109.

Comparing the overall release curves of the samples anodised in the 0.5M H_2SO_4 and 2.1M H_3PO_4 electrolytes , shown in Figure 110, it was found that at the 0.05M and 0.5M $AgNO_3$ concentrations {shown in Figure 110 (i) and (ii)} the anodic oxides formed using the 0.5M H_2SO_4 electrolyte had final Ag^+ releases of 251ppb and 295ppb respectively, compared to those samples anodised in the 2.1M H_3PO_4 electrolyte, which had final Ag^+ releases of 150 ppb and 210 ppb respectively, as seen in Figure 110 (i) and (ii). The reason for the higher Ag^+ release where samples were anodised in the 0.5M H_2SO_4 electrolyte was that the anatase crystal structure produced via the 0.5M H_2SO_4 electrolyte had a greater propensity to release oxygen, which could, in turn, facilitate the oxidative dissolution of the

AgNPs present within the surfaces of the anatase TiO_2 layers. At the 5.0M $AgNO_3$ ion exchange concentration, as seen in Figure 110 (iii), the 2.1M H_3PO_4 anodised samples (rutile) had a significantly high final Ag^+ release of 349 ppb. This was in contrast to the Ag^+ release of the samples anodised in the 0.5M H_2SO_4 electrolyte (anatase), which was measured at 60 ppb. This contrast in Ag^+ release can be attributed to the higher reactivity of the anatase crystal structure, which, as previously described, results in a lower Ag^+ uptake, with a subsequently lower Ag^+ release.

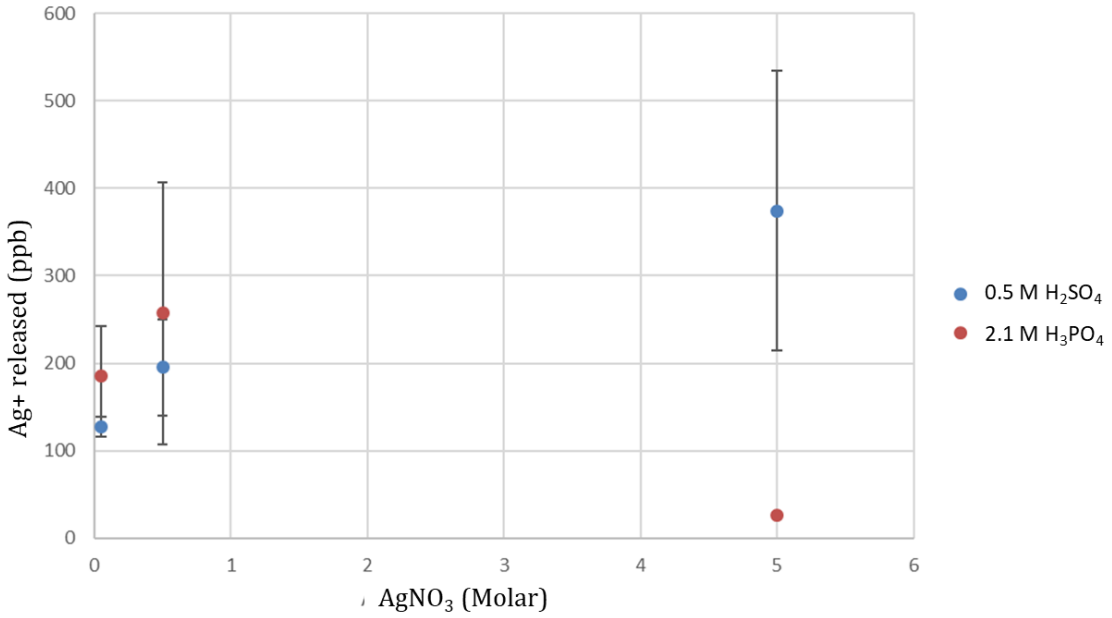

Figure 109 : Silver release after 24hrs @ 37°C for samples anodised in 2.1M H_3PO_4 and 0.5M H_2SO_4 at 100V.

When the Ag^+ release rates were compared logarithmically in Figure 110 (bottom row of graphs in Figure 110) it was found that the Ag^+ release rates for the samples anodised in the 0.5M H_2SO_4 electrolyte were slightly higher than those of the samples anodised in the 2.1M H_3PO_4 electrolyte when the $AgNO_3$ concentration used was 0.05M and 0.5M respectively {See second row Figure 110 (i) and (ii)}. Samples anodised in the 0.5M H_2SO_4 electrolyte, followed by Ag^+ exchange in 5.0M $AgNO_3$, showed a slower initial release rate relative to its 2.1M H_3PO_4 counterpart {See the second row of Figure 110 (iii)}.

The trend of the decreasing at% Ag, described in the RBS data in Section 5.1.4, for the samples that had been anodised in the 0.5M H_2SO_4 electrolyte correlated with the Ag^+ release trends observed in Figure 110, *i.e.* at the 0.05M $AgNO_3$ ion exchange concentration, where the at% Ag content {Figure 57(a)} and the Ag^+ release {Figure 110 (i)} were both high (at 1.9 at% and 250 ppb respectively), relative to those anodised in the 2.1M H_3PO_4 electrolyte (at 0.9 at% and 150 ppb respectively). For the samples anodised in the 0.5M H_2SO_4 electrolyte when the 5.0M $AgNO_3$ ion exchange solution was used, the RBS data correlated in terms of the Ag^+ release. RBS results showed a lower at% Ag of 0.8 at% (Figure 57(b)) and a lower Ag^+ release of 60 ppb (Figure 110 (iii)), relative to the higher at% Ag and Ag^+ release (5 at% and 340 ppb respectively) of the 2.1M H_3PO_4 anodised samples.

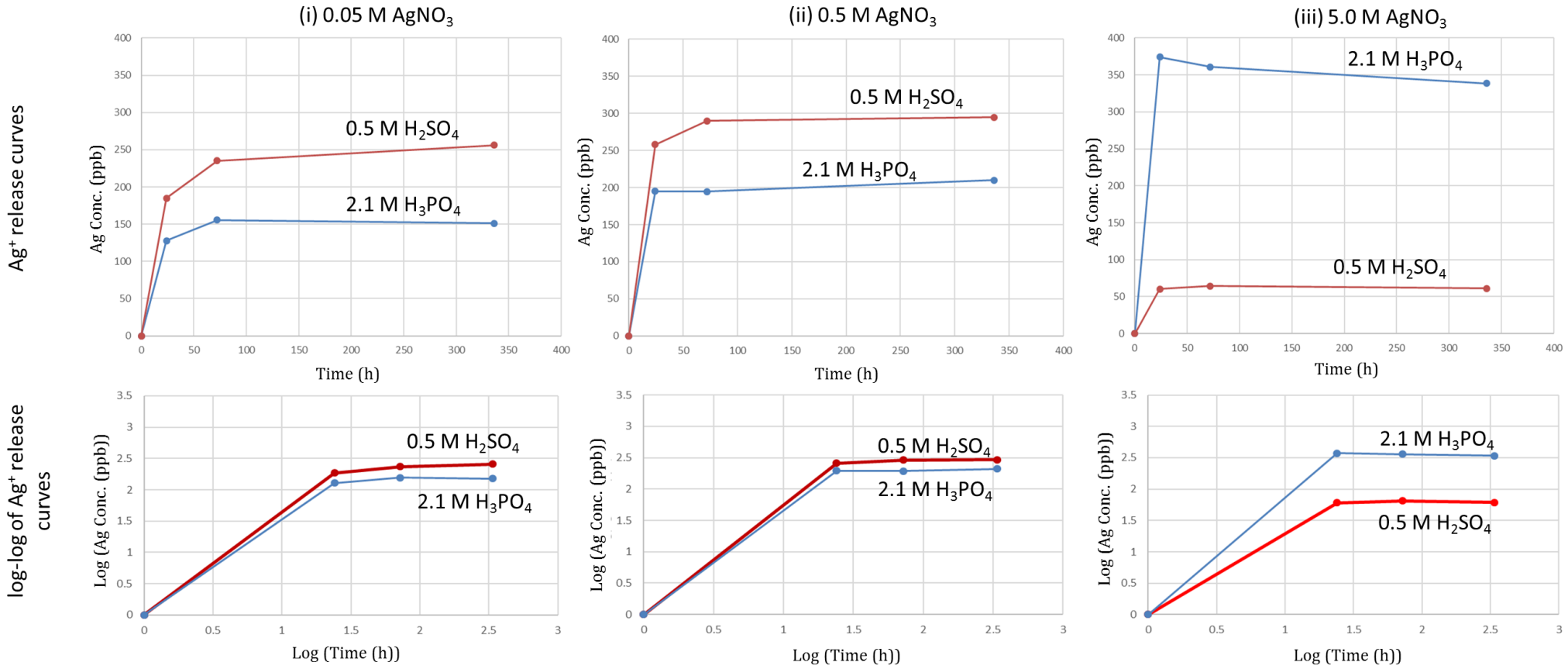

Figure 110 : Ag ion release curves for surfaces anodised in 2.1M Phosphoric acid and 0.5M Sulphuric acid at 100V anodised samples with ion exchange concentration (i) 0.05M $AgNO_3$, (ii) 0.5M $AgNO_3$ and (iii) 5.0M $AgNO_3$.

6.2 Ag-Doped Titanium oxide Particles Attached via Anodising

When comparing the initial Ag^+ release rates in Table 25 relating to the Ag-TiO_2 powders attached via anodising in the 2.1M H_3PO_4 electrolyte, it was found that the Ag^+ release rate over the first 24 hours increased incrementally from 0.29 ppb/h to 23.5 ppb/h, as the Ag concentration within the TiO_2 powders was increased from 0.48 wt% to 76.93 wt%.

Table 25 : 24h silver release rate for Titania powders doped with silver using varied concentrations of silver nitrate, followed by powder attachment via anodising in two different acid electrolytes under the same conditions. 5 replicates per condition.

Anodising conditions	Anodised in 2.1M H_3PO_4 at 100V			Anodised in 0.5M H_2SO_4 at 100V		
$AgNO_3$ Conc.	0.05M	0.5M	5 M	0.05M	0.5M	5M
Ag-TiO_2 (wt% Ag)	0.48	25.77	76.93	0.48	25.77	76.93
Initial Silver release rate(ppb/h) during the 1st 24h	0.29	1.8	23.5	2.4	16.1	30.9

When comparing the initial Ag^+ release rates in Table 25 relating to the Ag-TiO_2 powders attached via anodising in the 0.5M H_2SO_4 electrolyte against those achieved with anodising in the 2.1M H_3PO_4 electrolyte, it was found that the Ag^+ release rate over the first 24 hours for the 0.5M H_2SO_4 electrolyte demonstrated a similar trend (from 2.4 ppb/h to 16.1 ppb/h), as the Ag concentration within the TiO_2 powders was increased from 0.48 wt% to 25.77 wt%. Here, the initial Ag^+ release rate was 2.4 ppb/h for the attached 0.48wt% Ag-TiO_2 powders, which was higher than its 2.1M H_3PO_4 counterpart (0.29 ppb/h). By increasing the Ag concentration within the powders attached via anodising in the 0.5M H_2SO_4 electrolyte to 25.77 wt%, there was a significantly greater initial Ag^+ release rate, of 16.1 ppb/h, relative to the 1.79 ppb/h release rate exhibited by the same Ag-TiO_2 powders attached via the 2.1M H_3PO_4 anodising electrolyte. Furthermore, an increase in the Ag concentration in the former Ag-TiO_2 powder (*i.e.* via the 0.5M H_2SO_4 electrolyte) to 76.93 wt% Ag resulted in an increase in the Ag^+ release rate to 30.9 ppb/h, which was higher than that achieved using the same Ag-TiO_2 powders attached via anodising in the 2.1M H_3PO_4 electrolyte (*i.e.* to 23.5 ppb/h). Therefore, it could be concluded that using the the 0.5M H_2SO_4 electrolyte to attach the Ag-TiO_2 powders resulted in higher initial Ag^+ release rates for all the powder concentration conditions investigated.

The relationship between the wt% Ag in the TiO_2 powders and the corresponding Ag^+ release rate is shown graphically in Figure 111. It can be seen in Figure 111 that, for both the anodising electrolytes used, the relationships most closely followed 2nd order polynomials, with the relevant equations given on the graphs. In both cases, the fit between the experimental data and the 2nd order polynomials was satisfactory, because the R^2 values were closer to 1 than other attempted fits.

Figure 112 shows the Ag^+ release curves obtained from surfaces coated with Ag-TiO_2 via anodising in the 2.1M H_3PO_4 electrolyte. It was found that the final Ag^+ release, after 336 hours, had increased from 4 ppb to 90 ppb as the Ag concentration within the TiO_2 powder was increased from 0.48 wt% to 25.77 wt% and that there was a further increase in the Ag^+ release, to 550 ppb, when the Ag concentration was increased to 76.93 wt%. Figure 113 shows a similar trend in the Ag^+ release curves obtained from surfaces coated with Ag-TiO_2 via anodising in the 0.5M H_2SO_4 electrolyte. It was found that the final Ag^+ release, after 336 hours, had increased from 18 ppb to 256 ppb as the Ag concentration within the TiO_2 powder was increased from 0.48 wt% to 25.77 wt% and that there was a further increase in the Ag^+ release, to 600 ppb, when the Ag concentration was increased to 76.9

wt%. Therefore, it could be concluded that using the 0.5M H_2SO_4 electrolyte to attach the Ag-TiO_2 powders resulted in a higher Ag^+ release for all the powder concentration conditions investigated.

These increases in the Ag^+ release and release rates using the Ag-TiO_2 powders attached via the 0.5M H_2SO_4 electrolyte, as discussed above, could be due to the anatase phase present in the TiO_2 layer {See the XRD spectrum in Figure 78(b)}. Anatase has better oxidative properties relative to the rutile phase (present after anodising in the 2.1M H_3PO_4 electrolyte) and this would have increased the rate of oxidative dissolution of the AgNPs present within the Ag-TiO_2 powder fused surfaces. The relationship between the wt% Ag in the TiO_2 surfaces and the corresponding final Ag^+ release is shown graphically in Figure 114. The relationship closely matches the relationship in Figure 111, indicating that there is a linear relationship between the initial Ag^+ release rate and the final Ag^+ release. This relationship is shown graphically in Figure 115.

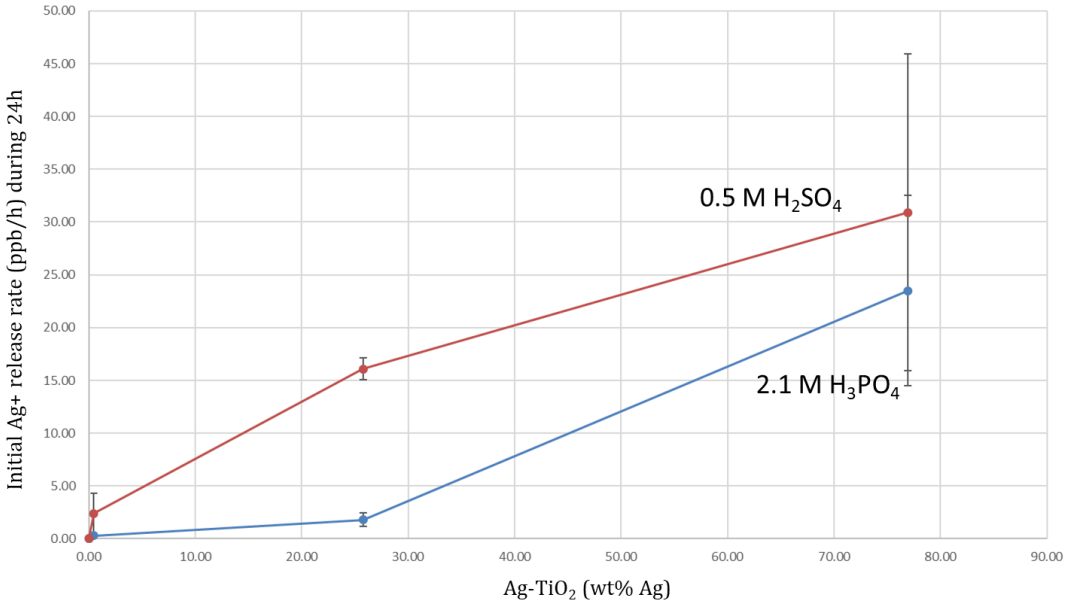

Figure 111 : Relationship between the wt% Ag in Ag-TiO_2 and the Initial Ag^+ release rate during 24 hours.

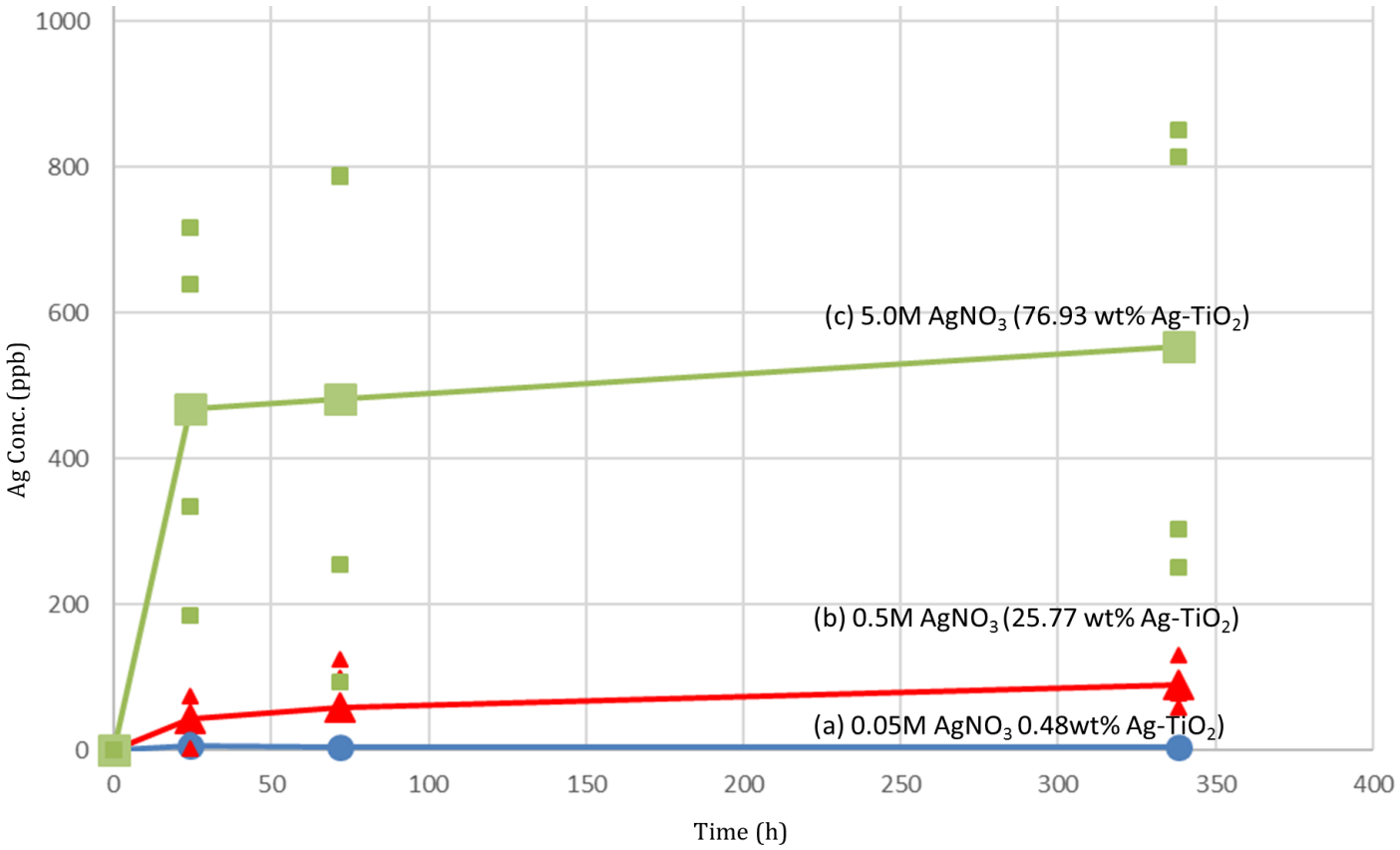

Figure 112 : Ag-doped TiO_2 powder attached via anodising in 2.1M H_3PO_4 @ 100V .

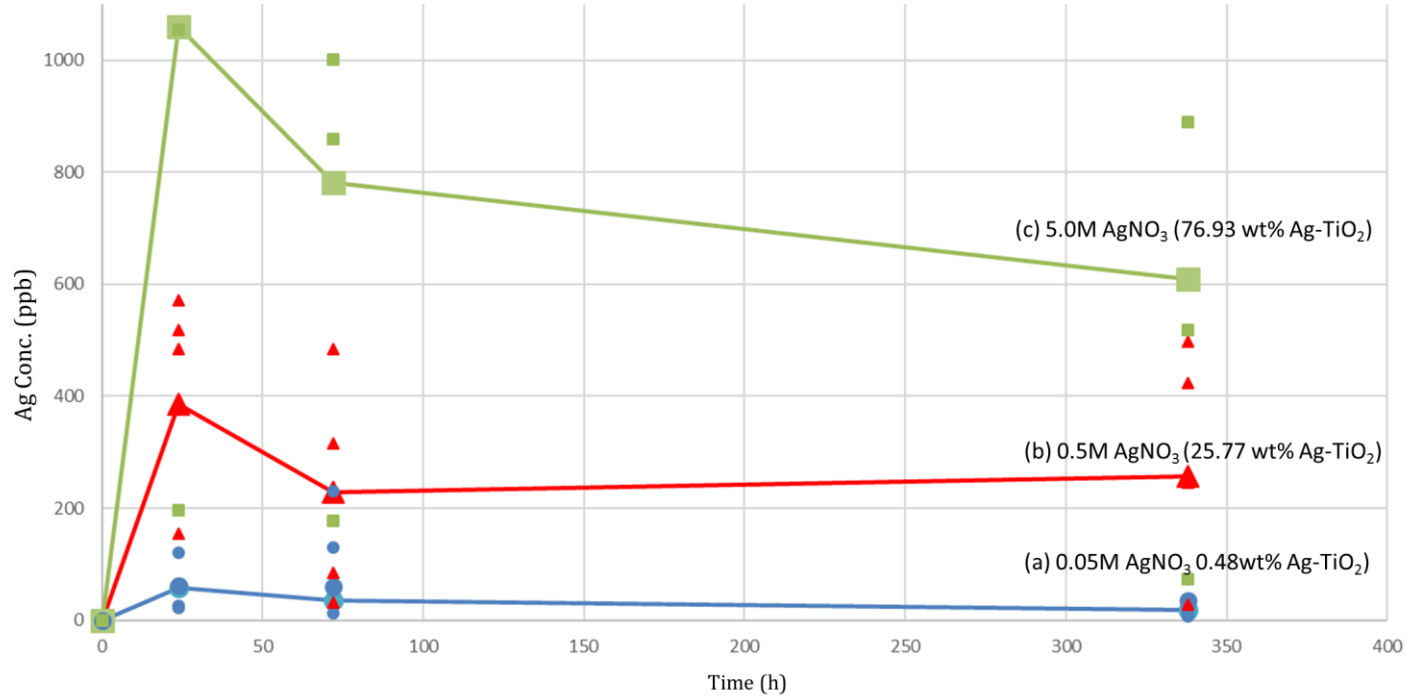

Figure 113 : Ag-doped TiO_2 powder attached via anodising in 0.5M H_2SO_4 at 100V.

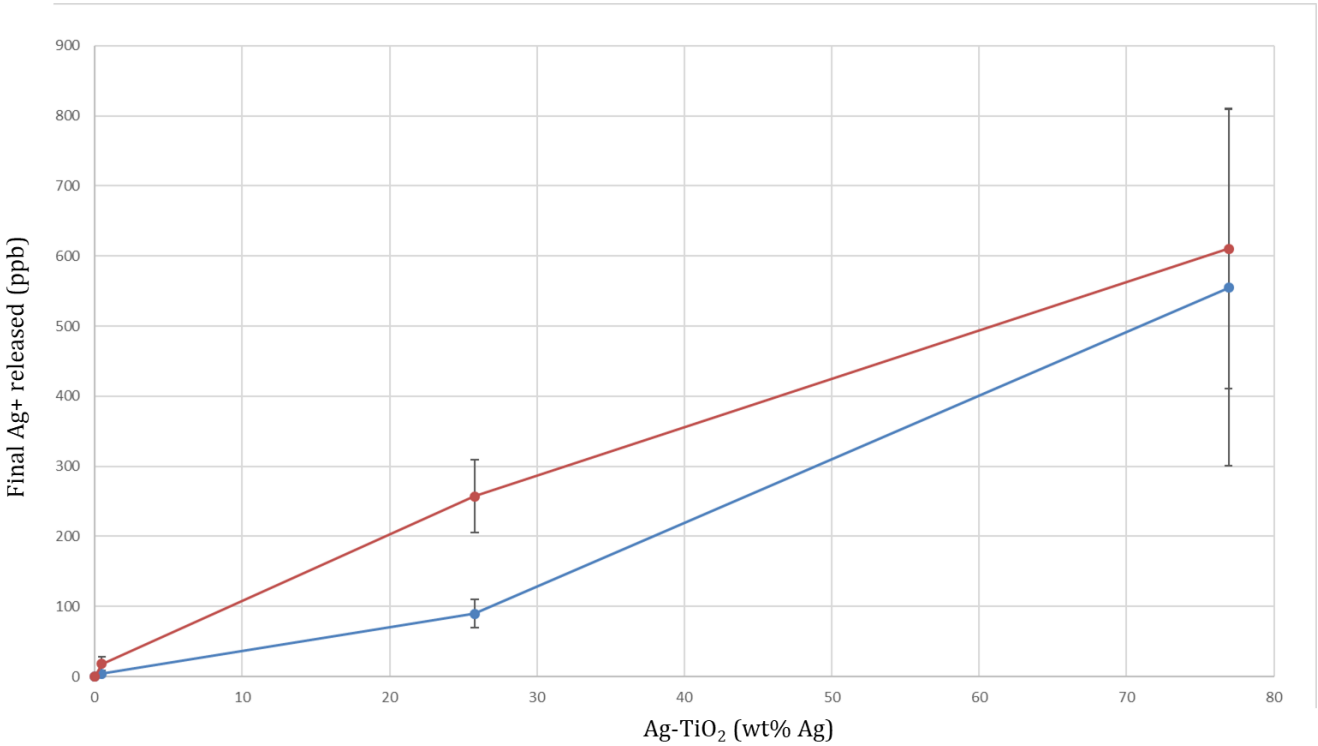

Figure 114 : Relationship between the wt% Ag in Ag-TiO2 and the Final Ag+ release.

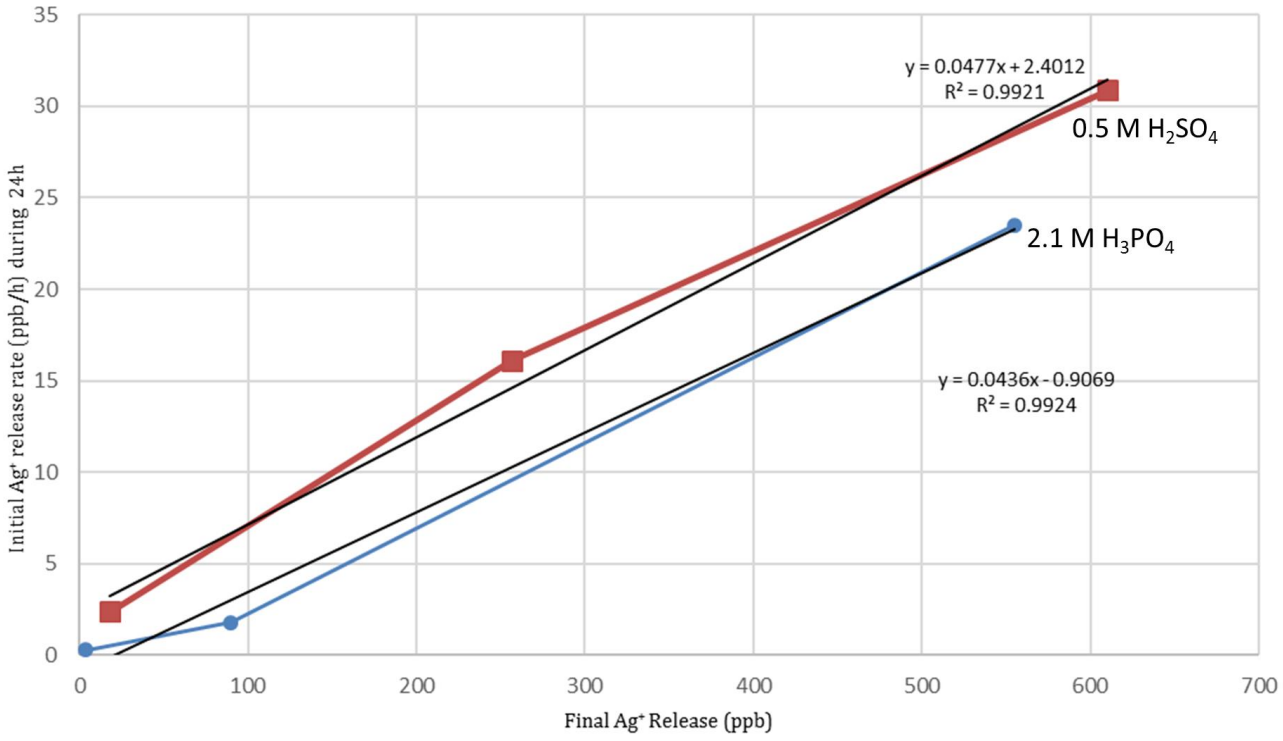

Figure 115 : Linear relationship between initial Ag^+ release rate and the final Ag^+ release.

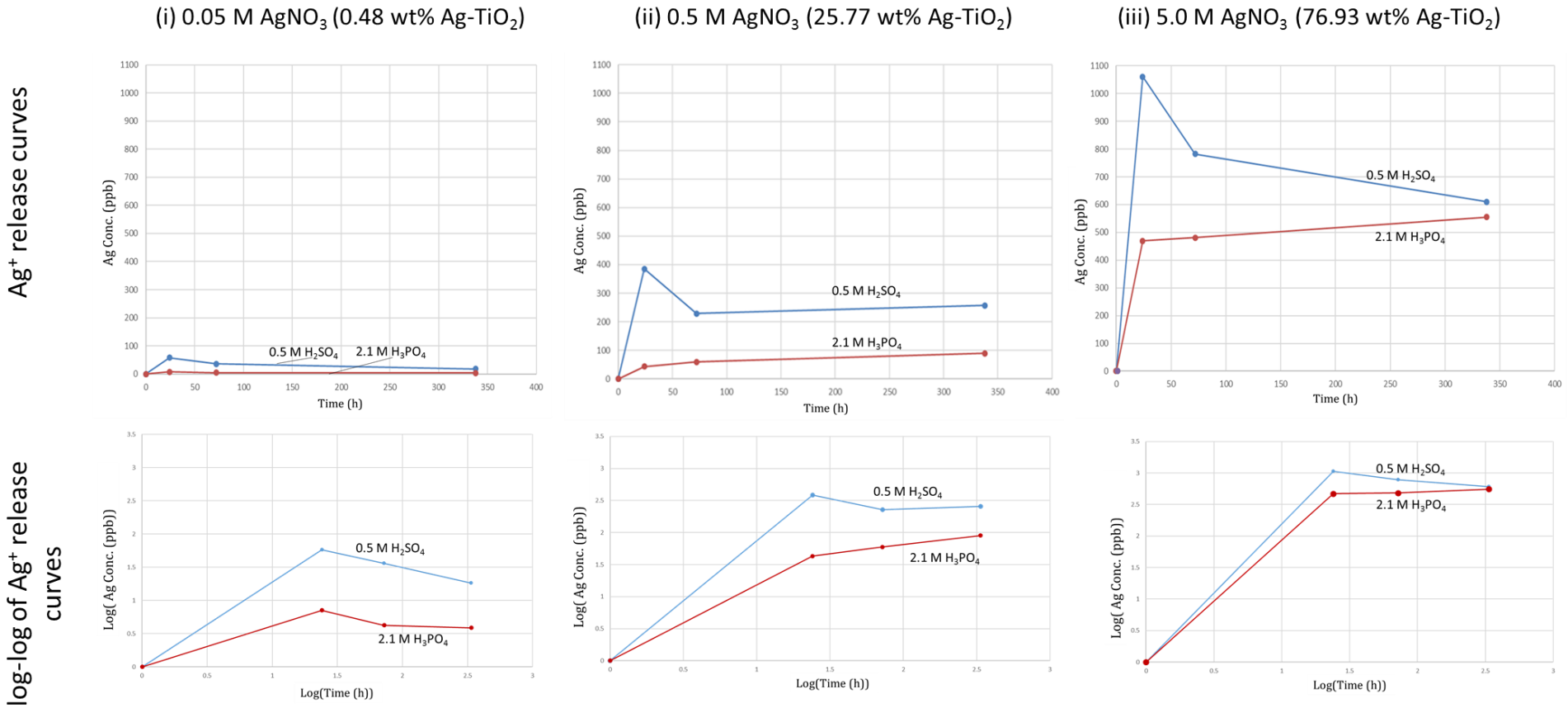

Figure 116: Ag release curves for TiO_2 synthesised in the presence of (i) 0.05M $AgNO_3$, (ii) 0.5M $AgNO_3$ and (iii) 5.0M $AgNO_3$ @ 100V 2.1M H_3PO_4 and 0.5M H_2SO_4.

As discussed previously, the Ag^+ release and release rates in Figure 116 show that, regardless of the concentration of Ag within the TiO_2 powders, those powders fused when the 0.5M H_2SO_4 electrolyte had been used, had a consistently higher Ag^+ release and Ag^+ release rate relative to those powders fused when the 2.1M H_3PO_4 electrolyte had been used. The RBS data described in Section 5.2.4 corroborated this result, *i.e* that the at% Ag detected via RBS in the surfaces coated with the 0.48 wt% Ag-TiO_2 and the 76.93 wt% Ag-TiO_2 powders and fused using the 0.5M H_2SO_4 electrolyte (0.7 at% and 4 at% respectively) was also consistently higher than the at%'s detected in the powders attached via the 2.1M H_3PO_4 electrolyte (0.6 at% and 1.3 at% respectively).

The logarithmic graphs in Figure 116 show that the TiO_2 powders fixated using the 0.5M H_2SO_4 electrolyte had consistently higher initial Ag^+ release rates relative to those attached using the 2.1M H_3PO_4 electrolyte. This trend may once again be attributed to the crystal structure of the anodic oxide formed during the fixation of the powders during anodisation. As mentioned in the previous section, anatase has high reactivity and oxidative properties. Section 3.4 in the Literature Review described the reaction mechanism that occurred between AgNPs and oxygen. Since anatase has the capability to release oxygen ions in contact with water, this speeds up the rate of oxidative dissolution of the AgNPs within the surface of the oxide film, resulting in higher Ag^+ release rates for the powders fused using the 0.5M H_2SO_4 electrolyte.

6.2.1 *Comparison of the Silver Ion Release between Ag-TiO_2 and Ag Ion Exchanged Samples*

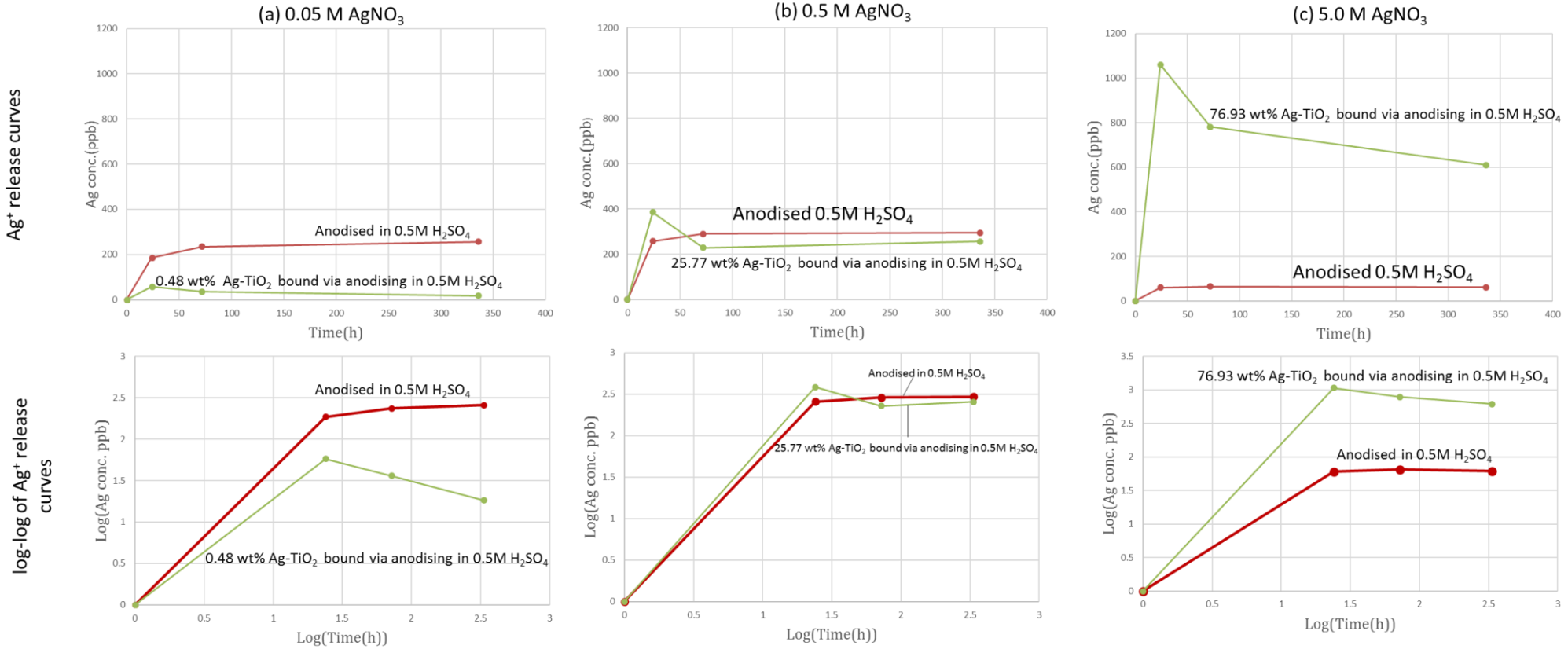

Figure 117 : Comparison between Ag^+ release of Anodised / Ion exchanged (in red) and Ag-TiO_2 surfaces (in green). Both surfaces used 0.5M H_2SO_4 as anodising electrolyte. $AgNO_3$ concentrations used during respective processes (a) 0.05M Ag, (b) 0.5M Ag and (c) 5.0M Ag.

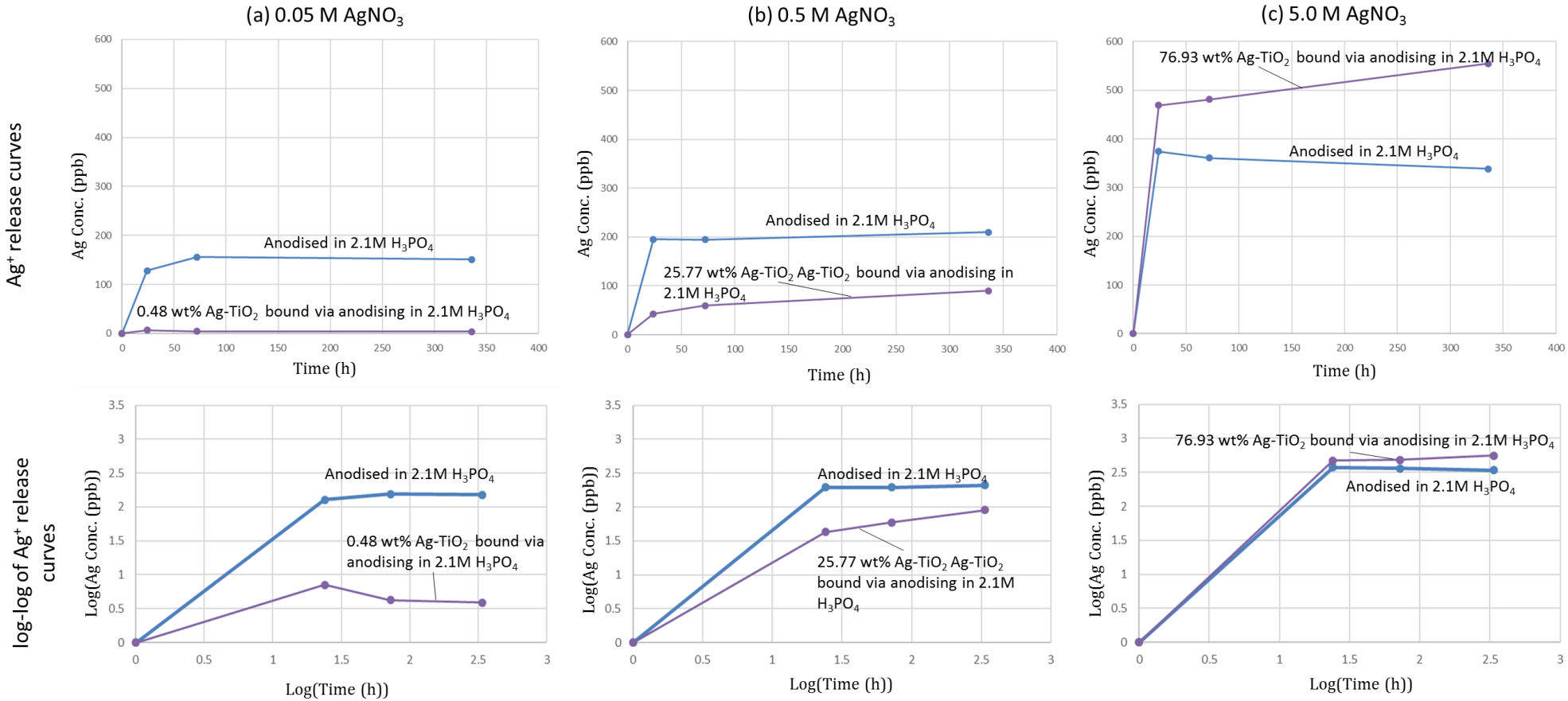

Figure 118 : Comparison between Ag^+ release of Anodised / Ion exchanged (in blue) and Ag-TiO_2 surfaces (in purple). Both surfaces used 2.1M H_3PO_4 as anodising electrolyte. $AgNO_3$ concentrations used during respective processes (a) 0.05M Ag, (b) 0.5M Ag and (c) 5.0M Ag.

Figure 117 compares the Ag^+ release curves of the 0.5M H_2SO_4 anodised and ion exchanged surfaces with the Ag-TiO_2 powder fused surfaces that had also been anodised using the 0.5M H_2SO_4 electrolyte. When using a low concentration of 0.05M $AgNO_3$ in these processes {Figure 117 (a)}, the anodised samples released larger quantities of Ag^+ in the first 24 hours, reaching a maximum concentration of *ca.* 210 ppb compared to the *ca.* 35 ppb in the case of the 0.48 wt% Ag-TiO_2 powder surfaces. The reason for the low Ag^+ release by the Ag-TiO_2 surfaces may be due to the experimental method. The synthesis of the powder took place within a 0.05M solution of $AgNO_3$ and, since the $AgNO_3$ concentration was low, there was a lower probability of Ag^+ incorporation into the TiO_2 matrix (See ICP results in Table 21), relative to when the higher $AgNO_3$ concentrations were used.

When a 0.5M $AgNO_3$ solution was used {See Figure 117 (b)}, the 0.5M H_2SO_4 anodised surfaces and the 25.77 wt% Ag-TiO_2 fused surfaces were found to have similar Ag^+ release curves, with the anodised samples achieving only a slightly higher maximum Ag^+ output of *ca.* 280 ppb, relative to the 25.77 wt% Ag-TiO_2 output of *ca.* 250 ppb. The logarithmic graph in (b) in the second row of Figure 117 also shows that the release rates were similar.

At the highest tested Ag^+ concentration of 5.0M $AgNO_3$ {See Figure 117 (c)}, the 76.93 wt% Ag-TiO_2 surfaces significantly outperformed their counterparts, *i.e.* those that had been anodised in 0.5M H_2SO_4 and ion exchanged in 5.0M $AgNO_3$. The 76.93 wt% Ag-TiO_2 fused surfaces released *ca.* 600 ppb, whereas the anodised surfaces released *ca.* 350 ppb. The reason for this difference in Ag^+ output was that there was a difference in the processes of generating the two Ag-doped surfaces discussed above. The synthesis of the Ag-TiO_2 powders was a diffusion-independent process, *i.e.* the Ag was trapped in the TiO_2 crystal structure while reacting in the 5.0M $AgNO_3$ solution. The Ag-TiO_2 powder was then fixated using the 0.5M H_2SO_4 electrolyte, which generated an anatase crystal structure. In contrast, the Ag^+ exchanged samples were first anodised, in this case in the 0.5M H_2SO_4, electrolyte, this generating an anatase crystal structure. The anodised samples were then placed in the 5.0M $AgNO_3$ solution in order for the Ag^+ exchange to occur. The Ag^+ exchange step was diffusion-dependent (and therefore time-dependent). Therefore, the anodised and Ag^+ exchanged surfaces did not have sufficient time in the 5.0M $AgNO_3$ solution to show an Ag^+ release comparable in output to the 76.93 wt% Ag-TiO_2 fused surfaces. In addition, the higher Ag^+ release exhibited by the Ag-TiO_2 fused surfaces might be due to the increased porosity of the Ag-TiO_2 layer, which resulted in a higher surface area of the AgNPs being exposed to the simulated body fluid, *i.e.* an increase in the rate of oxidative dissolution of the AgNPs.

Figure 118 compares the Ag^+ release curves of the 2.1M H_3PO_4 anodised and Ag^+ exchanged surfaces with the Ag-TiO_2 powder fused surfaces that had been anodised using the 2.1M H_3PO_4 electrolyte. When using a low concentration of 0.05M $AgNO_3$ in these processes {Figure 118 (a)}, the anodised samples released larger amounts of Ag ions in the first 24 hours, reaching a maximum concentration of *ca.* 140 ppb, compared to the *ca.* 5 ppb in the case of the 0.48 wt% Ag-TiO_2 powder fused surfaces. The reason for the low Ag^+ release by the Ag-TiO_2 fused surfaces may be due to the experimental method. The synthesis of the powder took place within a 0.05M solution of $AgNO_3$, and since the $AgNO_3$ concentration was low, there was a lower probability of Ag^+ incorporation into the TiO_2 matrix (See ICP results in Table 21), relative to when the higher $AgNO_3$ concentrations were used.

When a 0.5M $AgNO_3$ solution was used {See Figure 118 (b)}, the 2.1M H_3PO_4 anodised surfaces and the 25.77 wt% Ag-TiO_2 fused surfaces were found to have dissimilar Ag^+ release curves, with the anodised samples achieving a significantly higher maximum Ag^+ output of *ca.* 200 ppb, relative to the 25.77 wt% Ag-TiO_2 output of *ca.* 80 ppb. The logarithmic graph shown in the second row of Figure 118 (b) is in

agreement with the above observation because it shows that the Ag^+ release rate was greater for the anodised and Ag^+ exchanged surfaces relative to the 25.77 wt% Ag-TiO_2 surfaces.

At the highest tested Ag^+ concentration of 5.0M $AgNO_3$ {See Figure 118 (c)}, the 76.93 wt% Ag-TiO_2 surfaces significantly outperformed their counterparts, those that had been anodised in the 2.1M H_3PO_4 electrolyte and Ag^+ exchanged in the 5.0M $AgNO_3$ solutions. The 76.93 wt% Ag-TiO_2 fused surfaces released *ca.* 550 ppb, whereas the anodised surfaces released *ca.* 350 ppb. The reason for this difference in Ag^+ output was that there was a difference in the processes of generating the two Ag-doped surfaces discussed above. The synthesis of the Ag-TiO_2 powders was a diffusion-independent process, *i.e.* the Ag was trapped in the TiO_2 crystal structure while reacting in the 5.0M $AgNO_3$ solution. The Ag-TiO_2 powder was then fused using the 2.1M H_3PO_4 electrolyte, which generated a rutile crystal structure. In contrast, the process whereby the Ag^+ exchanged samples were first anodised, in this case in the 2.1M H_3PO_4, electrolyte, also generated a rutile crystal structure. Then the anodised samples were placed in the 5.0M $AgNO_3$ solution for Ag^+ exchange to occur. In this case, the Ag^+ exchange step was diffusion-dependent (and therefore time-dependent). Therefore, the anodised and Ag^+ exchanged surfaces did not have sufficient time in the 5.0M $AgNO_3$ solution to show a Ag^+ release comparable in output to the 76.93 wt% Ag-TiO_2 fused surfaces.

Between the $AgNO_3$ concentrations of 0.05M and 5M, the Ag^+ exchanged samples did not show incremental increases in Ag^+ release between each concentration increment, whereas in the case of the Ag-TiO_2 fused surfaces, the increase in Ag concentration showed a clear incremental upward trend in Ag^+ release. This demonstrated that the surface produced via the Ag-TiO_2 fusion showed more promise in terms of the tailorability of Ag^+ release relative to the ion exchanged samples, which could be useful in several applications in addition to orthopaedic implants.

6.3 Ag ion implanted samples

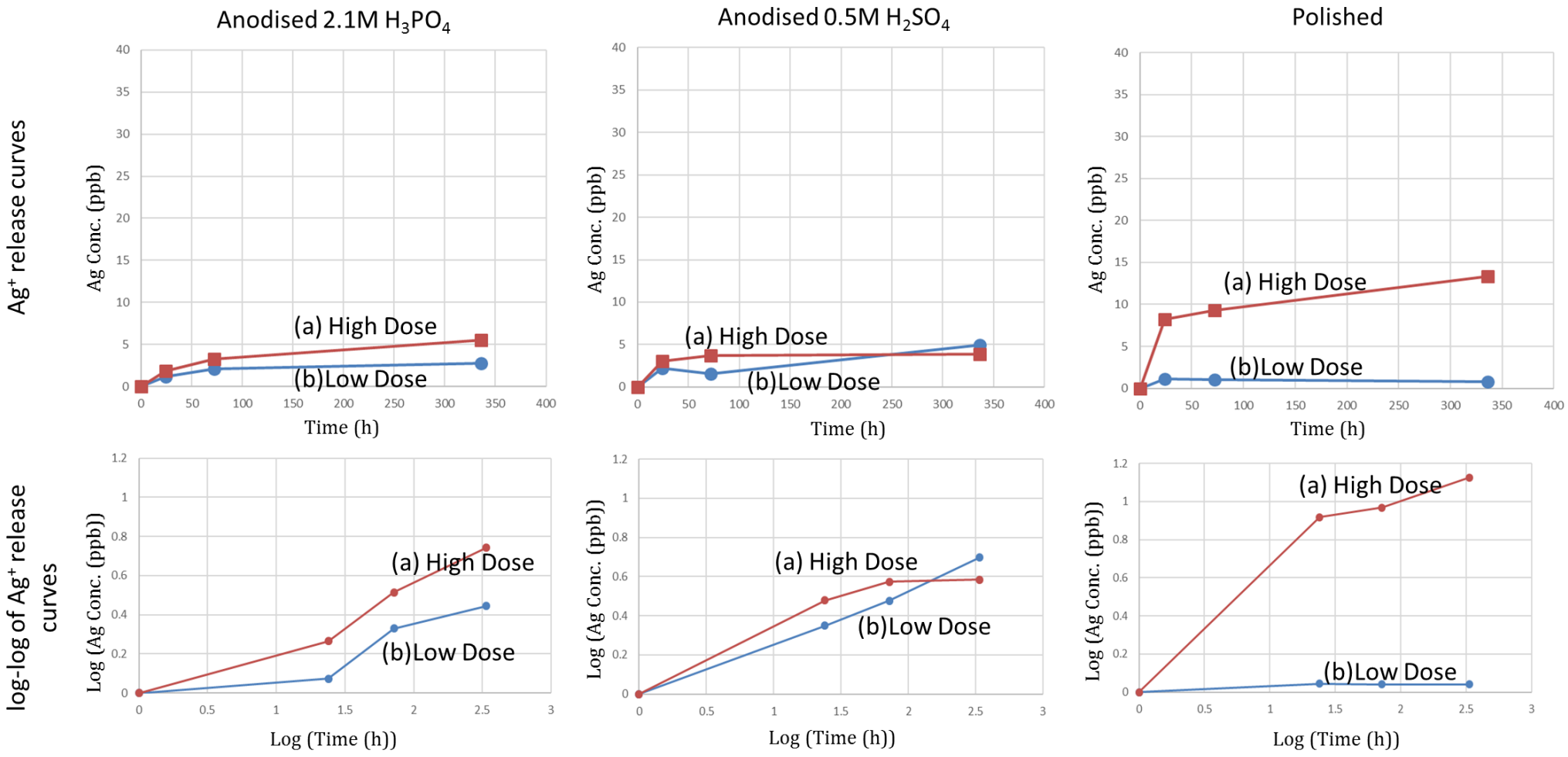

Figure 119 : Ag^+ release curves for samples (i) anodised in 2.1M H_3PO_4 at 100V, (ii) 0.5M H_2SO_4 at 100V, (iii) polished samples implanted at high dose (a) 1.2 x 10^{17} ions/cm^2 and low dose (b) 0.4 x 10^{17} ions/cm^2 .

The RBS analysis in Section 5.3.3 showed similar Ag contents for all the studied surfaces, with the exception of the polished Ti-6Al-4V surface that had been Ag^+ implanted at the high dose. Therefore, it was expected that the majority of the surfaces would behave similarly in terms of Ag^+ release, with the polished samples subjected to the high dose of Ag ions being different, as there was a much high silver content measured by RBS analysis. The achieved results corresponded exactly as anticipated. (See Figure 119, where the Ag^+ release curves of the anodised and polished Ag^+ implanted surfaces are compared). The 2.1M H_3PO_4 anodised and Ag^+ implanted samples {Figure 119 (i)}, where the high and low dose implanted samples showed a Ag^+ release of 3 ppb and 5 ppb Ag respectively, were similar in their Ag^+ release. In the 0.5M H_2SO_4 anodised and Ag^+ implanted samples {Figure 119 (ii)}, the difference in Ag^+ release between samples Ag^+ implanted at the low and high dose was also negligible, with both sample groups releasing *ca.* 4-5 ppb of Ag^+.

All polished Ti-6Al-4V samples showed a significant difference in Ag^+ release when the ion dosage was increased from the low dosage (*ca.* 2 ppb) to the high dosage (*ca.* 14 ppb) {See Figure 119 (iii)}. At the low Ag^+ dosage the Ag^+ release of the polished samples was comparable to the Ag^+ release of all the anodised and Ag^+ implanted surfaces (*ca*. 2 - 5 ppb). This was as expected, since the RBS data had suggested similar results in all these samples (*ca.* 14 at% - 16.5 at%). However, when the higher dosage was tested {Shown in Figure 119 (iii)}, there was a marked increase in Ag^+ release, to *ca.* 14 ppb. This indicated that the polished and Ag^+ implanted surfaces had a greater capacity to store Ag and subsequently release Ag^+ than the anodic oxides, which had already reached maximum Ag storage capacity at the lower Ag^+ implantation dose. This higher storage capacity and release of Ag ions could, as previously discussed, be interpreted as the polished titanium having a higher Ag saturation threshold.

When the Ag^+ release of the samples anodised in the 0.5M H_2SO_4 and the 2.1M H_3PO_4 electrolytes was compared, it was concluded that the Ag^+ release was not dependent on which anodising electrolyte had been used. This was because, as consequence of the ion implantation process, both the TiO_2 surfaces had become completely amorphous, *i.e.* they had lost all previous crystal structure regularity, and this would have reduced the oxidative or photocatalytic abilities of the oxides (especially in cases where anatase had formed prior to Ag^+ implantation). Therefore, the results suggest that AgNPs dissolve slowly. In addition, the ion implantation process caused the anodic oxide surfaces to lose their surface porosity, making it more difficult for the simulated body fluid to penetrate into the anodic oxides. This would inhibit the oxidative dissolution of the observed AgNPs.

Table 26 : Initial Ag release rate of Ag ion implanted samples.

Anodising conditions	**Anodised in 2.1M H_3PO_4 at 100V**		**Anodised in 0.5M H_2SO_4 at 100V**		**Polished-Not Anodised**	
Ion Dose (x10^{17} atoms/cm^2)	0.4	1.2	0.4	1.2	0.4	1.2
Initial Silver release rate(ppb/h) after 24h	0.071	0.144	0.196	0.321	0.0617	0.985

Table 26 above shows the initial Ag^+ release rates for the anodically oxidised and polished Ti-6Al-4V after Ag^+ implantation at the low and the high dose. An increase in the ion dosage did increase the initial Ag^+ release rates for the 2.1M H_3PO_4 anodised, the 0.5M H_2SO_4 anodised and the polished samples from 0.07 ppb/h, 0.20 ppb/h and 0.06 ppb/h respectively to 0.14 ppb/h, 0.3 ppb/h and 0.99 ppb/h respectively. The increased initial Ag^+ release rates for the anodic oxides, as previously discussed, as well as shown in Figure 119 (i) and (ii), did not necessarily translate into a higher net Ag^+ release. However, the increased initial Ag^+ release rates for the polished samples (from 0.06 pp/h to

0.985 ppb/h) did translate into higher net Ag^+ release (from 2 ppb to 14 ppb) {See Figure 119 (iii)}. In conclusion, the change in the initial Ag^+ release rates of all the Ag^+ implanted oxides from the low to the high dosage had no appreciable effect on the final Ag^+ release. Therefore, this change is not significant. However, in the case of the polished samples, there was an appreciable increase in the final Ag^+ release and this is of great significance in terms of the tailorability of Ag^+ release from titanium surfaces.

6.3.1 *Comparison of the Ag^+ Release and Predicted Antimicrobial Effect of Ag^+ implanted, Ag-TiO_2 and Ag^+ Exchanged Samples*

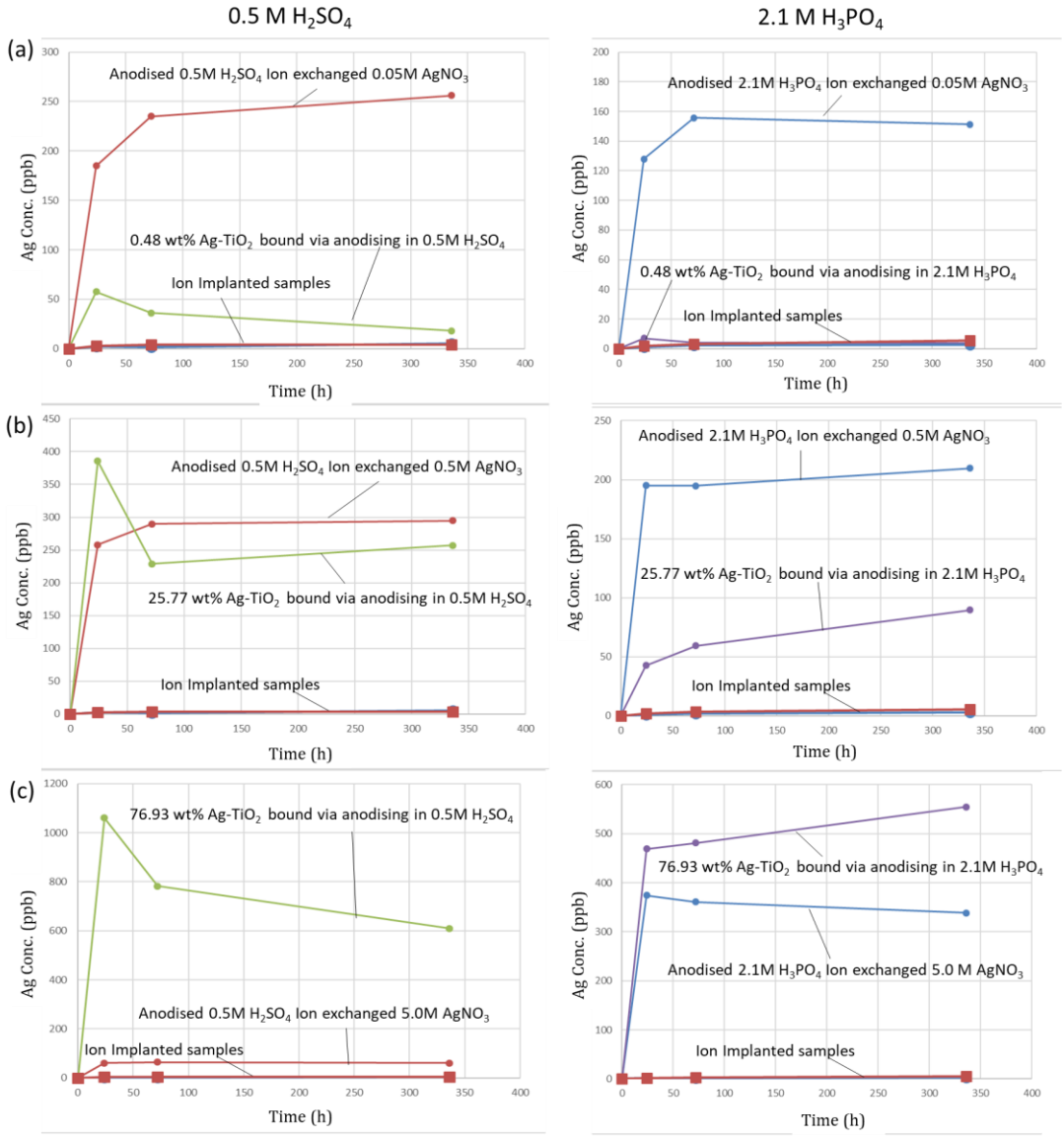

Figure 120 : Ag^+ release curves for anodised and ion exchanged, ion implanted and Ag-TiO_2 surfaces generated using 0.5M H_2SO_4 and 2.1M H_3PO_4 anodising electrolyte.

The Ag^+ release of most of the Ag^+ implanted samples was, in order of magnitude, lower than the Ag^+ release achieved by the surfaces generated via the Ag^+ exchange and Ag-TiO_2 fusion processes. Figure 120 illustrates this result for both the 0.5M H_2SO_4 and 2.1M H_3PO_4 electrolytes, used in their respective processes. It was only when the 2.1M H_3PO_4 electrolyte was used for anodisation in combination with ion implantation with the higher Ag^+ dose, that resulted in a Ag^+ release that was comparable to the Ag^+ release of the 0.48wt% Ag-TiO_2 powders that had been fused via anodising in the 2.1M H_3PO_4 electrolyte {See Figure 120 (a)}. Therefore, in this case, a direct comparison of the Ag^+ implanted

samples to the other two methods researched was deemed of little value. It was deemed more useful to compare the predicted anti-microbial effects (AE) of the three above sample groups. In a research study by D. Song *et al.* [70] it was reported that a minimum Ag^+ concentration of 0.10 ppb was necessary to obtain an antimicrobial surface. This value had been obtained from I.Sondi *et al.* [30]. Since the study by D. Song *et al.* [70] involved surfaces of a similar surface character to the Ag doped TiO_2 surfaces studied in this work (the fused TiO_2 samples and the Ag^+ exchanged samples), the value of 0.10 ppb served as a good benchmark for the evaluation of antimicrobial activity of these samples. Another study by Y.Z. Wan *et al.* [99] could be used as reference for the expected antimicrobial activity of the Ag^+ implanted samples (See plotted blue curve in Figure 121 below, where the Ag^+ implantation dosage is related to the AE).

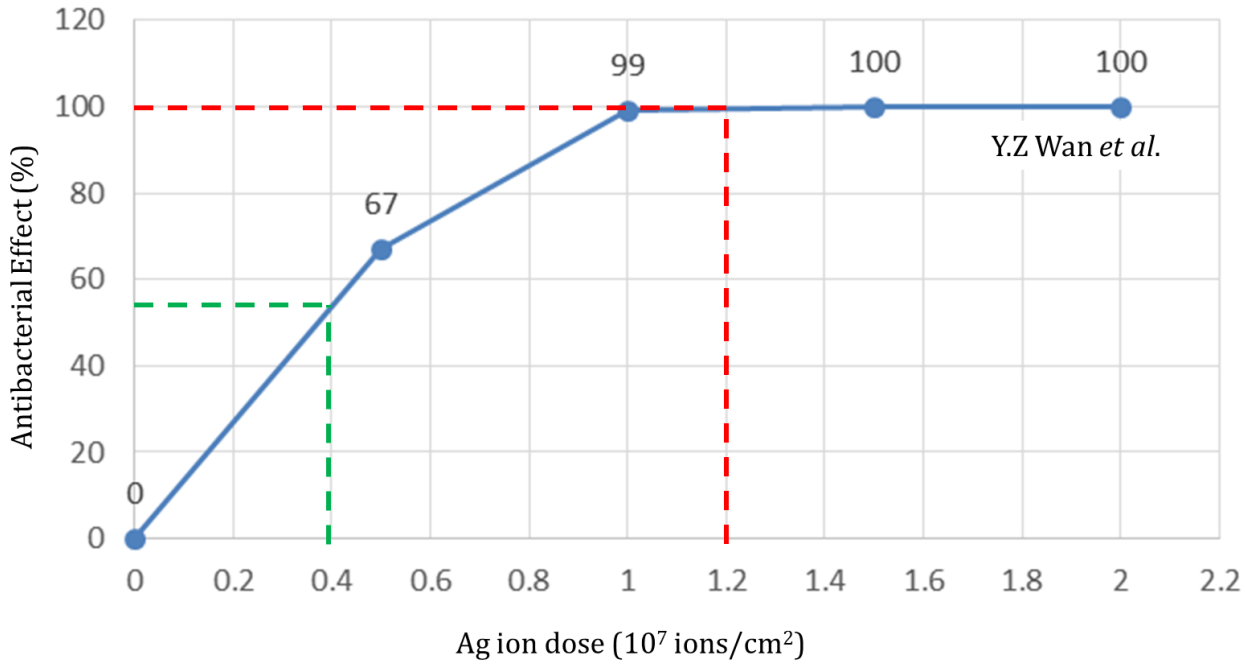

Figure 121 : Antibacterial effect as function of ion dosage for Ti-Al-Nb alloy.

Since the Ag^+ implantation conditions studied in this work were 0.4 x 10^{17} ions/cm^2 and 1.2 x 10^{17} ions/cm^2, it was probable that the antimicrobial effect (AE) of the polished Ti-6Al-4V and Ag^+ implanted samples would be similar to the AE of the Ag^+ implanted polished Ti-Al-Nb alloy investigated by Y.Z. Wan *et al.* [99]. The polished Ti-6Al-4V in this study that had been Ag^+ implanted at the low dose was predicted to achieve an AE of 55% (Green dotted line in Figure 121) and the same samples that had been Ag^+ implanted at the higher dosage were predicted to achieve 100% antimicrobial activity (Red dotted line in Figure 121). The RBS and Ag^+ release data for the polished Ag^+ implanted samples, shown in Figure 98 and Figure 119 (iii) respectively, both corroborate the above predictions, as there was a significantly higher at% Ag in the RBS data and a higher Ag^+ release for the polished samples that had been Ag^+ implanted at the high dose, relative to the low dose.

Since this research found that the all the Ag^+ implanted anodic oxide samples released a similar amount of Ag^+ in comparison to the polished samples that had been Ag^+ implanted at the low Ag^+ dose and that the RBS data between these groups were also similar, it could be predicted that the Ag^+ implanted anodic oxide samples would have a minimum AE of 55%. Considering the study by D. Song *et al.* [70], which predicted a 100% antimicrobial effect above a Ag^+ release of 0.1 ppb for Ag doped TiO_2, it would be expected that the maximum possible antimicrobial effect for the Ag^+ implanted oxides could be predicted at 100%, since even the lowest Ag^+ release amount obtained from the ICP analysis

for the Ag^+ implanted anodic oxides was 0.8ppb, which is eight times higher than the 0.1 ppb 100% AE threshold (See the threshold shown by the red-dotted line in Figure 122 below).

Since all the anodised and Ag^+ exchanged samples had a Ag^+ release significantly greater than 0.1 ppb, the study by D. Song *et al.* [70] suggests that these surfaces would be 100% antimicrobial.

The Ag^+ release predictions are summarised in Table 27 below. The low dose Ag^+ implanted polished Ti-6Al-4V has a predicted maximum of 55% AE, because these samples do not accurately fit the sample types used by D. Song *et al.* [70], *i.e.* they are not Ag doped TiO_2. Instead, they are Ag doped Ti.

Table 27: Predicted antibacterial effects for studied methods.

Technique	Anodising Electrolyte	$AgNO_3$ Conc. (M)	Ag Ion Dose (10^{17} ions/cm^2)	Predicted Antimicrobial Effect
Anodised followed by $AgNO_3$ Ion exchange	0.5M H_2SO_4	0.05	-	100%
		0.5	-	100%
		5.0	-	100%
	2.1M H_3PO_4	0.05	-	100%
		0.5	-	100%
		5.0	-	100%
Ag-TiO_2 Surfaces	0.5M H_2SO_4	0.05	-	100%
		0.5	-	100%
		5.0	-	100%
	2.1M H_3PO_4	0.05	-	100%
		0.5	-	100%
		5.0	-	100%
Ag Ion Implanted Surfaces	0.5M H_2SO_4	-	0.4	55 - 100%
		-	1.2	55 - 100%
		-	0.4	55 - 100%
	2.1M H_3PO_4	-	1.2	55 - 100%
		-	0.4	55%
		-	1.2	100%

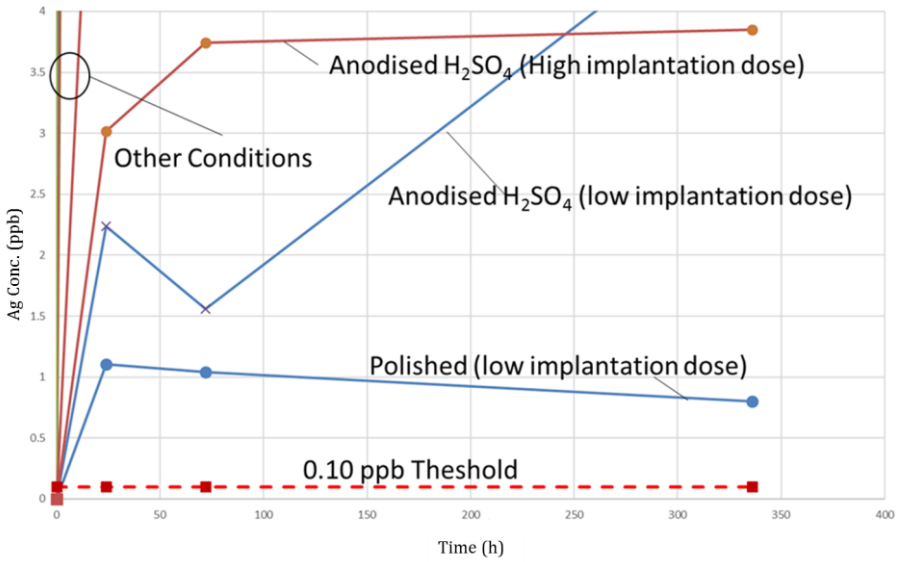

Figure 122 : Graphical depiction of various samples over the 0.16ppb Ag^+ release threshold.

6.4 Summary Discussion of the Silver ion integrated surfaces

Table 28: Comparison and rating of the overall Ag^+ release of the silver ion integrated surfaces.

Technique	Anodising Electrolyte	$AgNO_3$ Conc. (M) / Ag Ion Dose (10^{17} ions/cm^2)	Overall Ag^+ release (ppb)	Rating (based on Overall Ag^+ release)	Comment
Agluna	2.1M H_3PO_4	0.1	190	Good	Final step (20V for 20 mins) made no improvement to silver release
Anodised followed by $AgNO_3$ Ion exchange	0.5M H_2SO_4	0.05	251	Great	Ag incorporation is diffusion dependent
		0.5	295	Great	Ag incorporation is diffusion dependent
		5.0	60	Poor	Diffusion bottlenecking
	2.1M H_3PO_4	0.05	150	Good	Ag incorporation is diffusion dependant No diffusion bottlenecking
		0.5	210	Great	
		5.0	349	Great	
Ag-TiO_2 fused to surfaces	0.5M H_2SO_4	0.05	18	Poor	Excellent tailorability Higher Ag^+ release due to anatase phase Ag incorporation is diffusion independent
		0.5	256	Great	
		5.0	600	Excellent	
	2.1M H_3PO_4	0.05	4	Poor	Excellent tailorability lower Ag^+ release due to rutile phase Ag incorporation is diffusion independent
		0.5	90	Poor-good	
		5.0	550	Excellent	
Ag Ion Implanted Surfaces	0.5M H_2SO_4	0.4	4	Poor	No tailorability of Ag^+ release due to loss of crystal structure and Ag supersaturation reached at low dosage.
		1.2	5	Poor	
	2.1M H_3PO_4	0.4	3	Poor	
		1.2	6	Poor	
	Polished	0.4	2	Poor	Good tailorability of Ag^+ release, Ag supersaturation not reached.
		1.2	14	Poor	

6.4.1 *Summary Discussion of the Silver ion integrated surfaces*

In summary, in Section 6.1 it was shown that the initial Ag^+ release rates of the samples anodised in the 2.1M H_3PO_4 electrolyte increased (from 5.3 ppb/h to 11.4 ppb/h), as did the Ag^+ release (150 ppb to 350 ppb) when the $AgNO_3$ ion exchange solution concentration was increased from 0.05M to 5.0M. In addition, samples produced via the Agluna method, where the silver ion exchange solution was 0.1M $AgNO_3$, exhibited an initial Ag^+ release rate of 5.6 ppb/h. This was within the expected range of Ag^+ release rates exhibited by the conventional anodising procedure conducted using the same 0.1M $AgNO_3$ ion exchange solution (5.9 ppb/h). Thus, it was concluded that the additional step employed during the Agluna method (20V for 20 minutes) did not offer any advantage in terms of the Ag^+ release rate over the conventional anodising procedure. The above results were corroborated by the corresponding RBS data.

When the initial Ag^+ release rates of the samples that had been anodised in the 0.5M H_2SO_4 electrolyte were compared, it was found that there was no significant difference in the initial Ag^+ release rates (7.7 ppb/h and 7.3 ppb/h) when the $AgNO_3$ concentration was increased (from 0.05M to 0.5M). When the $AgNO_3$ ion exchange solution concentration was further increased to 5.0M, the initial Ag^+ release rate unexpectedly, but consistently, decreased to 4.37 ppb/h. Two explanations for this anomaly were proposed, the first being related to "diffusion bottlenecking" and the second to the different reactivity of the crystal structures (anatase and rutile) that formed, depending on which anodising electrolyte had been used (0.5M H_2SO_4 or 2.1M H_3PO_4).

When samples that had been anodised in the 0.5M H_2SO_4 and the 2.1M H_3PO_4 electrolytes were compared at $AgNO_3$ concentrations from 0.1M and below, it was observed that the initial Ag^+ release rates for the anodic oxide layer formed via the 0.5M H_2SO_4 electrolyte were significantly higher (*ca.* 7.8 ppb/h, relative to those produced via the 2.1M H_3PO_4 electrolyte, *ca.* 5.6 ppb/h). When these same

sample groups were compared at a $AgNO_3$ concentration of 0.5M, the initial Ag^+ release rates were similar (*ca.* 7.3 ppb and *ca.* 8.1 ppb). It was concluded that only above an $AgNO_3$ ion exchange solution concentration of 0.5M did crystal structure reactivity start to play a role in the Ag^+ uptake and subsequent release rates.

When the Ag^+ release of the samples that had been anodised in the 0.5M H_2SO_4 and the 2.1M H_3PO_4 electrolyte were compared, it was found that at the $AgNO_3$ concentrations of 0.05M and 0.5M, the anodic oxides formed using the 0.5M H_2SO_4 electrolyte had final Ag^+ releases of 251 ppb and 295 ppb respectively, compared to those samples anodised in the 2.1M H_3PO_4 electrolyte, which had final Ag^+ releases of 150 ppb and 210 ppb respectively. Furthermore, at the 5.0M $AgNO_3$ ion exchange concentration, the 2.1M H_3PO_4 anodised samples (rutile) had a significantly higher final Ag^+ release, of 349 ppb, relative to that of the 0.5M H_2SO_4 anodised (anatase) samples (60 ppb). These trends correlated with the trends found in the Ag^+ release rate data for the same reasons (diffusion bottlenecking and/or crystal structure differences). The RBS results corroborated the observed trends.

6.4.2 *Summary Discussion of the Ag-Doped Titanium oxide Particles Attached via Anodising*

In summary of Section 6.2, it was found that the Ag-TiO_2 that had been fused via anodising in the 2.1M H_3PO_4 and 0.5M H_2SO electrolytes both showed increasing initial Ag^+ release rates, as the Ag concentration within the powders was increased from 0.48 wt% (4 ppb and 18 ppb respectively) to 76.93 wt% (550 ppb and 600 ppb). Therefore, it was concluded that using the 0.5M H_2SO_4 electrolyte to fuse the Ag-TiO_2 powders to the surface resulted in an increase in the final Ag^+ release relative to those fused using 2.1M H_3PO_4 (for all investigated powder concentrations).

The Ag-TiO_2 fused via anodising in the 2.1M H_3PO_4 and 0.5M H_2SO electrolytes both showed increasing Ag^+ release rates as the Ag concentration within the powders was increased from 0.48 wt% (0.29 ppb/h and 2.4 ppb/h respectively) to 76.93 wt% (23.5 ppb/h and 30.89 ppb/h). Therefore, it was concluded that using the 0.5M H_2SO_4 electrolyte to fuse the Ag-TiO_2 powders to the surfaces resulted in an increase in the initial Ag^+ release rate relative to those fused using 2.1M H_3PO_4 (for all investigated powder concentrations). The increases in Ag^+ release rates and Ag^+ releases when the Ag-TiO_2 powders had been fused to the surface using the 0.5M H_2SO_4 electrolyte might have been due to the increased oxidative abilities of the anatase oxide generated by anodisation in the 0.5M H_2SO electrolyte. Owing to the O_2 released by the anatase crystal structures, there would have been an increase in the rate of oxidative dissolution of the AgNPs and, therefore, greater Ag^+ release rates and Ag^+ release. Comparison of the Ag^+ release curves of the Ag-TiO_2 samples fused via anodising in the 2.1M H_3PO_4 and the 0.5M H_2SO_4 electrolytes it was found that the final amount of Ag^+ released by the Ag-TiO_2 fused via 0.5M H_2SO_4 was consistently higher across all Ag-TiO_2 powder concentrations. The RBS data corroborated these results.

It was found that there existed a relationship between the wt% Ag in the Ag-TiO_2 powders fused to the sample surfaces and the initial Ag^+ release rates from these surfaces. A similar relationship was found between the wt% Ag in the same Ag-TiO_2 powders and the overall final Ag^+ release. These two corresponding relationships indicate a linear relationship between the initial Ag^+ release rates and the final Ag^+ release.

In Section 6.2.1, when comparing the Ag^+ release of the Ag-TiO_2 samples that had been fused via anodising using the 0.5M H_2SO_4 electrolyte with the samples anodised using the same electrolyte and then Ag^+ exchanged, it was found that the samples that had been Ag^+ exchanged in 0.05M $AgNO_3$

demonstrated a Ag^+ release of 210 ppb, thereby outperforming the fused 0.48 wt% Ag-TiO_2 powder samples, which had an Ag^+ release of 35 ppb. The Ag^+ releases of the 25.77 wt% Ag-TiO_2 fused samples and the 0.5M $AgNO_3$ ion exchanged samples, both of which were anodised in the 0.5M H_2SO_4 electrolyte, were found to be similar (250 ppb and 280 ppb respectively). When comparing the Ag^+ release of the 76.93 wt% Ag-TiO_2 powder that had been fused via the 0.5M H_2SO_4 electrolyte with the anodised and 5.0M $AgNO_3$ ion exchanged samples, it was found that the former samples demonstrated a significantly higher Ag^+ release (600 ppb), in contrast to the Ag^+ released by the latter ion exchanged samples (80 ppb). The reasons for these observed results were concluded to be related to the differences in the experimental procedures that produced the Ag-TiO_2 powders (where silver incorporation was diffusion-independent) and the Ag^+ ion exchanged surfaces (where silver incorporation was diffusion-dependent). In addition, the increased surface porosity of the anatase-oxide layers generated during the powder attachment also acted to increase the exposed surface area of the AgNPs to the SBF solution, which in turn increased the rate of oxidative dissolution of these AgNPs.

When comparing the Ag^+ release of the Ag-TiO_2 samples that had been fused via anodising using the 2.1M H_3PO_4 electrolyte with the samples that had been anodised in the same electrolyte and then Ag^+ exchanged, it was found that the samples that had been Ag^+ exchanged in the 0.05M $AgNO_3$ solution demonstrated a Ag^+ release of 140 ppb, thereby outperforming the fused 0.48 wt% Ag-TiO_2 powder samples, which demonstrated an Ag^+ release of 5 ppb. Comparing the Ag^+ release of the 25.77 wt% Ag-TiO_2 fused samples with the 0.5M $AgNO_3$ ion exchanged samples, both of which were anodised in the 2.1M H_3PO_4 electrolyte, the Ag^+ releases were found to be dissimilar (80 ppb and 200 ppb respectively). Finally, when the 76.93 wt% Ag-TiO_2 powder samples fused via the 0.5M H_2SO_4 electrolyte and the anodised and 5.0M $AgNO_3$ ion exchanged samples were compared, it was found that the fused samples had a significantly higher Ag^+ release of 550 ppb *versus* the 350 ppb of Ag^+s released by the ion exchanged samples. The reason for these observed results were concluded to be related to the differences in the experimental procedures that produced the Ag-TiO_2 powders (where silver incorporation was diffusion-independent, in the case of the fused samples) and the Ag^+ ion exchanged surfaces (where silver incorporation was diffusion-dependent, in the case of the ion exchanged samples). It was concluded that the samples that had Ag-TiO_2 powder fused on to their surfaces exhibited a greater degree of Ag^+ release tailorability, relative to that of the ion exchanged samples.

6.4.3 *Summary Discussion of the Ag ion implanted samples*

In Section 6.3 it was found that, after Ag^+ implantation, the anodic oxides generated via anodising in the 2.1M H_3PO_4 and 0.5M H_2SO_4 electrolytes had similar Ag^+ releases, irrespective of which Ag^+ dosage was used (*ca.* 3 ppb - 5 ppb). There was a slight increase in the initial Ag^+ release rates when the ion implantation dosage was increased, but these slight increases were found to be insignificant. The reason for the similar Ag^+ release and Ag^+ release rates of all the anodic oxide samples were concluded to be in consequence of the ion implantation process, which amorphised the crystal structures of both anodic oxide layers. Since no anatase was present in either oxides, there was little to no assistance given in the oxidative dissolution of the AgNPs at the surface. Therefore, both anodic oxides were shown to perform similarly under all conditions tested. In addition, it was found that the ion implantation process reduced surface porosity, making it more difficult for the SBF to penetrate the anodic oxide surfaces, thereby inhibiting the oxidative dissolution of the AgNPs. The RBS data corroborated these results.

However, there was a difference in the Ag^+ release and Ag^+ release rates in the polished Ag^+ implanted samples. The results showed significant increases in the final Ag^+ released (from 2 ppb to 14 ppb) and

the initial Ag^+ release rates (0.0617 ppb/h to 0.985 ppb/h) when the Ag^+ ion dose was increased from low to high. Since there were no AgNPs observed in the TEM imaging, it was concluded that the Ag might be interstitially located within the crystal structure of the polished samples. This was partly due to the increased stability of the ionic Ag species within the metallically-bonded titanium matrix *versus* within the covalently-bonded ceramic TiO_2 matrix. Thus, it was concluded that if the Ag were present within polished sample surfaces in the ionic state, the initial Ag^+ release rate would mainly be driven by the concentration gradient and, therefore, a higher Ag^+ implantation dose would lead to the observed increase in both the initial Ag^+ release rate and the final Ag^+ release. Furthermore, it was concluded that, since no AgNPs had formed at the high ion implantation dose, the titanium surfaces had yet to reach Ag^+ supersaturation within their crystal structures.

Section 6.3.1 compared the Ag^+ release and the predicted antimicrobial effect (AE) of the three sample groups, *viz.* samples with Ag^+ implanted surfaces, samples with Ag-TiO_2 fused on to the surfaces and the Ag^+ exchanged samples. It was found that, relative to the Ag-TiO_2 samples and the Ag^+ exchanged samples, the Ag^+ implanted samples demonstrated a final Ag^+ release and initial Ag^+ release rates that were significantly lower than those of the other two sample groups. It was then concluded that a direct comparison of the final Ag^+ release and the initial Ag^+ release rates relating to the three sample groups would be of no significant value. It was found to be more valuable to compare the anti-microbial effects (AE) that could be predicted from literature that pertained to these sample groups. By comparing the Ag^+ release of the polished and the anodically oxidised Ag^+ implanted samples in this study to results of similar studies by Y.Z. Wan *et al.* [99] and D. Song *et al.* [70], it was predicted that the antimicrobial effect of the polished ion implanted samples would be 55% and 100% for the low and high Ag^+ doses respectively. For the anodically oxidised Ag^+ implanted samples, a range of 55% - 100% AE was predicted (irrespective of the electrolyte used and the ion dose). For the Ag-TiO_2 fused samples and the Ag^+ exchanged samples, the study by D. Song *et al.* [70] showed that, above a 0.1 ppb threshold, antimicrobial effectiveness was 100%. Since in this research these samples were shown to have a significantly higher Ag^+ release than the threshold value, it was concluded that the Ag-TiO_2 fused samples and the Ag^+ exchanged samples would have a 100% AE under all testing conditions.

6.5 Scalability

There are multiple variables that would need to be considered in order to compare the three methods of silver incorporation in terms of scalability, the most important criteria being equipment cost and complexity (the level of complexity determining the skill level of the practitioner and therefore the cost), production time and tailorability.

In terms of equipment cost, the ion implantation equipment would cost in excess of R15 million and would require a highly-skilled technician to operate it. Both the anodising and Ag^+ exchanging process and the TiO_2 powder synthesis and fusion process require similar equipment that can cost upward of R5000. The anodising and Ag^+ exchanging process would not require a highly-skilled technician as the method requires the worker only to follow a prescribed "recipe" in order to achieve satisfactory results. The TiO_2 powder synthesis and fusion process may require a person with some chemistry background to synthesise and dope the powders with silver.

Production time of the ion implantation method would depend on the size of the implant, ranging from four hours to twelve hours per implant. The production time of both the other methods would take approximately two hours and could be scaled-up by increasing the equipment cost to accommodate more implants during a batch process.

It was determined from the experimental data that ion implantation does have the potential to be tailorable in terms of Ag^+ release when ion implanting into polished Ti-6Al-4V surfaces. However, the tailorability was not observed in the Ag^+ release from the anodically oxidised samples. It is suspected that the amorphisation of the TiO_2 crystal structure was responsible for this and further study should be conducted to reintroduce anatase and rutile structure into the oxide. The anodising and Ag^+ exchanging process was not significantly tailorable, because large increases in the $AgNO_3$ concentration did not lead to distinct increases in Ag^+ release in all cases. The TiO_2 powder synthesis and fusion process showed high tailorability as an increase in Ag concentration within the powders showed an corresponding increase in Ag^+ release.

7. Conclusions

The aim of this study was to investigate methodologies for the incorporation of silver into a modified surface of Ti-6Al-4V in order to facilitate an antimicrobial effect for use in orthopaedic implants. The methodologies investigated for the incorporation of silver on to the surface were ion exchange, fused Ag-TiO_2 and ion implantation. Each technique was used on a range of modified surfaces. Results show that for maximum silver ion release and associated antimicrobial effect, the technique of Ag-TiO_2 fused to the surface using the 2.1M H_3PO_4 and 0.5M H_2SO_4 electrolytes yields the best results, with silver ion release of 550 and 600 ppb respectively over two weeks. This technique also satisfies the research aim in that the methodology offers a combination of tailorability of silver release and commercial scalability.

The above overall conclusion was made based on the addressing of the objectives laid out in Section 1.2.2. The following conclusions were made relating to the objectives and research questions.

- Results from the Ag ion exchanged samples showed that, microstructurally, the surfaces produced via anodising in 0.5M H_2SO_4 and 2.1M H_3PO_4 were different in terms of pore morphology, R_a, pore homogeneity across the surface and crystal structure. Sub-surface analysis via FIB/TEM found that the *ca*. 200nm thick TiO_2 samples all contained silver nanoparticles (AgNPs). Samples anodised in 0.5M H_2SO_4 produced an anatase crystal structure, whilst those anodised in 2.1M H_3PO_4 produced rutile crystal structures.

- In the context of surface modification and its effect on silver release, the presence of anatase in the oxide layers, as produced using the 0.5M H_2SO_4 electrolyte surface modification techniques, for both the ion exchange and the fused Ag-TiO_2, resulted in an increase in the silver ion release. The exception was in the case where diffusion bottlenecking occurred at high $AgNO_3$ concentrations for the ion exchange methodology. For diffusion bottlenecking to occur the silver incorporation technique must be silver diffusion dependent. In addition, there must be a combination of anatase and high silver ion concentration at the surface.

- Greater amounts of Ag-TiO_2 powder fusion was observed in areas were downward pressure was exerted during the anodising process. The presence of downward pressure during anodisation will have to be incorporated into the commercial scalability of the process.

- In the case of ion implantation, surface modification through anodisation creates an oxide layer which supersaturates at a low dosage during Ag^+ implantation. In addition, this layer also becomes amorphous during the implantation process. Consequently, ion implantation results in poor silver ion release, regardless of surface characteristics, when compared to the ion exchange and Ag-TiO_2 fused methodologies. This process was also deemed un-scalable and showed no tailorability. However, silver supersaturation did not occur when the ion implantation process was applied to polished Ti-6Al-4V samples. In the case of the polished samples the silver release was tailorable, but also deemed un-scalable in comparison to the ion exchanged and Ag-TiO_2 fused methodologies.

- All the test methodologies would achieve at least 55 – 100% antimicrobial effect, when based on studies by Y.Z. Wan *et al*. [99] , D. Song *et al*. [70] and I.Sondi *et al*. [30]. The 76.93 wt% Ag-TiO_2 (5.0M $AgNO_3$) fused surfaces had the highest silver ion release and would be expected to offer a antimicrobial effect for longer periods of time. This would require further testing for confirmation.

8. Recommendations

Based on the results achieved in this work, the following recommendations are made for further research:

- Conduct further studies on the attachment of TiO_2 powders via anodising, in order to improve particle attachment. Particular focus should be placed on the study of methods to impart downward pressure during anodising.

- Investigate the use of a second anodising procedure to restore the surface porosity of the ion implanted samples. This is important for release and biomimetic purposes.

- Study the biocompatibility of the surfaces generated in this study.

- Conduct antimicrobial testing on all the studied samples in this work.

- A study to determine the Ag supersaturation point of anodic anatase and rutile TiO_2 by changing the ion implantation dose.

- A study of the ion implant oxides where the dosage is below the Ag saturation point to determine the Ag release characteristics.

- Investigate the effect of a constant flow environment on the Ag^+ release, as well as investigating cyclic emersion under static conditions, both in simulated body fluid.

9. References

1. Davis, A. M., Devlin, M., Griffin, A. M., Wunder, J. S. & Bell, R. S. Functional outcome in amputation verses limb sparing of patients with lower extremity sarcoma: a matched case-control study. *Achives Phys. Med. Rehabil.* **80**, 615–618 (1999).
2. Velten, D. *et al.* Preparation of TiO2 layers on cp-Ti and Ti6Al4V by thermal and anodic oxidation and by sol-gel coating techniques and their characterization. *J. Biomed. Mater. Res.* **59**, 18–28 (2002).
3. Oldani, C., Dominguez, A. & Eli, T. Titanium as a Biomaterial for Implants. in *Recent Advances in Arthroplasty* (ed. Fokter, D. S.) 149–161 (InTech, 2012).
4. Pavon, J. *et al.* Anodic oxidation of titanium for implants and prosthesis: Processing, characterization and potential improvement of osteointegration. *IFMBE Proc.* **33 IFMBE**, 176–179 (2013).
5. Racano, A., Pazionis, T., Farrokhyar, F., Deheshi, B. & Ghert, M. High infection rate outcomes in long-bone tumor surgery with endoprosthetic reconstruction in adults: a systematic review. *Clin. Orthop. Relat. Res.* **471**, 2017–27 (2013).
6. Jeys, L. M., Grimer, R. J., Carter, S. R. & Tillman, R. M. Risk of amputation following limb salvage surgery with endoprosthetic replacement, in a consecutive series of 1261 patients. *Int. Orthop.* **27**, 160–163 (2003).
7. Implants, S. Extremely Educational. in *Infection:an Extremely difficult challenge,an extremely elegant solution* 1–6 (2013).
8. Rai, M., Yadav, A. & Gade, A. Silver nanoparticles as a new generation of antimicrobials. *Biotechnol. Adv.* **27**, 76–83 (2009).
9. Matsumura, Y., Yoshikata, K., Kunisaki, S. & Tsuchido, T. Mode of bactericidal action of silver zeolite and its comparison with that of silver nitrate mode of bactericidal action of silver zeolite and its comparison with that of silver nitrate. *Appl. Environ. Microbiol.* **69**, 4278–4281 (2003).
10. Lin, Y., Vidic, R., Stout, J. & Yu, V. Negative effect of high pH on biocidal efficacy of copper and silver ions in controlling Legionella pneumophila. *Appl. Environ.* **68**, 2711–2715 (2002).
11. Feng, Q. L. *et al.* A mechanistic study of the antibacterial effect of silver ions on Escherichia coli and Staphylococcus aureus. *J.Biomed.Mater.Res* **4**, 662–668 (2000).
12. Panyala, N. R., Peña-Méndez, E. M. & Havel, J. Silver or silver nanoparticles: a hazardous threat to the environment and human health? *J. Appl. Biomed.* **6**, 117–129 (2008).
13. Gong, D. *et al.* Titanium oxide nanotube arrays prepared by anodic oxidation. *J. Mater. Res.* **16**, 3331–3334 (2001).
14. Uttiya, S. *et al.* Anodic Oxidation of Titanium in Sulphuric Acid and Phosphoric Acid Electrolytes. **1**, 1–8 (2014).
15. Kuromoto, N. K., Simão, R. A. & Soares, G. A. Titanium oxide films produced on commercially pure titanium by anodic oxidation with different voltages. *Mater. Charact.* **58**, 114–121 (2007).
16. Kim, H. S. *et al.* Fabrication and characterization of functionally graded nano-micro porous titanium surface by anodizing. *J. Biomed. Mater. Res. - Part B Appl. Biomater.* **88**, 427–435 (2009).
17. Song, H., Park, S., Jeong, S. & Park, Y. Surface characteristics and bioactivity of oxide films formed by anodic spark oxidation on titanium in different electrolytes. **9**, 864–870 (2008).
18. El-wassefy, N. A., Hammouda, I. M., Habib, A. N. E. D., El-awady, G. Y. & Marzook, H. A. Assessment of anodized titanium implants bioactivity. *Clin. Oral Implants Res.* **25**, 1–9 (2014).
19. Diamanti, M. V. & Pedeferri, M. P. Effect of anodic oxidation parameters on the titanium oxides formation. *Corros. Sci.* **49**, 939–948 (2007).
20. Uttiya, S. *et al.* Anodic Oxidation of Titanium in Sulphuric Acid and Phosphoric Acid Electrolytes. **1**, 1–8 (2014).
21. H.Z. Abdullah, C. C. S. Preparation and characterisation ofTiO2 thick films fabricated by anodic oxidation.pdf. *Mater. Sci. Forum* **561–565**, 2159–2162 (2007).
22. Yang, B. Preparation of bioactive titanium metal via anodic oxidation treatment. *Biomaterials* **25**, 1003–1010 (2004).
23. He, C., Yu, Y., Hu, X. & Larbot, A. Influence of silver doping on the photocatalytic activity of

titania films. *Appl. Surf. Sci.* **200**, 239–247 (2002).
24. Thiel, J. *et al.* Antibacterial properties of silver-doped titania. *Small* **3**, 799–803 (2007).
25. Almajhdi, F. N. *et al.* In-vitro anticancer and antimicrobial activities of PLGA/silver nanofiber composites prepared by electrospinning. *J. Mater. Sci. Mater. Med.* **25**, 1045–1053 (2014).
26. Teoh, S. H. *Engineering materials for biomedical applications*. (World Scientific Pub, 2004).
27. RD Knutsen. Manufacturing with Metals: Module 3 – Metallurgy and Properties of Non-Ferrous Metals Author. (University of Cape Town, 2015).
28. Lansdown, A. B. G. Silver in Healthcare: Its Antimicrobial Efficacy and Safety in Use. **33**, 261 (2010).
29. Jung, W. K. *et al.* Antibacterial activity and mechanism of action of the silver ion in Staphylococcus aureus and Escherichia coli. *Appl. Environ. Microbiol.* **74**, 2171–2178 (2008).
30. Sondi, I. & Salopek-sondi, B. Silver nanoparticles as antimicrobial agent : a case study on E . coli as a model for Gram-negative bacteria. **275**, 177–182 (2004).
31. Lok, C. N. *et al.* Silver nanoparticles: partial oxidation and antibacterial activities. *J. Biol. Inorg. Chem.* **12**, 527–534 (2007).
32. Ouay, B. Le & Stellacci, F. Antibacterial activity of silver nanoparticles : A surface science insight. *Nano Today* **10**, 339–354 (2015).
33. Xiu, Z., Zhang, Q., Puppala, H. L., Colvin, V. L. & Alvarez, P. J. J. Negligible Particle-Speci fi c Antibacterial Activity of Silver Nanoparticles. 10–14 (2012). doi:10.1021/nl301934w
34. Liu, J., Sonshine, D. A., Shervani, S. & Hurt, R. H. Controlled release of biologically active silver from nanosilver surfaces. *ACS Nano* **4**, 6903–6913 (2010).
35. Milenkovic, M. *et al.* Acta Biomaterialia Multifunctional PLGA particles containing poly (L - glutamic acid) -capped silver nanoparticles and ascorbic acid with simultaneous antioxidative and prolonged antimicrobial activity. (2013). doi:10.1016/j.actbio.2013.08.030
36. Kittler, S., Greulich, C., Diendorf, J., Köller, M. & Epple, M. Toxicity of silver nanoparticles increases during storage because of slow dissolution under release of silver ions. *Chem. Mater.* **22**, 4548–4554 (2010).
37. Otto, M. Staphylococcus epidermidis — the 'accidental' pathogen. *Nat. Rev. Microbiol.* **7**, 555 (2009).
38. Vuong, C. & Otto, M. Staphylococcus epidermidis infections. *Microbes Infect.* **4**, 481–489 (2002).
39. Swedish University of Agricultural Sciences - Faculty of Veterinary Medicine and Animal Science. Staphylococcus epidermidis. 1 (2017). Available at: http://www.vetbact.org/index.php?artid=205&vbsearchstring=Staphylococcus epidermidis. (Accessed: 23rd January 2018)
40. Swedish University of Agricultural Sciences - Faculty of Veterinary Medicine and Animal. Staphylococcus aureus. 1 (2017). Available at: http://www.vetbact.org/index.php?artid=20&vbsearchstring=Staphylococcus aureus#. (Accessed: 23rd January 2018)
41. Franklin, L. Staphylococcus aureus Infections. *N. Engl. J. Med.* **339**, 520–532 (1998).
42. Klevens, R., Morrison, M. & Nadle, J. Invasive methicillin-resistant staphylococcus aureus infections in the united states. *JAMA* **298**, 1763–1771 (2007).
43. Toole, G. O., Kaplan, H. B. & Kolter, R. Biofilm Formation as Microbial Development. 49–79 (2000).
44. Gristina, A. G. *et al.* Biomaterial-Centered Infection : Microbial Adhesion Versus Tissue Integration Published by : American Association for the Advancement of Science Stable URL : http://www.jstor.org/stable/1699782 REFERENCES Linked references are available on JSTOR for this . **237**, 1588–1595 (2016).
45. Odekerken, J. C. E., Welting, T. J. M., Arts, J. J. C., Walenkamp, G. H. I. M. & Emans, P. J. Modern Orthopaedic Implant Coatings — Their Pro ' s , Con ' s and Evaluation Methods.
46. Diebold, U. The surface science of titanium dioxide. *Surf. Sci. Rep.* **48**, 53–229 (2003).
47. Luttrell, T. *et al.* Why is anatase a better photocatalyst than rutile? - Model studies on epitaxial TiO2films. *Sci. Rep.* **4**, 1–8 (2015).
48. Lund, A., Shiotani, M. & Shimada, S. *Principles and applications of ESR spectroscopy*. (Springer Science & Business Media, 2011).
49. Samat, M. H., Ali, A. M. M., Taib, M. F. M., Hassan, O. H. & Yahya, M. Z. A. Hubbard U calculations on optical properties of 3d transition metal oxide TiO2. *Results Phys.* **6**, 891–896 (2016).

50. Sul, Y., Johansson, C. B., Jeong, Y. & Albrektsson, T. The electrochemical oxide growth behaviour on titanium in acid and alkaline electrolytes. **23**, 329–346 (2001).
51. Cochran, D. L., Simpson, J., Weber, H. P. & Buser, D. Attachment and growth of periodontal cells on smooth and rough titanium. *Int. J. Oral Maxillofac. Implants* **9**, (1994).
52. Baharloo, B., Textor, M. & Brunette, D. M. Substratum roughness alters the growth, area, and focal adhesions of epithelial cells, and their proximity to titanium surfaces. *J. Biomed. Mater. Res. Part A* **74**, 12–22 (2005).
53. Francois, P. *et al.* Influence of surface treatments developed for oral implants on the physical and biological properties of titanium.(II) Adsorption isotherms and biological activity of immobilized fibronectin. *Clin. Oral Implants Res.* **8**, 217–225 (1997).
54. Le Guéhennec, L., Soueidan, a., Layrolle, P. & Amouriq, Y. Surface treatments of titanium dental implants for rapid osseointegration. *Dent. Mater.* **23**, 844–854 (2007).
55. Netshifhefhe, T. Investigation into the surface modification of Ti-6Al-4V to facilitate antimicrobial ionic silver integration for use in implantable orthopeadic devices. (Mechanical Engineerinng, 2014).
56. Variola, F. *et al.* Tailoring the surface properties of Ti6Al4V by controlled chemical oxidation. *Biomaterials* **29**, 1285–1298 (2008).
57. Gaul, E. Coloring titanium and related metals by electrochemical oxidation. *J. Chem. Educ.* **70**, 176–178 (1993).
58. Sharma, A. K. Anodizing titanium for space applications. *Thin Solid Films* **208**, 48–54 (1992).
59. Sadat-Shojai, M., Khorasani, M. T., Dinpanah-Khoshdargi, E. & Jamshidi, A. Synthesis methods for nanosized hydroxyapatite with diverse structures. *Acta Biomater.* **9**, 7591–7621 (2013).
60. Oh, H. J., Lee, J. H., Jeong, Y., Kim, Y. J. & Chi, C. S. Microstructural characterization of biomedical titanium oxide film fabricated by electrochemical method. *Surf. Coatings Technol.* **198**, 247–252 (2005).
61. Sul, Y.-T., Johansson, C. B., Kang, Y., Jeon, D.-G. & Albrektsson, T. Bone reactions to oxidized titanium implants with electrochemical anion sulphuric acid and phosphoric acid incorporation. *Clin. Implant Dent. Relat. Res.* **4**, 78–87 (2002).
62. Turner, A. D. Metal treatment to form a surface layer. *United States Patent Application Publication* 1–6 (2012).
63. Chao, H. E., Yun, Y. U., Xingfang, H. U. & Larbot, a. Effect of silver doping on the phase transformation and grain growth of sol-gel titania powder. *J. Eur. Ceram. Soc.* **23**, 1457–1464 (2003).
64. López, T. *et al.* Effect of pH on the incorporation of platinum into the lattice of sol-gel titania phases. *Mater. Lett.* **40**, 59–65 (1999).
65. Di Paola, A., Bellardita, M. & Palmisano, L. *Brookite, the Least Known TiO2 Photocatalyst*. *Catalysts* **3**, (2013).
66. Spitzlsperger, G. *Very brief Introduction to Ion Implantation for Semiconductor Manufacturing*. (2003).
67. Stepanov, A. L. Synthesis of silver nanoparticles in dielectric matrix by ion implantation: A review. *Rev.Adv.Mater.Sci* **26**, 1–29 (2010).
68. Zhang, J.-S. Environmental Damage at High Temperature. in *High Temperature Deformation and Fracture of Materials* (ed. Zhang, J.-S.) 330–348 (Woodhead Publishing, 2010). doi:https://doi.org/10.1533/9780857090805.2.330
69. Wan, Y. Z. *et al.* Surface modification of medical metals by ion implantation of silver and copper. *Appl. Surf. Sci.* **253**, 9426–9429 (2007).
70. Song, D. H., Uhm, S. H., Lee, S. B., Han, J. G. & Kim, K. N. Antimicrobial silver-containing titanium oxide nanocomposite coatings by a reactive magnetron sputtering. *Thin Solid Films* **519**, 7079–7085 (2011).
71. Stanić, V. *et al.* Synthesis, characterization and antimicrobial activity of copper and zinc-doped hydroxyapatite nanopowders. *Appl. Surf. Sci.* **256**, 6083–6089 (2010).
72. Wang, Y., Chen, J., Wei, K., Zhang, S. & Wang, X. Surfactant-assisted synthesis of hydroxyapatite particles. *Mater. Lett.* **60**, 3227–3231 (2006).
73. Saha, S. K., Banerjee, A., Banerjee, S. & Bose, S. Synthesis of nanocrystalline hydroxyapatite using surfactant template systems: Role of templates in controlling morphology. *Mater. Sci. Eng. C* **29**, 2294–2301 (2009).

74. Ye, F., Guo, H. & Zhang, H. Biomimetic synthesis of oriented hydroxyapatite mediated by nonionic surfactants. *Nanotechnology* **19**, 245605 (2008).
75. Cüneyt Tas, a. Synthesis of biomimetic Ca-hydroxyapatite powders at 37°C in synthetic body fluids. *Biomaterials* **21**, 1429–1438 (2000).
76. Paz, A. *et al.* A comparative study of hydroxyapatite nanoparticles synthesized by different routes. *Quim. Nova* **35**, 1724–1727 (2012).
77. Kim, I. Y., Kikuta, K. & Ohtsuki, C. Formation of oriented hydroxyapatite rods by hydrothermal treatment of calcite single crystal. *Korean J. Mater. Res.* **22**, 397–402 (2012).
78. Liu, J. *et al.* The influence of pH and temperature on the morphology of hydroxyapatite synthesized by hydrothermal method. *Ceram. Int.* **29**, 629–633 (2003).
79. Rameshbabu, N. *et al.* Antibacterial nanosized silver substituted hydroxyapatite: synthesis and characterization. *J. Biomed. Mater. Res. Part A* **80**, 581–591 (2007).
80. Makadia, H. K. & Siegel, S. J. Poly Lactic-co-Glycolic Acid (PLGA) as biodegradable controlled drug delivery carrier. *Polymers (Basel).* **3**, 1377–1397 (2011).
81. Chasin, M. *et al. Polyanhydrides as Drug Delivery Systems*. *Biodegradable Polymers as Drug Delivery Systems* (1990). doi:10.1016/0223-5234(91)90162-G
82. Agarwal, S., Wendorff, J. H. & Greiner, A. Use of electrospinning technique for biomedical applications. *Polymer (Guildf).* **49**, 5603–5621 (2008).
83. Leach, M. K., Feng, Z., Tuck, S. J. & Corey, J. M. Electrospinning Fundamentals : Optimizing Solution and Apparatus Parameters. 2–5 (2011). doi:10.3791/2494
84. N.Nihant. Microencapsulation by Coacervation of Poly(lactide-co-glycolide) II. *Poymer Int.* 171–176 (1993).
85. Stefanaki, E. Electron Microscopy : The Basics. 1–11 (2008).
86. Holzer, L. & Marco, C. Reveiw of FIB Tomography. in *Nanofabrication Using Focused Ion and Electron Beams* 410–435 (2014).
87. Kato, N. I. Reducing focused ion beam damage to transmission electron microscopy samples. *J. Electron Microsc. (Tokyo).* **53**, 451–458 (2004).
88. Palmquist, A. *On a novel technique for preparation and analysis of the implant surface and its interface to bone*. (Inst of Clincial Sciences. Dept of Biomaterials, 2008).
89. Blanchard, C. R. Atomic Force Microscopy. *Chem. Educ.* **1**, 1–8 (1996).
90. Jalili, N. & Laxminarayana, K. A review of atomic force microscopy imaging systems: Application to molecular metrology and biological sciences. *Mechatronics* **14**, 907–945 (2004).
91. Mayer, M. Rutherford Backscattering Spectrometry (RBS). *Work. Nucl. Data Sci. Tecnol. Matelials Anal.* 59–78 (2003). doi:10.1016/1359-6454(95)00193-X
92. Kaxiras, E. A. Rutherford Backscattering Spectrometry (RBS). (2005). Available at: http://www.mrsec.harvard.edu/cams/RBS.html. (Accessed: 10th February 2017)
93. Birkholz, M. Thin Film Analysis by X-Ray Scattering. in *Thin Film Analysis by X-Ray Scattering* 1–378 (2005). doi:10.1002/3527607595.ch1
94. Li, W., Liang, R., Hu, A., Huang, Z. & Norman Zhou, Y. Generation of oxygen vacancies in visible light activated one-dimensional iodine TiO2 photocatalysts. *RSC Adv.* **4**, (2014).
95. Kaygili, O., Bulut, N., Tatar, C., Ates, T. & İnce, T. Sol-gel sythesis and charaterisation of TiO2 powder. *Int. J. Innov. Eng. Appl.* **1**, 38–40 (2017).
96. Ruth E. Wolf. What is ICP-MS? … and more importantly, what can it do? (2005). Available at: https://crustal.usgs.gov/laboratories/icpms/What_is_ICPMS.pdf. (Accessed: 10th February 2017)
97. Tanner, S. D., Baranov, V. I. & Bandura, D. R. Reaction cells and collision cells for ICP-MS : a tutorial review. **57**, 1361–1452 (2002).
98. Rao, B. & Tang, R. Green synthesis of silver nanoparticles with antibacterial activities using aqueous Eriobotrya japonica leaf extract. *Adv.Nat.Sci.Nanotechnol.* **8**, 8 (2017).
99. Wan, Y. Z. *et al.* Modification of medical metals by ion implantation of copper. *Appl. Surf. Sci.* **253**, 9426–9429 (2007).